Nanotechnology enabled microfluidics/Raman spectroscopy systems for bio applications

A thesis submitted in fulfilment of the requirements for the degree of
Doctor of Philosophy

Adam Francis Chrimes

BEng.

School of Electrical and Computer Engineering

RMIT University

May 2013

Nanotechnology enabled microfluidics/Raman spectroscopy systems for bio applications

Adam Francis Chrimes

(*Doctor of Philosophy*)

2012

RMIT University

Declaration

I certify that except where due acknowledgement has been made, the work is that of the author alone; the work has not been submitted previously, in whole or in part, to qualify for any other academic award; the content of the thesis is the result of work which has been carried out since the official commencement date of the approved research program; any editorial work, paid or unpaid, carried out by a third party is acknowledged; and, ethics procedures and guidelines have been followed.

…………………………………………..

Adam Francis Chrimes

Date: 14/05/2013

Acknowledgements

There have been many people who have helped me through the completion of this dissertation. Most importantly I would like to thank my senior supervisor Professor Kourosh Kalantar-zadeh for providing supervision over the PhD research program. In particular, I express my appreciation for his creative ideas, his thorough approach to writing and his advice for my future. He is passionately and genuinely interested in research, and his passion has helped to drive me towards success.

I am blessed to have been able to make several interdisciplinary contacts as part of this program, specifically Professor Paul Mulvaney from Melbourne University, Associate Professor Paul Stoddart from Swinburne University of Technology and Associate Professor Bayden Wood from Monash University. These people have provided fantastic suggestions and creative solutions for my work, as well as providing access to facilities, software and particles which would normally be unavailable to me. I would also like to thank my second supervisor, Associate Professor Vipul Bansal for his valuable suggestions and supervisory inputs into my PhD research program.

I also wish to thank several current and former researchers and students within the Microplatforms Research Group at the School of Electrical and Computer Engineering (SECE), RMIT University: Dr. Khashayar Khoshmanesh, Dr. Chen Zhang, Mr. Mahyar Nasabi, Ms. Pyshar Yi, Mr. Shi-yang Tang, Dr. Brendan McGrath, Dr. Jerry Yu, Dr. Jian Ou, Mr. Sumeet Walia, Mr. David Yao and Mr. Shiva Balendhran for their assistance, and for providing an atmosphere conducive for conducting the research. My work would not be possible without access to the proper facilities; as such I would like to thank the people who work hard to keep these facilities operational. Specifically, Mr. Philip Francis of the Department of Applied Physics, RMIT University, for his oversight of the RMIT Microscopy and Microanalysis Facility as well has his specific interests in helping me achieve high resolution imaging using the electron microscopes. Additionally, I would like to thank Mr. Paul Jones, Mr. Yuxun Cao and Ms. Chiping Wu of the Microelectronics, Materials and Technology Centre, RMIT University, for their technical expertise and advice using vacuum, clean room and miro-machining equipment.

My work would not have been possible if it were not for the Australian Department of Industry, Innovation, Science, Research and Tertiary Education for providing me with the Australian Postgraduate Awards (APA) scholarship. I would also like to acknowledge financial support from the School of Electrical and Computer engineering for providing funding for research equipment, software and top-up payments. I would also like to thank the School of Graduate Research, the School of Electrical and Computer Engineering and the Pro Vice Chancellor Research and Innovation’s office for providing me with funding to attend two international conferences, which provided invaluable opportunities to present my work to a much wider audience, and allowed me to develop several international contacts. I would also like to mention the inputs from the Commonwealth Scientific and Industrial Research Organisation (CSIRO) for providing me with a travel grant to attend and present at a conference at their research campus in New South Wales, Australia.

Dedication

To my beloved wife Chenoa, who stuck by me and supported me throughout the entire process.

Abstract

The vision for this PhD research project was born out of a desire to study the *in situ* behaviour of suspended nano-materials; specifically, implementing a Raman microscopy system for investigating suspended materials in the microfluidic environment. The author developed a set of innovative research goals to achieve this vision, which include: (1) forming a suitable microfluidic system which can apply controlled forces onto the suspended materials on demand, (2) implementing Raman microscopy to study the behaviour of particles under the influence of such forces while inside the microfluidic system and (3) incorporating the developed microfluidic system for investigating suspended materials of low concentration, including biological cells and surface-enhanced Raman scattering studies.

The author comprehensively reviewed devices and concepts that integrate both Raman microscopy and microfluidic systems, which are progressively finding their way into real world applications for characterising chemical species and cells. Additionally, the author also reviewed many data analytical techniques used for the interpretation of Raman microscopic data. Dielectrophoresis (DEP), the force induced on a particle in the presence of a non-uniform electric field, was chosen as a suitable candidate for manipulating suspended particles in microfluidics, as it is capable of controlling particles with minimal damage or interference. Consequently, using the DEP force, the author demonstrated the novel integration of Raman microscopy with microfluidic systems for the study of inorganic, organic and cellular materials.

The author implemented the research in three distinct stages such that the work in earlier stages could provide the platform for the future work. In the first stage, the author designed a microfluidic dielectrophoresis platform consisting of curved microelectrodes. This platform was integrated with a micro Raman spectroscopy system for creating a novel system capable of detecting suspended particles of various types and spatial concentrations. The curved DEP microelectrodes were patterned on a quartz substrate, which has insignificant Raman response. The system was benchmarked using polystyrene and tungsten trioxide suspended particles, and the outcomes of this novel integrated system showed its strong potential for the determination of suspended particles types and their direct mapping, with several

unique advantages over conventional optical systems.

In the second stage of this research, the author developed a novel microfluidic-DEP system that could manipulate suspended silver nanoparticles' spacing in three dimensions. Silver nanoparticles are capable of producing strong surface enhanced Raman scattering (SERS) signals, allowing the Raman system to detect very low concentrations of suspended analytes. DEP provided facile control of the positions and spacings of the suspended silver nanoparticles, and allowed for the creation of SERS hot-spots. The system was studied to determine the optimum DEP and microfluidic flow parameters for generating SERS, and the author was able to demonstrate this as a reversible process. This stage of the research used dipicolinic acid as the target analyte, and the system was demonstrated to have detection limits as small as ~1 ppm concentration levels. The validity of the results was investigated using several complementing characterization scenarios.

In the third stage, the microfluidic-DEP platform was used for trapping and isolating yeast cells. Silver nanoparticles were again used for SERS applications, where the silver nanoparticles were incubated with the cells, attaching to the yeast cell wall. The trapped cells were interrogated by the Raman system in order to obtain deeper understandings of cells functionalities and their communications. As such, the SERS response of cells was examined under various physical conditions: live *vs.* dead and isolated *vs.* grouped. Live *vs.* dead experiments were conducted as a benchmark, to observe whether SERS is capable of differentiating cells based on the life condition. Additionally, multivariable analysis was utilized to determine what Raman signatures were contributing to the differences between the dead and live cell spectrum, and hence what chemical signatures contribute to such a difference. This stage of the research was expanded to study cells that were isolated from one another, and compared those Raman signatures to those from cells in grouped clusters. Multivariable analysis was again used for determining the differences in cell wall chemical constituents between the two experimental conditions. The author was able to extract unique information from such studies, including the importance of glycine, or proteins with glycine subunits, in the proliferation of yeast cells. The developed system showed great potential as a universal platform for the *in situ* study of cells, their communications and functionalities.

List of symbols

T	absolute temperature
A	aspect ratio
k	Boltzmann constant
$f_{CM}(\omega)$	Clausius-Mossotti (CM) factor
σ	conductivity
ρ	density
$\vec{F}_{DEP}$	dielectrophoretic force
x	displacement
E	electric field
ω	electric field angular frequency
f	focal length
f	friction factor
g_z	gravitational acceleration
P	induced dipole moment
kHz	kilohertz
D	lens diameter
MHz	megahertz
$K_{surface}$	particle surface conductivity
μ	permeability
ε	permittivity
ε_o	permittivity of free space
φ	phase component of the applied electric field
r	radius
$\varepsilon_{\mathrm{medium}}$	relative permittivity of the medium
d	spot size diameter
t	time
ϕ	volume fraction
λ	wavelength
$\Delta\lambda$	wavelength shift

List of abbreviations

AC	alternating current
ADS	advanced design systems
AFM	atomic force microscopy
BSA	bovine serum albumin
CARS	coherent anti-Stokes Raman spectroscopy
CCD	charged couple device
CHO	Chinese hamster ovary
CNC	computer numerical control
DEP	dielectrophoresis
DI	de-ionised
DNA	deoxyribonucleic acid
DPA	dipicolinic acid (2,6-Pyridinedicarboxylic acid)
FTIR	Fourier transform infrared spectroscopy
HCA	hierarchal cluster analysis
IVF	*in vitro* fertilisation
LOC	lab-on-a-chip
NA	numerical aperture
NIR	near-infrared
PAA	polyacrylic acid
PC	principal component
PCA	principal component analysis
PCR	principal component regression
PDMS	polydimethylsiloxane
PLS	partial least squares
ppm	parts per million
rms	root-mean-squared
RNA	ribonucleic acid
SERRS	surface-enhanced resonance Raman spectroscopy
SERS	surface-enhanced Raman scattering

SORS	spatially offset Raman spectroscopy
SRG	stimulated Raman gain
SRL	stimulated Raman loss
SRS	stimulated Raman scattering
SWCNT	single-wall carbon nanotube
TERS	tip-enhanced Raman spectroscopy
UDS	user defined scalar
UV	ultraviolet
UV-Vis	ultraviolet visible absorption
WO_3	tungsten trioxide
XPS	x-ray photoemission spectroscopy

List of figures

Table of contents

Chapter 1

Introduction

1.1 Motivation

Microfluidics is currently a highly active field, particularly in the context of lab-on-a-chip (LOC) systems. The field of microfluidics emerged in the early 1980s and it is now routinely used in a variety of commercial applications including inkjet print-heads, LOC systems, deoxyribonucleic acid (DNA) chips, and micro-thermal cooling devices to name just a few. In brief, microfluidics includes systems that allow for precise manipulation of fluids that are geometrically constrained to small volumes, in the order of micro- and pico-litres [1, 2].

Microfluidic systems are becoming increasingly attractive in chemistry and biochemistry, as they allow for the miniaturisation of systems that are normally employed in those laboratories. Microfluidic systems are also useful tools for the handling of fluids and suspended materials. As such, they improve the efficiency of procedures by enhancing material mobility and vastly reducing required sample volumes. Advances in microfluidics have resulted in the creation of many innovative technologies in molecular biology processes, proteomics and DNA analysis [2-5]. These systems will attract more users for applications in health and safety, diagnostics, industrial processes, pharmaceuticals, forensics, food and quality control, to name just a few.

The measurement of parameters in microfluidics is performed using transducers, which are required to operate with high sensitivity on small volumes of fluids. Examples of potential parameters to monitor include flow rate [6, 7], viscosity [8], heat transfer [9], temperature [10], electrical impedance [11, 12], permittivity [13], refractive index [14] and other optical properties [15]. Transducers can be integrated into microfluidic devices, onto the surface of the substrates, on the walls of the microchannels or integrated within the microfluidic structures. They can be in direct contact with the fluids, or they can be fabricated so as to enable contactless detection. Some examples of non-optical, non-contact methods of detection that exist include capacitance sensors [11], piezoelectric transducers [16-18] and magnetoelectronic detection [19]. Transducers can be electrochemical, acoustic, thermal, electromagnetic and optical.

Optical and spectroscopic analysis techniques that are integrated into microfluidic platforms can exploit both absorption and scattering techniques, and have been extensively reported [20-22]. Different types of spectroscopy systems have been used with microfluidics, including ultraviolet visible absorption (UV-Vis), Fourier transform infrared spectroscopy (FTIR), fluorescence spectroscopy and Raman spectroscopy (inelastic scattering). Amongst these techniques, Raman spectroscopy has proven to be highly compatible with microfluidics. Driven by improvements in hardware, this technique has largely overcome the concern that it is a “weak effect,” as Raman scattering signal intensities are much smaller than their other spectroscopic counterparts [23]. When dealing with low volume samples, and possibly low concentration analytes, Raman microscopy provides sub-micron spatial resolution with very high sensitivity and selectivity for microfluidic systems. Raman microscopy can also provide information regarding target materials very rapidly, with latencies measured in the order of seconds, or even fractions of a second, allowing for real-time monitoring processes to be practically considered in such systems. Furthermore, Raman-microfluidic systems can be employed for the study of suspended materials and particles in liquids.

The investigation of suspended micro and nanoparticles’ properties is of utmost importance for the understanding and determination of their optical, electronic, mechanical and chemical behaviours. These studies are used for answering fundamental questions such as: how particles interact with each other in suspended forms [24]; how they exchange electrons, photons or phonons when they are in the close affinity to each other in liquid media [25, 26]; and how they interact with the chemical components surrounding them [27]. Raman microscopy provides the ideal method for the in situ monitoring of suspended materials. Raman spectroscopic data provides an optical ‘fingerprint’ of the target materials, detailing their structure, composition and chemical interactions.

Nanoparticles with strong Raman activity are ideal candidates for in-depth study and characterisation of systems which integrate Raman microscopy microfluidics. Nanoparticles of metal oxides or polymers are ideal nanoparticles, and can be used for Raman mapping and depth profiling of microfluidic systems. Raman microscopy is able to determine the local concentrations of suspended materials, and using the correct data processing techniques, can be used to generate Raman images of the system under differing operating conditions. This novel implementation of Raman-microfluidics will help shed light on an as-yet unknown phenomenon.

Additionally, microfluidic systems can enhance such studies by implementing active control of the nanoparticles positions and concentrations within the fluids. This is especially useful for microfluidic systems which implement surface-enhanced Raman scattering (SERS) [25, 28-30], as accurate control of the SERS generating materials can create localized optical ‘hot-spots’ for enhanced detection. The integration of SERS spectroscopy with microfluidics offers additional benefits including the significant reduction in analyte and reagent volumes required for analysis, accurate control of flow rates and other environmental parameters, facile manipulation of analytes, and moreover, low costs of both instruments and measurement processes [31, 32].

However, SERS bio applications are still mainly limited to research laboratories. The main reason arises from the fact that the current systems are mostly passive, and there is minimal control over the formation of SERS enhancing nanostructures in either two or three dimensions in microfluidics [33].

Current limitation for SERS-microfluidic systems is focused on the difficulties in the integration of nanoparticles and nanostructures into microfluidics, control of their spacing, limitation in the formation of nanostructures on the surfaces rather than in the bulk of the microfluidics and costly procedures [34]. Amongst these, the control of spacing between the flowing nanoparticles or the spacing between nanostructures anchored to the surface appears to be a crucial step, as this significantly influences the SERS signal intensity. The intensities of SERS signals are of particular importance for obtaining the low detection limits necessary for many bio-applications [30].

Implementing nanoparticles in microfluidics, instead of the nanostructured surfaces, provides the opportunity of controlling their spacings. There are several examples of SERS using suspended silver nanoparticles, including the recent works by Guerrini *et al.* [35] and Futama *et al.* [36] who successfully demonstrated the detection of selected analytes using suspended and dry silver nanoparticle aggregates. However, such examples are based on aggregating chemical agents, which suffer from many limitations. Obviously, these passive methods of the aggregation of nanoparticles are still limited in the control of the spacing to desired values and are mostly based on trial and error approaches. Additionally, the duration of the aggregation process is not readily controllable using chemicals, and the SERS signals are generally lost when the process continues.

This demonstrates a need for an alternative approach for controlling the location of SERS generating nanoparticles - one that does not need aggregating chemicals, does not interfere with Raman spectroscopy or require large amounts of power (optical or otherwise), and can provide real-time manipulation of the inter-particle spacing. An external force can be more efficiently used to control the real-time spacing between the particles. One advantage of such external forces, as opposed to passive chemical methods, is that the SERS analysis will become independent of the chemical aggregating agent. Another advantage is that any possible interference by aggregating agents on the SERS signals will be removed, creating a more reliable SERS platform for the target analyte. Finally, the system can be universally used for all SERS measurement scenarios with minimal requirements for changing the chemical recipes each time.

The high sensitive of SERS in microfluidics opens the door to many potential applications. As such, it would be possible to measure very small levels of analytes and molecules suspended in liquid. Specifically, molecules exchanged between cells. The study of suspended cells using microfluidics had been studied [4, 37, 38], however the author proposes that SERS is capable of measuring chemical ‘signals’ exchanged between cells, and with the application of suitable forces, it is possible to immobilise cells into specific clusters and study their interactions.

1.2 Objectives

The research work for this PhD thesis will use a controllable, active and non-contact force for manipulation of suspended materials. In the following work, dielectrophoresis (DEP), the induced motion of neutral particles in non-uniform electric fields [39, 40], provides the controlling feature. Dielectrophoretic manipulations have been widely applied to nano, meso and micro scale materials in microfluidics [41]. By changing the applied voltage and frequency, materials can be focused to, or repelled from pre-determined locations within the microchannels. Such a capability provides a perfect base for the demonstration of microfluidics and Raman spectroscopy as a tool for the mapping, recognizing and measuring of materials. The integration of microfluidics and DEP has been the key in the development of many new and exciting micro-platforms. These platforms have been used in applications such as particle counting [42, 43], particle sorting of both organic [44-49] and inorganic [41, 50] particles, opto-fluidics [51, 52] and for the creation of electronic devices [53, 54].

Throughout his PhD candidature, the author has focussed on studying the integration of Raman microscopy with microfluidics, while utilising dielectrophoresis as a controlling feature. The gaps in current knowledge have been highlighted and as such, the primary objectives of this PhD work are targeted towards those gaps as follows:

1. The author of this PhD thesis will first demonstrate that by integrating Raman spectroscopy with a microfluidic system, the resultant system can be used to map the concentration and type of suspended nanoparticles within the microchannel. In order to show the functionality of this system, DEP is used to manipulate suspended nanoparticles, producing regions of high and low particle concentrations within the microchannel. It will be shown that the integration of DEP and Raman spectroscopy can be a powerful tool for *in situ* analysis of suspended inorganic (WO_3) and organic (polystyrene) particles.

2. Raman-microfluidic systems can be improved with the application of SERS. SERS is capable of detecting low concentration analytes, such as dipicolinic acid. Silver colloid will be used for generating SERS, as it is commercially available for such applications. DEP forces are used for the manipulation of the positions, and hence, the inter-particle spacing of suspended silver nanoparticles dynamically. This will demonstrate the advantages of the integrated Raman-DEP microfluidic system to actively control the spacing of nanoparticles for generating large SERS signals. A series of benchmarking measurements with different chemical analytes is presented using dipicolinic acid as the target analyte in order to prove the validity of the approach.

3. Furthermore, the author uses the DEP-microfluidic platform with SERS for studying the chemical signals being exchanged between cells. Yeast cells will be introduced to the Raman-microfluidic device, where the trapping forces will immobilise a desired number of yeast cells in either direct contact or greater than 10 µm from each other. It will be shown that SERS can clearly differentiate between live and dead cells. Subsequently, live cells are immobilized into “isolated” and “grouped” cell clusters in order to investigate the differences in molecule secretion.

1.3 Thesis organisation

This thesis is primarily dedicated to investigating the integrations of Raman microscopy within microfluidics, while implementing DEP as a control component in the microfluidic environment. The major sections of this thesis are listed as below:

Chapter 2 provides the literature review of this thesis. This chapter begins by briefly describing the principals of operation for Raman microscopy and microfluidics. The author then discusses current applications of such systems, organising applications based on the type of materials being detected. Raman microscopy data analysis is also discussed, with focus on both quantitative and qualitative analysis methods. The chapter concludes with a summary review of dielectrophoresis, including both theory and applications.

Chapter 3 describes in detail, the design and fabrication of the experimental platform used in this PhD thesis.

Chapter 4 begins with numerical simulations of the designed platform for use with suspended nanoparticles of WO_3 and polystyrene, in order to determine its operating characteristics in terms of dielectrophoretic performance. Subsequently, the platform was thoroughly studied with Raman microscopy for spatial and depth profiling of the resulting *in situ* particle aggregates.

Chapter 5 presents the SERS detection of analytes using well-controlled suspended silver colloid. DEP was used to provide precise control over the spacings of the silver colloid in order to optimise the SERS measurements of the analyte. Dipicolinic acid at 10 and 100 ppm concentrations were successfully detected and studied using the platform, with only minor modifications needed to the DEP microelectrode design.

Chapter 6 presents the study of trapped yeast cells in a microfluidic environment. The cells were coated with silver nanocolloid to enable SERS detection. DEP was implemented in the microchannel in order to trap the cells, where cells were capable of being trapped into various group sizes (1 cell, 2 cells, or many cells). The resulting SERS spectra were analysed using principal component analysis, where it was found that glycine was a potential biomarker for the onset of cell proliferation.

Finally, Chapter 7 presents the concluding remarks and suggests possible future works.

References

[1] West, J., M. Becker, S. Tombrink, and A. Manz, Micro total analysis systems: Latest achievements. *Analytical Chemistry,* vol. 80, pp. 4403-4419, 2008.

[2] Zhang, C. and D. Xing, Single-Molecule DNA Amplification and Analysis Using Microfluidics. *Chemical Reviews,* vol. 110, pp. 4910-4947, 2010.

[3] Chandra, H., P.J. Reddy, and S. Srivastava, Protein microarrays and novel detection platforms. *Expert review of proteomics,* vol. 8, pp. 61-79, 2011.

[4] Chao, T.-C. and A. Ros, Microfluidic single-cell analysis of intracellular compounds. *Journal of The Royal Society Interface,* vol. 5, pp. S139-S150, 2008.

[5] Mairhofer, J., K. Roppert, and P. Ertl, Microfluidic Systems for Pathogen Sensing: A Review. *Sensors,* vol. 9, pp. 4804-4823, 2009.

[6] Rasmussen, A., C. Mavriplis, M. Zaghloul, O. Mikulchenko, and K. Mayaram, Simulation and optimization of a microfluidic flow sensor. *Sensors and Actuators A: Physical,* vol. 88, pp. 121-132, 2001.

[7] Lien, V. and F. Vollmer, Microfluidic flow rate detection based on integrated optical fiber cantilever. *Lab on a Chip,* vol. 7, pp. 1352-1356, 2007.

[8] Etchart, I., H. Chen, P. Dryden, J. Jundt, C. Harrison, K. Hsu, F. Marty, and B. Mercier, MEMS sensors for density–viscosity sensing in a low-flow microfluidic environment. *Sensors and Actuators A: Physical,* vol. 141, pp. 266-275, 2008.

[9] Yi, P., A.A. Kayani, A.F. Chrimes, K. Ghorbani, S. Nahavandi, K. Kalantar-zadeh, and K. Khoshmanesh, Thermal analysis of nanofluids in microfluidics using an infrared camera. *Lab on a Chip,* vol. 12, pp. 2520-2525, 2012.

[10] Gosse, C., C. Bergaud, and P. Löw, Molecular Probes for Thermometry in Microfluidic Devices. in *Thermal Nanosystems and Nanomaterials*. vol. 118, Volz, S., Ed., ed: Springer Berlin Heidelberg, 2009, pp. 301-341.

[11] Murran, M.A. and H. Najjaran, Capacitance-based droplet position estimator for digital microfluidic devices. *Lab on a Chip,* vol. 12, pp. 2053-2059, 2012.

[12] Collins, J. and A.P. Lee, Microfluidic flow transducer based on the measurement of electrical admittance. *Lab on a Chip,* vol. 4, pp. 7-10, 2003.

[13] Seo, S., T. Stintzing, I. Block, D. Pavlidis, M. Rieke, and P.G. Layer, High frequency wideband permittivity measurements of biological substances using coplanar waveguides and application to cell suspensions. in *Microwave Symposium Digest, 2008 IEEE MTT-S International*, 2008, pp. 915-918.

[14] Kayani, A.A., A.F. Chrimes, K. Khoshmanesh, K. Kalantar-zadeh, and A. Mitchell, Tuneable Optical Waveguide Based on Dielectrophoresis and Microfluidics. Presented at the Micro- and Nanotechnology Sensors, Systems, and Applications Iii - SPIE, 2011.

[15] Kayani, A.A., K. Khoshmanesh, S.A. Ward, A. Mitchell, and K. Kalantar-zadeh, Optofluidics incorporating actively controlled micro- and nano-particles. *Biomicrofluidics,* vol. 6, pp. 031501-32, 2012.

[16] Lee, A.P., M.V. Patel, A.R. Tovar, and Y. Okabe, Microfluidic Air-Liquid Cavity Acoustic Transducers for On-Chip Integration of Sample Preparation and Sample Detection. *Jala,* vol. 15, pp. 449-454, 2010.

[17] Lee, A. and M. Patel, Microfluidic air-liquid cavity acoustic transducers for point-of-care diagnostics applications. *The Journal of the Acoustical Society of America,* vol. 132, pp. 1953-1953, 2012.

[18] Patel, M.V., A.R. Tovar, and A.P. Lee, Lateral cavity acoustic transducer as an on-chip cell/particle microfluidic switch. *Lab on a Chip,* vol. 12, pp. 139-145, 2012.

[19] Miller, M.M., P.E. Sheehan, R.L. Edelstein, C.R. Tamanaha, L. Zhong, S. Bounnak, L.J. Whitman, and R.J. Colton, A DNA array sensor utilizing magnetic microbeads and magnetoelectronic detection. *Journal of Magnetism and Magnetic Materials,* vol. 225, pp. 138-144, 2001.

[20] Gupta, R., B. Bastani, N.J. Goddard, and B. Grieve, Absorption spectroscopy in microfluidic flow cells using a metal clad leaky waveguide device with a porous gel waveguide layer. *Analyst,* vol. 138, pp. 307-314, 2013.

[21] Sabuncu, A.C., J. Zhuang, J.F. Kolb, and A. Beskok, Microfluidic impedance spectroscopy as a tool for quantitative biology and biotechnology. *Biomicrofluidics,* vol. 6, pp. 034103-15, 2012.

[22] Kayani, A.A., A.F. Chrimes, K. Khoshmanesh, V. Sivan, E. Zeller, K. Kalantar-zadeh, and A. Mitchell, Interaction of guided light in rib polymer waveguides with dielectrophoretically controlled nanoparticles. *Microfluidics and Nanofluidics,* vol. 11, pp. 93-104, 2011.

[23] Adar, F., M. Delhaye, and E. DaSilva, Evolution of Instrumentation for Detection of the Raman Effect as Driven by Available Technologies and by

Developing Applications. *Journal of Chemical Education,* vol. 84, p. 50, 2007.

[24] Piorek, B.D., S.J. Lee, J.G. Santiago, M. Moskovits, S. Banerjee, and C.D. Meinhart, Free-surface microfluidic control of surface-enhanced Raman spectroscopy for the optimized detection of airborne molecules. Presented at the Proceedings of the National Academy of Sciences of the United States of America, 2007.

[25] Hou, D., S. Maheshwari, and H.C. Chang, Rapid bioparticle concentration and detection by combining a discharge driven vortex with surface enhanced Raman scattering. *Biomicrofluidics,* vol. 1, p. 014106, 2007.

[26] Walsh, A.G., A.N. Vamivakas, Y. Yin, S.B. Cronin, M.S. Unlu, B.B. Goldberg, and A.K. Swan, Screening of excitons in single, suspended carbon nanotubes. *Nano Letters,* vol. 7, pp. 1485-1488, 2007.

[27] de Almeida, M.P.S., K.L. Caiado, P.P.C. Sartoratto, D. Silva, A.R. Pereira, and P.C. Morais, Preparation and size-modulation of silica-coated maghemite nanoparticles. *Journal of Alloys and Compounds,* vol. 500, pp. 149-152, 2010.

[28] Keir, R., E. Igata, M. Arundell, W.E. Smith, D. Graham, C. McHugh, and J.M. Cooper, SERRS. In situ substrate formation and improved detection using microfluidics. *Analytical Chemistry,* vol. 74, pp. 1503-1508, 2002.

[29] Connatser, R.M., L.A. Riddle, and M.J. Sepaniak, Metal-polymer nanocomposites for integrated microfluidic separations and surface enhanced Raman spectroscopic detection. *Journal of Separation Science,* vol. 27, pp. 1545-1550, 2004.

[30] Park, T., S. Lee, G.H. Seong, J. Choo, E.K. Lee, Y.S. Kim, W.H. Ji, S.Y. Hwang, and D.G. Gweon, Highly sensitive signal detection of duplex dye-labelled DNA oligonucleotides in a PDMS microfluidic chip: confocal surface-enhanced Raman spectroscopic study. *Lab on a Chip,* vol. 5, pp. 437-442, 2005.

[31] Figeys, D. and D. Pinto, Lab-on-a-chip: A revolution in biological and medical sciences. *Analytical Chemistry,* vol. 72, pp. 330A-335A, 2000.

[32] Skoog, D.A., *Fundamentals of analytical chemistry*. 8 ed. 2004: Thomson-Brooks/Cole.

[33] Canamares, M.V., J.V. Garcia-Ramos, S. Sanchez-Cortes, M. Castillejo, and M. Oujja, Comparative SERS effectiveness of silver nanoparticles prepared by different methods: A study of the enhancement factor and the interfacial properties. *Journal of Colloid and Interface Science,* vol. 326, pp. 103-109, 2008.

[34] Lee, S., S. Joo, S. Park, S. Kim, H.C. Kim, and T.D. Chung, SERS decoding of micro gold shells moving in microfluidic systems. *Electrophoresis,* vol. 31, pp. 1623-1629, 2010.

[35] Guerrini, L., S. Sanchez-Cortes, V.L. Cruz, S. Martinez, S. Ristori, and A. Feis, Surface-enhanced Raman spectra of dimethoate and omethoate. *Journal of Raman Spectroscopy,* vol. 42, pp. 980-985, 2011.

[36] Futamata, M., Y.Y. Yu, and T. Yajima, Elucidation of Electrostatic Interaction between Cationic Dyes and Ag Nanoparticles Generating Enormous SERS Enhancement in Aqueous Solution. *Journal of Physical Chemistry C,* vol. 115, pp. 5271-5279, 2011.

[37] Bantz, K.C., A.F. Meyer, N.J. Wittenberg, H. Im, O. Kurtulus, S.H. Lee, N.C. Lindquist, S.H. Oh, and C.L. Haynes, Recent progress in SERS biosensing.

Physical Chemistry Chemical Physics, vol. 13, pp. 11551-11567, 2011.

[38] Bhagat, A., H. Bow, H. Hou, S. Tan, J. Han, and C. Lim, Microfluidics for cell separation. *Medical & Biological Engineering & Computing,* vol. 48, pp. 999-1014, 2010.

[39] Krupke, R., S. Linden, M. Rapp, and F. Hennrich, Thin films of metallic carbon nanotubes prepared by dielectrophoresis. *Advanced Materials,* vol. 18, pp. 1468-1470, 2006.

[40] Pohl, H.A., *Dieletrophoresis*. 1978, Oklahoma: Cambridge University Press.

[41] Zhang, C., K. Khoshmanesh, F.J. Tovar-Lopez, A. Mitchell, W. Wlodarski, and K. Kalantar-zadeh, Dielectrophoretic separation of carbon nanotubes and polystyrene microparticles. *Microfluidics and Nanofluidics,* vol. 7, pp. 633-645, 2009.

[42] Constantino, C.J.L., T. Lemma, P.A. Antunes, and R. Aroca, Single-molecule detection using surface-enhanced resonance Raman scattering and Langmuir-Blodgett monolayers. *Analytical Chemistry,* vol. 73, pp. 3674-3678, 2001.

[43] Ghubade, A., S. Mandal, R. Chaudhury, R.K. Singh, and S. Bhattacharya, Dielectrophoresis Assisted Concentration of Micro-particles and their Rapid Quantitation Based on Optical Means. *Biomedical Microdevices,* vol. 11, pp. 987-995, 2009.

[44] Bhatt, K.H. and O.D. Velev, Control and Modeling of the Dielectrophoretic Assembly of On-chip Nanoparticle Wires. *Langmuir,* vol. 20, pp. 467-476, 2004.

[45] Fiedler, S., S.G. Shirley, T. Schnelle, and G. Fuhr, Dielectrophoretic Sorting of Particles and Cells in a Microsystem. *Analytical Chemistry,* vol. 70, pp. 1909-1915, 1998.

[46] Khoshmanesh, K., C. Zhang, F.J. Tovar-Lopez, S. Nahavandi, S. Baratchi, A. Mitchell, and K. Kalantar-zadeh, Dielectrophoretic-activated cell sorter based on curved microelectrodes. *Microfluidics and Nanofluidics,* vol. 9, pp. 411-426, 2010.

[47] Lapizco-Encinas, B.H., B.A. Simmons, E.B. Cummings, and Y. Fintschenko, Dielectrophoretic concentration and separation of live and dead bacteria in an array of insulators. *Analytical Chemistry,* vol. 76, pp. 1571-1579, 2004.

[48] Lapizco-Encinas, B.H., B.A. Simmons, E.B. Cummings, and Y. Fintschenko, Insulator-based dielectrophoresis for the selective concentration and separation of live bacteria in water. *Electrophoresis,* vol. 25, pp. 1695-1704, 2004.

[49] Pohl, H.A. and J.S. Crane, Dielectrophoresis of cells. *Biophysical Journal,* vol. 11, pp. 711-727, 1971.

[50] Green, N.G. and H. Morgan, Dielectrophoretic separation of nano-particles. *Journal of Physics D: Applied Physics,* vol. 30, pp. L41-L44, 1997.

[51] Kalantar-zadeh, K., K. Khoshmanesh, A.A. Kayani, S. Nahavandi, and A. Mitchell, Dielectrophoretically tuneable optical waveguides using nanoparticles in microfluidics. *Applied Physics Letters,* vol. 96, p. 101108, 2010.

[52] Kayani, A.A., C. Zhang, K. Khoshmanesh, J.L. Campbell, A. Mitchell, and K. Kalantar-zadeh, Novel tuneable optical elements based on nanoparticle suspensions in microfluidics. *Electrophoresis,* vol. 31, pp. 1071-1079, 2010.

[53] Lee, S.Y., T.H. Kim, D.I. Suh, N.K. Cho, H.K. Seong, S.W. Jung, H.J. Choi, and S.K. Lee, A study of dielectrophoretically aligned gallium nitride nanowires in metal electrodes and their electrical properties. *Chemical*

Physics Letters, vol. 427, pp. 107-112, 2006.

[54] Wang, D.Q., R. Zhu, Z.Y. Zhou, and X.Y. Ye, Controlled assembly of zinc oxide nanowires using dielectrophoresis. *Applied Physics Letters,* vol. 90, p. 103110, 2007.

Chapter 2

Literature review

2.1 Introduction

The author of this thesis conducted a comprehensive literature review on Raman microscopy integrations with microfluidic devices. This was to reveal the state of the art application and methods in the field, and provide the information needed prior to the conduction of the PhD research. As such, the material of this chapter has been published as an invited paper to the prestigious journal of Chemical Society Reviews [1].

In this chapter, the author reviews Raman microscopy and microfluidics, with a focus on their integration and applications. This review is of the utmost importance as it highlights the considerations that must be understood for successful integration of Raman microscopy with microfluidic devices used in this PhD research. The author organises this into three categories, Raman microscopy, microfluidic configuration and applications.

Additionally, the author reviews the data analysis techniques that can be used for studying Raman spectroscopic data. This knowledge is essential for proper interpretation and characterisation of the data, and is organised into either qualitative or quantitative techniques. Both of these techniques are relevant for this PhD research. This chapter also includes an extended review of dielectrophoresis (DEP), including both theory and applications.

2.2 Microfluidics and Raman microscopy: a brief background

Microfluidics is currently a highly active field, particularly in the context of lab-on-a-chip (LOC) systems. Microfluidics allows for the flexible and highly controlled manipulation of liquids, suspended particles and biological samples. It is also well-known that Raman microscopy is a powerful tool that can provide unparalleled insight into the organic and inorganic chemical components and biomaterials at low sample volumes. Combining Raman microscopy with microfluidics allows for the accurate monitoring, analysis and detection of a wide range of samples in microfluidic environments.

The Raman phenomenon was first discovered by Sir Chandrasekhara V. Raman in the 1920s [2], and since then, progress has been made in understanding the mechanisms and theoretical descriptions of the effect. Raman spectroscopy is particularly suited for analytical chemistry, given that it is generally non-destructive, requires little or no sample preparation, offers high discrimination between sample components and is capable of studying gaseous, aqueous and solid samples [3-6].

Raman microscopy is an advanced spectroscopic technique, incorporating optical microscopes, excitation lasers, optical filtering and manipulation devices, and spectrometers, which offer the advantages of high spatial resolution and optical sensitivity, due to the increased photon flux from the highly focused laser source and high collection efficiency of the objective lens. By providing specific information about the vibrational energy levels of chemical bonds and molecules, Raman microscopy is an invaluable tool for ‘fingerprinting’ materials, and is certainly finding increasing applications in medicine, biotechnology, material sciences and even forensics [7-10].

The field of microfluidics emerged in the early 1980s and it is now routinely used in a variety of commercial applications including inkjet print-heads, LOC systems, deoxyribonucleic acid (DNA) chips, and micro-thermal cooling devices to name just a few. In brief, microfluidics includes systems that allow for precise manipulation of fluids that are geometrically constrained to small volumes, in the order of micro- and pico-litres [11, 12].

Microfluidic systems are becoming increasingly attractive in chemistry and biochemistry, as they allow for the miniaturisation of systems that are normally employed in those laboratories. Microfluidic systems are also useful tools for the handling of fluids and suspended materials. As such, they improve the efficiency of procedures by enhancing material mobility and vastly reducing required sample volumes. Advances in microfluidics have resulted in the creation of many innovative technologies in molecular biology processes, proteomics and DNA analysis [12-15].

Microfluidic platforms that integrate optical and spectroscopic analysis, exploiting both absorption and scattering techniques, have been extensively reported [16, 17]. Different types of spectroscopy systems have been used with microfluidics, including ultraviolet visible absorption (UV-Vis), Fourier transform infrared spectroscopy (FTIR), fluorescence spectroscopy and Raman spectroscopy (inelastic scattering). Amongst these techniques, Raman spectroscopy has proven to be highly compatible with microfluidics. Driven by improvements in hardware, the technique has largely overcome the concern that it is a “weak effect,” as Raman scattering signal intensities are much smaller than their other spectroscopic counterparts [18]. When dealing with low volume samples, and possibly low concentration analytes, Raman microscopy provides sub-micron spatial resolution with very high sensitivity and selectivity for microfluidic systems. Raman microscopy can also provide information regarding target materials very rapidly, with latencies measured in the order of seconds, or even fractions of a second, allowing for real-time monitoring processes to be practically considered in such systems.

Raman microscopy integrations with microfluidic systems (“Raman-microfluidics”) have already found a plethora of applications in the analysis of materials from low volume liquid media, especially when samples are rare and expensive (medical samples; forensic traces and pharmaceuticals), in microreactors for which constant monitoring is required (pre-processing of biochemical samples and tissue engineering) and monitoring of environmental samples (water quality and biosensing). This track record suggests that the integration of Raman microscopy as a powerful analytical tool, with the unique properties of microfluidics, will open the door to many other important applications.

2.3 Raman microscopy: methods of application

2.3.1 Instrument details and optimization

The Raman effect takes place when light illuminates a region, interacting with the molecules that are present in this region. The incident photons do not have sufficient energy to excite a quantum transition from one stable electron configuration to another, but the photon interaction does perturb the electron configuration of the molecule exciting it to an intermediate, unstable ‘virtual’ state. The molecules relax rapidly from this virtual state, reemitting a photon. Most commonly, this photon has the same energy, (and therefore frequency and wavelength) as that of the incident photon. However, a small fraction of photons, (on the order of 1 in 10^6), are reemitted with a change in energy (and hence frequency). The difference in energy can be attributed to energy gained or lost to vibrational energy in the molecule. As such, the photon energy can be shifted to lower or higher frequencies depending on whether they lose or gain energy. These shifts in frequencies are called Stokes and anti-Stokes shifts respectively. For molecules to exhibit the Raman effect they must have non-zero polarisability, that is to say that an incident photon must be able to effectively deform the electron configuration of the molecule. The degree of this deformation determines the Raman scattering intensity, due to resonant interactions with the rotational and vibrational states of the molecule.

In Raman microscopy, a laser beam is focussed onto the target sample through a microscope objective lens. The lens also collects the light, which is backscattered from the sample, and passes it to the spectrometer via a dichroic (colour separating) filter. Before entering the spectrometer, the elastically scattered Rayleigh wavelength (with the same wavelength as the incident beam) is removed by the dichroic filter, while the in-elastic Raman components are passed. A conventional Raman microscopy system is shown in Figure 2.1, which is comprised of a dichroic filter and a pin-hole with a controllable diameter to ensure that only signals from the small volume at the focal point are collected. The spectrometer counts the intensity of light collected at various frequencies.

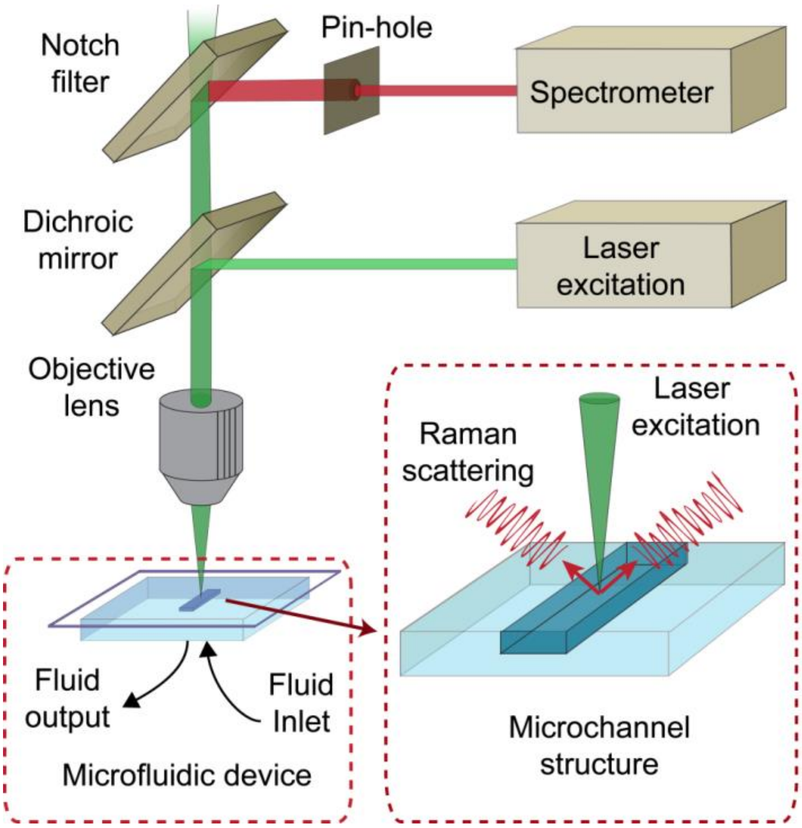

Figure 2.1: Schematic image of a confocal Raman system integrated with a microfluidic unit.

Raman spectroscopy allows for the integration with microscopic analysis techniques and is capable of collecting spectra from very small volumes (< 1 μL), making it suitable for analysis on the microfluidics size scale. Raman microscopy can approach very high spatial resolutions. For example, using a 633 nm laser source with a pinhole of 50 μm in radius and a 60×/1.2 numerical aperture (NA) objective, lateral and depth resolutions of approximately 0.25 and 1.7 μm, respectively, can be achieved.

The unit for Raman spectroscopy is the wavenumber, the reciprocal of the wavelength shift expressed as $1/\Delta\lambda$ with units of cm^{-1}. Raman shifts in the range 10–400 cm^{-1} can be used to study the rotational aspect of molecular bonds, whereas the range 400–4000 cm^{-1} contains vibrations associated with vibrational-rotational structures. For organic molecules the range from 500–2000 cm^{-1} is known as the ‘fingerprint’ region.

2.3.2 Variations of Raman spectroscopy

Raman spectroscopy signals are inherently weak; therefore much effort has been invested to design Raman systems with enhanced sensitivity and spectral resolution. Some of the key Raman spectroscopic enhancement variations are described in the following:

2.3.2.1 Surface-enhanced Raman spectroscopy (SERS)

SERS was first observed by Fleischmann *et al*. [19] The effect originates from nanocolloids of metals, such as silver or gold, which generate localised surface plasmon resonances when excited by a laser source. These plasmonic effects can be observed in nanostructured surfaces of such metals as well. The existence of plasmon fields enhance the intensity of the Raman signals from chemicals within their range, with enhancements as high as 10^8 reported for well optimised systems. Although the fundamental electromagnetic basis of SERS is now well established, surface enhancement has also been associated with charge transfer effects in the metal-adsorbate system (chemical enhancements) [20, 21]. A large number of excellent reviews, describing SERS and its principles are already available [21-24]. Access to a variety of commercially available colloidal suspensions makes SERS suitable for microfluidics.

2.3.2.2 Resonance Raman spectroscopy

Vibrational modes associated with excited states are enhanced by matching the wavelength of the excitation source to the electronic transitions of the target material. This method is capable of distinguishing Raman peak shifts of specific bonds in large organic molecules, which would otherwise show complex Raman signatures in the spectral region of interest [25].

2.3.2.3 Surface-enhanced resonance Raman spectroscopy (SERRS)

The effects observed using SERS can be studied in more detail by combining them with resonance Raman spectroscopy. This combination allows the study of specific bonds together with enhanced Raman scattering due to the SERS effects [26-28]. SERRS can be readily implemented in microfluidic systems to provide the possibility of analysing large proteins and other macro molecules.

2.3.2.4 Angle-resolved Raman spectroscopy

By changing the angle between the laser beam and the sample in Raman microscopy, it is possible to gather information about the inelastic photon scattering from the various molecular bonds. This point can become quite relevant when dealing with large and non-uniform biomaterials, such as live cells in microfluidics. The surface morphology of a cell exposes differing physical angles to the incident laser depending on the morphology of the cell at that particular location [29-31].

2.3.2.5 Coherent anti-Stokes Raman spectroscopy (CARS)

In CARS, two pulsed laser beams, known as pump and probe beams, are used to generate an enhanced anti-Stokes photon. This method has been proven to be far more sensitive than traditional Raman microscopy, and is gaining recognition in the scientific community [32-34]. CARS microscopy has been particularly effective in monitoring the structure and local environment of lipids and water molecules, which may be useful for specialised applications in microfluidics [35]. However, CARS is a non-linear optical effect that is induced by high peak power laser pulses of short duration. The pulses may be subject to dispersive broadening when passing through an optical window.

2.3.2.6 Stimulated Raman scattering (SRS)

SRS microscopy is similar to CARS in that pump and Stokes probe beams are used to make the molecular bonds oscillate in phase while actively pumping the vibrational states, leading to significant enhancement of the Raman signal. The intensity of the scattered light at the pump wavelength experiences a stimulated Raman loss (SRL), while the intensity of the scattered light at the Stokes wavelength experiences a stimulated Raman gain (SRG). SRS microscopy has a major advantage over CARS in that it provides low-background imaging with improved chemical contrast [36], both of which are potentially important for microfluidics where water is often the major source of non-resonant background signal in the sample. However, applications in microfluidics may once again be limited by dispersive broadening when passing through an optical window.

2.3.2.7 Tip-enhanced Raman spectroscopy (TERS)

Atomically sharp tips, such as those used in atomic force microscopy (AFM) machines, are used in TERS. When coated with nanostructured, plasmonically active metals, these tips produce strong plasmon fields in their vicinity. Hence, TERS can have the spatial resolution as small as 10 nm, which has been demonstrated with single molecule sensitivity [37-39]. Furthermore, with the development of AFMs that operate in liquids, this technology has the potential to be incorporated into microfluidic devices [40].

2.3.2.8 Transmission Raman

This method is used to observe Raman signals that are transmitted through the entire sample, and hence produce signatures indicative of the bulk material rather than just the surface or confocal regions (as is usually the case in traditional Raman methods). The most prominent application for transmission Raman spectroscopy is for the analysis of pharmaceutical products in microfluidics [41], however other applications have also been explored recently, such as protein analysis [21] and studies of nanowires [42, 43].

2.3.2.9 Spatially offset Raman spectroscopy (SORS)

Using this method it is possible to obtain Raman signatures for objects beneath an obscuring surface by obtaining Raman spectra at two distinct depths, and plotting the difference between them. This technique can potentially be used for detecting objects hidden by opaque covers, such as detecting packaged explosives, determining the ripeness of fruits [7, 44], or combined with an implanted SERS substrate to measure transcutaneous glucose levels [45]. Hence, the technique provides the possibility of applications in microfluidics under polymeric structures that produce strong diffuse scattering or interfering Raman spectra.

2.3.3 Considerations for Raman microscopy in microfluidics

Although Raman microscopy systems are relatively versatile tools, there are still some limitations which must be considered. Some of these issues are discussed below.

2.3.3.1 Droplet surfaces

The convex/concave shape of a droplet surface can adversely affect the Raman systems ability to accurately measure materials suspended in such droplets. This is partly due to the fact that there is a refractive index difference between the droplet and the air. Additionally, the shape of the droplet surface creates a lensing effect that distorts the focus and reduces the spatial resolution. Therefore, it may be necessary to flatten the surface of droplets either by manipulating the surface tension, or by sandwiching the droplet using an optically transparent substrate, such as glass or quartz [46].

2.3.3.2 Focal length

As microfluidic walls and substrates can be several millimetres thick, the focal length must be long enough so as to penetrate inside the liquid media. The focal length of a Raman system is determined by the optical arrangement of the microscope, but most importantly by the objective lens. Lower magnification objective lenses tend to have longer focal distances, making them more suitable for microfluidic systems. High magnification, long working distance objectives can also be used, at the expense of optical intensity and hence, reduced signal to noise ratio. Water and oil immersion objectives can also be considered.

2.3.3.3 Detection volume

Raman microscope systems focus the excitation beam into a small volume using an objective lens. The size of the detection area is dominated by the spot size, or diameter, of the excitation beam at the focal point (Figure 2.2). This diameter (d) is proportional to f the focal length of the lens and λ the wavelength of the laser source and it is inversely proportional to D, the lens diameter ($d \propto f\lambda/D$). The other important parameter for the detection volume is the depth of focus. The depth of focus (also known as the confocal parameter) is generally estimated as twice the Rayleigh range (the distance between the $\sqrt{2}d$ spot size points). The value can be approximated as $\pi d^2/2\lambda$. In order to achieve a small depth of focus the microscope must be operated in confocal mode, where the size of the spectrometer entrance slit is reduced to the smallest value compatible with the required signal throughput.

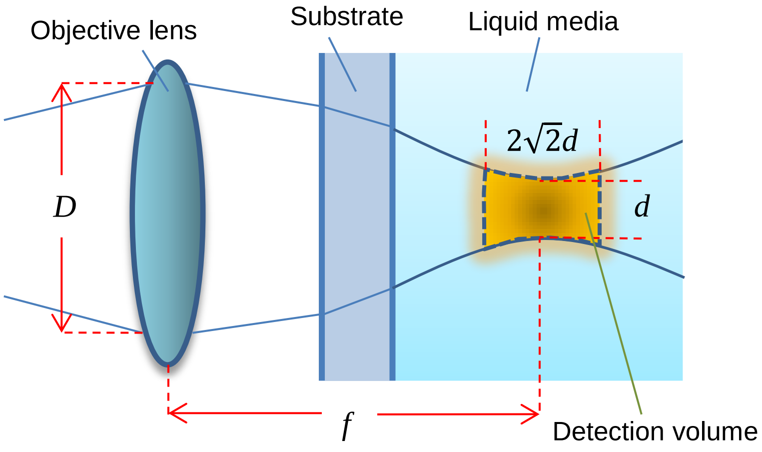

Figure 2.2: Schematic of the optical system showing the definitions of spot size, depth of field, focal length and detection volume.

In microfluidic measurements, the full focal volume is generally placed within the liquid medium to ensure that the Raman signals primarily arise from interactions with the target analytes. As mentioned previously, the use of high magnification microscope objectives for Raman spectroscopy tends to increase the signal to noise ratio and reduces the minimum detection limit by focusing the beam more tightly, and increasing the collection angle. Targeted detection is also possible in microfluidics using mechanical sample stages to move the targets with sub-micron spatial accuracy (e.g. piezoelectric stages).

2.3.3.4 Excitation wavelength

The optimum choice of excitation laser wavelength is important for Raman spectroscopic applications. The intensity of Raman scattering scales inversely as the fourth power of the wavelength, so it is generally preferable to use shorter excitation wavelengths. However, issues arise when Raman microscopy of biological samples is required, since when the photon energy increases, there is the potential to produce large interfering fluorescence signals, which can hide the desired Raman signatures of the samples [47]. The majority of biological samples are also strong absorbers of optical energy, particularly at shorter wavelengths (blue and UV). Modern Raman microscopes usually offer several different options for excitation wavelength, however for these systems the diffraction grating efficiency and detector sensitivity must also be taken into account for each operating wavelength.

For biological samples, the use of a typical excitation wavelength of 532 nm can produce such fluorescent signals. One solution is to use longer wavelength lasers such as red, or near infrared, so that the photon energy is below the fluorescence excitation band. While this may reduce the fluorescence in the sample, it also reduces the Raman scattering efficiency of the system, requiring higher power lasers or longer integration times. Additionally, the choice of excitation wavelength is critical for resonance, and surface-enhanced resonance Raman scattering. Wavelengths which encourage resonance must be chosen, however other wavelengths will also provide smaller intensity Raman signatures of non-resonant bonds [48, 49].

2.3.3.5 Optical power

In general, the scattering intensity can be increased simply by increasing the excitation power, but high power densities at the focal point can cause damage to thermally liable biological samples. Additionally, high laser power at the focal point can cause localised turbulence or induce tweezing effects on nanocolloids in the microfluidics [50, 51]. Therefore, the optical power for Raman excitation should be carefully optimised in each case to ensure that the sample is not damaged during the measurement. Much work has been done in determining the damage threshold for optical power applied to biological samples [51, 52].

Another strategy to reduce the potential damage to biological samples is to reduce the laser exposure time by lowering integration times. However, as the integration time is reduced, the signal-to-noise ratio of the Raman spectrum is also reduced. The operator must determine a balance between biological material damage and signal strength. The choice of the laser power, together with the magnification of the objective lens, governs the power applied per unit volume of the microfluidics. A larger spot size allows the use of larger powers. Generally, at magnifications of 40× or higher it is better to keep the laser power under 1 mW for large exposure times. Note that flowing fluids will tend to dissipate heat energy and remove damaged analytes from the focal region, thereby allowing high laser powers to be used.

2.3.3.6 Memory effect

Aside from the many benefits of Raman-microfluidic integrations, there are still a few drawbacks. One such drawback is the possible “memory effect”. This is due to some particles and analytes sticking to the surface of the microchannels, causing permanent Raman background signals. Many strategies can be devised to eliminate this problem. For example, disposable chips can be used to avoid such memory effects. However, if reusable chips are desired then the walls should be carefully cleaned after each usage or they should be protected during the process to avoid any target analyte interaction with them. For instance, a segmented flow system can be implemented, in which a thin layer of oil is used to protect the microchannel walls from contamination [53-56]. There are also many other methods that can be applied to alter the hydrophobicity of the walls and substrate, reducing the occurrence of memory effect issues [57].

2.3.3.7 Portability

The creation of portable LOC devices is the ultimate goal of current microfluidics research. The dimensions of Raman microscopy equipment are largely determined by their accuracy and resolution. Low cost hand-held Raman spectrometers have spectral resolutions not exceeding 20 cm^{-1} Raman shifts, while the resolution of laboratory spectrometers with optimised diffraction gratings, optical path lengths and cooled charged-coupled detectors can be as small as 0.1 cm^{-1}. Similar concerns also apply to spatial resolution, while cost is a major determining factor for the sensitivity of the detector. Lower sensitivity spectrometers require higher laser power, which in turn limits the types of samples that can be analysed, particularly organic materials that can be damaged at high powers. Methods to reduce the size and complexity of the supporting optical equipment are underway; covering ideas such as creating on-chip laser sources [58, 59] and replacing the confocal lens with other devices such as waveguides [60] and fibres [61, 62]. Recently designed “Kinoform” microlenses for focussing into microfluidic channels can potentially be used in Raman systems [63]. Despite these advances, the greatest difficulty in achieving portability is reducing the size of the optical spectrometer while maintaining acceptable resolutions.

2.3.4 Materials

2.3.4.1 Metals

Pure metals in bulk form do not produce any Raman signature; this is due to the presence of free electrons in the metal structure, which block the incident light from reaching the material bonds. This property makes metals reflective and gives them their high electrical conductivity [64]. However, very thin films of pure metals have been shown to produce Raman signatures, as the conductivity of nanometre thin films is low enough to allow phonons to reach the metallic lattice bonds [65]. Nano-colloids and other roughened nanostructures are also capable of producing surface-enhanced Raman signatures, as discussed in the “Variations of Raman spectroscopy” section.

2.3.4.2 Non-metals

Raman microscopy is capable of providing a good representation of inorganic, non-metallic materials; providing information regarding their chemical bonds, lattice and crystal arrangements. This capability is particularly useful for identifying different morphologies of materials, inorganic polymorphs as well as differentiation of amorphous and crystalline material phases [64]. Metallic oxides have unique Raman signatures as seen in examples such as TiO_2 [65], and MoO_3 [66-68]. Additionally, Raman scattering can provide unique information regarding the structure of materials like graphene where it is possible to identify the number of layers and degree of oxidation in its structure [69].

2.3.4.3 Organic materials

Changes in the character or quantity of particular organic bonds can be readily assessed by the location, strength and width of the Raman peak shifts. As mentioned earlier, the Raman signatures provide detailed information regarding rotational and vibrational properties of organic bonds. These Raman signatures can be well correlated with FTIR signatures. FTIR spectroscopy is usually used together with Raman microscopy for the analysis of organic materials. Although FTIR and Raman spectra are similar, their signatures are not always identical. The assessment of polar organic molecular bonds, such as C-O, N-O and O-H, produces weak Raman signatures but strong FTIR signatures. Conversely, neutral bonds such as C-C, C-H and C=C, are less easy to identify with FTIR however they produce strong Raman peaks (Figure 2.3).

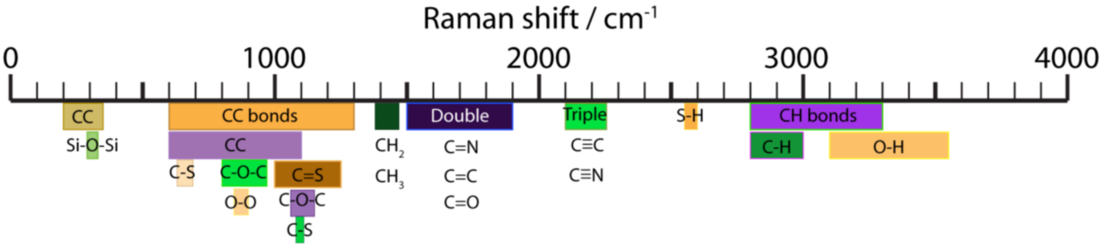

Figure 2.3: Raman shift peak ranges for organic bonds.

Raman microscopy is very sensitive to changes in cell metabolites and proteins, demonstrating distinct differences between cells at various stages of cancerous growth [70] and can distinguish between healthy tissue, cancerous tissue and even pre-cancerous tissue [71, 72]. Raman microscopy is also useful in measuring the type of polymeric materials in microfluidics, and their degree of polymerization. However, organic materials can be damaged by high energy, low wavelength excitation sources as they expose the organic bonds to high energy photons. To accommodate this issue, Raman microscopy for organic, biological and medical specimens uses near infrared (NIR) lasers, such as 785 nm or 1064 nm, to reduce the photon energy. This, however, reduces the intensity of the Raman scattering process and necessitates highly sensitive Raman spectrometers and longer integration times. Regardless, NIR Raman microscopy has successfully been implemented in microfluidics to classify epithelial pre-cancers and cancers [73, 74].

The ability of Raman microscopy to produce small detection volumes can be used for the targeted analysis of larger organic objects such as cells and tissues. Raman microscopy can be used for the identification of individual cells, allowing them to be categorised and sorted. The system can produce even more targeted information, with Raman signatures being taken from various parts of a larger object, for example, targeting a cell where the Raman spectra of the nucleus, cell wall, cell membrane and cytoplasm can be acquired [3]. This powerful option allows the detailed analysis of a cell’s health, or the ability to monitor the absorption of certain chemical drugs [75]. Another example has shown that different locations on a yeast cell produce markedly different SERS spectra [76, 77]. Optical power density is again an important consideration when dealing with biological materials. Exposure to high optical powers has very detrimental effects on a cell, not only thermally, but the high energy can irreversibly damage and even kill a cell [51, 78].

2.3.4.4 Aqueous media and microfluids

Aqueous media are the basis of microfluidics. Pure water produces weak Raman peaks at 1640 cm^{-1} and at 3300 cm^{-1} (Figure 2.4) and can be readily used for suspending organic materials, particles and analytes [79-83]. Water is also the main media used to store and culture living bio-materials. These benefits are what make Raman microscopy so powerful for microfluidics. The confocal ability of Raman microscopy allows targeting specific areas inside an aqueous suspension, with the ability to perform 3D Raman mapping. Furthermore, the intensity of the Raman peaks can be used to determine the local concentrations of suspended materials in addition to material identification as described previously.

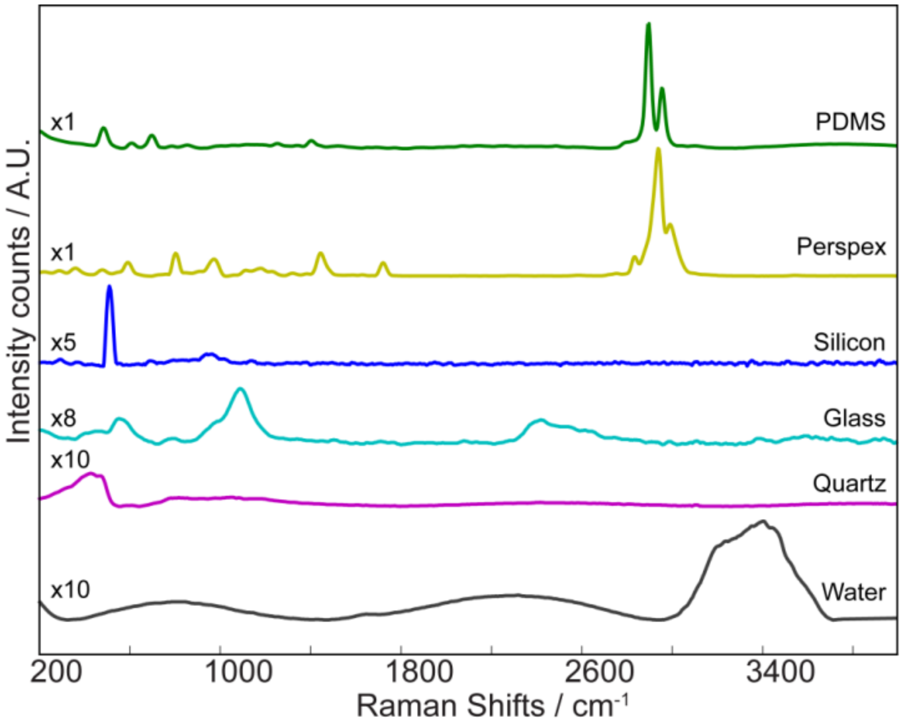

Figure 2.4: Normalised Raman spectra of possible microfluidic substrates such as PDMS, perspex, silicon, glass, quartz and water.

Some fluids have strong Raman signatures, which can be used for their identification and assessing their concentration in the microfluidics. Some of the examples of such measurements are presented in the 'Applications' section. Examples of Raman studies of aqueous media include alcohols, which show a strong presence of CH and

C=C bonds and produce Raman peaks at 1400–1900 cm^{-1}. Additionally, Raman spectroscopy operates not only on transparent samples but also on many semi-opaque and opaque environments in microfluidics, for which many other optical systems fail.

2.4 Microfluidic configurations and requirements

2.4.1 Materials and fabrication

Microfluidic systems are designed to deal with the behaviour, manipulation and precise control of fluids [84, 85]. Microchannels are used to constrain the fluids to small scale areas, with some microchannels being less than 100 nm wide [86]. This small size allows for the accurate control of flow, making such channels suitable for the study of suspended materials and spatial mapping with high resolution. Microfluidics not only enable very precise flow control, but also has the potential for manipulation of materials suspended in the liquid media by utilising mixing and separating to optimise different chemical constituents [87, 88]. Microfluidic systems can easily be interfaced with standard laboratory equipment such as syringe pumps, microscopes and electronic equipment to enhance the usefulness of their application [89].

A further benefit of microfluidic devices is the ease of fabrication. “Soft lithography”, a phrase coined by Whitesides *et al.* [90], is used to describe the processes for polydimethylsiloxane (PDMS) microfluidic device fabrication. Many other materials, such as glass, silicon and SU-8, can also be used for creating microfluidic devices, each with a focus on a different application [91]. As such, studies have been conducted on understanding the properties of these materials, their biocompatibility, their effects on analysis performed in microfluidics [92]. Much research has been conducted into microfluidic substrate choice and fabrication methods, with detailed analysis of such methods available in references [11, 91, 93-97].

Microfluidic devices based on rigid materials such as glass and silicon are often the basis of reusable systems and where severe chemical environments might be used in the microfluidics. However, the fabrication processes can be lengthy and require the use of high cost facilities and harsh chemicals. Conversely, PDMS is a relatively cheap material for the rapid fabrication of microfluidic devices. However, for PDMS based microchannels there is still a need for a rigid structural platform. This substrate can be made from anything with solid structural integrity, biocompatibility and preferably optical transparency. In fact, for Raman microscopy, a Raman transparent material is necessary.

Microfluidic devices can introduce significant Raman ‘background noise’ from the substrate and structures surrounding the microchannels. Such background noise is more noticeable if the channels are made of polymers with strong Raman signals (e.g. PDMS) and if the detection site is within close proximity to the polymer, or the imaging must be done through a polymer membrane. This can be overcome by adding a Raman transparent window into the microdevice [98]. Raman signatures of various materials have been acquired using a 532 nm laser source and are depicted in Figure 2.4. PDMS and Perspex have many characteristic Raman peaks throughout the entire spectral range, making them unsuitable for use in the path of the excitation laser. Silicon is usually used to ensure the correct alignment of Raman spectrometers, as it has a predictable and strong Raman peak at 520 cm^{-1}. Glass has a very large and broad Raman peak near 1000 cm^{-1} making it unsuitable as a microchannel substrate for detecting analytes with signatures around this range. Advantageously, quartz has relatively few Raman peaks, with only a broad peak at around 350 cm^{-1}. As a result, quartz is an excellent material as the substrate of choice for Raman-microfluidics systems.

2.4.2 Optical transducers and environmental control

The measurement of parameters in microfluidics is performed using transducers, which are required to operate with high sensitivity on small volumes of fluids. Examples of potential parameters to monitor include flow rate [99, 100], viscosity [101], heat transfer [102], temperature [103], electrical impedance [104, 105], permittivity [106], refractive index [107] and other optical properties [108].

Transducers can be integrated into microfluidic devices; onto the surface of the substrates, on the walls of the microchannels or integrated within the microfluidic structures. They can be in direct contact with the fluids, or they can be fabricated so as to enable contactless detection. Some examples of non-optical, non-contact methods of detection that exist include capacitance sensors [104], piezoelectric transducers [109-111] and magnetoelectronic detection [112]. Transducers can be electrochemical, acoustic, thermal, electromagnetic and optical. The emphasis of this review is the integration of Raman spectroscopy; however other transducers are in place to assist this purpose. A good example for integrated optical detection is shown in Figure 2.5(a), in which an optical fibre is used for Raman spectroscopic detection of the analyte in a microfluidic channel [113]. Similar fibre based Raman and SERS systems with direct fluid contact have been proposed by others [60, 114]. This method requires the optical fibre probes to be in direct contact with the fluid, exposing the fibre to possible fouling and eventual damage. On the other hand, contactless optical detection in microfluidics can also be implemented, in which the laser is focused via an objective lens onto the area of interest for detection in microfluidics. Some recent examples include the evaluation of microfluidic mixing using confocal optical imaging to monitor the mixing of water and fluorescein die [115] and the detection of gas using a PDMS microchannel design integrated with confocal fluorescence imaging [116]. Studies of CO_2 solubility in water (Figure 2.5(b)) [117] and pharmaceutics of promethazine hydrochloride and mitoxantrone dihydrochloride are [54] examples of Raman-microfluidic systems for online monitoring applications. A number of excellent review papers summarise the many optical transduction methods used in microfluidics [6, 118, 119].

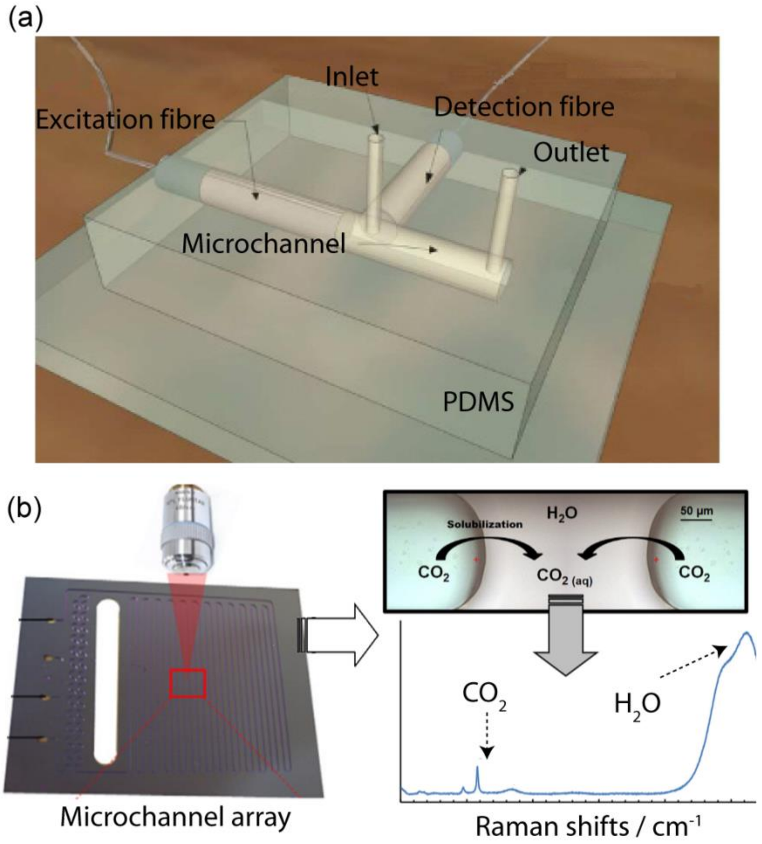

Figure 2.5: Raman system integration with microfluidic environments. (a) Integration of optical fibre detection into a microfluidic device for the purpose of *in situ* Raman detection. Reproduced from Ref. [113]. (b) Confocal Raman microscopy demonstrating the detection of CO_2 solubility in water. Reproduced from Ref. [117].

2.4.3 Considerations on flow, mixing, filtering and trapping

In order to obtain the most benefit from Raman-microfluidics, environmental factors must be well controlled: flow rates must be chosen which are appropriate for the intended application, especially if laminar flow is desired. Additionally, mixing between different fluids, suspended particles, analytes and even gases can be achieved. These factors must be controlled in order to assure that the target materials are efficiently concentrated into the area of the Raman laser beam focal point, so as to achieve the maximum Raman scattering. Microfluidic techniques can also be employed for filtering, trapping and sorting of suspended materials that enhance the selectivity towards the targets [108].

2.4.3.1 Flow systems and mixers

One advantage of microfluidic systems is the ability to provide continuous flow, while still using small volumes of samples. Flow in microfluidics can be driven by pressure or vacuum using external pumps [120]. Other mechanisms also exist, such as capillary and electro-osmotic flows. The flow mechanisms in the microfluidic environment have been comprehensively reviewed [121-123].

Mixing is an important aspect to be considered in Raman-microfluidics, as most microfluidic systems have low Reynolds numbers and therefore intermixing is diffusion limited [124]. Low Reynolds number systems are characterised by the absence of turbulence, and the dominance of a laminar flow within the system. Examples of laminar flows are seen in many microfluidic structures, especially in T-junctions (Figure 2.6(a)), in which the fluids are not immediately mixed after entering the junction and only intermix gradually through diffusion [125]. Raman beam rasterising is one of the most efficient ways of assessing the degree of diffusive intermixing, which will be discussed further in the "Applications" section. Additionally, laminar flow systems can be manipulated and used for diverting streams of fluids, as shown in Figure 2.6(b) – (e) [126].

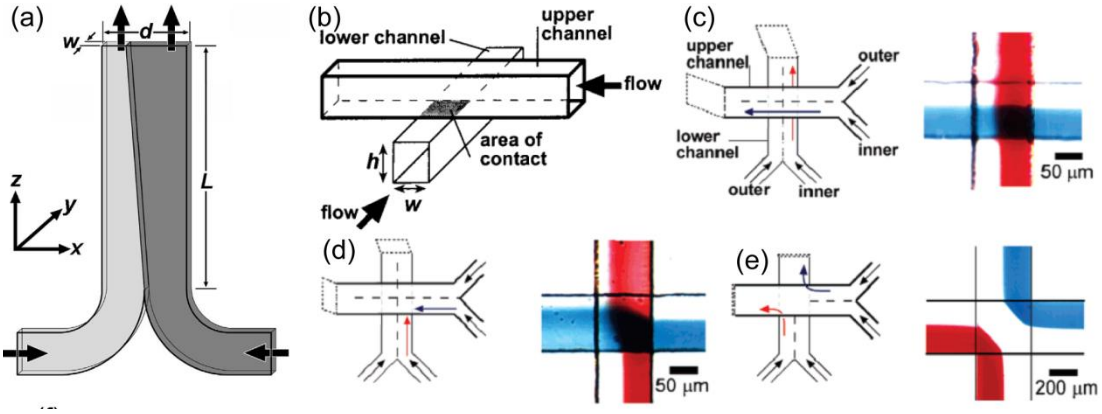

Figure 2.6: Microfluidic methods demonstrating flow principals, mixers and traps. (a) Conceptual rendering of the simplest form of the T-section system, where two fluid inputs enter through channels at the bottom and slowly diffuse over the length of the microchannel. Reprinted from Ref. [125]. (b) Schematic drawing of tangential microchannels, where the channels can exchange fluid through the shaded area of contact. Laminar flow experiments with the aspect ratio, A, of the contact areas as: (c) 100 × 160, A=1.6; (d) 100 × 44, A=0.44; (e) 400 × 25, A=0.063. Adapted from Ref. [126].

If liquid mixing is desired, then special systems must be implemented in order to induce disturbances and enhance the mixing ability. Microfluidic mixers are often used for accelerating the reaction of chemical constituents. Mixers can also be used for the creation of precisely controlled nanoparticles, such as polymer beads [127] or metallic colloids [128]. Microfluidic mixers are frequently used with Raman microscopy. They are implemented to enhance SERS signals, as mixing is vital for initiating chemical reactions and introducing particles or nanostructures that enhance Raman through SERS. The mixing between a silver or gold colloid and a target analyte must be as comprehensive as possible for obtaining high intensity SERS signals. To this end, micropillar microchannels for the mixing of silver colloids with chemicals such as dipicolinic acid have been demonstrated [129]. In a similar concept, alligator teeth-shaped PDMS channels were used for effective mixing of silver colloid with DNA oligonucleotides [130].

2.4.3.2 Traps, filters and sorters

Trapping, filtering and sorting of suspended materials can be implemented in a microfluidic environment. All of these functions can be performed through the application of some type of force. The separation of materials, especially biological materials, is essential for processes where purer samples are desired. The active separation forces that can be readily applied include optical, mechanical, electrokinetic, magnetic and acoustic (Figure 2.7(a) – (f)) [108].

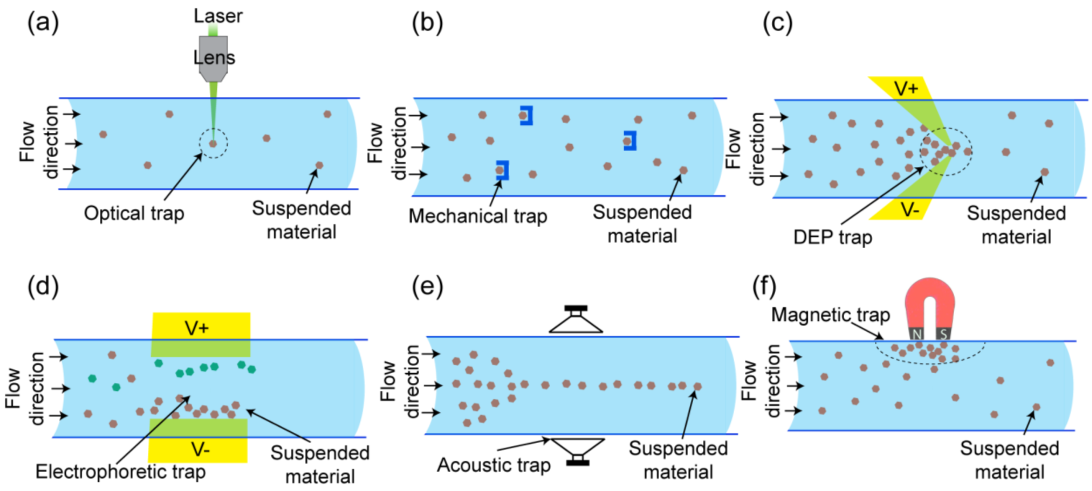

Figure 2.7: Schematic examples of microfluidic traps using forces of: (a) optical (b) mechanical (c) dielectrophoretic (d) electrophoretic (e) acoustic and (f) magnetic.

In microfluidics, optical beams are commonly used for trapping (also known as tweezing) suspended objects, allowing interrogation of these particles using optical methods such as fluorescence or Raman microscopy (Figure 2.7(a)) [131]. Optical trapping can be performed using the Raman excitation laser or a separate laser beam using single or multiple objectives or fibres. In a recent example, optical traps have been used for isolating bacterial cells in liquid media [50]. It is possible to then change the content of the fluid environment surrounding the cells by tweezing them in the traps while continuing to monitor their response. In a recent example, a waveguide optical trap was used on yeast cells [132]. The waveguide trap has the advantage of causing minimal damage to the cells due to the low optical power of the evanescent field. The use of optical traps is widespread for analysing cells in fluid environments, and many trap designs have been demonstrated [61, 133-140].

In microfluidics, mechanical traps require no external inputs beyond the fluid flow itself in order to operate, and can also allow for the controlled release of the trapped objects through manipulation of the flow. Mechanical traps use specifically designed barriers for holding objects in position, and are usually implemented for long term studies, including studies of cells (Figure 2.7(b)). If an object in such a mechanical trap is to be interrogated using Raman microscopy, it has to be considered that the materials used in fabricating such traps can also interfere with the Raman signals. Examples of mechanical traps include those for holding single cells, where air bubbles are then used to eject the cells at the end of the measurement cycles [141]. Other examples use mechanical traps for the optical imaging of live cells in microfluidics, while allowing for the ability to modify the fluid environment without disturbing the imaging process [142].

Electrokinetics is a broad term that covers many phenomena that occur in fluid environments, specifically involving the double-layer surrounding the suspended materials and the electrical properties of both the media and materials. The most studied concepts of these effects, implemented in microfluidics for separation and trapping, are dielectrophoresis (DEP) and electrophoresis [108, 143-148]. DEP is defined as the force exerted on a suspended dielectric particle in the presence of a non-uniform electric field. The magnitude and direction of the force is related to the electric field intensity, particle radius, permittivity of the particle and suspending fluid, as well as the conductivity of both the particle and suspending fluid (Figure 2.7(c)). DEP can be used for trapping and sorting almost any type of suspended materials ranging from nanoparticles and carbon nanotubes [149] to cells [150] and DNA [151]. DEP based cell traps have been used for quantifying the per-cell levels of lactic acid production [152] as well as the trapping of DNA with specific strand lengths [151, 153]. Sorting systems based on DEP have been used for sorting cervical cells into healthy and tumorous types and can potentially be used as an early detection device for cervical cancer [154]. Other systems demonstrate the separation of bacteria and yeast cells based on their differing dielectric properties [149, 150].

In microfluidics, electrophoresis can be used to move suspended particles under the influence of uniform electric fields. For particles with a surface electric charge, the electrophoresis process is affected by surface adsorbed species, and as a result the external electric field exerts a motive Coulomb force (Figure 2.7(d)). An application of electrophoresis has been demonstrated for the separation and detection of chemicals in a hybrid SERS nanocomposite device [155].

There are many more methods of trapping and sorting objects in microfluidics [156], including acoustic [157] and magnetophoretic processes [158], which are yet to be integrated with Raman systems. The schematics regarding their operations are presented in (Figure 2.7(e) – (f)). Thermal procedures can also be considered [159]. Interested readers are referred to comprehensive reports which dissect the various methods into two categories, active and passive, and proceed to analyse their resolution, throughput and efficiency [160]. It is also noteworthy to include a final example reported by Lutza *et al*. [161] who used Raman spectroscopy to image the eddy concentration distribution for various acoustic oscillations in microfluidics.

2.5 Applications

As discussed, both microfluidics and Raman spectroscopy are extremely useful methods in their own right. The integration of the two allows us to capitalise on all of the benefits available to microfluidics, such as low analyte volume, tight control of the microfluidic environment and portability. Additionally, Raman microscopy provides detailed analysis of the target materials, including information from solid, liquid and gaseous samples and their environments.

2.5.1 Investigation of analytes

One of the most important features of Raman spectroscopy is that it provides information relevant to the quantity and types of chemical bonds in the sample. The Raman laser beam can be readily focused into a small volume of material within a microfluidic system and allows analysis of only that very small volume. Raman-microfluidic devices also show great promise for the detection of analytes in complex mixtures, as accurate measurements of different analytes can be simultaneously conducted [119].

Many organic liquids can be efficiently detected with Raman microscopy as they have a strong Raman cross-section. There are many reported examples that have exploited this property. For instance, Fletcher et al. [162] studied a T-shape microfluidic device for the mixing of ethanol and acetic acid. Raman microscopic mapping was used for detecting the two analytes at various mixing stages. The results show a very well controlled laminar flow in the system. Figure 2.8 depicts the Raman beam rasterised image of the T-channel, demonstrating the accuracy of analyte detection in a microfluidic environment. This method uses two distinct Raman peaks for the detection of ethanol (882 cm^{-1}) and acetic acid (893 cm^{-1}), and can only be applied to those analytes which have non-overlapping Raman peaks. There are many more examples of such applications [125, 163-165].

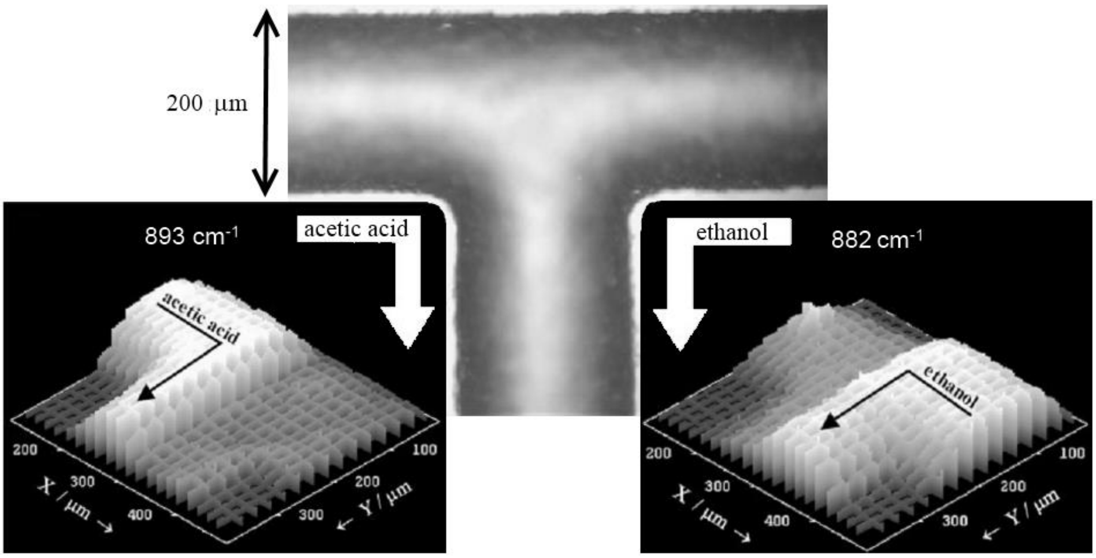

Figure 2.8: A T-junction microfluidic channel approx. 200 µm wide for the purpose of mixing ethanol and acetic acid. Insert images show rasterised Raman images of acetic acid and ethanol using their respective Raman peaks. Adapted from Ref. [162].

Microfluidic micro-reactors are used for the careful control and study of reactions. Raman microscopy can be incorporated in such systems to investigate small volumes, determining the presence of analytes and catalysts during the entire reaction process. Raman microscopy offers high-information content, in-line detection within microfluidic based micro-reactors. A very good example is found in the work of Leung *et al.* who used a continuous flow micro-reactor with in-line confocal Raman microscopy to measure the concentration of output constituents [166]. In their work, the catalytic oxidization of isopropyl alcohol into acetone was monitored in real-time. They were able to use the microfluidic environment to vary the input chemicals and control the product conversion to precise levels.

Detection of specific analytes in a liquid is something which is generally of interest for sensing, monitoring low concentrations of precious materials, and many other process control applications. When dealing with low concentration analytes it is important to have a good understanding of the target analyte and to assure that the parameters of the incorporated Raman system have been well tuned for the detection of those targets. For instance, Raman systems which use NIR excitation can be efficiently used for detecting, and accurately measuring the concentration of organic samples such as glucose, lactic acid and creatinine [119].

Detecting low concentration analytes can be difficult using conventional Raman systems; however using SERS, SERRS, and TERS, with either fixed nanostructures or colloidal suspensions, it is possible to increase the apparent Raman cross-section of the target analyte. For these systems, pre-processors, such as mixers (see section “Considerations on flow, mixing, filtering and trapping” in this chapter), are required to encourage the efficient bonding of target analytes onto the nanostructures that are used for enhancing the signals. Such systems have been used for sensing concentration levels in the part-per -million or even -billion levels of analytes such as cyanide, dipicolinic acid and malachite green [129, 167]. There are many good review papers covering relevant topics in this field [21, 23, 168].

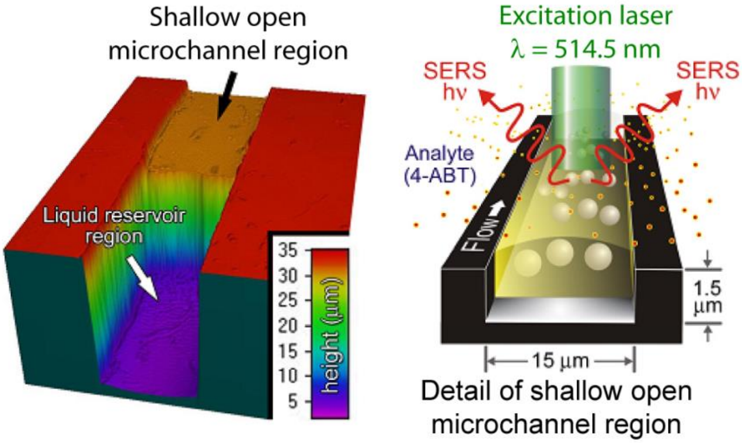

Figure 2.9: Detection of 4-ABT using an open microchannel design. Reproduced from Ref. [169].

Further enhancements of Raman signals can be achieved by controlling the spacing between the SERS colloid at the detection area. It has been shown that colloid spacings in the range of 1 – 10 nm produce significant enhancement over randomly positioned colloid [170]. This control can be either static or dynamic in nature. Static methods use organic and/or inorganic spacers that chemically attach onto the surface of colloids, which can be used for obtaining desired gaps between the particles [171, 172]. The main drawback of such static systems is the lack of real-time tuning ability and the interfering Raman signatures seen from the spacers.

The application of fixed nanostructures in a microfluidic channel for the SERS enhancement of analytes is also presented for the detection of many organic samples such as components of blood [173]. One of the challenges associated with these methods is ensuring enough analyte makes contact with the nanostructures within the microfluidic flow. Physical forces such as electrophoretic force can be used for bringing the target materials into the enhancement range of the nanostructures.

The use of similar techniques to detect airborne analytes presents a challenge, as these analytes must first be captured either by absorption onto solid substrates or suspended in water, after which Raman analysis can occur. In order to accommodate this, open channel microfluidics, where one side of the channel is exposed to the air environment, have been integrated with colloidal SERS (Figure 2.9) [169].

2.5.2 Materials sciences – nano/micro particles

The ability to identify and measure suspended materials is very useful with applications in assessing water contaminants and micro-reactor outputs, determining the concentration of mixtures and identifying unknown suspended materials. Raman-microfluidics can be employed for determining the quality of soil ingredients (after required pre-processing), chemical interactions, catalyst activities and corrosion effects.

Traditional methods of detection involve long preparation procedures, such as drying samples and/or centrifuging liquid samples to obtain more concentrated solutions. Raman microscopy is capable of identifying many materials, delivering their chemical 'fingerprint' [174, 175]. A good example is demonstrated in the work of Chan *et al*. [176] where CARS detection of suspended sub-micron sized polystyrene beads was shown. This concept was then expanded for the trapping of unilamellar vesicles, where the Raman analysis indicated peaks present at 1440 cm^{-1} due to the CH_2 component in the lipids structure of the vesicles.

Many nanoparticles are synthesised and kept in colloidal forms, which are suitable for microfluidic processing. Raman microscopy can provide invaluable non-invasive information about such colloidal systems: the type of suspended nanoparticles can be identified, the colloid concentration can be determined using the intensity of Raman peaks and even the size of nanoparticles can be measured from the Raman peak shifts and their widths [177]. Raman microscopy can be efficiently employed for nanoparticles that generate surface plasmon resonances, such as gold and silver colloids, and can be used to determine their size during synthesis [178]. Raman-microfluidic systems are well-suited to analyse the interaction of chemicals and organic analytes on plasmonic nanoparticles [179]. Additionally, Raman microscopy can be used to determine other nanoparticles such as carbon based particles (carbon nanotubes, carbon black and graphene) metal oxides and chalcogenides using their strong Raman peaks [177, 180].

One difficulty with handling suspended materials in microfluidic environments is the 'memory effect'. This effect is due to the attachment of materials to the inside surfaces of the microchannels, as discussed in the "Considerations for Raman microscopy in microfluidics" section. This memory effect can introduce unwanted

Raman signals, giving false readings of concentration, and requiring the regular replacement or cleaning of microdevices. In an effort to minimise these issues an oil/water interface is created on the inside surface of the microchannel to minimise the chance of material attachment. Additionally, the flow system is performed as micro-bubbles, or nanodroplets, of liquid in order to minimise the time the microchannel surface is exposed to potential fouling materials [53, 54].

2.5.3 Analysing biological samples

Raman-microfluidic devices are ideal for analysing biological samples, and have found many applications in biology and biomedicine. They are attractive devices for non-invasive biological studies as live samples can be analysed, they have high sensitivity to even molecular scale interactions and hence only very small sample volumes are required. This section addresses biological applications of Raman-microfluidic devices and highlights their uses in specific studies.

2.5.3.1 Proteins

Proteins play important roles in many biological functions such as cell signalling, immune responses, cell structuring, cell adhesion and cell life-cycles. They are sensitive biological constituents requiring non-invasive and non-destructive measurement methods. Proteins are made up of chains of amino acids, which produce strong Raman signatures, specific to the type of amino acids. As a result, they can be differentiated using Raman microscopy with a good accuracy.

Proteins such as enzymes and antibodies, as well as carriers and membrane proteins, have been studied extensively in microfluidics [13, 52, 181, 182]. Raman-microfluidic devices can be efficiently utilised in the study of the behaviour of proteins, their functionalities and their responses under various stimuli. Microfluidics can also be used for purification of proteins from other components of a cell and this entire process can be continuously monitored using Raman microscopy [183]. Enzymes and antibodies can be incorporated into microfluidics to establish highly sensitive Raman microscopy based label free molecule specific biosensors [184, 185]. Additionally, SERS, SERRS and TERS can be used for enhancing the detection of suspended proteins. A good example involves the SERS detection of cytochrome *c* and lysozyme proteins from a suspension at various concentration levels by Yang et al. [186] Additionally, the SERS detection of bovine serum albumin (BSA) has been demonstrated using gold colloid, with detection limits shown to be as low as 100 pM [187].

2.5.3.2 Deoxyribonucleic acid (DNA) and ribonucleic acid (RNA)

DNA and RNA are the storage media for genetic information and are constructed from either ribose or deoxyribose sugars. The importance of nucleic acids is clear, and their identification and characterization is paramount for many research fields. From a technical view, DNA strands are the most specific bio-components that are latched onto their complimentary strands. DNA samples are employed in many applications including the recognition of genetic abnormalities and also used heavily for forensic identification. Other uses for DNA include genetic engineering, bioinformatics, disease identification and biosensing [188-192]. DNA produces Raman spectroscopic signatures and can be readily dispersed in aqueous media, makes Raman microscopy well suited for detection in microfluidic systems for processing of DNA. The Raman detection of DNA is widespread through the use of SERS, as SERS provides the ability to coat colloids in DNA friendly substances [193, 194]. The use of a microfluidic SERS mixer to detect single DNA oligonucleotides has been shown to accurately determine their concentrations [130]. The simultaneous detection of multiple DNA oligonucleotides using SERS has also been demonstrated, where a multi-gradient microfluidic channel was used for controlling the microfluidic environment. Labelling the DNA oligonucleotides can also assist in differentiating between the Raman signals (Figure 2.10) [195].

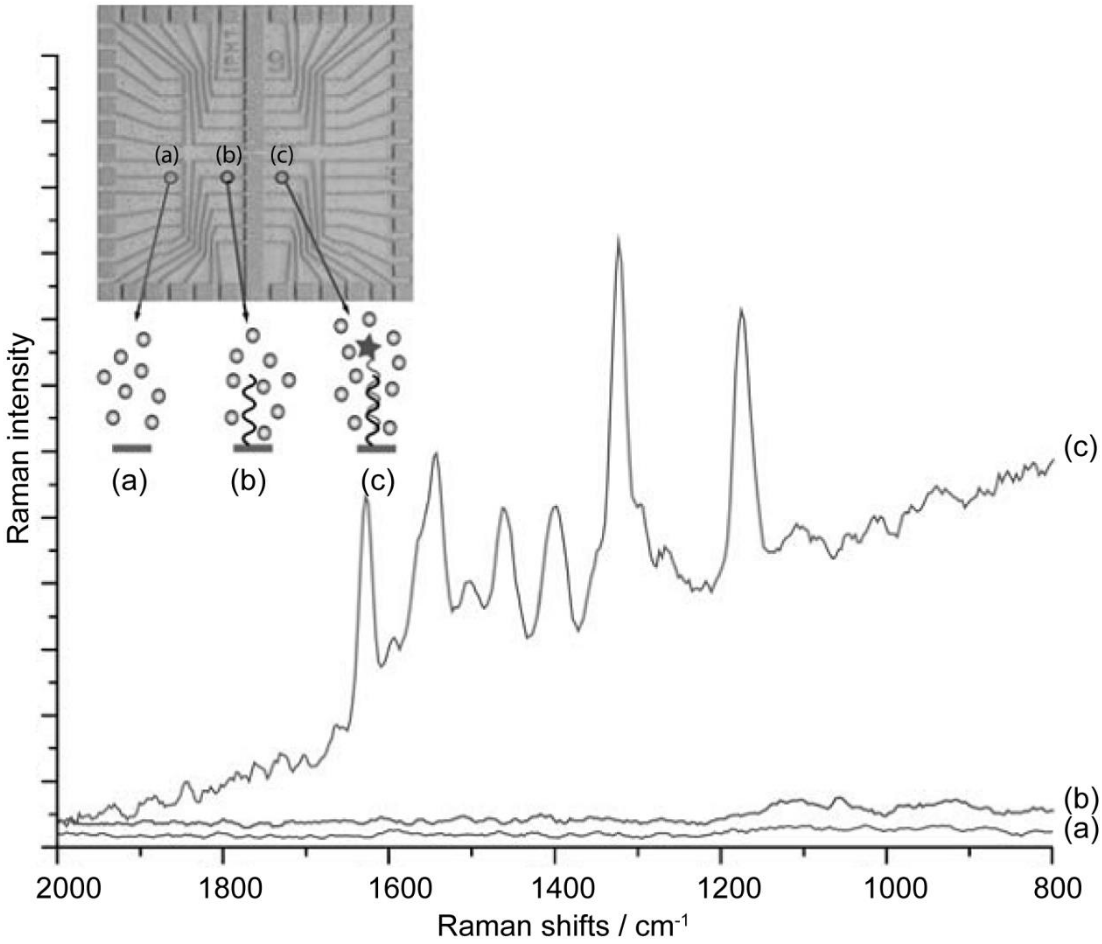

Figure 2.10: Raman-microfluidic devices for the mixing and detection of DNA: (a) Without immobilized DNA (b) With non-complementary immobilized DNA (c) After treatment with carboxyfluroscein for creating complimentary immobilized DNA. Reproduced from Ref. [195].

For DNA monitoring in microfluidics, many issues should be taken into consideration. Polymerase chain reaction systems can be integrated into the Raman-microfluidic device, providing enough DNA strands for the detection. The application of linkers, dyes and surface seeking groups are important factors as they allow for the efficient adhesion and immobilisation of the DNA strands for monitoring processes [26, 27]. Pre-processing procedures such as mixing and filtering are also important in DNA Raman-microfluidics. As an alternative to colloid mixing there are reported implementations which use solid microchannel features to achieve mixing and Raman enhancement [195, 196].

2.5.3.3 Cells

The structure of a cell is complex, with many biological constituents in its make-up, such as proteins, DNA, amino acids and various other components. Raman microscopy is well suited to the simultaneous detection and selective analysis of the components of such complex mixtures. Additionally, cells are more active in liquid environments, where nutrients can be absorbed from the liquid, and communication chemicals released [197, 198]. Microfluidic systems are ideal for sustaining cells in an aqueous environment where constant control of the chemical makeup and other aspects of this environment is possible [197, 198]. Such control is especially important for extended studies where cells are cultured through their entire life-cycle. Furthermore, Raman-microscopy can be used to monitor the chemical signatures of each stage of this life cycle and hence allows for the classification of cells into lifecycle states, including viable, necrotic and apoptotic [199-201].

Raman-microfluidic systems are capable of identifying and studying contaminating cells, including bacteria, for situations such as water quality control and studying the effects of antibiotics on particular strains. A practical example of how Raman-microfluidic devices are used in such applications is demonstrated by Knauer *et al*. [202] A water quality monitor was developed in order to ensure that no single *E. coli* cell be present per 100 ml of water, and was designed to have internal antibody capture sites for *E. coli*. (Figure 2.11(a)) The system operation required a specific volume of water to pass through a microfluidic channel, fitted with *E. coli* trapping sites, after which silver colloid was introduced to coat any trapped *E. coli* cells. Using the prominent 565 cm^{-1} Raman peak, the system was capable of detecting the presence of any *E. coli* cells, even down to the single cell level.

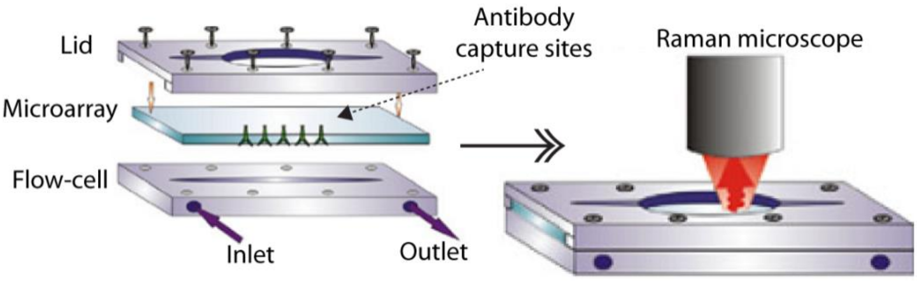

Figure 2.11: Schematic of a Raman-microfludic device fitted with antibody capture sites. Cells are captured at these sites, were Raman interrogation of the sample occurs. Image not to scale. Reproduced from Ref. [202].

It is possible to take advantage of the high confocality offered by Raman microscopic systems for the analysis of individual components of cells, avoiding the need to destroy the cell. As an example, Raman analysis has been performed on suspended *Bacillus anthracis* spores to determine the amount of calcium dipicolinate contained inside the spores [203]. It is also possible to classify tumour cells depending on their internal chemicals, demonstrating how Raman-microfluidic devices can be used to identify specific types of tumour cells from a larger sample of unknown cells [61].

Microfluidic systems can be implemented to filter and sort cells, with the ability to create highly pure cell samples. Raman microscopy is able to detect differences and defects in cells, and coupled with suitable microfluidics, can be used as the sensor component of a cell sorting system. An optical trap has been used for such sorting, where lymphocytes were identified and sorted. Lymphocytes are vital to the human immune system and there are many variants with a range of specific functions [204]. The cells are trapped at a Raman detection site where they are then categorised and positioned inside special holding areas, creating pure sample batches of the lymphocyte types. Microfluidic traps provide Raman-microfluidic systems with the capacity to study cells that are exposed to changing environmental conditions, with systems being used for studying the effects of medical drugs on cells. To this end, a Raman-microfluidic system to study the behaviour of yeast cells under various environmental conditions has been demonstrated [205].

Temporal studies of cells are possible with Raman-microfluidic systems. As an example, Chinese hamster ovary (CHO) cells have been studied using a Y-shaped microfluidic channel used to mix cells with SERS colloid [206]. The cells were monitored over time using Raman microscopy, and it was found that Amide I levels reduced over time. Furthermore, spatial experiments were also conducted on the CHO cells, creating an x–y Raman map, together with a z–axis profile showed that there was a strong indication of C–H deformation peaks from proteins near the centre of the nucleus.

2.5.3.4 Tissue

Raman-microfluidics has found applications in tissue engineering, where the benefits of such systems include the continuous flow of nutrition and vital gases like oxygen, as well as the constant withdrawal of waste products [207, 208]. Additionally, microfluidics provides the perfect platform for studying fundamental biological phenomena, including exposing tissue to environmental variations at critical growth stages to monitor its effects [209]. The applications of this technology are particularly important for the study of drugs, where tests can be implemented safely on live human tissue samples in a highly controlled environment while allowing for accurate measurements. This could drastically reduce the failure rate of potential drugs involved in human clinical trials [210]. Some examples extend this concept as far as ‘organ-on-a-chip’ microsystems, which allow for *in vitro* organ-level studies, as opposed to cell-based systems [211]. Raman microscopy can be applied to these ‘organ-on-a-chip’ systems for the inline detection and monitoring of samples, providing accurate measurements of chemical constituents. Raman microscopy would allow for non-invasive and non-contact detection in the LOC environments, providing contamination free and well controlled results. With the use of SORS or transmission Raman it is possible to analyse 3D tissue samples, with penetration below the surface of the tissue samples, proving valuable feedback on the internal process of tissue samples [4, 212-217].

2.5.3.5 Other organic samples

In addition to the aforementioned organic samples, Raman-microfluidic systems are capable of studying many other biological candidates, including DNA-cell, DNA-protein, virus, toxins and cell-protein complexes [218], and their compositions with non-organic chemicals [192].

Raman microfluidic systems are also excellent tools for investigating zygotes and embryos. The monitoring of zygotes and embryos in microfluidic environments that simulate their host are particularly important for the investigation of genetic deformations, abnormalities and other such issues and provide invaluable information about the process of their growth. Raman microscopy has already been used to identify and study yeast zygote cells in an effort to apply such Raman mapping for the label free study of cell proliferation [219, 220].

In vitro fertilisation (IVF) treatments currently rely on visual inspection of the morphology of an embryo in order to determine its viability as an IVF candidate. Research currently suggests that Raman microscopy can assist in the identification of ideal candidates, in combination with morphology characteristics [221, 222], with the potential to increase the IVF success rates [221, 222]. Furthermore, microfluidic environments can be used to enhance the monitoring and handling of embryonic cells, as microfluidics would allow for high throughput approaches [223-225]. The microfluidic environment can even be used for the fertilisation process of embryos, allowing the initial stages to be carefully monitored before placing it into the host [223, 224, 226].

2.5.4 Pharmaceuticals

Raman microscopy can be used for investigating the effectiveness of developed drugs in the controlled microfluidic environment. Different scenarios can be ‘simulated’ and tested using Raman-microfluidic systems, using low cost processes and small volume samples, before the pharmaceuticals are tested on animals and human. Multi-component pharmaceuticals can also be tested and the results could be categorised using different data analysis processes [227].

Microfluidic micro-reactors can be used for pharmaceutical production and testing, and every stage of the process can be carefully controlled. Raman microscopy can be used to give real-time feedback on the chemical reactions in such systems [228]. For example, Raman microscopy can support the screening of polymorphic structures, and support the chemical development process as it is scaled-up [229]. Lipids are often essential components of colloidal pharmaceutics. Raman microscopy has proven particularly sensitive to lipids, which contain unique Raman signal producing hydrocarbon chains. Raman microscopy can determine the structure of lipids to determine the packing behaviour and phase transitions [230].

2.5.5 Forensics

Accurate forensic analysis is required by authorities for obtaining successful prosecutions. Current systems rely on electrophoretic DNA chips, which require pre-processing, filtering and polymerase chain reactions to enhance the number of DNA strands [231]. Alternatives to these DNA chips include optical options such as fluorescent systems, which require the use of fluorescent tags [232, 233]. Raman systems can also be used for DNA characterisation, providing a quick and thorough analysis of biological forensic markers. Raman analysis has been used for the forensic analysis of body fluid traces [234] including whole blood [235], vaginal fluids [236], forensic pharmaceutical investigations [237], explosives [7] and drugs of abuse [238].

Microfluidics has the potential to enhance this field, as the majority of the forensic samples are organic in nature and can be suspended in liquid, and therefore can be measured in Raman-microfluidic devices. Furthermore, microfluidics provide ideal lab-on-a-chip environments, therefore sample preparation can be conducted in a fast and portable fashion. Samples of DNA and other body fluids can be stored in their liquid forms, and Raman microscopy provides a non-destructive method of testing, allowing the sample to be re-used if required. With all these benefits there is still the issue of portability and costs, which have been thoroughly discussed in the "Considerations for Raman spectroscopy in microfluidics" section. Low cost devices and access to the right data banks are required for widespread forensic analysis using Raman-microfluidic devices.

2.6 Data analysis

Analysis of Raman spectroscopic information is extremely important for gaining the correct insights. Raman spectroscopy data is not as definitive as the information obtained from a DNA characterisation, but it is far more specific than most other optical analytical tools such as normal light microscopy and UV-Vis absorption spectroscopy. Complex organic compounds generate a large number of Raman peaks which are hard to distinguish and categorise. Therefore the accurate analysis of data from Raman- microfluidic systems is an important issue. Raman data can be used for not only qualitative analysis (determining the type of materials in the microfluidics environment), but also for quantitative analysis (determining the concentration of materials). A brief table for comparison of the major Raman spectra data analysis techniques is presented in Table 2.1.

Table 2.1: Comparison of Raman spectra analysis techniques.

Technique	Description	Qualitative	Quantitative	Examples
Hierarchal cluster analysis (HCA)	Order Raman spectra into hierarchy of commonalities	YES	NO	Bacteria strain [239] respiratory syncytial virus strain [240] Bacteria on milk [241] Bacteria in food [242] Counterfeit drugs [243] Human blood [244]
Principal component analysis (PCA)	Reduce Raman spectra down to several principal components, determining the score values for each spectrum	YES	NO	Tetracycline antibiotics [245] Suppositories [246] Preeclampsia [247] Medicine counterfeits [248] Saliva from lung cancer patents [249] Laryngeal cancer diagnosis [250]
Partial least squares (PLS)	Multivariate regression technique where a set of known (expected) chemicals is compared against the complex spectra in order to extract a linear relationship between the known concentration of a particular component and the intensity of Raman spectral information	NO	YES	Pharmaceutical tables [251] Prednisone in tablets [252] Tetracycline antibiotics[245] Illicit street drugs [253] Suppositories [254] Human blood plasma [255]
Principal component regression (PCR)	Linear regression is used on the principal components of the Raman spectral data to obtain the quantity of the Raman principal components within a Raman spectrum (similar to PLS, without the known spectra)	NO	YES	Polyurethane [256] Gestational hypertension [247] Identification of medicine counterfeits [248] Laryngeal cancer diagnosis [250] Saliva from lung cancer patents [249]
Deconvolution	Breakdown of complex Raman spectra into known bond peak in order to identify and quantify its components	YES	NO	Human skin samples [257] Cancer cells [258] Carbon nanotubes [259]
Wavenumber correlation	Comparing a known Raman spectrum to the unknown and determining its correlation	YES	NO	Graphites [260] Poly(L-lysine) [261]
Linear regression	The concentration of the sample is measured using the intensity and/or widths of Raman peaks, where a linear relationship between the known concentration values and the Raman spectral data is made	NO	YES	Dipicolinic acid [129, 262] Promethazine [54] Glucose [263, 264]

2.6.1 Qualitative analysis

Qualitative analysis focusses on Raman spectral information that describes the types of materials being detected, essentially using a chemical’s ‘fingerprint’ to determine its presence in the microfluidic system. For simple Raman spectra it is convenient to compare a known Raman spectrum to the unknown spectrum and determine the correlation in terms of peak positions and relative intensities.

Wavenumber and peak intensity can be readily applied for analysing single targets or multiple targets where the peaks of the different components do not overlap excessively. In microfluidics it is likely that, due to presence of multiple chemicals, spectral data will be multivariate in character, containing Raman signatures from many components simultaneously. Analysis of multivariate data should provide researchers with statistical information about the type a relative abundance of the analyte in the environment. These analysis methods are most suited to biological candidates such as proteins, amino acids, sugars, DNA, RNA, lipids and gases, where the Raman spectrum would contain the peaks from a large number of chemical constituents.

There are a number of different multivariate analysis techniques that exist for determining the components of complex Raman spectra. These techniques are capable of extracting useful information using a variety of data-driven processes for analysing Raman-microfluidics data.

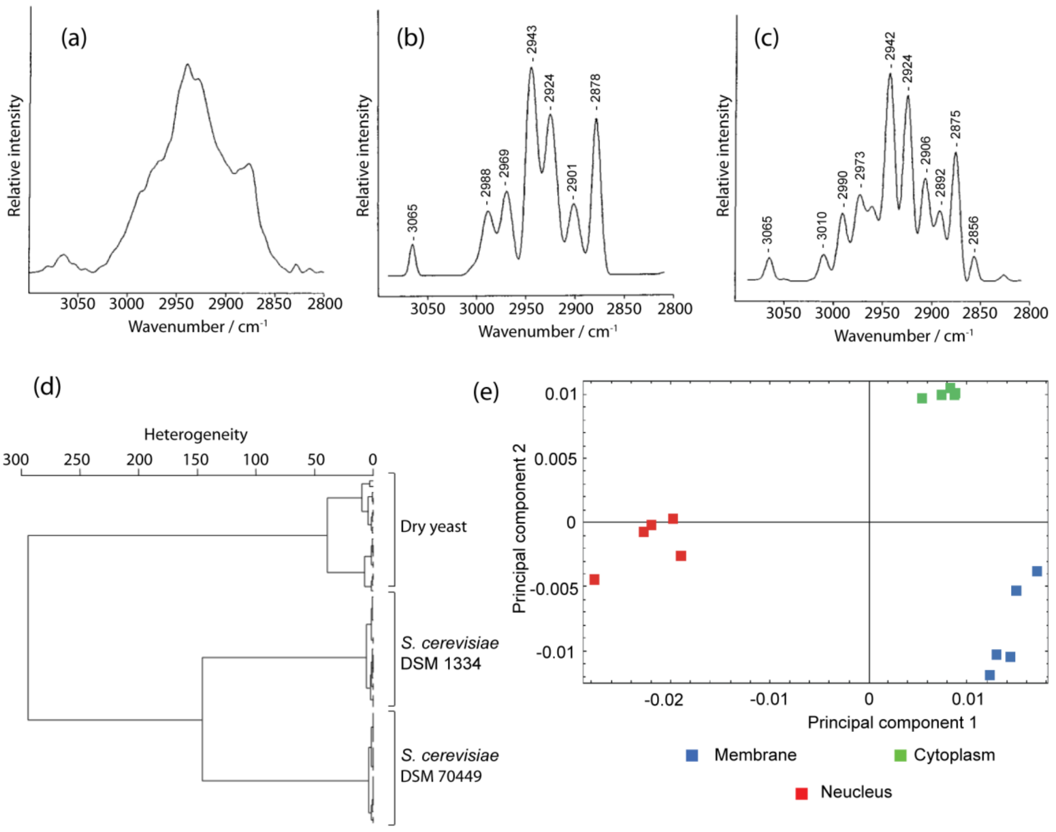

Figure 2.12: Examples of qualitative evaluation of multivariable using Raman microscopic data. (a) Raman spectrum of β-lactoglobulin (b) deconvoluted spectrum using Lorentzian peak shape and (c) deconvoluted spectrum using Gaussian peak shape. Adapted from Ref. [257] (d) Hierarchical cluster analysis from the average Raman spectra of three yeast cells types. Adapted from Ref. [265]. (e) 2-D plots show the separation of data based on different components of a cell. Reproduced from Ref. [78].

2.6.1.1 Deconvolution of Raman spectra

Multivariate Raman spectra can be deconvolved, or broken down, into the known peaks for various Raman-active bonds. The resulting deconvolved spectra can then be analysed using direct wavelength correlation to determine its components. Two main techniques are used for the blind deconvolution of Raman spectroscopic data, the Lorentzian and Gaussian methods, which help to narrow the scope of the blind deconvolution process [257, 266]. These two techniques have been compared against each other for the study of several proteins, where deconvoluted Raman data was used to determine the effect of heat treatment on C-H bonds of the proteins (Figure 2.12(a) – (c)) [257]. Other examples where deconvolution has been used for Raman spectral analysis include the study of human tissue samples [267], studies of single-wall carbon nanotube (SWCNT) exposure on mice [259] and prostate cancer cells [258].

2.6.1.2 Hierarchical cluster analysis (HCA)

HCA seeks to order a series of spectra into clusters based on a hierarchy of commonalities found in the Raman data [268]. This technique is used mostly for categorising biological samples, where they can be organised and identified into their types using Raman microscopy information. Examples of HCA for Raman data analysis include investigating and classifying single yeast cell types (Figure 2.12(d)) [265], cells grown in different environmental media [269] and various bacterial samples [270].

2.6.1.3 Principal component analysis (PCA)

PCA compresses Raman spectral data into a fixed number of features (principal components), by calculating the orthogonal directions (scores), associated with the maximum variance in the Raman data. This method implies that there is a fair amount of redundant data in the Raman spectrum, as one element can contribute to many Raman bands [271]. The score points are then plotted against one another and used to identify trends and groups of common Raman signatures. PCA is commonly used for qualitative analysis of biological Raman spectra, including the analysis of coronary artery tissue [272], both primary human keratinocyte and human cervical squamous carcinoma cells (Figure 2.12(e)) [78], leukaemia cell life cycle states [201], breast cancer diagnosis [273] and ethanol content in consumable tequila [274]. Other recent work has shown the application of PCA for studying the outputs of hyper-spectral Raman imaging in an effort to map the locations and intensities of specific components over the image [275].

2.6.2 Quantitative analysis

Raman spectroscopy is capable of providing quantitative information on target materials, allowing determinations of particle sizes [276] and concentrations of materials and components in the target area. For particles between 5 and 50 nm it is possible to determine their size by using the broadening characteristic of certain Raman peaks [276-279]. Other examples for diamond structures use Raman peak shifts for determining sizes between 0.1 and 2 nm [280, 281] or to determine the strain on a particular bonds [282].

For quantitative measurements of concentration, it is common to use methods such as regression analysis, where the concentration of the sample is measured using the intensity and/or area of Raman peaks. Regression analysis creates an analytical relationship between the known concentration values and the Raman spectral data. Once the concentration relationships have been determined it becomes possible to assess the concentration of some unknown sample. Examples which implement this technique to determine concentration include analytes such as dipicolinic acid [129, 262], promethazine [54], mitoxantrone [54] and glucose (Figure 2.13(a)) [263, 264].

Quantitative analysis of several components simultaneously, especially when these components have overlapping Raman peaks, can be a complex issue. However, this is a scenario which is commonly seen for many measurements where contaminants and interfering reagents exist. There is always a trade-off between the number of pre-processing stages for purification of samples and the complexity of the quantitative analysis. Obviously a high degree of qualitative analysis is also included in determining the quantities of chemicals in complex systems, as these systems are multivariate in nature and require some form of statistical analysis.

Partial least squares (PLS) is a multivariate regression technique where a set of known (expected) chemicals is compared against a complex spectrum in order to extract a linear relationship between the known concentration of a particular component and the intensity of Raman spectral information. As PLS requires prior knowledge of the target chemicals it is usually coupled with a qualitative technique, such as PCA, for determining the presence of any target chemicals. PLS has been used for detection of glucose, lactic acid and creatinine at various concentrations (Figure 2.13(b)) [119]. Further examples include the analysis of mass fractions of $Ba(NO_3)_2$ [283], concentrations of oxytetracycline [245] and sample fractions of carbon, magnesium, sodium and potassium from soil samples [284].

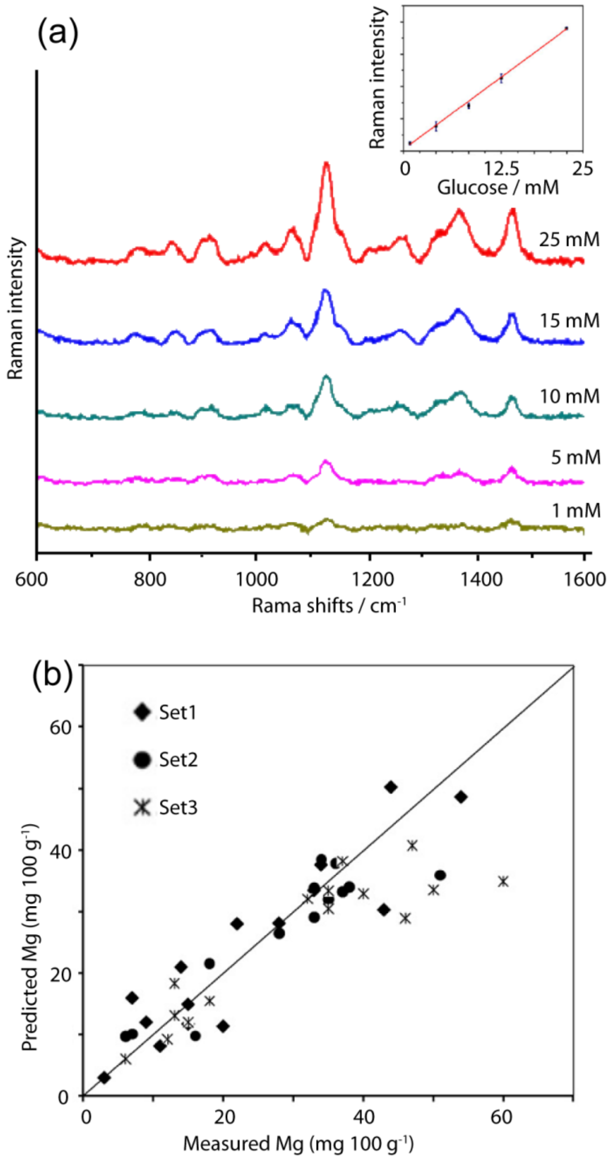

Figure 2.13: Examples of quantitative evaluation using Raman microscopic data. (a) SERS spectra of varying concentrations of glucose. The calibration plot obtained from the spectra is shown as an inset. Reproduced from Ref. [264]. (b) PLS prediction of magnesium (Mg) content of soil samples. Reproduced from Ref. [284].

Principal component recognition (PCR) is a multivariate quantification technique that is, in some ways, is similar to PLS. PCR uses the principal components of the Raman data to generate the linear concentration relationships, as opposed to the expected chemical specific Raman spectra from PLS strategies. PCR requires the calculation of principal components, similar to PCA, and also assumes the presence of redundant data in the Raman spectra. Unlike PLS, this method does not require the Raman signature of the target chemical, as it uses the principal component. However, this fact also makes PCR analysis less stable for determining concentration behaviour, as the principal component may not only contain Raman information from the desired material, but also information from other materials. Nevertheless, PCR has been widely used for determining quantitative data from Raman spectra in examples such as thermoplastic polyurethane analysis [256], preeclampsia (gestational hypertension) studies [247], identification of medicine counterfeits [248], laryngeal cancer diagnosis [250] and for the study of saliva from lung cancer patents [249].

2.7 Extended review on dielectrophoresis

The author employed dielectrophoresis (DEP) for the manipulation of nanoparticles in this PhD research. In this section, the fundamentals that describe the DEP force will be described and the justification for its use by the author of this PhD thesis will be presented.

2.7.1 Dielectrophoretic force

DEP is defined as the interaction of a non-uniform electric field, *E,* with a particle, inducing motion in the particle [285, 286]. The DEP force, of which motion is the result, is defined as [287]:

$$\vec{F}_{DEP} = (P.\nabla)E \tag{2.1}$$

where P is the induced dipole moment of a polarisable particle and E is the quasi-static electric field, expressed as [288]:

$$E(x,y,z,t) = E_x \cos(\omega t + \varphi_x)\vec{i} + E_y \cos(\omega t + \varphi_y)\vec{j} + E_z \cos(\omega t + \varphi_z)\vec{k} \tag{2.2}$$

where φ is the phase component of the applied electric field, t is the time, and ω is the angular frequency of the electric field. The dipole moment, P, is dependent on the geometry of the particle. For a spherical particle, the dipole moment is defined as [287]:

$$P = 4\pi r^3 \varepsilon_0 \varepsilon_{medium} f_{CM}(\omega) E \tag{2.3}$$

where r is the radius of the particle, $\varepsilon_o = 8.854\times10^{-12}$ (F·m^{-1}) is the permittivity of free space, $\varepsilon_{\text{medium}}$ is the relative permittivity of medium and $f_{CM}(\omega)$ is the Clausius-Mossotti (CM) factor, which was defined for spherical particles as [144]:

$$f_{CM} = \frac{\varepsilon^{*}_{particle} - \varepsilon^{*}_{medium}}{\varepsilon^{*}_{particle} + 2\varepsilon^{*}_{medium}} \tag{2.4}$$

where, $\varepsilon_{particle}{}^{*}$ and $\varepsilon_{medium}{}^{*}$ are the complex permittivities of the particle and the suspending medium, respectively, each defined as:

$$\varepsilon^{*} = \varepsilon - \frac{i\sigma}{\omega} \tag{2.5}$$

where, ε^{*} is the complex permittivity, ε is the relative permittivity, σ is the conductivity of the particle/medium and ω is the applied electric field frequency. After combining equations (2.1)-(2.3), the DEP force applied on a spherical particle can be calculated as [287, 289]:

$$\vec{F}_{DEP} = 2\pi r^{3}\varepsilon_{0}\varepsilon_{medium}\operatorname{Re}\left[f_{CM}(\omega)\right]\nabla E^{2}_{rms} + 4\pi r^{3}\varepsilon_{0}\varepsilon_{medium}\operatorname{Im}\left[f_{CM}(\omega)\right]\sum_{x,y,z}\nabla E^{2}_{rms}\nabla\varphi \tag{2.6}$$

The DEP force equation above consists of the addition of two distinct types of DEP force. The first DEP force is proportional to the real part of the CM factor and the spatial non-uniformity of the electric field. This force is referred to as the classical DEP force, and is responsible for pushing the particle away from, or towards, the regions of highest electric field gradients.

The second DEP force term is called travelling wave DEP, and it is proportional to the imaginary part of the CM factor [290]. This force is also proportional to the spatial and electrical phase non-uniformities of the applied electric fields. This force pulls particles towards, or away from, the direction of electrical wave propagation. This force is only present when there is an electrical phase difference present, and when this is not employed the classical DEP force equation is dominant.

2.7.2 Clausius-Mossotti spectrum

The polarity of the DEP force equation (equation (2.6)) is governed by the CM factor, and can be used to predict the behaviour of the particles when they are exposed to non-uniform electric fields at a particular frequency. The CM factor accounts for five important factors of a DEP system, including: (i) the shape of the particles (i.e. spherical, cylindrical or ellipsoidal) (ii) the interior structure of the particles (i.e. multilayer structures) (iii) the dielectric properties of the particle and its structures, composed of its conductivity and permittivity (iv) the dielectric properties of the suspending medium and (v) the frequency of the applied electric field [143]. The last parameter can be adjusted for the desired DEP behaviour, while the first four parameters are intrinsic to the particles and medium.[291]

The CM factor is usually simulated over a wide range of electric field frequencies in order to determine at what frequency the DEP force will be ‘positive’ or ‘negative’ in magnitude. A positive DEP force (when $\mathrm{Re}[f_{\mathrm{CM}}(\omega)] > 0$) causes the suspended particles to be attracted the areas of highest electric field gradients. A negative DEP force (when $\mathrm{Re}[f_{\mathrm{CM}}(\omega)] < 0$) causes the suspended particles to be repelled from those areas. Additionally, the ‘cross-over’ frequency is where the DEP force is neither positive nor negative, and indicates the transition between the two states. For complex multi-layer particles there can be more than one cross-over frequency. Prior knowledge of the polarity of $\mathrm{Re}[f_{\mathrm{CM}}(\omega)]$ over the desired frequency range provides the information needed to tune the DEP force for the intended application. In this thesis, the CM factor is simulated for each of the suspended materials at each stage of the project, calculated and simulated in chapters 4, 5 and 6.

2.7.3 Microelectrode designs

The non-uniform electric field gradients that are required for inducing DEP force can be generated through a number of various microelectrode configurations. Each configuration can be designed to produce distinct electric field gradients for trapping, sorting and moving suspended particles [292-294]. Some selected microelectrode designs which allow trapping and concentration of suspended particles under flow include: (i) interdigitated (ii) oblique and (iii) curved microelectrode configurations. The dominating features of each design are briefly described as follows:

i. Interdigitated

Interdigitated, or parallel microelectrodes, generate high electric field gradients directly above their surface. This property is useful for microfluidic DEP applications, where the DEP force is applied to particles in the areas above the electrodes. This design offers an additional benefit to microfluidics, whereby the electrodes can be designed wide enough to cover the entire microchannel floor. There have been many applications and discussion regarding DEP trapping and sorting in microfluidics using interdigitated microelectrodes [295-300].

ii. Oblique

The oblique microelectrode configuration is advantageous to microfluidic systems where constant flow is desired. These microelectrodes produce the highest electric field gradients at the tip regions, allowing particles to be trapped in those regions. Compared to the interdigitated microelectrodes, this electrode design captures only a small amount of suspended particles from the fluids. These electrodes have been extensively demonstrated for DEP trapping of particles in microfluidic flow systems [301-303].

iii. Curved

The curved microelectrode generates its highest electric field gradient between the microelectrode tips, similar to the oblique design. However, the curved design of these electrodes also enhances electric field gradients along the channels centre line in order to ‘funnel’ suspended materials towards the microelectrode tips. This effect increases the trapping efficiency of this design, allowing more particles to be trapped using DEP. This design has been investigated for applications of cell sorting [150, 304, 305], carbon nanotube capture [149] and optofluidics [108, 306, 307].

2.7.4 Motivation for DEP integration

The aim of this PhD research project is to implement a Raman microscopy *in situ* monitoring system in microfluidics. The DEP force was chosen to enhance the controllability and trapping of suspended materials, while still allowing for constant flow microfluidics. The author implemented the curved microelectrode configuration as it provided high density trapping at the microelectrode tips, while still allowing for strong DEP forces across the entire microchannel centreline. Using this design the DEP force can be accurately tuned for trapping materials at the microelectrode tips, while allowing the concentration of materials at the tips to be accurately controlled by varying both the frequency and magnitude of the applied AC signals. This is particularly useful for Raman microscopy, where high concentrations of suspended particles can be readily created at the microelectrode tips, allowing for strong Raman signals to be captured (as will be seen in chapter 4). Additionally, silver nanocolloids can be manipulated using DEP for creating SERS hot-spots. The these hot-spots can be readily controlled using DEP forces, where DEP can help optimize the spacing between the suspended silvers, as will be seen in chapter 5.

DEP forces can be readily applied to cells, where the DEP force is capable of trapping them without damage. This is advantageous, especially for Raman microscopy where the cells must be immobilised before a Raman spectrum from the cell can be taken. DEP is capable of controlling the distribution of trapped cells, and is able to trap cells isolated from one another, or in larger cluster (as will be seen in chapter 6). These are the motivations for implementing curved microelectrode DEP in this PhD research project.

2.8 Summary

In this chapter, the author presented applications of Raman microscopy integrations with microfluidic devices, Raman-microfluidics. In addition, he presented several statistical techniques for use with Raman-microfluidic data as well as a brief overview of DEP and its applications for this PhD research. A major portion of this chapter was submitted for publication consideration in Chemical Society Reviews.

In this PhD research program, DEP force was chosen as the controlling feature in the microfluidics. The curved microelectrode design provides consistent and predictable trapping locations, while still maintaining acceptable trapping efficiency and controllability. The integrations of Raman-microfluidic devices with DEP will be further elaborated in chapters 4, 5 and 6. In the next chapter the author describes the fabrication and testing of a microfluidic-DEP platform used in his PhD research project.

References

[1] Chrimes, A.F., K. Khoshmanesh, P.R. Stoddart, A. Mitchell, and K. Kalantar-zadeh, Microfluidics and Raman microscopy: current applications and future challenges. *Chemical Society Reviews*, 2013.

[2] Raman, C.V. and K.S. Krishnan, A new type of secondary radiation. *Nature*, vol. 121, pp. 501-502, 1928.

[3] Drescher, D. and J. Kneipp, Nanomaterials in complex biological systems: insights from Raman spectroscopy. *Chemical Society Reviews,* vol. 41, pp. 5780-5799, 2012.

[4] Matousek, P., Deep non-invasive Raman spectroscopy of living tissue and powders. *Chemical Society Reviews,* vol. 36, pp. 1292-1304, 2007.

[5] Clark, R.J.H., Raman Microscopy - Applications to the Identification of Pigments on Medieval Manuscripts. *Chemical Society Reviews,* vol. 24, pp. 187-196, 1995.

[6] Ashok, P. and K. Dholakia, Microfluidic Raman Spectroscopy for Bio-chemical Sensing and Analysis. in *Optical Nano- and Microsystems for Bioanalytics*. vol. 10, Fritzsche, W. and J. Popp, Eds., ed Berlin Heidelberg: Springer, 2012, pp. 247-268.

[7] Buckley, K. and P. Matousek, Non-Invasive Detection of Concealed Liquid and Powder Explosives Using Spatially Offset Raman spectroscopy. in *Infrared and Raman Spectroscopy in Forensic Science,* ed: John Wiley & Sons, Ltd, 2012, pp. 289-294.

[8] Otieno-Alego, V., Raman-a useful crime fighting tool in forensic laboratories. *Science Access,* vol. 2, pp. 492-493, 2004.

[9] Vandenabeele, P., J. Tate, and L. Moens, Non-destructive analysis of museum objects by fibre-optic Raman spectroscopy. *Analytical and Bioanalytical Chemistry,* vol. 387, pp. 813-819, 2007.

[10] Vandenabeele, P., B. Wehling, L. Moens, H. Edwards, M. De Reu, and G. Van Hooydonk, Analysis with micro-Raman spectroscopy of natural organic binding media and varnishes used in art. *Analytica Chimica Acta,* vol. 407, pp. 261-274, 2000.

[11] West, J., M. Becker, S. Tombrink, and A. Manz, Micro total analysis systems: Latest achievements. *Analytical Chemistry,* vol. 80, pp. 4403-4419, 2008.

[12] Zhang, C. and D. Xing, Single-Molecule DNA Amplification and Analysis Using Microfluidics. *Chemical Reviews,* vol. 110, pp. 4910-4947, 2010.

[13] Chandra, H., P.J. Reddy, and S. Srivastava, Protein microarrays and novel detection platforms. *Expert review of proteomics,* vol. 8, pp. 61-79, 2011.

[14] Chao, T.-C. and A. Ros, Microfluidic single-cell analysis of intracellular compounds. *Journal of The Royal Society Interface,* vol. 5, pp. S139-S150, 2008.

[15] Mairhofer, J., K. Roppert, and P. Ertl, Microfluidic Systems for Pathogen Sensing: A Review. *Sensors,* vol. 9, pp. 4804-4823, 2009.

[16] Gupta, R., B. Bastani, N.J. Goddard, and B. Grieve, Absorption spectroscopy in microfluidic flow cells using a metal clad leaky waveguide device with a porous gel waveguide layer. *Analyst,* vol. 138, pp. 307-314, 2013.

[17] Sabuncu, A.C., J. Zhuang, J.F. Kolb, and A. Beskok, Microfluidic impedance spectroscopy as a tool for quantitative biology and biotechnology. *Biomicrofluidics,* vol. 6, pp. 034103-15, 2012.

[18] Adar, F., M. Delhaye, and E. DaSilva, Evolution of Instrumentation for Detection of the Raman Effect as Driven by Available Technologies and by Developing Applications. *Journal of Chemical Education,* vol. 84, p. 50, 2007.

[19] Fleischmann, M., P.J. Hendra, and A.J. McQuillan, Raman spectra of pyridine adsorbed at a silver electrode. *Chemical Physics Letters,* vol. 26, pp. 163-166, 1974.

[20] Tong, L., T. Zhu, and Z. Liu, Approaching the electromagnetic mechanism of surface-enhanced Raman scattering: from self-assembled arrays to individual gold nanoparticles. *Chemical Society Reviews*, vol. 40, pp. 1296-1304, 2011.

[21] Kneipp, K., M. Moskovits, and H. Kneipp, *Surface-enhanced raman scattering: physics and applications*. 2006: Springer.

[22] Guerrini, L. and D. Graham, Molecularly-mediated assemblies of plasmonic nanoparticles for Surface-Enhanced Raman Spectroscopy applications. *Chemical Society Reviews,* vol. 41, pp. 7085-7107, 2012.

[23] Rodriguez-Lorenzo, L., L. Fabris, and R.A. Alvarez-Puebla, Multiplex optical sensing with SERS. A critical review. *Analytica Chimica Acta,* vol. 745, pp. 10-23, 2012.

[24] Jeanmaire, D.L. and R.P. Van Duyne, Surface raman spectroelectrochemistry: Part I. Heterocyclic, aromatic, and aliphatic amines adsorbed on the anodized silver electrode. *Journal of Electroanalytical Chemistry and Interfacial Electrochemistry,* vol. 84, pp. 1-20, 1977.

[25] Chao, R., R. Khanna, and E. Lippincott, Theoretical and experimental resonance Raman intensities for the manganate ion. *Journal of Raman Spectroscopy,* vol. 3, pp. 121-131, 1975.

[26] Docherty, F.T., P.B. Monaghan, R. Keir, D. Graham, W.E. Smith, and J.M. Cooper, The first SERRS multiplexing from labelled oligonucleotides in a microfluidics lab-on-a-chip. *Chemical Communications*, vol. 1, pp. 118-119, 2004.

[27] Graham, D. and K. Faulds, Quantitative SERRS for DNA sequence analysis. *Chemical Society Reviews,* vol. 37, pp. 1042-1051, 2008.

[28] Kneipp, K., Y. Wang, R.R. Dasari, and M.S. Feld, Approach to Single-Molecule Detection Using Surface-Enhanced Resonance Raman-Scattering (SERRS) - A Study Using Rhodamine 6G on Colloidal Silver. *Applied Spectroscopy,* vol. 49, pp. 780-784, 1995.

[29] Smith, Z.J. and A.J. Berger, Integrated Raman-and angular-scattering microscopy. *Optics Letters,* vol. 33, pp. 714-716, 2008.

[30] Smith, Z.J. and A.J. Berger, Validation of an integrated Raman-and angular-scattering microscopy system on heterogeneous bead mixtures and single human immune cells. *Applied Optics,* vol. 48, pp. D109-D120, 2009.

[31] Smith, Z.J. and A.J. Berger, Construction of an integrated Raman-and angular-scattering microscope. *Review of Scientific Instruments,* vol. 80, pp. 044302:2-8, 2009.

[32] Begley, R., A. Harvey, and R.L. Byer, Coherent anti-Stokes Raman spectroscopy. *Applied Physics Letters*, vol. 25, pp. 387-390, 1974.

[33] Wipfler, A., T. Buckup, and M. Motzkus, Multiplexing single-beam coherent anti-stokes Raman spectroscopy with heterodyne detection. *Applied Physics Letters,* vol. 100, pp. 071102:2-4, 2012.

[34] Lütgens, M., S. Chatzipapadopoulos, and S. Lochbrunner, Coherent anti-Stokes Raman scattering with broadband excitation and narrowband probe. *Optics Express,* vol. 20, pp. 6478-6487, 2012.

[35] Evans, C.L. and X.S. Xie, Coherent anti-Stokes Raman scattering microscopy: chemical imaging for biology and medicine. *Annual Review of Analytical Chemistry,* vol. 1, pp. 883-909, 2008.

[36] Freudiger, C.W., W. Min, B.G. Saar, S. Lu, G.R. Holtom, C. He, J.C. Tsai, J.X. Kang, and X.S. Xie, Label-Free Biomedical Imaging with High Sensitivity by Stimulated Raman Scattering Microscopy. *Science,* vol. 322,

pp. 1857-1861, 2008.

[37] Stadler, J., T. Schmid, and R. Zenobi, Developments in and practical guidelines for tip-enhanced Raman spectroscopy. *Nanoscale,* vol. 4, pp. 1856-1870, 2012.

[38] Hermann, P., A. Hermelink, V. Lausch, G. Holland, L. Möller, N. Bannert, and D. Naumann, Evaluation of tip-enhanced Raman spectroscopy for characterizing different virus strains. *Analyst,* vol. 136, pp. 1148-1152, 2011.

[39] Kim, H., K.M. Kosuda, R.P. Van Duyne, and P.C. Stair, Resonance Raman and surface- and tip-enhanced Raman spectroscopy methods to study solid catalysts and heterogeneous catalytic reactions. *Chemical Society Reviews,* vol. 39, pp. 4820-4844, 2010.

[40] Higgins, M.J., T. Fukuma, and S.P. Jarvis, AFM In Liquid: A High Sensitivity Study On Biological Membranes. *Imaging & Microscopy,* vol. 8, pp. 47-50, 2006.

[41] Matousek, P. and A. Parker, Bulk Raman analysis of pharmaceutical tablets. *Applied Spectroscopy,* vol. 60, pp. 1353-1357, 2006.

[42] Schulmerich, M.V., M.J. Walsh, M. Gelber, R. Kong, M. Kole, S. Harrison, J. McKinney, D. Thompson, L. Kull, and R. Bhargava, Protein and oil composition predictions of single soybeans by transmission Raman spectroscopy. *Journal of Agricultural and Food Chemistry,* vol. 60, pp. 8097-8102, 2012.

[43] Ketterer, B., E. Uccelli, and A.F. i Morral, Mobility and carrier density in p-type GaAs nanowires measured by transmission Raman spectroscopy. *Nanoscale,* vol. 4, pp. 1789-1793, 2012.

[44] Qin, J., K. Chao, and M.S. Kim, Nondestructive evaluation of internal maturity of tomatoes using spatially offset Raman spectroscopy. *Postharvest Biology and Technology,* vol. 71, pp. 21-31, 2012.

[45] Ma, K., J.M. Yuen, N.C. Shah, J.T. Walsh, M.R. Glucksberg, and R.P. Van Duyne, In Vivo, Transcutaneous Glucose Sensing Using Surface-Enhanced Spatially Offset Raman Spectroscopy: Multiple Rats, Improved Hypoglycemic Accuracy, Low Incident Power, and Continuous Monitoring for Greater than 17 Days. *Analytical Chemistry,* vol. 83, pp. 9146-9152, 2011.

[46] Smith, C.L., Basic Confocal Microscopy. in *Current Protocols in Microbiology,* ed: John Wiley & Sons, Inc., 2005.

[47] Ghomi, M., *Advances in Biomedical Spectroscopy* vol. 5. 2012, Amsterdam: IOS Press.

[48] Ward, Y., R.J. Young, and R.A. Shatwell, Effect of excitation wavelength on the Raman scattering from optical phonons in silicon carbide monofilaments. *Journal of Applied Physics,* vol. 102, pp. 023512-7, 2007.

[49] McFarland, A.D., M.A. Young, J.A. Dieringer, and R.P. Van Duyne, Wavelength-Scanned Surface-Enhanced Raman Excitation Spectroscopy. *The Journal of Physical Chemistry B,* vol. 109, pp. 11279-11285, 2005.

[50] Enger, J., M. Goksor, K. Ramser, P. Hagberg, and D. Hanstorp, Optical tweezers applied to a microfluidic system. *Lab on a Chip,* vol. 4, pp. 196-200, 2004.

[51] König, K., H. Liang, M. Berns, and B. Tromberg, Cell damage in near-infrared multimode optical traps as a result of multiphoton absorption. *Optics Letters,* vol. 21, pp. 1090-1092, 1996.

[52] Ramser, K., J. Enger, M. Goksor, D. Hanstorp, K. Logg, and M. Kall, A

microfluidic system enabling Raman measurements of the oxygenation cycle in single optically trapped red blood cells. *Lab on a Chip,* vol. 5, pp. 431-436, 2005.

[53] Strehle, K.R., D. Cialla, P. Rosch, T. Henkel, M. Kohler, and J. Popp, A Reproducible Surface-Enhanced Raman Spectroscopy Approach. Online SERS Measurements in a Segmented Microfluidic System. *Analytical Chemistry,* vol. 79, pp. 1542-1547, 2007.

[54] Ackermann, K.R., T. Henkel, and J. Popp, Quantitative online detection of low-concentrated drugs via a SERS microfluidic system. *ChemPhysChem,* vol. 8, pp. 2665-2670, 2007.

[55] März, A., K.R. Ackermann, D. Malsch, T. Bocklitz, T. Henkel, and J. Popp, Towards a quantitative SERS approach – online monitoring of analytes in a microfluidic system with isotope-edited internal standards. *Journal of Biophotonics,* vol. 2, pp. 232-242, 2009.

[56] Wang, G., C. Lim, L. Chen, H. Chon, J. Choo, J. Hong, and A.J. deMello, Surface-enhanced Raman scattering in nanoliter droplets: towards high-sensitivity detection of mercury (II) ions. *Analytical and Bioanalytical Chemistry,* vol. 394, pp. 1827-1832, 2009.

[57] Gras, S.L., T. Mahmud, G. Rosengarten, A. Mitchell, and K. Kalantar-zadeh, Intelligent Control of Surface Hydrophobicity. *ChemPhysChem,* vol. 8, pp. 2036-2050, 2007.

[58] Rong, H., Y.-H. Kuo, S. Xu, A. Liu, R. Jones, M. Paniccia, O. Cohen, and O. Raday, Monolithic integrated Raman silicon laser. *Opt. Express,* vol. 14, pp. 6705-6712, 2006.

[59] Rong, H., S. Xu, Y.-H. Kuo, V. Sih, O. Cohen, O. Raday, and M. Paniccia, Low-threshold continuous-wave Raman silicon laser. *Nature Photonics,* vol. 1, pp. 232-237, 2007.

[60] Ashok, P.C., G.P. Singh, H.A. Rendall, T.F. Krauss, and K. Dholakia, Waveguide confined Raman spectroscopy for microfluidic interrogation. *Lab on a Chip,* vol. 11, pp. 1262-1270, 2011.

[61] Dochow, S., C. Krafft, U. Neugebauer, T. Bocklitz, T. Henkel, G. Mayer, J. Albert, and J. Popp, Tumour cell identification by means of Raman spectroscopy in combination with optical traps and microfluidic environments. *Lab on a Chip,* vol. 11, pp. 1484-1490, 2011.

[62] Stoddart, P.R. and D.J. White, Optical fibre SERS sensors. *Analytical and Bioanalytical Chemistry,* vol. 394, pp. 1761-1774, 2009.

[63] Hunt, H.C. and J.S. Wilkinson, Kinoform microlenses for focusing into microfluidic channels. *Opt. Express,* vol. 20, pp. 9442-9457, 2012.

[64] Lewis, I.R. and H.G.M. Edwards, *Handbook of Raman Spectroscopy: From the Research Laboratory to the Process Line*. 2001: Taylor & Francis.

[65] Nemanich, R.J., C.C. Tsai, and G.A.N. Connell, Interference-Enhanced Raman Scattering of Very Thin Titanium and Titanium Oxide Films. *Physical Review Letters,* vol. 44, pp. 273-276, 1980.

[66] Dieterle, M. and G. Mestl, Raman spectroscopy of molybdenum oxides Part II. Resonance Raman spectroscopic characterization of the molybdenum oxides Mo4O11 and MoO2. *Physical Chemistry Chemical Physics,* vol. 4, pp. 822-826, 2002.

[67] Baltrus, J.P., L.E. Makovsky, J.M. Stencel, and D.M. Hercules, Quantitative Raman spectrometric determination of molybdenum trioxide and tungsten trioxide in supported catalysts. *Analytical Chemistry,* vol. 57, pp. 2500-2503,

1985.

[68] Wachs, I.E. and C.A. Roberts, Monitoring surface metal oxide catalytic active sites with Raman spectroscopy. *Chemical Society Reviews,* vol. 39, pp. 5002-5017, 2010.

[69] Wang, Y.Y., Z.H. Ni, Z.X. Shen, H.M. Wang, and Y.H. Wu, Interference enhancement of Raman signal of graphene. *Applied Physics Letters,* vol. 92, pp. 043121-3, 2008.

[70] Badizadegan, K., V. Backman, C.W. Boone, C.P. Crum, R.R. Dasari, I. Georgakoudi, K. Keefe, K. Munger, S.M. Shapshay, and E.E. Sheets, Spectroscopic diagnosis and imaging of invisible pre-cancer. *Faraday Discussions,* vol. 126, pp. 265-279, 2003.

[71] Bigio, I.J. and S.G. Bown, Spectrroscopic Sensing of Cancer and Cancer Therapy: Current Status of Translational Research. *Cancer Biology & Therapy,* vol. 3, pp. 259-267, 2004.

[72] Hung, J., S. Lam, J.C. Leriche, and B. Palcic, Autofluorescence of normal and malignant bronchial tissue. *Lasers in Surgery and Medicine,* vol. 11, pp. 99-105, 1991.

[73] Stone, N., C. Kendall, N. Shepherd, P. Crow, and H. Barr, Near-infrared Raman spectroscopy for the classification of epithelial pre-cancers and cancers. *Journal of Raman Spectroscopy,* vol. 33, pp. 564-573, 2002.

[74] Stone, N., C. Kendall, J. Smith, P. Crow, and H. Barr, Raman spectroscopy for identification of epithelial cancers. *Faraday Discussions,* vol. 126, pp. 141-157, 2003.

[75] Nabiev, I., H. Morjani, and M. Manfait, Selective analysis of antitumor drug interaction with living cancer cells as probed by surface-enhanced Raman spectroscopy. *European biophysics journal,* vol. 19, pp. 311-316, 1991.

[76] Sujith, A., T. Itoh, H. Abe, K.I. Yoshida, M.S. Kiran, V. Biju, and M. Ishikawa, Imaging the cell wall of living single yeast cells using surface-enhanced Raman spectroscopy. *Analytical and Bioanalytical Chemistry,* vol. 394, pp. 1803-1809, 2009.

[77] Sujith, A., T. Itoh, H. Abe, A.A. Anas, K. Yoshida, V. Biju, and M. Ishikawa, Surface enhanced Raman scattering analyses of individual silver nanoaggregates on living single yeast cell wall. *Applied Physics Letters,* vol. 92, pp. 103901:1-3, 2008.

[78] Jess, P.R.T., V. Garcés-Chávez, D. Smith, M. Mazilu, L. Paterson, A. Riches, C.S. Herrington, W. Sibbett, and K. Dholakia, Dual beam fibre trap for Raman micro-spectroscopy of single cells. *Opt. Express,* vol. 14, pp. 5779-5791, 2006.

[79] Loeffen, P.W., G. Maskall, S. Bonthron, M. Bloomfield, C. Tombling, and P. Matousek, Spatially offset Raman spectroscopy (SORS) for liquid screening. in *Optical Materials in Defence Systems Technology VIII*, Prague, Czech Republic, 2011, p. 81890C:1:4.

[80] Galvin, M. and D. Zerulla, The Extreme Low-Frequency Raman Spectrum of Liquid Water. *ChemPhysChem,* vol. 12, pp. 913-914, 2011.

[81] Lall, R., T.J. Donohue, S. Marino, and J.C. Mitchell, Optimizing ethanol production selectivity. *Mathematical and Computer Modelling,* vol. 53, pp. 1363-1373, 2011.

[82] Egashira, K. and N. Nishi, Low-frequency Raman spectroscopy of ethanol−water binary solution: evidence for self-association of solute and solvent molecules. *The Journal of Physical Chemistry B,* vol. 102, pp. 4054-

4057, 1998.

[83] Mammone, J.F., S.K. Sharma, and M. Nicol, Raman spectra of methanol and ethanol at pressures up to 100 kbar. *The Journal of Physical Chemistry,* vol. 84, pp. 3130-3134, 1980.

[84] Mark, D., S. Haeberle, G. Roth, F. von Stetten, and R. Zengerle, Microfluidic lab-on-a-chip platforms: requirements, characteristics and applications. *Chemical Society Reviews,* vol. 39, pp. 1153-1182, 2010.

[85] Tsukahara, T., K. Mawatari, and T. Kitamori, Integrated extended-nano chemical systems on a chip. *Chemical Society Reviews,* vol. 39, pp. 1000-1013, 2010.

[86] Jo, B.H., L.M. Van Lerberghe, K.M. Motsegood, and D.J. Beebe, Three-dimensional micro-channel fabrication in polydimethylsiloxane (PDMS) elastomer. *Microelectromechanical Systems, Journal of,* vol. 9, pp. 76-81, 2000.

[87] Marre, S. and K.F. Jensen, Synthesis of micro and nanostructures in microfluidic systems. *Chemical Society Reviews,* vol. 39, pp. 1183-1202, 2010.

[88] Lenshof, A. and T. Laurell, Continuous separation of cells and particles in microfluidic systems. *Chemical Society Reviews,* vol. 39, pp. 1203-1217, 2010.

[89] Anderson, R.C., G.J. Bogdan, Z. Bamiv, T.D. Dawes, J. Winkler, and K. Roy, Microfluidic bischemical analysis system. in *International Conference on Solid State Sensors and Actuators,* Chicago, 1997, pp. 477-480 vol.1.

[90] Xia, Y. and G.M. Whitesides, Soft Lithography. *Annual Review of Materials Science,* vol. 28, pp. 153-184, 1998.

[91] Abgrall, P., V. Conedera, H. Camon, A.M. Gue, and N.T. Nguyen, SU-8 as a structural material for labs-on-chips and microelectromechanical systems. *Electrophoresis,* vol. 28, pp. 4539-4551, 2007.

[92] Kuo, J.S. and D.T. Chiu, Disposable microfluidic substrates: Transitioning from the research laboratory into the clinic. *Lab on a Chip,* vol. 11, pp. 2656-2665, 2011.

[93] Sia, S.K. and G.M. Whitesides, Microfluidic devices fabricated in poly(dimethylsiloxane) for biological studies. *Electrophoresis,* vol. 24, pp. 3563-3576, 2003.

[94] Kim, P., K.W. Kwon, M.C. Park, S.H. Lee, S.M. Kim, and K.Y. Suh, Soft lithography for microfluidics: a review. *Biochip Journal,* vol. 2, pp. 1-11, 2008.

[95] Dittrich, P.S., K. Tachikawa, and A. Manz, Micro total analysis systems. Latest advancements and trends. *Analytical Chemistry,* vol. 78, pp. 3887-3907, 2006.

[96] Ohno, K., K. Tachikawa, and A. Manz, Microfluidics: Applications for analytical purposes in chemistry and biochemistry. *Electrophoresis,* vol. 29, pp. 4443-4453, 2008.

[97] Fiorini, G.S. and D.T. Chiu, Disposable microfluidic devices: fabrication, function, and application. *BioTechniques,* vol. 38, pp. 429-446, 2005.

[98] Keir, R., E. Igata, M. Arundell, W.E. Smith, D. Graham, C. McHugh, and J.M. Cooper, SERRS. In situ substrate formation and improved detection using microfluidics. *Analytical Chemistry,* vol. 74, pp. 1503-1508, 2002.

[99] Rasmussen, A., C. Mavriplis, M. Zaghloul, O. Mikulchenko, and K. Mayaram, Simulation and optimization of a microfluidic flow sensor. *Sensors*

and Actuators A: Physical, vol. 88, pp. 121-132, 2001.

[100] Lien, V. and F. Vollmer, Microfluidic flow rate detection based on integrated optical fiber cantilever. *Lab on a Chip,* vol. 7, pp. 1352-1356, 2007.

[101] Etchart, I., H. Chen, P. Dryden, J. Jundt, C. Harrison, K. Hsu, F. Marty, and B. Mercier, MEMS sensors for density–viscosity sensing in a low-flow microfluidic environment. *Sensors and Actuators A: Physical,* vol. 141, pp. 266-275, 2008.

[102] Yi, P., A.A. Kayani, A.F. Chrimes, K. Ghorbani, S. Nahavandi, K. Kalantar-zadeh, and K. Khoshmanesh, Thermal analysis of nanofluids in microfluidics using an infrared camera. *Lab on a Chip,* vol. 12, pp. 2520-2525, 2012.

[103] Gosse, C., C. Bergaud, and P. Löw, Molecular Probes for Thermometry in Microfluidic Devices. in *Thermal Nanosystems and Nanomaterials*. vol. 118, Volz, S., Ed., ed: Springer Berlin Heidelberg, 2009, pp. 301-341.

[104] Murran, M.A. and H. Najjaran, Capacitance-based droplet position estimator for digital microfluidic devices. *Lab on a Chip,* vol. 12, pp. 2053-2059, 2012.

[105] Collins, J. and A.P. Lee, Microfluidic flow transducer based on the measurement of electrical admittance. *Lab on a Chip,* vol. 4, pp. 7-10, 2003.

[106] Seo, S., T. Stintzing, I. Block, D. Pavlidis, M. Rieke, and P.G. Layer, High frequency wideband permittivity measurements of biological substances using coplanar waveguides and application to cell suspensions. in *Microwave Symposium Digest, 2008 IEEE MTT-S International*, 2008, pp. 915-918.

[107] Kayani, A.A., A.F. Chrimes, K. Khoshmanesh, K. Kalantar-zadeh, and A. Mitchell, Tuneable Optical Waveguide Based on Dielectrophoresis and Microfluidics. Presented at the Micro- and Nanotechnology Sensors, Systems, and Applications Iii - SPIE, 2011.

[108] Kayani, A.A., K. Khoshmanesh, S.A. Ward, A. Mitchell, and K. Kalantar-zadeh, Optofluidics incorporating actively controlled micro- and nano-particles. *Biomicrofluidics,* vol. 6, pp. 031501-32, 2012.

[109] Lee, A.P., M.V. Patel, A.R. Tovar, and Y. Okabe, Microfluidic Air-Liquid Cavity Acoustic Transducers for On-Chip Integration of Sample Preparation and Sample Detection. *Jala,* vol. 15, pp. 449-454, 2010.

[110] Lee, A. and M. Patel, Microfluidic air-liquid cavity acoustic transducers for point-of-care diagnostics applications. *The Journal of the Acoustical Society of America,* vol. 132, pp. 1953-1953, 2012.

[111] Patel, M.V., A.R. Tovar, and A.P. Lee, Lateral cavity acoustic transducer as an on-chip cell/particle microfluidic switch. *Lab on a Chip,* vol. 12, pp. 139-145, 2012.

[112] Miller, M.M., P.E. Sheehan, R.L. Edelstein, C.R. Tamanaha, L. Zhong, S. Bounnak, L.J. Whitman, and R.J. Colton, A DNA array sensor utilizing magnetic microbeads and magnetoelectronic detection. *Journal of Magnetism and Magnetic Materials,* vol. 225, pp. 138-144, 2001.

[113] Ashok, P.C., G.P. Singh, K.M. Tan, and K. Dholakia, Fiber probe based microfluidic raman spectroscopy. *Optics Express,* vol. 18, pp. 7642-7649, 2010.

[114] Kostovski, G., D.J. White, A. Mitchell, M.W. Austin, and P.R. Stoddart, Nanoimprinted optical fibres: Biotemplated nanostructures for SERS sensing. *Biosensors and Bioelectronics,* vol. 24, pp. 1531-1535, 2009.

[115] Yasui, T., Y. Omoto, K. Osato, N. Kaji, N. Suzuki, T. Naito, Y. Okamoto, M. Tokeshi, E. Shamoto, and Y. Baba, Confocal Microscopic Evaluation of Mixing Performance for Three-Dimensional Microfluidic Mixer. *Analytical*

Sciences, vol. 28, pp. 57-57, 2012.

[116] Mitsuhisa, I., S. Keita, K. Shinya, K. Yasuhiro, S. Yohei, and H. Koichi, Evaluation methodology of gas permeable characterization in a polymer-based microfluidic device by confocal fluorescence imaging. *Journal of Micromechanics and Microengineering,* vol. 22, p. 065023, 2012.

[117] Liu, N., C. Aymonier, C. Lecoutre, Y. Garrabos, and S. Marre, Microfluidic approach for studying CO2 solubility in water and brine using confocal Raman spectroscopy. *Chemical Physics Letters,* vol. 551, pp. 139-143, 2012.

[118] Kuswandi, B., Nuriman, J. Huskens, and W. Verboom, Optical sensing systems for microfluidic devices: A review. *Analytica Chimica Acta,* vol. 601, pp. 141-155, 2007.

[119] Berger, A.J., Y. Wang, and M.S. Feld, Rapid, noninvasive concentration measurements of aqueous biological analytes by near-infrared Raman spectroscopy. *Applied Optics,* vol. 35, pp. 209-212, 1996.

[120] Laser, D.J. and J.G. Santiago, A review of micropumps. *Journal of Micromechanics and Microengineering,* vol. 14, p. R35, 2004.

[121] Squires, T.M. and S.R. Quake, Microfluidics: Fluid physics at the nanoliter scale. *Reviews of modern physics,* vol. 77, p. 977, 2005.

[122] van Dinther, A., C. Schroën, F. Vergeldt, R. van der Sman, and R. Boom, Suspension flow in microfluidic devices—A review of experimental techniques focussing on concentration and velocity gradients. *Advances in Colloid and Interface Science,* vol. 173, pp. 23-34, 2012.

[123] Lee, C.Y., C.L. Chang, Y.N. Wang, and L.M. Fu, Microfluidic mixing: a review. *International Journal of Molecular Sciences,* vol. 12, pp. 3263-3287, 2011.

[124] Schulte, T.H., R.L. Bardell, and B.H. Weigl, Microfluidic technologies in clinical diagnostics. *Clinica Chimica Acta,* vol. 321, pp. 1-10, 2002.

[125] Kamholz, A.E. and P. Yager, Theoretical Analysis of Molecular Diffusion in Pressure-Driven Laminar Flow in Microfluidic Channels. *Biophysical Journal,* vol. 80, pp. 155-160, 2001.

[126] Ismagilov, R.F., D. Rosmarin, P.J.A. Kenis, D.T. Chiu, W. Zhang, H.A. Stone, and G.M. Whitesides, Pressure-Driven Laminar Flow in Tangential Microchannels: an Elastomeric Microfluidic Switch. *Analytical Chemistry,* vol. 73, pp. 4682-4687, 2001.

[127] Nie, Z., S. Xu, M. Seo, P.C. Lewis, and E. Kumacheva, Polymer Particles with Various Shapes and Morphologies Produced in Continuous Microfluidic Reactors. *Journal of the American Chemical Society,* vol. 127, pp. 8058-8063, 2005.

[128] Wagner, J. and J.M. Köhler, Continuous Synthesis of Gold Nanoparticles in a Microreactor. *Nano Letters,* vol. 5, pp. 685-691, 2005.

[129] Quang, L.X., C. Lim, G.H. Seong, J. Choo, K.J. Do, and S.K. Yoo, A portable surface-enhanced Raman scattering sensor integrated with a lab-on-a-chip for field analysis. *Lab on a Chip,* vol. 8, pp. 2214-2219, 2008.

[130] Park, T., S. Lee, G.H. Seong, J. Choo, E.K. Lee, Y.S. Kim, W.H. Ji, S.Y. Hwang, and D.G. Gweon, Highly sensitive signal detection of duplex dye-labelled DNA oligonucleotides in a PDMS microfluidic chip: confocal surface-enhanced Raman spectroscopic study. *Lab on a Chip,* vol. 5, pp. 437-442, 2005.

[131] Moffitt, J.R., Y.R. Chemla, S.B. Smith, and C. Bustamante, Recent Advances in Optical Tweezers. *Annual Review of Biochemistry,* vol. 77, pp. 205-228,

2008.

[132] Helleso, O.G., P. Lovhaugen, A.Z. Subramanian, J.S. Wilkinson, and B.S. Ahluwalia, Surface transport and stable trapping of particles and cells by an optical waveguide loop. *Lab on a Chip,* vol. 12, pp. 3436-3440, 2012.

[133] Liang, H., K.T. Vu, P. Krishnan, T.C. Trang, D. Shin, S. Kimel, and M.W. Berns, Wavelength dependence of cell cloning efficiency after optical trapping. *Biophysical Journal,* vol. 70, pp. 1529-1533, 1996.

[134] Singh, G.P., G. Volpe, C.M. Creely, H. Grotsch, I.M. Geli, and D. Petrov, The lag phase and G_1 phase of a single yeast cell monitored by Raman microspectroscopy. *Journal of Raman Spectroscopy,* vol. 37, pp. 858-864, 2006.

[135] Thalhammer, G., R. Steiger, S. Bernet, and M. Ritsch-Marte, Optical macro-tweezers: trapping of highly motile micro-organisms. *Journal of Optics,* vol. 13, p. 044024, 2011.

[136] Tong, L.M., V.D. Miljkovic, and M. Kall, Optical Manipulation of Plasmonic Nanoparticles Using Laser Tweezers. in *Optical Trapping and Optical Micromanipulation Vii*. vol. 7762, Dholakia, K. and G. C. Spalding, Eds., ed Bellingham: Spie-Int Soc Optical Engineering, 2010.

[137] Xie, C.G., M.A. Dinno, and Y.Q. Li, Near-infrared Raman Spectroscopy of Single Optically Trapped Biological Cells. *Optics Letters,* vol. 27, pp. 249-251, 2002.

[138] Xie, C.G. and Y.Q. Li, Raman spectra and optical trapping of highly refractive and nontransparent particles. *Applied Physics Letters,* vol. 81, pp. 951-953, 2002.

[139] Xie, C.G. and Y.Q. Li, Confocal micro-Raman spectroscopy of single biological cells using optical trapping and shifted excitation difference techniques. *Journal of Applied Physics,* vol. 93, pp. 2982-2986, 2003.

[140] Tong, L., K. Ramser, and M. Käll, Optical Tweezers for Raman Spectroscopy. in *Raman Spectroscopy for Nanomaterials Characterization*, Kumar, C. S. R., Ed., ed: Springer Berlin Heidelberg, 2012, pp. 507-530.

[141] Tan, W.-H. and S. Takeuchi, A trap-and-release integrated microfluidic system for dynamic microarray applications. *Proceedings of the National Academy of Sciences,* vol. 104, pp. 1146-1151, 2007.

[142] Lee, P.J., N.C. Helman, W.A. Lim, and P.J. Hung, A microfluidic system for dynamic yeast cell imaging. *BioTechniques,* vol. 44, pp. 91-95, 2008.

[143] Khoshmanesh, K., S. Nahavandi, S. Baratchi, A. Mitchell, and K. Kalantar-zadeh, Dielectrophoretic platforms for bio-microfluidic systems. *Biosensors & Bioelectronics,* vol. 26, pp. 1800-1814, 2011.

[144] Zhang, C., K. Khoshmanesh, A. Mitchell, and K. Kalantar-zadeh, Dielectrophoresis for manipulation of micro/nano particles in microfluidic systems. *Analytical and Bioanalytical Chemistry,* vol. 396, pp. 401-420, 2010.

[145] Sandlin, Z.D., M. Shou, J.G. Shackman, and R.T. Kennedy, Microfluidic Electrophoresis Chip Coupled to Microdialysis for in Vivo Monitoring of Amino Acid Neurotransmitters. *Analytical Chemistry,* vol. 77, pp. 7702-7708, 2005.

[146] Fox, M.B., D.C. Esveld, A. Valero, R. Luttge, H.C. Mastwijk, P.V. Bartels, A. Berg, and R.M. Boom, Electroporation of cells in microfluidic devices: a review. *Analytical and Bioanalytical Chemistry,* vol. 385, pp. 474-485, 2006.

[147] Jesús-Pérez, N.M. and B.H. Lapizco-Encinas, Dielectrophoretic monitoring

of microorganisms in environmental applications. *Electrophoresis,* vol. 32, pp. 2331-2357, 2011.

[148] Lapizco-Encinas, B.H., R.V. Davalos, B.A. Simmons, E.B. Cummings, and Y. Fintschenko, An insulator-based (electrodeless) dielectrophoretic concentrator for microbes in water. *Journal of Microbiological Methods,* vol. 62, pp. 317-326, 2005.

[149] Zhang, C., K. Khoshmanesh, F.J. Tovar-Lopez, A. Mitchell, W. Wlodarski, and K. Kalantar-zadeh, Dielectrophoretic separation of carbon nanotubes and polystyrene microparticles. *Microfluidics and Nanofluidics,* vol. 7, pp. 633-645, 2009.

[150] Khoshmanesh, K., S. Baratchi, F. Tovar-Lopez, S. Nahavandi, D. Wlodkowic, A. Mitchell, and K. Kalantar-zadeh, On-chip separation of *Lactobacillus* bacteria from yeasts using dielectrophoresis. *Microfluidics and Nanofluidics,* vol. 12, pp. 597-606, 2012.

[151] Asbury, C.L., A.H. Diercks, and G. van den Engh, Trapping of DNA by dielectrophoresis. *Electrophoresis,* vol. 23, pp. 2658-2666, 2002.

[152] Kano, T., T. Inaba, G. Ye, and N. Miki, A microfluidic device for bacteria immobilization in a microporous carrier by dielectrophoresis. *Journal of Micro-Nano Mechatronics,* vol. 7, pp. 61-68, 2012.

[153] Miccio, L., P. Memmolo, S. Grilli, and P. Ferraro, All-optical microfluidic chips for reconfigurable dielectrophoretic trapping through SLM light induced patterning. *Lab on a Chip,* vol. 12, pp. 4449-4454, 2012.

[154] Salmanzadeh, A., H. Kittur, M.B. Sano, P.C. Roberts, E.M. Schmelz, and R.V. Davalos, Dielectrophoretic differentiation of mouse ovarian surface epithelial cells, macrophages, and fibroblasts using contactless dielectrophoresis. *Biomicrofluidics,* vol. 6, pp. 024104:4-13, 2012.

[155] Connatser, R.M., M. Cochran, R.J. Harrison, and M.J. Sepaniak, Analytical optimization of nanocomposite surface-enhanced Raman spectroscopy/scattering detection in microfluidic separation devices. *Electrophoresis,* vol. 29, pp. 1441-1450, 2008.

[156] Nilsson, J., M. Evander, B. Hammarstrom, and T. Laurell, Review of cell and particle trapping in microfluidic systems. *Analytica Chimica Acta,* vol. 649, pp. 141-157, 2009.

[157] Jeong, J.S., J.W. Lee, C.Y. Lee, S.Y. Teh, A. Lee, and K.K. Shung, Particle manipulation in a microfluidic channel using acoustic trap. *Biomedical Microdevices,* vol. 13, pp. 779-788, 2011.

[158] Basore, J.R. and L.A. Baker, Applications of microelectromagnetic traps. *Analytical and Bioanalytical Chemistry,* vol. 403, pp. 2077-2088, 2012.

[159] Weinert, F.M., C.B. Mast, and D. Braun, Optical fluid and biomolecule transport with thermal fields. *Physical Chemistry Chemical Physics,* vol. 13, pp. 9918-9928, 2011.

[160] Bhagat, A., H. Bow, H. Hou, S. Tan, J. Han, and C. Lim, Microfluidics for cell separation. *Medical & Biological Engineering & Computing,* vol. 48, pp. 999-1014, 2010.

[161] Lutz, B.R., J. Chen, and D.T. Schwartz, Microfluidics without microfabrication. *Proceedings of the National Academy of Sciences,* vol. 100, pp. 4395-4398, 2003.

[162] Fletcher, P.D.I., S.J. Haswell, and X. Zhang, Monitoring of chemical reactions within microreactors using an inverted Raman microscopic spectrometer. *Electrophoresis,* vol. 24, pp. 3239-3245, 2003.

[163] Widjaja, E., S.Y. Teh, and M. Garland, Characterizing Diffusion and Transport in Microfluidics Channels: A Combined Raman Microscopy and Band-Target Entropy Minimization Study. *Applied Spectroscopy,* vol. 66, pp. 1226-1232, 2012.

[164] Fiedler, S., S.G. Shirley, T. Schnelle, and G. Fuhr, Dielectrophoretic Sorting of Particles and Cells in a Microsystem. *Analytical Chemistry,* vol. 70, pp. 1909-1915, 1998.

[165] Campagnolo, L., M. Nikolić, J. Perchoux, Y. Lim, K. Bertling, K. Loubière, L. Prat, A. Rakić, and T. Bosch, Flow profile measurement in microchannel using the optical feedback interferometry sensing technique. *Microfluidics and Nanofluidics,* vol. 14, pp. 113-119, 2013.

[166] Leung, S.-A., R.F. Winkle, R.C.R. Wootton, and A.J. deMello, A method for rapid reaction optimisation in continuous-flow microfluidic reactors using online Raman spectroscopic detection. *Analyst,* vol. 130, pp. 46-51, 2005.

[167] Yea, K.-h., S. Lee, J.B. Kyong, J. Choo, E.K. Lee, S.-W. Joo, and S. Lee, Ultra-sensitive trace analysis of cyanide water pollutant in a PDMS microfluidic channel using surface-enhanced Raman spectroscopy. *Analyst,* vol. 130, pp. 1009-1011, 2005.

[168] Bantz, K.C., A.F. Meyer, N.J. Wittenberg, H. Im, O. Kurtulus, S.H. Lee, N.C. Lindquist, S.H. Oh, and C.L. Haynes, Recent progress in SERS biosensing. *Physical Chemistry Chemical Physics,* vol. 13, pp. 11551-11567, 2011.

[169] Piorek, B.D., S.J. Lee, J.G. Santiago, M. Moskovits, S. Banerjee, and C.D. Meinhart, Free-surface microfluidic control of surface-enhanced Raman spectroscopy for the optimized detection of airborne molecules. Presented at the Proceedings of the National Academy of Sciences of the United States of America, 2007.

[170] Hao, E. and G.C. Schatz, Electromagnetic fields around silver nanoparticles and dimers. *Journal of Chemical Physics,* vol. 120, pp. 357-366, 2004.

[171] Zwemer, D.A., C.V. Shank, and J.E. Rowe, Surface-enhanced raman scattering as a function of molecule-surface separation. *Chemical Physics Letters,* vol. 73, pp. 201-204, 1980.

[172] Otto, A. and M. Futamata, Electronic Mechanisms of SERS. in *Surface-Enhanced Raman Scattering*. vol. 103, Kneipp, K., M. Moskovits, and H. Kneipp, Eds., ed: Springer Berlin Heidelberg, 2006, pp. 147-182.

[173] Connatser, R.M., L.A. Riddle, and M.J. Sepaniak, Metal-polymer nanocomposites for integrated microfluidic separations and surface enhanced Raman spectroscopic detection. *Journal of Separation Science,* vol. 27, pp. 1545-1550, 2004.

[174] Ramadan, Q. and M.M. Gijs, Microfluidic applications of functionalized magnetic particles for environmental analysis: focus on waterborne pathogen detection. *Microfluidics and Nanofluidics,* vol. 13, pp. 529-542, 2012.

[175] Nitahara, S., M. Maeki, H. Yamaguchi, K. Yamashita, M. Miyazaki, and H. Maeda, Three-dimensional Raman spectroscopic imaging of protein crystals deposited on a nanodroplet. *Analyst,* vol. 137, pp. 5730-5735, 2012.

[176] Chan, J.W., H. Winhold, S.M. Lane, and T. Huser, Optical trapping and coherent anti-Stokes Raman scattering (CARS) spectroscopy of submicron-size particles. *Selected Topics in Quantum Electronics, IEEE Journal of,* vol. 11, pp. 858-863, 2005.

[177] Soler, M.G. and F. Qu, Raman Spectroscopy of Iron Oxide Nanoparticles. in *Raman Spectroscopy for Nanomaterials Characterization,* Kumar, C. S. R.,

Ed., ed: Springer Berlin Heidelberg, 2012, pp. 379-416.

[178] Wells, S.M., S.D. Retterer, J.M. Oran, and M.J. Sepaniak, Controllable Nanofabrication of Aggregate-like Nanoparticle Substrates and Evaluation for Surface-Enhanced Raman Spectroscopy. *ACS Nano,* vol. 3, pp. 3845-3853, 2009.

[179] Driskell, J.D., R.J. Lipert, and M.D. Porter, Labeled Gold Nanoparticles Immobilized at Smooth Metallic Substrates: Systematic Investigation of Surface Plasmon Resonance and Surface-Enhanced Raman Scattering. *The Journal of Physical Chemistry B,* vol. 110, pp. 17444-17451, 2006.

[180] Dongjin, L., Y. Zhijiang, S.A. Campbell, and C. Tianhong, Suspended carbon nanotube thin film structures with high degree of alignment for NEMS switch applications. in *Solid-State Sensors, Actuators and Microsystems Conference, Transducers 2011 16th International*, Beijing, China, 2011, pp. 625-628.

[181] Ashok, P.C. and K. Dholakia, Microfluidic Raman Spectroscopy for Bio-chemical Sensing and Analysis. *Optical Nano-and Microsystems for Bioanalytics,* pp. 247-268, 2012.

[182] Çulha, M. and S. Keskin, Surface-enhanced Raman scattering for label-free protein detection and identification. in *Plasmonics in Biology and Medicine IX*, San Francisco, California, 2012, p. 823407.

[183] Jun, B.-H., M.S. Noh, G. Kim, H. Kang, J.-H. Kim, W.-J. Chung, M.-S. Kim, Y.-K. Kim, M.-H. Cho, D.H. Jeong, and Y.-S. Lee, Protein separation and identification using magnetic beads encoded with surface-enhanced Raman spectroscopy. *Analytical Biochemistry,* vol. 391, pp. 24-30, 2009.

[184] Khandurina, J. and A. Guttman, Bioanalysis in microfluidic devices. *Journal of Chromatography A,* vol. 943, pp. 159-183, 2002.

[185] Mao, H., P. Lv, and W. Wu, Microfluidic surface-enhanced raman scattering sensors for online monitoring trace chemical mixing and reaction. in *Solid-State Sensors, Actuators and Microsystems Conference, Transducers 2011 16th International*, Beijing, China, 2011, pp. 1970-1973.

[186] Yang, X., C. Gu, F. Qian, Y. Li, and J.Z. Zhang, Highly Sensitive Detection of Proteins and Bacteria in Aqueous Solution Using Surface-Enhanced Raman Scattering and Optical Fibers. *Analytical Chemistry,* vol. 83, pp. 5888-5894, 2011.

[187] Zhou, J., K. Ren, Y. Zhao, W. Dai, and H. Wu, Convenient formation of nanoparticle aggregates on microfluidic chips for highly sensitive SERS detection of biomolecules. *Analytical and Bioanalytical Chemistry,* vol. 402, pp. 1601-1609, 2012.

[188] Gulati, S., V. Rouilly, X. Niu, J. Chappell, R.I. Kitney, J.B. Edel, and P.S. Freemont, Opportunities for microfluidic technologies in synthetic biology. *Journal of The Royal Society Interface,* vol. 6, pp. S493-S506, 2009.

[189] Trevors, J. and L. Masson, DNA technologies: what's next applied to microbiology research? *Antonie van Leeuwenhoek,* vol. 98, pp. 249-262, 2010.

[190] Lim, D.K., A. Kumar, and J.M. Nam, Engineered Nanostructures for the Ultrasensitive DNA Detection. in *Detection of Non-Amplified Genomic DNA, Soft and Biological Matter,* ed: Springer Science+Business Media Dordrecht, 2012, pp. 67-87.

[191] Bissonnette, L. and M.G. Bergeron, Next revolution in the molecular theranostics of infectious diseases: microfabricated systems for personalized medicine. *Expert review of molecular diagnostics,* vol. 6, pp. 433-450, 2006.

[192] Zhang, H., M.H. Harpster, W.C. Wilson, and P.A. Johnson, Surface-Enhanced Raman Scattering Detection of DNAs Derived from Virus Genomes Using Au-Coated Paramagnetic Nanoparticles. *Langmuir,* vol. 28, pp. 4030-4037, 2012.

[193] Strelau, K.K., R. Kretschmer, R. Möller, W. Fritzsche, and J. Popp, SERS as tool for the analysis of DNA-chips in a microfluidic platform. *Analytical and Bioanalytical Chemistry,* vol. 396, pp. 1381-1384, 2010.

[194] Myers, F.B. and L.P. Lee, Innovations in optical microfluidic technologies for point-of-care diagnostics. *Lab on a Chip,* vol. 8, pp. 2015-2031, 2008.

[195] Strelau, K., R. Kretschmer, R. Möller, W. Fritzsche, and J. Popp, SERS as tool for the analysis of DNA-chips in a microfluidic platform. *Analytical and Bioanalytical Chemistry,* vol. 396, pp. 1381-1384, 2010.

[196] Strelau, K.K., K. Weber, R. Möller, W. Fritzsche, and J. Popp, A microfluidic platform for chip-based DNA detection using SERS and silver colloids. in *Biophotonics: Photonic Solutions for Better Health Care II*, Brussels, Belgium, 2010, pp. 771514-771514.

[197] Quake, S.R., Versatile, fully automated, microfluidic cell culture system. *Analytical Chemistry,* vol. 79, pp. 8557-8563, 2007.

[198] Paguirigan, A.L. and D.J. Beebe, Microfluidics meet cell biology: bridging the gap by validation and application of microscale techniques for cell biological assays. *BioEssays,* vol. 30, pp. 811-821, 2008.

[199] Valero, A., F. Merino, F. Wolbers, R. Luttge, I. Vermes, H. Andersson, and A. van den Berg, Apoptotic cell death dynamics of HL60 cells studied using a microfluidic cell trap device. *Lab on a Chip,* vol. 5, pp. 49-55, 2004.

[200] Koch, S., M. Dreiling, M. Gutekunst, C. Bolwien, H. Thielecke, and H. Mertsching, Discrimination of microorganisms and cells in tissue engineering by Raman spectroscopy. in *European Conference on Biomedical Optics*, 2009.

[201] Ong, Y.H., M. Lim, and Q. Liu, Comparison of principal component analysis and biochemical component analysis in Raman spectroscopy for the discrimination of apoptosis and necrosis in K562 leukemia cells. *Opt. Express,* vol. 20, pp. 22158-22171, 2012.

[202] Knauer, M., N. Ivleva, R. Niessner, and C. Haisch, A flow-through microarray cell for the online SERS detection of antibody-captured E. coli bacteria. *Analytical and Bioanalytical Chemistry,* vol. 402, pp. 2663-2667, 2012.

[203] Huang, S.-s., D. Chen, P.L. Pelczar, V.R. Vepachedu, P. Setlow, and Y.-q. Li, Levels of Ca2+-Dipicolinic Acid in Individual Bacillus Spores Determined Using Microfluidic Raman Tweezers. *Journal of Bacteriology,* vol. 189, pp. 4681-4687, 2007.

[204] Lau, A.Y., L.P. Lee, and J.W. Chan, An integrated optofluidic platform for Raman-activated cell sorting. *Lab on a Chip,* vol. 8, pp. 1116-1120, 2008.

[205] Eriksson, E., J. Scrimgeour, A. Granéli, K. Ramser, R. Wellander, J. Enger, D. Hanstorp, and M. Goksör, Optical manipulation and microfluidics for studies of single cell dynamics. *Journal of Optics A: Pure and Applied Optics,* vol. 9, p. S113, 2007.

[206] Zhang, X., H. Yin, J. Cooper, and S. Haswell, Characterization of cellular chemical dynamics using combined microfluidic and Raman techniques. *Analytical and Bioanalytical Chemistry,* vol. 390, pp. 833-840, 2008.

[207] Huh, D., D.C. Leslie, B.D. Matthews, J.P. Fraser, S. Jurek, G.A. Hamilton,

K.S. Thorneloe, M.A. McAlexander, and D.E. Ingber, A Human Disease Model of Drug Toxicity–Induced Pulmonary Edema in a Lung-on-a-Chip Microdevice. *Science Translational Medicine,* vol. 4, p. 159ra147, 2012.

[208] Ghaemmaghami, A.M., M.J. Hancock, H. Harrington, H. Kaji, and A. Khademhosseini, Biomimetic tissues on a chip for drug discovery. *Drug discovery today,* vol. 17, pp. 173-181, 2011.

[209] Andersson, H. and A. Van Den Berg, Microfabrication and microfluidics for tissue engineering: state of the art and future opportunities. *Lab on a Chip,* vol. 4, pp. 98-103, 2004.

[210] Ingber, D.E. and G.M. Whitesides, Lab on a chip: United States of America. *Lab on a Chip,* vol. 12, pp. 2089-2090, 2012.

[211] Huh, D., B.D. Matthews, A. Mammoto, M. Montoya-Zavala, H.Y. Hsin, and D.E. Ingber, Reconstituting organ-level lung functions on a chip. *Science,* vol. 328, pp. 1662-1668, 2010.

[212] Matousek, P., E.R.C. Draper, A.E. Goodship, I.P. Clark, K.L. Ronayne, and A.W. Parker, Noninvasive Raman Spectroscopy of Human Tissue *In Vivo*. *Applied Spectroscopy,* vol. 60, pp. 758-763, 2006.

[213] Keller, M.D., S.K. Majumder, and A. Mahadevan-Jansen, Spatially offset Raman spectroscopy of layered soft tissues. *Optics Letters,* vol. 34, pp. 926-928, 2009.

[214] Xie, H., R. Stevenson, N. Stone, A. Hernandez-Santana, K. Faulds, and D. Graham, Tracking Bisphosphonates through a 20 mm Thick Porcine Tissue by Using Surface-Enhanced Spatially Offset Raman Spectroscopy. *Angewandte Chemie,* vol. 124, pp. 8637-8639, 2012.

[215] Stone, N. and P. Matousek, Advanced transmission Raman spectroscopy: a promising tool for breast disease diagnosis. *Cancer Research,* vol. 68, pp. 4424-4430, 2008.

[216] Caspers, P.J., G.W. Lucassen, and G.J. Puppels, Combined In Vivo Confocal Raman Spectroscopy and Confocal Microscopy of Human Skin. *Biophysical Journal,* vol. 85, pp. 572-580, 2003.

[217] Matousek, P. and N. Stone, Recent advances in the development of Raman spectroscopy for deep non-invasive medical diagnosis. *Journal of Biophotonics,* vol. 6, pp. 7-19, 2013.

[218] Uzunbajakava, N., A. Lenferink, Y. Kraan, B. Willekens, G. Vrensen, J. Greve, and C. Otto, Nonresonant Raman imaging of protein distribution in single human cells. *Biopolymers,* vol. 72, pp. 1-9, 2002.

[219] Onogi, C. and H. Hamaguchi, Photobleaching of the “Raman Spectroscopic Signature of Life” and Mitochondrial Activity in Rho− Budding Yeast Cells. *The Journal of Physical Chemistry B,* vol. 113, pp. 10942-10945, 2009.

[220] Chiu, L.-d., F. Hullin-Matsuda, T. Kobayashi, H. Torii, and H.-o. Hamaguchi, On the origin of the 1602 cm–1 Raman band of yeasts; contribution of ergosterol. *Journal of Biophotonics,* vol. 5, pp. 724-728, 2012.

[221] Davidson, B., N. Spears, A. Murray, and A. Elfick, The changing biochemical composition and organisation of the murine oocyte and early embryo as revealed by Raman spectroscopic mapping. *Journal of Raman Spectroscopy,* vol. 43, pp. 24-31, 2012.

[222] Shen, A.G., J. Peng, Q.H. Zhao, L. Su, X.H. Wang, J.M. Hu, and Q. Yang, Accurate and noninvasive embryos screening during in vitro fertilization (IVF) assisted by Raman analysis ofembryos culture medium. *Laser Physics Letters,* vol. 9, pp. 322-328, 2012.

[223] Suh, R.S., X. Zhu, N. Phadke, D.A. Ohl, S. Takayama, and G.D. Smith, IVF within microfluidic channels requires lower total numbers and lower concentrations of sperm. *Human Reproduction,* vol. 21, pp. 477-483, 2006.

[224] Smith, G., J. Swain, and C. Bormann, Microfluidics for gametes, embryos, and embryonic stem cells. in *Seminars in reproductive medicine*, 2011, p. 5.

[225] Glasgow, I.K., H.C. Zeringue, D.J. Beebe, S.J. Choi, J.T. Lyman, N.G. Chan, and M.B. Wheeler, Handling individual mammalian embryos using microfluidics. *Biomedical Engineering, IEEE Transactions on,* vol. 48, pp. 570-578, 2001.

[226] Cabrera, L.M., G.D. Smith, and S. Takayama, Real time culture and analysis of embryo metabolism using a microfluidic device with deformation based actuation. *Lab on a Chip,* vol. 12, pp. 2240-6, 2012.

[227] Widjaja, E. and M. Garland, Detailed spectroscopic analysis of complex multi-component materials using a combination of Raman mapping with BTEM. *Journal of Raman Spectroscopy,* vol. 43, pp. 828-833, 2012.

[228] Yue, J., J.C. Schouten, and T.A. Nijhuis, Integration of Microreactors with Spectroscopic Detection for Online Reaction Monitoring and Catalyst Characterization. *Industrial & Engineering Chemistry Research,* vol. 51, pp. 14583-14609, 2012.

[229] Vankeirsbilck, T., A. Vercauteren, W. Baeyens, G. Van der Weken, F. Verpoort, G. Vergote, and J.P. Remon, Applications of Raman spectroscopy in pharmaceutical analysis. *TrAC Trends in Analytical Chemistry,* vol. 21, pp. 869-877, 2002.

[230] Wartewig, S. and R.H.H. Neubert, Pharmaceutical applications of Mid-IR and Raman spectroscopy. *Advanced Drug Delivery Reviews,* vol. 57, pp. 1144-1170, 2005.

[231] Kopp, M.U., A.J. De Mello, and A. Manz, Chemical amplification: continuous-flow PCR on a chip. *Science,* vol. 280, pp. 1046-1048, 1998.

[232] Ruiz-Martinez, M.C., J. Berka, A. Belenkii, F. Foret, A.W. Miller, and B.L. Karger, DNA sequencing by capillary electrophoresis with replaceable linear polyacrylamide and laser-induced fluorescence detection. *Analytical Chemistry,* vol. 65, pp. 2851-2858, 1993.

[233] Xiang, D., C. Zhang, L. Chen, X. Ji, and Z. He, Tricolour fluorescence detection of sequence-specific DNA with a new molecular beacon and a nucleic acid dye TOTO-3. *Analyst,* vol. 137, pp. 5898-5905, 2012.

[234] Sikirzhytski, V., A. Sikirzhytskaya, and I.K. Lednev, Advanced statistical analysis of Raman spectroscopic data for the identification of body fluid traces: Semen and blood mixtures. *Forensic Science International,* vol. 222, pp. 259-65, 2012.

[235] Premasiri, W.R., J. Lee, and L.D. Ziegler, Surface Enhanced Raman Scattering of Whole Human Blood, Blood Plasma and Red Blood Cells: Cellular Processes and Bioanalytical Sensing. *The Journal of Physical Chemistry B,* vol. 116, pp. 9376-86, 2012.

[236] Sikirzhytskaya, A., V. Sikirzhytski, and I.K. Lednev, Raman spectroscopic signature of vaginal fluid and its potential application in forensic body fluid identification. *Forensic Science International,* vol. 216, pp. 44-48, 2012.

[237] Miller, M.A., M.R. Cavaliere, M. Zhou, and P. Few, Confocal Raman Microscopy in Forensic Pharmaceutical Investigations. *Spectroscopy,* vol. 2, pp. 1-3, 2012.

[238] Faulds, K. and W.E. Smith, Detection of Drugs of Abuse Using Surface

Enhanced Raman Scattering. in *Infrared and Raman Spectroscopy in Forensic Science*. vol. 6c, Chalmers, J. M., H. G. M. Edwards, and M. D. Hargreaves, Eds., ed Chichester, UK. : John Wiley & Sons, Ltd, 2012, pp. 357-366.

[239] Jarvis, R.M. and R. Goodacre, Discrimination of bacteria using surface-enhanced Raman spectroscopy. *Analytical Chemistry,* vol. 76, pp. 40-47, 2004.

[240] Shanmukh, S., L. Jones, Y.P. Zhao, J.D. Driskell, R.A. Tripp, and R.A. Dluhy, Identification and classification of respiratory syncytial virus (RSV) strains by surface-enhanced Raman spectroscopy and multivariate statistical techniques. *Analytical and Bioanalytical Chemistry,* vol. 390, pp. 1551-1555, 2008.

[241] Gaus, K., P. Rösch, R. Petry, K.D. Peschke, O. Ronneberger, H. Burkhardt, K. Baumann, and J. Popp, Classification of lactic acid bacteria with UV-resonance Raman spectroscopy. *Biopolymers*, vol. 82, pp. 286-290, 2006.

[242] Lu, X., H. Al-Qadiri, M. Lin, and B. Rasco, Application of Mid-infrared and Raman Spectroscopy to the Study of Bacteria. *Food and Bioprocess Technology*, vol. 4, pp. 919-935, 2011.

[243] Sacré, P.Y., E. Deconinck, and J. De Beer, Analytical strategies for the detection of counterfeit erectile dysfunction drugs. in *Counterfeit Medicines Volume II: Detection, Identification and Analysis*, Wang, P. and A. Wertheimer, Eds., ed St Albans, UK: ILM Publications, 2012.

[244] Polakovs, M., N. Mironova-Ulmane, A. Pavlenko, E. Reinholds, M. Gavare, and M. Grube, EPR and FTIR Spectroscopies Study of Human Blood after Irradiation. *Spectroscopy: An International Journal,* vol. 27, pp. 367-371, 2012.

[245] Xiaoyun, C., L. Weizi, Y. Chunmei, L. Wang, and B. Minghai, Simultaneous quantitative detection of tetracyclines derivatives by raman spectroscopy. in *Virtual Environments Human-Computer Interfaces and Measurement Systems (VECIMS), 2012 IEEE International Conference,* 2012, pp. 111-114.

[246] Szostak, R. and S. Mazurek, Quantification of active ingredients in suppositories by FT-Raman spectroscopy. *Drug Testing and Analysis,* vol. 5, pp. 126-129, 2013.

[247] Basar, G., U. Parlatan, S. Seninak, T. Gunel, A. Benian, and I. Kalelioglu, Investigation of Preeclampsia Using Raman Spectroscopy. *Spectroscopy: An International Journal,* vol. 27, pp. 239-252, 2012.

[248] Dégardin, K., Y. Roggo, F. Been, and P. Margot, Detection and chemical profiling of medicine counterfeits by Raman spectroscopy and chemometrics. *Analytica Chimica Acta,* vol. 705, pp. 334-341, 2011.

[249] Li, X., T. Yang, S. Lib, and T. Yu, Surface-enhanced Raman spectroscopy differences of saliva between lung cancer patients and normal people. in *Clinical and Biomedical Spectroscopy and Imaging II,* Munich, Germany, 2011, p. 808722.

[250] Lin, K., D.L.P. Cheng, and Z. Huang, Optical diagnosis of laryngeal cancer using high wavenumber Raman spectroscopy. *Biosensors and Bioelectronics,* vol. 35, pp. 213-217, 2012.

[251] Hargreaves, M.D., N.A. Macleod, M.R. Smith, D. Andrews, S.V. Hammond, and P. Matousek, Characterisation of transmission Raman spectroscopy for rapid quantitative analysis of intact multi-component pharmaceutical capsules. *Journal of Pharmaceutical and Biomedical Analysis,* vol. 54, pp.

463-468, 2011.

[252] Mazurek, S. and R. Szostak, Quantitative Determination of Prednisone in Tablets by Infrared Attenuated Total Reflection and Raman Spectroscopy. *Journal of AOAC International,* vol. 95, pp. 744-750, 2012.

[253] Fenton, O.S., L.A. Tonge, T.H. Moot, and K.A. Frederick, Quantitative Analysis of Simulated Illicit Street-Drug Samples Using Raman Spectroscopy and Partial Least Squares Regression. *Spectroscopy Letters,* vol. 44, pp. 229-234, 2011.

[254] Szostak, R. and S. Mazurek, Quantification of active ingredients in suppositories by FT-Raman spectroscopy. *Drug Testing and Analysis,* 2012, DOI: 10.1002/dta.379.

[255] Poon, K.W.C., F.M. Lyng, P. Knief, O. Howe, A.D. Meade, J.F. Curtin, H.J. Byrne, and J. Vaughan, Quantitative reagent-free detection of fibrinogen levels in human blood plasma using Raman spectroscopy. *Analyst,* vol. 137, pp. 1807-1814, 2012.

[256] Weakley, A.T., P.C.T. Warwick, T.E. Bitterwolf, and D.E. Aston, Multivariate Analysis of Micro-Raman Spectra of Thermoplastic Polyurethane Blends Using Principal Component Analysis and Principal Component Regression. *Applied Spectroscopy*, vol. 66, pp. 1269-1278, 2012.

[257] Howell, N.K., G. Arteaga, S. Nakai, and E.C.Y. Li-Chan, Raman Spectral Analysis in the C−H Stretching Region of Proteins and Amino Acids for Investigation of Hydrophobic Interactions. *Journal of Agricultural and Food Chemistry,* vol. 47, pp. 924-933, 1999.

[258] Pallaoro, A., G.B. Braun, and M. Moskovits, Quantitative ratiometric discrimination between noncancerous and cancerous prostate cells based on neuropilin-1 overexpression. *Proceedings of the National Academy of Sciences,* vol. 108, pp. 16559-16564, 2011.

[259] Ingle, T., E. Dervishi, A.R. Biris, T. Mustafa, R.A. Buchanan, and A.S. Biris, Raman spectroscopy analysis and mapping the biodistribution of inhaled carbon nanotubes in the lungs and blood of mice. *Journal of Applied Toxicology,* 2012, DOI: 10.1002/jat.2796.

[260] Nikiel, L. and P.W. Jagodzinski, Raman spectroscopic characterization of graphites: A re-evaluation of spectra/ structure correlation. *Carbon,* vol. 31, pp. 1313-1317, 1993.

[261] Ashton, L., L.D. Barron, B. Czarnik-Matusewicz, L. Hecht, J. Hyde, and E.W. Blanch, Two-dimensional correlation analysis of Raman optical activity data on the α-helix-to-β-sheet transition in poly(L-lysine). *Molecular Physics,* vol. 104, pp. 1429-1445, 2006.

[262] Bell, S.E.J., J.N. Mackle, and N.M.S. Sirimuthu, Quantitative surface-enhanced Raman spectroscopy of dipicolinic acid-towards rapid anthrax endospore detection. *Analyst*, vol. 130, pp. 545-549, 2005.

[263] Wu, Z.-S., G.-Z. Zhou, J.-H. Jiang, G.-L. Shen, and R.-Q. Yu, Gold colloid-bienzyme conjugates for glucose detection utilizing surface-enhanced Raman scattering. *Talanta,* vol. 70, pp. 533-539, 2006.

[264] Yang, X., A. Zhang, D. Wheeler, T. Bond, C. Gu, and Y. Li, Direct molecule-specific glucose detection by Raman spectroscopy based on photonic crystal fiber. *Analytical and Bioanalytical Chemistry,* vol. 402, pp. 687-691, 2012.

[265] Rosch, P., M. Harz, M. Schmitt, and J. Popp, Raman spectroscopic identification of single yeast cells. *Journal of Raman Spectroscopy,* vol. 36, pp. 377-379, 2005.

[266] Rull, F., A.C. Prieto, J.M. Casado, F. Sobron, and H.G.M. Edwards, Estimation of crystallinity in polyethylene by Raman spectroscopy. *Journal of Raman Spectroscopy*, vol. 24, pp. 545-550, 1993.

[267] Edwards, H.G.M., D.W. Farwell, A.C. Williams, B.W. Barry, and F. Rull, Novel spectroscopic deconvolution procedure for complex biological systems: vibrational components in the FT-Raman spectra of ice-man and contemporary skin. *Journal of the Chemical Society, Faraday Transactions*, vol. 91, pp. 3883-3887, 1995.

[268] Baker, F.B. and L.J. Hubert, Measuring the power of hierarchical cluster analysis. *Journal of the American Statistical Association*, vol. 70, pp. 31-38, 1975.

[269] Stephen, K.E., D. Homrighausen, G. DePalma, C.H. Nakatsu, and J. Irudayaraj, Surface enhanced Raman spectroscopy (SERS) for the discrimination of Arthrobacter strains based on variations in cell surface composition. *Analyst*, vol. 137, pp. 4280-4286, 2012.

[270] Kniggendorf, A.-K., T.W. Gaul, and M. Meinhardt-Wollweber, Hierarchical Cluster Analysis (HCA) of Microorganisms: An Assessment of Algorithms for Resonance Raman Spectra. *Applied Spectroscopy,* vol. 65, pp. 165-173, 2011.

[271] O'Connell, M.-L., T. Howley, A.G. Ryder, M.N. Leger, and M.G. Madden, Classification of a target analyte in solid mixtures using principal component analysis, support vector machines, and Raman spectroscopy. in *Opto-Ireland 2005: Optical Sensing and Spectroscopy*, Ireland, 2005, pp. 340-350.

[272] Deinum, G., D. Rodriguez, T.J. Romer, M. Fitzmaurice, J.R. Kramer, and M.S. Feld, Histological Classification of Raman Spectra of Human Coronary Artery Atherosclerosis Using Principal Component Analysis. *Applied Spectroscopy,* vol. 53, pp. 938-942, 1999.

[273] Haka, A.S., K.E. Shafer-Peltier, M. Fitzmaurice, J. Crowe, R.R. Dasari, and M.S. Feld, Diagnosing breast cancer by using Raman spectroscopy. *Proceedings of the National Academy of Sciences of the United States of America*, vol. 102, pp. 12371-12376, 2005.

[274] Frausto-Reyes, C., C. Medina-Gutiérrez, R. Sato-Berrú, and L.R. Sahagún, Qualitative study of ethanol content in tequilas by Raman spectroscopy and principal component analysis. *Spectrochimica Acta Part A: Molecular and Biomolecular Spectroscopy,* vol. 61, pp. 2657-2662, 2005.

[275] Berman, M., A. Phatak, R. Lagerstrom, and B.R. Wood, ICE: a new method for the multivariate curve resolution of hyperspectral images. *Journal of Chemometrics*, vol. 23, pp. 101-116, 2009.

[276] Gouadec, G. and P. Colomban, Raman Spectroscopy of nanomaterials: How spectra relate to disorder, particle size and mechanical properties. *Progress in Crystal Growth and Characterization of Materials*, vol. 53, pp. 1-56, 2007.

[277] Pócsik, I. and M. Koós, Cluster size determination in amorphous structures using the Boson peak. *Solid State Communications,* vol. 74, pp. 1253-1256, 1990.

[278] Tamura, A., K. Higeta, and T. Ichinokawa, Lattice vibrations and specific heat of a small particle. *Journal of Physics C: Solid State Physics,* vol. 15, p. 4975, 1982.

[279] Ferrari, M., F. Gonella, M. Montagna, and C. Tosello, Waveguide Raman Spectroscopy as a Tool for the Detection of Nanometric Metallic Particles in Glasses. *Journal of Raman Spectroscopy,* vol. 27, pp. 793-797, 1996.

[280] Yoshikawa, M., Y. Mori, H. Obata, M. Maegawa, G. Katagiri, H. Ishida, and A. Ishitani, Raman scattering from nanometer-sized diamond. *Applied Physics Letters,* vol. 67, pp. 694-696, 1995.

[281] Yoshikawa, M., Y. Mori, M. Maegawa, G. Katagiri, H. Ishida, and A. Ishitani, Raman scattering from diamond particles. *Applied Physics Letters,* vol. 62, pp. 3114-3116, 1993.

[282] Sriram, S., M. Bhaskaran, S. Chen, S. Jayawardhana, P.R. Stoddart, J.Z. Liu, N.V. Medhekar, K. Kalantar-zadeh, and A. Mitchell, Influence of Electric Field on SERS: Frequency Effects, Intensity Changes, and Susceptible Bonds. *Journal of the American Chemical Society,* vol. 134, pp. 4646-4653, 2012.

[283] Chen, Z.-P., L.-M. Li, J.-W. Jin, A. Nordon, D. Littlejohn, J. Yang, J. Zhang, and R.-Q. Yu, Quantitative Analysis of Powder Mixtures by Raman Spectrometry: the influence of particle size and its correction. *Analytical Chemistry,* vol. 84, pp. 4088-4094, 2012.

[284] Mouazen, A.M., B. Kuang, J. De Baerdemaeker, and H. Ramon, Comparison among principal component, partial least squares and back propagation neural network analyses for accuracy of measurement of selected soil properties with visible and near infrared spectroscopy. *Geoderma,* vol. 158, pp. 23-31, 2010.

[285] Pohl, H.A., *Dieletrophoresis*. 1978, Oklahoma: Cambridge University Press.

[286] Pohl, H.A. and J.S. Crane, Dielectrophoresis of cells. *Biophysical Journal,* vol. 11, pp. 711-727, 1971.

[287] Morgan, H. and N.G. Green, *AC Electrokinetics: Colloids and Nanoparticles*. 2003, Baldock: Research Studies Press.

[288] Lei, U., C.W. Huang, J. Chen, C.Y. Yang, Y.J. Lo, A. Wo, C.F. Chen, and T.W. Fung, A travelling wave dielectrophoretic pump for blood delivery. *Lab on a Chip,* vol. 9, pp. 1349-1356, 2009.

[289] Pethig, R., Dielectrophoresis: Status of the theory, technology, and applications. *Biomicrofluidics,* vol. 4, pp. 022811-35, 2010.

[290] Cen, E.G., C. Dalton, Y.L. Li, S. Adamia, L.M. Pilarski, and K. Kaler, A Combined Dielectrophoresis, Traveling Wave Dielectrophoresis and Electrorotation Microchip for the Manipulation and Characterization of Human Malignant Cells. *Journal of Microbiological Methods,* vol. 58, pp. 387-401, 2004.

[291] Urdaneta, M. and E. Smela, Multiple frequency dielectrophoresis. *Electrophoresis,* vol. 28, pp. 3145-3155, 2007.

[292] Park, B.Y. and M.J. Madou, 3-D electrode designs for flow-through dielectrophoretic systems. *Electrophoresis,* vol. 26, pp. 3745-3757, 2005.

[293] Ramos, A., H. Morgan, N.G. Green, and A. Castellanos, Ac electrokinetics: a review of forces in microelectrode structures. *Journal of Physics D-Applied Physics,* vol. 31, pp. 2338-2353, 1998.

[294] Takano, N., L.M. Doeswijk, M.A.F. van den Boogaart, J. Auerswald, H.F. Knapp, O. Dubochet, T. Hessler, and J. Brugger, Fabrication of metallic patterns by microstencil lithography on polymer surfaces suitable as microelectrodes in integrated microfluidic systems. *Journal of Micromechanics and Microengineering,* vol. 16, pp. 1606-1613, 2006.

[295] Auerswald, J. and H.F. Knapp, Quantitative assessment of dielectrophoresis as a micro fluidic retention and separation technique for beads and human blood erythrocytes. *Microelectronic Engineering,* vol. 67, pp. 879-886, 2003.

[296] Crews, N., J. Darabi, P. Voglewede, F. Guo, and A. Bayoumi, An analysis of interdigitated electrode geometry for dielectrophoretic particle transport in micro-fluidics. *Sensors and Actuators B: Chemical,* vol. 125, pp. 672-679, 2007.

[297] Gascoyne, P.R.C., X.B. Wang, Y. Huang, and F.F. Becker, Dielectrophoretic separation of cancer cells from blood. *Industry Applications, IEEE Transactions on,* vol. 33, pp. 670-678, 1997.

[298] Li, H. and R. Bashir, Dielectrophoretic separation and manipulation of live and heat-treated cells of *Listeria* on microfabricated devices with interdigitated electrodes. *Sensors and Actuators B: Chemical,* vol. 86, pp. 215-221, 2002.

[299] Huang, Y., X.B. Wang, F.F. Becker, and P. Gascoyne, Introducing dielectrophoresis as a new force field for field-flow fractionation. *Biophysical Journal,* vol. 73, pp. 1118-1129, 1997.

[300] Yang, L., P.P. Banada, M.R. Chatni, K.S. Lim, A.K. Bhunia, M. Ladisch, and R. Bashir, A multifunctional micro-fluidic system for dielectrophoretic concentration coupled with immuno-capture of low numbers of Listeria monocytogenes. *Lab on a Chip,* vol. 6, pp. 896-905, 2006.

[301] Hu, X., P.H. Bessette, J. Qian, C.D. Meinhart, P.S. Daugherty, and H.T. Soh, Marker-specific sorting of rare cells using dielectrophoresis. *Proceedings of the National Academy of Sciences of the United States of America,* vol. 102, pp. 15757-15761, 2005.

[302] Kim, U., J. Qian, S.A. Kenrick, P.S. Daugherty, and H.T. Soh, Multitarget dielectrophoresis activated cell sorter. *Analytical Chemistry,* vol. 80, pp. 8656-8661, 2008.

[303] Pommer, M.S., Y. Zhang, N. Keerthi, D. Chen, J.A. Thomson, C.D. Meinhart, and H.T. Soh, Dielectrophoretic separation of platelets from diluted whole blood in microfluidic channels. *Electrophoresis,* vol. 29, pp. 1213-1218, 2008.

[304] Khoshmanesh, K., C. Zhang, F.J. Tovar-Lopez, S. Nahavandi, S. Baratchi, K. Kalantar-zadeh, and A. Mitchell, Dielectrophoretic manipulation and separation of microparticles using curved microelectrodes. *Electrophoresis,* vol. 30, pp. 3707-3717, 2009.

[305] Khoshmanesh, K., C. Zhang, F.J. Tovar-Lopez, S. Nahavandi, S. Baratchi, A. Mitchell, and K. Kalantar-zadeh, Dielectrophoretic-activated cell sorter based on curved microelectrodes. *Microfluidics and Nanofluidics,* vol. 9, pp. 411-426, 2010.

[306] Kalantar-zadeh, K., K. Khoshmanesh, A.A. Kayani, S. Nahavandi, and A. Mitchell, Dielectrophoretically tuneable optical waveguides using nanoparticles in microfluidics. *Applied Physics Letters,* vol. 96, p. 101108, 2010.

[307] Kayani, A.A., C. Zhang, K. Khoshmanesh, J.L. Campbell, A. Mitchell, and K. Kalantar-zadeh, Novel tuneable optical elements based on nanoparticle suspensions in microfluidics. *Electrophoresis,* vol. 31, pp. 1071-1079, 2010.

Chapter 3

Design and fabrication

3.1 Introduction

This PhD thesis focusses on the integration of Raman microscopy with microfluidics, while utilising dielectrophoresis (DEP) as a controlling feature. The microfluidic device was designed and fabricated in order to interface with the existing Raman microscopy equipment. The PhD work uses two different DEP-microfluidic platforms; each platform targeted a different size category of suspended materials. Both platforms implemented a DEP microelectrode array patterned onto a quartz slide. A microfluidic channel was then fabricated and attached to the patterned electrode structure. The two devices were differentiated by the size of the microfluidic channel and the DEP microelectrode spacing. The reason for these differences will be discussed further in the “Design” section.

In this chapter, the author details the fabrication process of the microfluidic platforms, including details of the DEP microelectrode and microfluidic channel dimensions. Simulations relevant to the platforms, and why the dimensions were chosen, will be presented prior to their respective results and outcomes in Chapters 4, 5 and 6, as each simulation module varies depending on the materials and fluids used.

3.2 Design

3.2.1 DEP microelectrodes

In the following chapters the author presents experiments where curved DEP electrodes are used. This particular design allows control of both hydrodynamic and dielectrophoretic forces to create a highly focused stream of particles in the microchannel [1-4]. Curved microelectrodes provide controlled and repeatable areas of high and low particle concentrations under constant flow conditions. Constant flow conditions are desirable as they allow for the constant refreshing of particles at the electrode tip regions. The curved microelectrodes do not produce electrothermally induced vortices near the electrode tips, which is a requirement for the repeatable *in situ* Raman microscopy studies of suspended nanoparticles particles. Other electrode designs are more optimised for low flow or no flow microfluidic systems, which are not desired in this case. The DEP microelectrode designs contain 40 electrode pairs spanning the entire length of the microfluidic channel with individual dimensions of both designs detailed in Figure 3.. The DEP microelectrode mask was designed by the author's collaboration, Dr. Aminuddin Kayani, using the Advanced Design Systems (ADS) software package.

The initial DEP microelectrode design used curved microelectrodes with tip spacings of 20 µm. This spacing was most suitable for experiments involving suspended metal oxide nanoparticles, as strong positive and negative DEP forces could be applied to them. However, experiments involving smaller nanoparticles did not experience strong DEP forces at 20 µm spacing; therefore in order to increase the DEP force applied to them the electric field intensity was increased. This increase was implemented by reducing the electrode tip spacing to just 5 µm, increasing the peak electric field intensity by a factor of 10. These smaller electrode spacings were more difficult to fabricate, as the presence of smallest contaminants of dusts could produce short circuited microelectrodes in the development process.

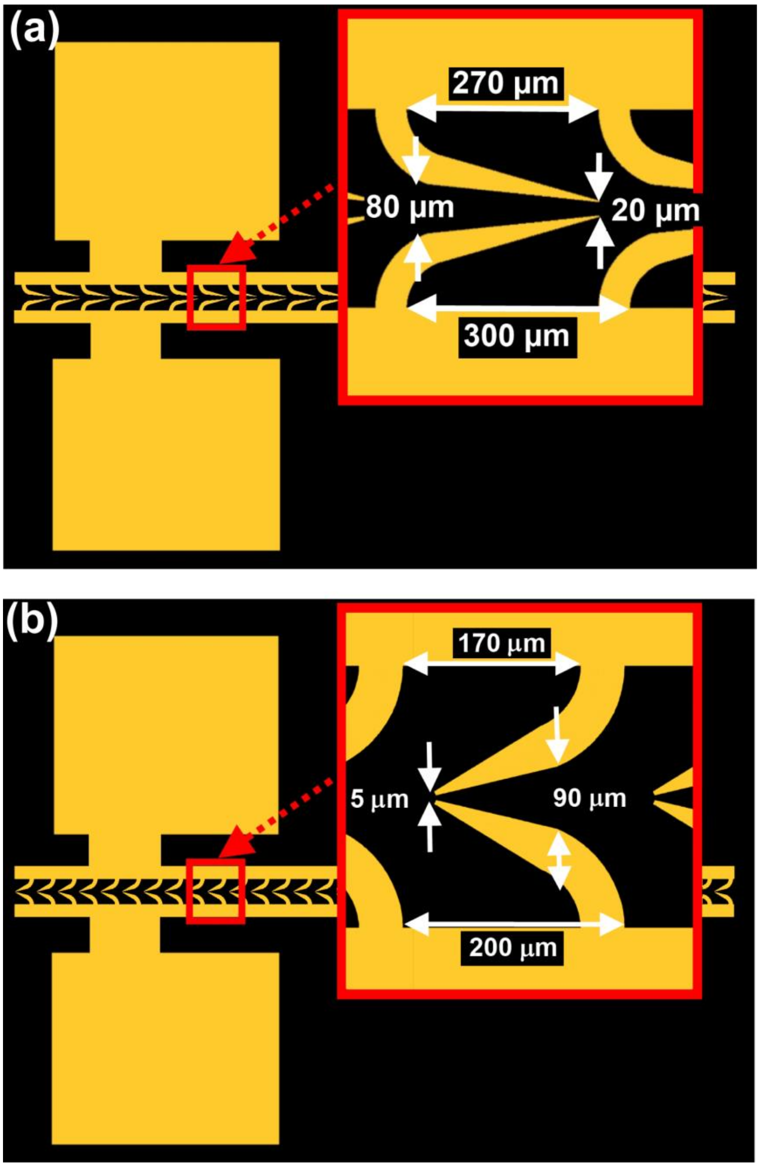

Figure 3.1: Dielectrophoresis electrode mask designs: (a) microelectrode design with 20 µm tip spacings and (b) microelectrode design with 5 µm tip spacings.

3.2.2 Microfluidic channels

The microfluidic channel was a simple rectangular structure, which was formed from polydimethylsiloxane (PDMS). The channel designs are shown in Figure 3.2, where 3 mm diameter reservoirs were introduced at the ends of the channel to introduce and exhaust liquid.

Two different microchannel designs were used for this work. The first microchannel design was used in conjunction with the larger 20 µm spaced microelectrodes. The width of the channel was chosen as 400 µm such that the entire structure of the electrodes could be exposed to the suspended particles. The channel was 16 mm long in order to accommodate 40 microelectrode pairs along the channel. A depth of 80 µm was chosen as it provided enough depth to avoid the blocking of the channel by clustered nanoparticles as well as contaminations entering the reservoir. These microchannel dimensions were well suited to experiments involving suspended metal oxide particles; however the microchannel volume was unnecessarily large for experiments involving more high cost samples. Therefore a new channel design was required for precious silver nanoparticle mixtures.

The smaller microchannel was designed to be used in conjunction with the 5 µm tip spaced electrodes. As such, the width of the microchannel was reduced to 120 µm so that only the high electric field areas of the microelectrodes were present inside the channel. Not all of the microelectrode pairs were required for these experiments, therefore the channel was shortened to 10 mm long to capture approximately 2/3 of the total number of microelectrode pairs. Finally, the depth was set to 50 µm, as it provided sufficient depth so the particles would not block the microchannel, but was also sufficiently shallow such that the electric fields produced by the microelectrodes could capture particles at the far reaches of the microchannel.

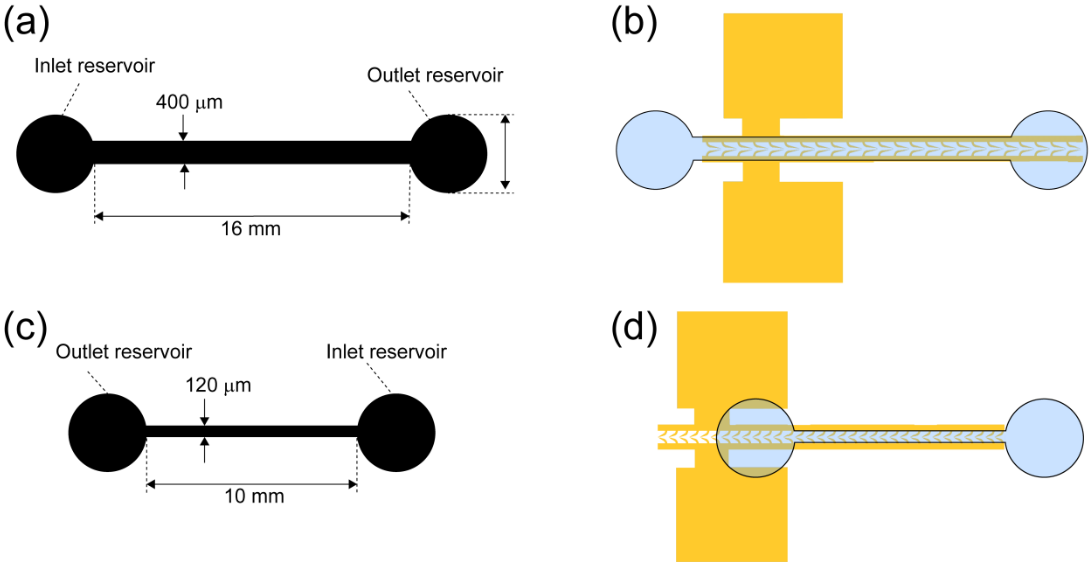

Figure 3.2: Schematics of microfluidic channel designs. (a) Larger microchannel design which is 80 µm deep, 400 µm wide and 16 mm long. (b) Microchannel alignment with electrodes of 20 µm tip spacing. (c) Smaller microchannel design which is 50 µm deep, 120 µm wide and 10 mm long. (d) Microchannel alignment with electrodes of 5 µm tip spacing.

3.2.3 Device substrate

The PDMS material forming the walls of the channel exhibit inherent Raman peaks [5], which can interfere with the performance of Raman spectroscopy. To reduce the effect of PDMS interference, the channel floor was formed from a transparent substrate. The electrodes were patterned on this substrate and confocal Raman spectroscopy was performed through the substrate in an inverted configuration (Figure 3.3). This ensured minimal interfering signal was collected from the PDMS.

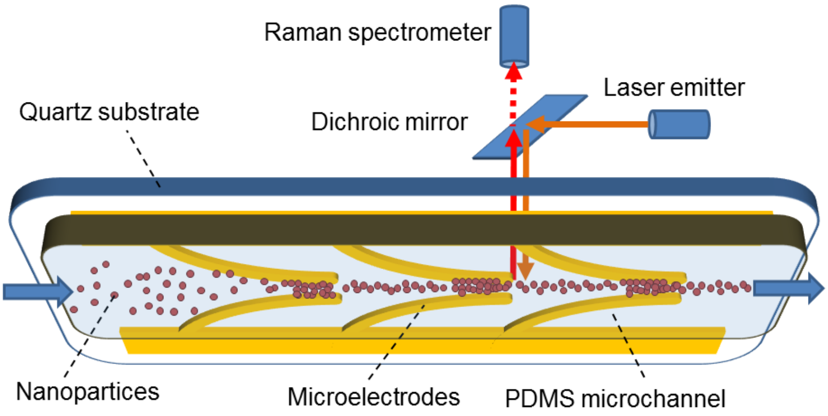

Figure 3.3: Graphical schematic of the Raman-microfluidic systems principal of operation.

Glass is the substrate most favoured for the fabrication of DEP electrodes [6-11] as it is cheap, non-conductive (essential for DEP electrode use), transparent at visible wavelengths and non-reactive to most biological materials. However, glass is Raman active in the low wavenumber region and also exhibits a broad peak at 1000 cm^{-1} [12]. Other substrates widely used in microfluidics include silicon wafers coated with thin non-conductive silica layers [13] and polymer-based substrates [14]. However these substrates are also Raman active. Alternatively, quartz was used in this work as the substrate for the electrode pattering. The Raman response of quartz is insignificant compared to the Raman signals of interest [15, 16].

3.3 Fabrication

The fabrication process for the microfluidic-dielectrophoretic device is detailed in two distinct phases: DEP microelectrode fabrication and microfluidic channel fabrication. The final phase involves fabricating the function generator interface device.

The process for fabrication of the DEP microelectrodes constitutes a top-down photolithography process, whereby a desired microelectrode pattern is used to block exposure of photoresist to UV radiation [17]. The resulting pattern in the photoresist is developed, and consequently used to prevent etching of the underlying metallic layers. This process is very similar to that used for the fabrication of printed circuit boards.

The PDMS microchannels are fabricated using ‘soft-lithography’, a phrase coined by Whitesides *et al.* [18]. Briefly, the process first involves creating a rigid microchannel relief structure, typically using SU-8 photoresist on a silicon substrate. Wet PDMS is placed over the structure and left to cure. The cured PDMS structure, once removed from the mould, has the microchannel patterned into it. The fabrication processes of both the electrode patterns and the PDMS microchannel will be described in further detail in the following sections.

3.3.1 DEP microelectrodes

In this section, the author will detail the procedures for the fabrication of the DEP microelectrodes onto a quartz substrate. A flowchart summary of the microelectrode fabrication process is shown in Figure 3.4.

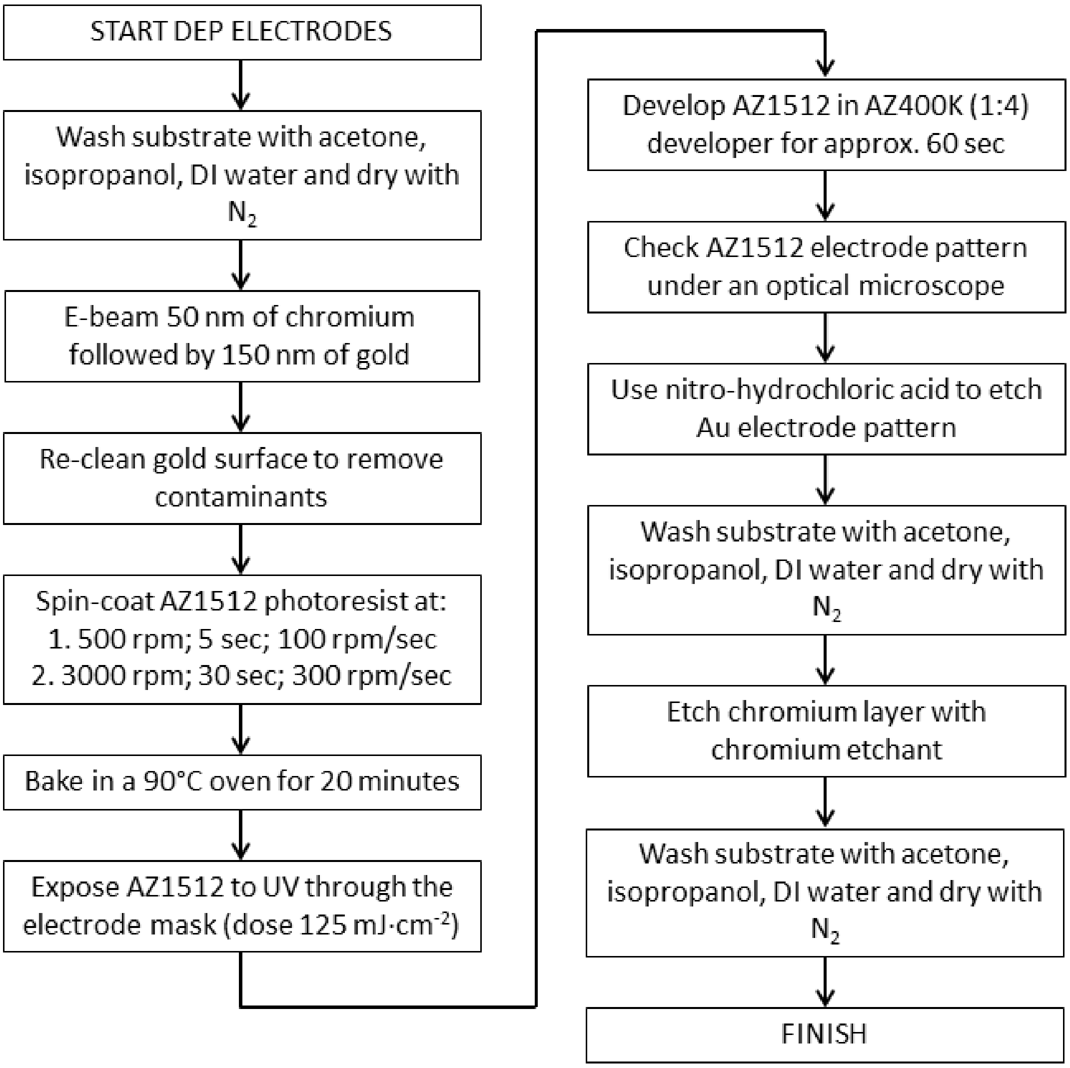

Figure 3.4: Flowchart summary of DEP microelectrode fabrication process.

3.3.1.1 Substrate preparation

A standard process for cleaning the substrates was devised to ensure the quality of the fabricated devices. The presences of particles and contaminants on the substrate surface or exposure masks would result in irreversible defects in the final product.

The cleaning begins using acetone to remove grease and particles from the surface, and is applied using a lint-free swab. The surface is rinsed with 2-propanol (isopropanol) and de-ionized (DI) water to remove acetone and particles, and blow dried using compressed nitrogen (N_2). Visual inspection is carried out to ensure proper cleaning prior to subsequent fabrication steps.

3.3.1.2 Chromium and gold layers

The quartz substrate was electron-beam coated with 50 nm of chromium (Cr), followed by 150 nm of gold (Au) as in Figure 3.5(a). This created a total microelectrode thickness of 200 nm. The thickness of the Cr layer is critical to the adhesion ability of the electrode structures to the quartz substrate. If the Cr layer is too thin, the electrodes will not adhere adequately to the quartz and will readily washed away. The disadvantage of making a thicker Cr layer is the increased fabrication time, as the Cr layer must be chemically etched away. As for the Au layer, this layer provides a highly conductive and relatively inert surface. If the Au layer is too thin there is a chance that fluid will come into contact with the Cr layer and begin to corrode the electrodes. If the Au layer is too thick it can disturb the laminar flow movements close to the bottom surface of the channel. In the case of this research project, the choice of electrode thickness was as small as possible so as to avoid the aforementioned issues.

3.3.1.3 Photolithography

All photolithography process, including those needed for the microfluidic PDMS, were conducted in a class-1000 clean room with a relative humidity of 40 % and a temperature of 22 °C. The quartz substrate was spin coated with AZ1512 (Microchem) photoresist using a Karl Suss RC8 spinner. The spin cycle begins at a rotational speed of 500 rpm for 5 seconds, with an acceleration of 100 rpm/sec, in order to spread out the deposited photoresist. This is followed by a spinning cycle of 3000 rpm for 30 seconds, with an acceleration of 300 rpm/sec.

The quartz substrate is then baked in an oven at 90°C for 20 min (Figure 3.5(b)) in order to evaporate solvents from the photoresist. The substrate was exposed to ultraviolet (UV) light through a chromium mask, which contained the pattern of the microelectrodes show in Figure 3.1, using a MJB3 mask aligner. The exposure dose was adjusted to match that required by the microchem datasheet (125 $\mathrm{mJ \cdot cm^{-2}}$). The substrate is placed in a solution of AZ400K developer (1:4) in order to develop the microelectrode pattern in the photoresist (Figure 3.5(c)). The microelectrode pattern was examined under an optical microscope to ensure the pattern was not under or over developed, and to ensure the electrode parts would not develop with a short circuit between them. If the microelectrode pattern was not ideal, the AZ1512 was removed using acetone, and the photolithographic processes repeated.

3.3.1.4 Wet etching

The etching of undesired gold, which constitutes the top layer of the Au:Cr stack, is removed using nitro-hydrochloric acid, formed by mixing 1 part nitric acid (HNO_3) with 4 parts hydrochloric acid (HCl). The etching process for the Au layer takes approximately 40 seconds, and is monitored by sight, after which it is thoroughly rinsed with DI water.

The substrate is rinsed and cleaned using the process in “substrate preparation,” after which a chromium etchant is then used to remove the excess chromium (Figure 3.5(d)) in a process that takes approximately 75 seconds. The chromium etchant is a solution of 4% nitric acid (HNO_3), 11% ceric ammonium nitrate ($Ce(NH_4)_2(NO_3)_6$) and 85% water (H_2O).

Finally, the substrate is thoroughly cleaned with acetone, isopropanol, DI water and blow dried with N_2. The microelectrodes are examined under an optical microscope to ensure no photoresist remained after washing, and to ensure the microelectrode patterns were not under/over etched.

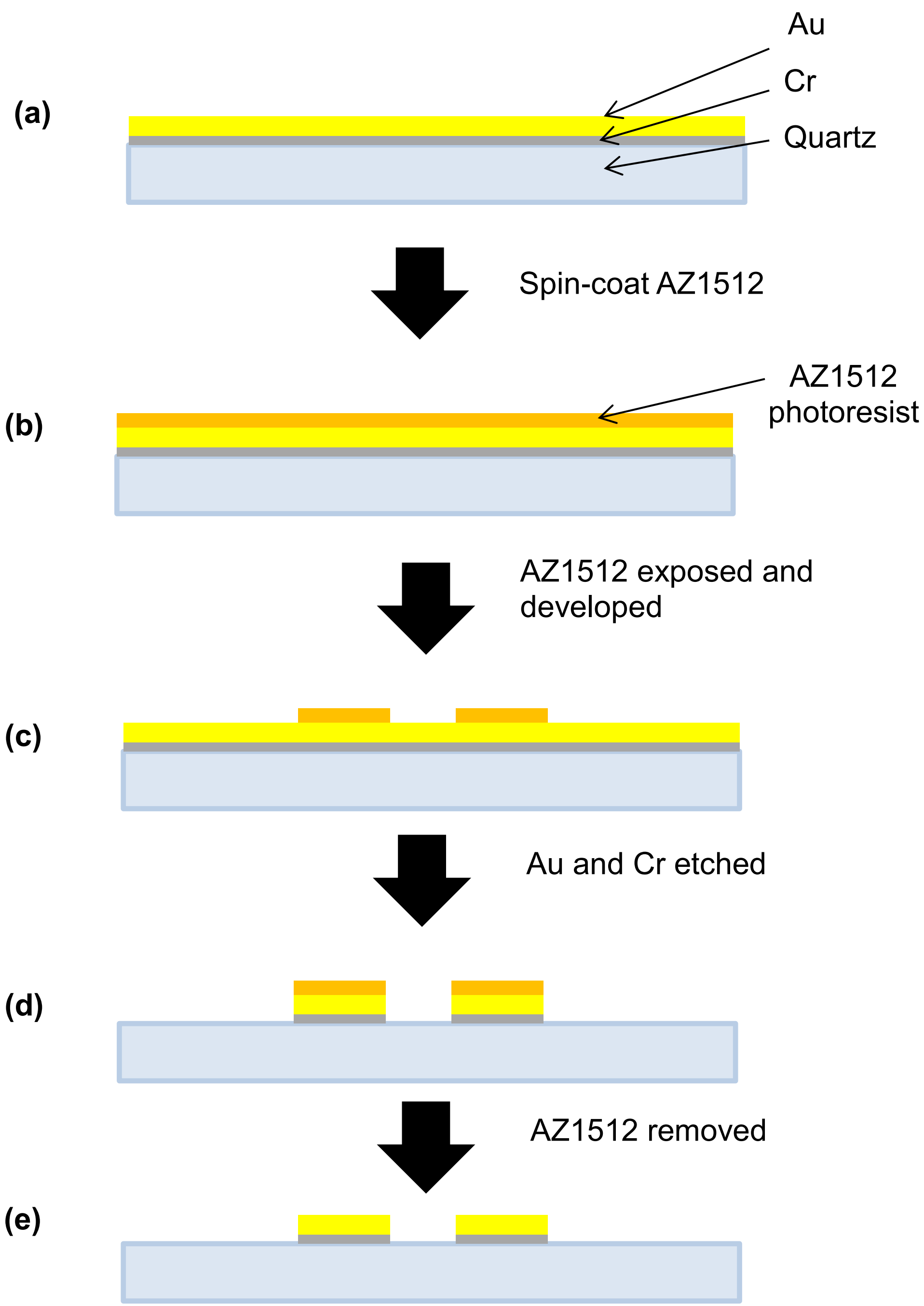

Figure 3.5: Detailed cross-sectional images of the fabrication process.

3.3.2 PDMS microfluidic channels

The microfluidic devices was fabricated in a class 1000 clean room using standard ‘soft lithography’ fabrication procedures [18]. The procedure involves two stages; the first stage involves the creation of an SU-8 mould onto a silicon wafer. The second stage utilizes the SU-8 mould to create a PDMS relief structure of the microchannel. A summary flow chart of the PDMS microchannel fabrication process is shown in Figure 3.6.

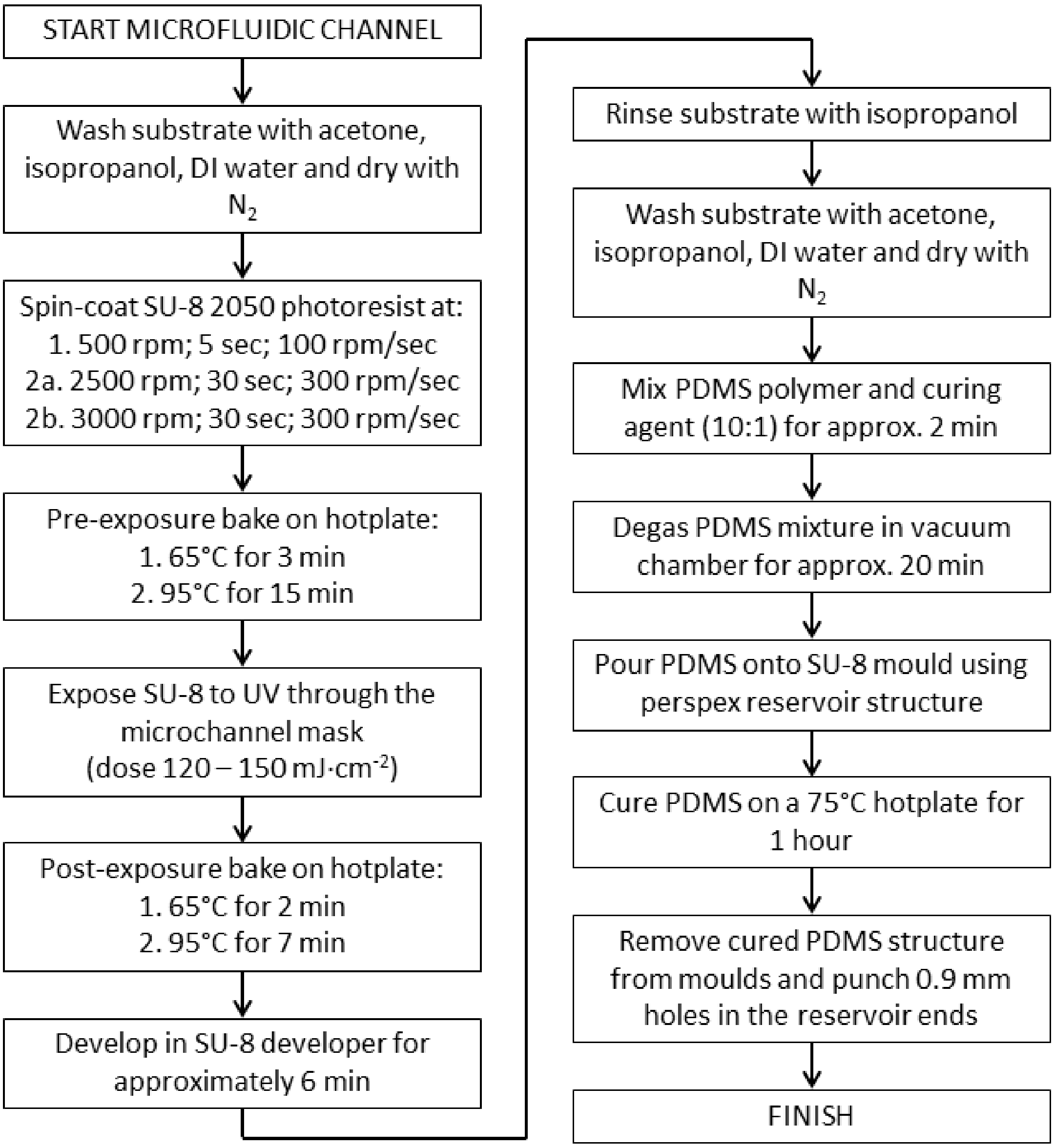

Figure 3.6: Flowchart summary of PDMS microchannel fabrication process.

3.3.2.1 Microchannel mould fabrication

The process begins using SU-8 2050 (Microchem), which was spin coated (using a Karl Suss RC8 spinner) onto a clean silicon wafer to form a layer either 80 or 50 µm thick, depending on the device design. The settings for the spin coater involved a 500 rpm, 5 second spread cycle, with an acceleration of 100 rpm/sec. The next stage of the spin cycle was lasted for 30 seconds, with an acceleration of 300 rpm/sec at either 2500 or 3000 rpm depending on the required thickness. The photoresist was baked at 65°C for 3 minutes, followed by 95°C for 15 minutes, as stated in the microchem datasheet.

The expose dosage of UV through a printed mask using an MJB3 mask aligner was either 120 or 150 $mJ \cdot cm^{-2}$ depending on the SU-8 thickness. Post-exposure baking took place with 2 minutes at 65°C followed by 7 minutes at 95°C. The SU-8 was then developed in microchem SU-8 developer for approximately 6 minutes, and hard baked on a hotplate at 190°C for 20 minutes. The remaining structure is used as the PDMS master mould.

3.3.2.2 Fabrication of PDMS microchannel block

A perspex mould is created in 3 mm thick Perspex by using computer numerical control (CNC) milling machine fitted with a 3 mm milling bit. The mould is cleaned and placed over the hard-baked SU8 channel created in the previous step.

Wet polydimethylsiloxane (PDMS, Sylgard Dow), which is mixed at a 10:1 ratio of polymer to curing agent, was stirred for 2 minutes to ensure proper mixing. The mixture placed in a vacuum chamber to remove air bubbles. The PDMS was poured into the SU8 master mould and left to cure at 75°C for 1 hour. Once the PDMS was fully cured, it was peeled off the mould structure where holes of 0.9 mm diameter were punched in the ends to facilitate the input-output of fluids.

3.3.2.3 Assembly with microelectrode substrate

The PDMS was aligned and attached to the electrode structure on the quartz slide as seen in Figure 3.2. No special procedure was used to ensure bondage of PDMS to the quartz slide, as it was found the natural sticky quality of the PDMS was enough to hold it in place. However, to ensure a reliable PDMS-quartz bond the microfluidic system was always run in ‘refill’ mode, where the syringe is pulling the liquid through the channel. This action creates negative pressure inside the microchannel, ensuring the PDMS does not de-laminate from the quartz.

Microtubes, with an internal diameter of ~400 μm, were placed into the holes punched into the PDMS. These tubes allowed the interfacing of syringe pumps and samples with the microchannel. Wires were also bonded to electrode pads on the quartz slide using conductive copper tape.

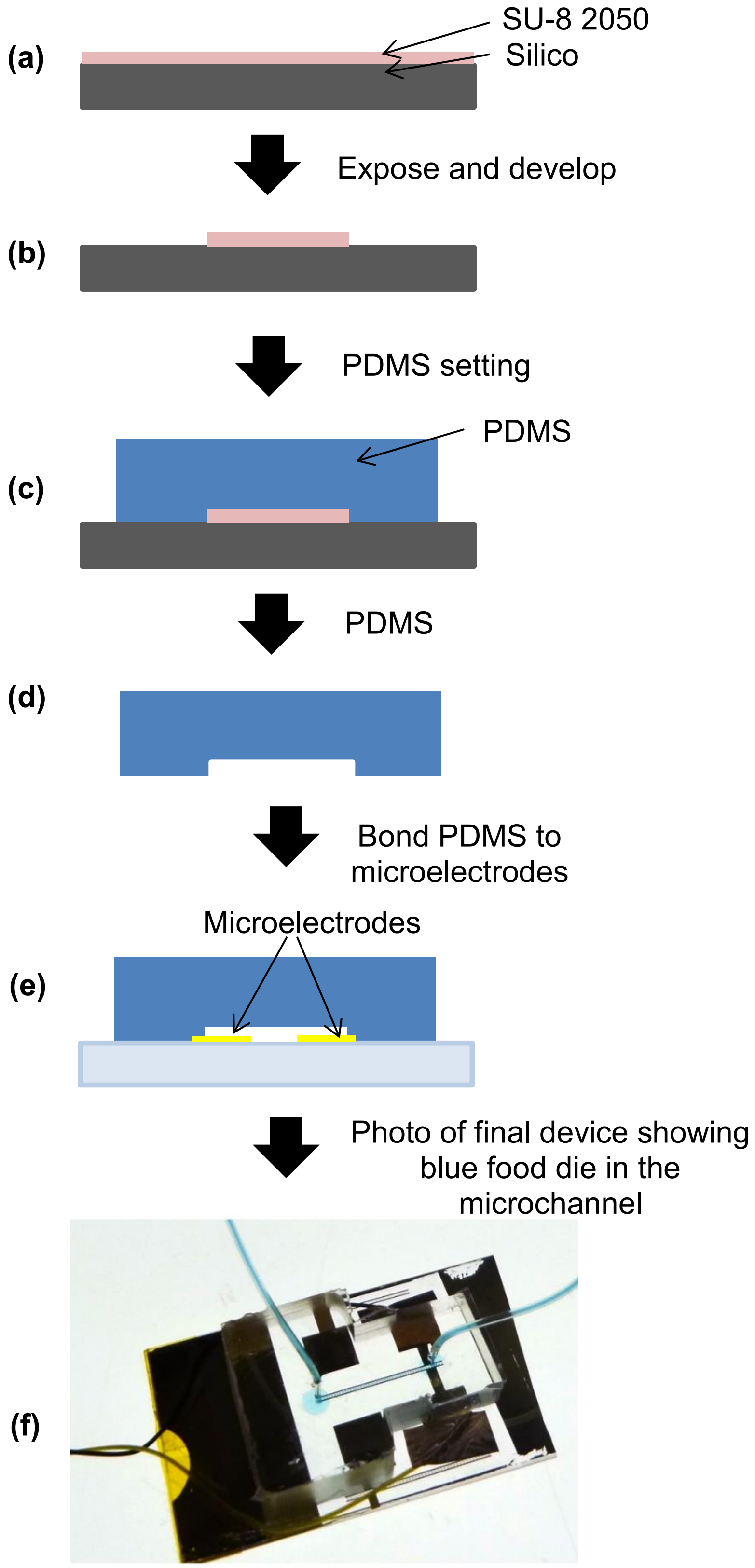

Figure 3.7: Fabrication process for microchannel PDMS block. (a) SU-8 photoresist on silocon wafer. (b) Developed SU-8 mould of microchannel. (c) Wet PDMS over SU-8 mould. (d) Fabricated PDMS microchannel structure. (e) PDMS microchannel structure attached to quartz electrode slide. (f) Photograph of completed microfluidic device with blue food die in the microchannel.

3.3.3 Function generator interface

In order to facilitate the connection between the DEP microelectrodes and the function generator, an interface device was designed and built. The function generator used in these experiments utilizes a BNC female connector for its output. The function generator is designed to have a 50 Ω output impedance (Figure 3.8). The DEP microelectrodes are connected using thin wire and conductive copper tape connected to the designed tabs. The ends of the wire are fitted with a suitable 2-pin PCB plug, allowing quick connection to the interface device. The interface device is designed to accept both BNC and 'banana' plug style connectors from the function generator. The interface device has an additional 1 kΩ, ¼ watt resistor placed across the terminals of the function generator to provide the function generator with a relatively constant load impedance. The interface device allowed for quicker experimental set-up times, and reduced wear-and-tear on the delicate wires attached to the DEP microelectrodes.

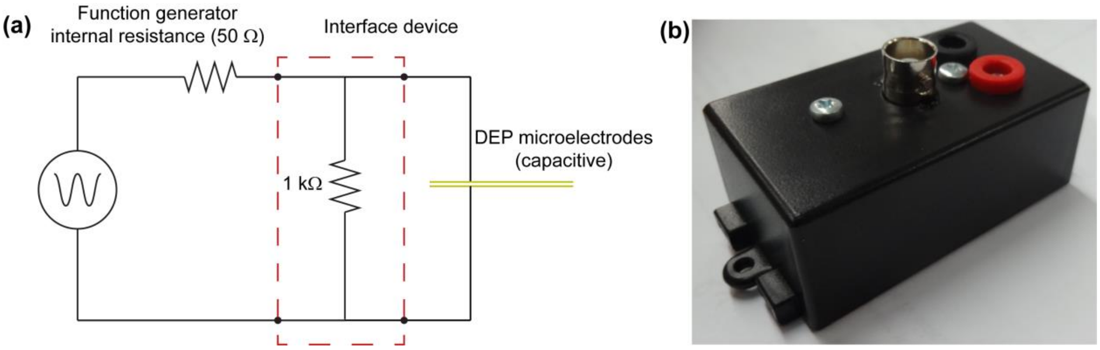

Figure 3.8: Function generator interface device (a) electronic schematic of DEP system (b) photograph of function generator – DEP electrodes interface device.

3.4 Summary

The author presented the fabrication of the experimental platforms used in the research. The fabrication process was described with sufficient details so the procedures could be readily replicated and verified.

In chapter 4 the author will demonstrate the use of this platform for Raman microscopy study of suspended metal oxide and polystyrene particles. Chapters 5 and 6 will demonstrate the use of the platforms with smaller feature dimensions for manipulating silver nanocolloids and cells for surface enhanced Raman scattering

(SERS) applications. Simulations of the devices' performance and operation with the respective suspended materials will be presented in each chapter so as to confirm the required operating parameters of the device.

References

[1] Kayani, A.A., C. Zhang, K. Khoshmanesh, J.L. Campbell, A. Mitchell, and K. Kalantar-zadeh, Novel tuneable optical elements based on nanoparticle suspensions in microfluidics. *Electrophoresis,* vol. 31, pp. 1071-1079, 2010.

[2] Khoshmanesh, K., C. Zhang, F.J. Tovar-Lopez, S. Nahavandi, S. Baratchi, K. Kalantar-zadeh, and A. Mitchell, Dielectrophoretic manipulation and separation of microparticles using curved microelectrodes. *Electrophoresis,* vol. 30, pp. 3707-3717, 2009.

[3] Khoshmanesh, K., C. Zhang, F.J. Tovar-Lopez, S. Nahavandi, S. Baratchi, A. Mitchell, and K. Kalantar-zadeh, Dielectrophoretic-activated cell sorter based on curved microelectrodes. *Microfluidics and Nanofluidics,* vol. 9, pp. 411-426, 2010.

[4] Zhang, C., K. Khoshmanesh, F.J. Tovar-Lopez, A. Mitchell, W. Wlodarski, and K. Kalantar-zadeh, Dielectrophoretic separation of carbon nanotubes and polystyrene microparticles. *Microfluidics and Nanofluidics,* vol. 7, pp. 633-645, 2009.

[5] Bae, S.C., H. Lee, Z. Lin, and S. Granick, Chemical Imaging in a Surface Forces Apparatus: Confocal Raman Spectroscopy of Confined Poly(dimethylsiloxane). *Langmuir,* vol. 21, pp. 5685-5688, 2005.

[6] Bhatt, K.H. and O.D. Velev, Control and Modeling of the Dielectrophoretic Assembly of On-chip Nanoparticle Wires. *Langmuir,* vol. 20, pp. 467-476, 2004.

[7] Fiedler, S., S.G. Shirley, T. Schnelle, and G. Fuhr, Dielectrophoretic Sorting of Particles and Cells in a Microsystem. *Analytical Chemistry,* vol. 70, pp. 1909-1915, 1998.

[8] Lapizco-Encinas, B.H., B.A. Simmons, E.B. Cummings, and Y. Fintschenko, Dielectrophoretic concentration and separation of live and dead bacteria in an array of insulators. *Analytical Chemistry,* vol. 76, pp. 1571-1579, 2004.

[9] Lapizco-Encinas, B.H., B.A. Simmons, E.B. Cummings, and Y. Fintschenko, Insulator-based dielectrophoresis for the selective concentration and separation of live bacteria in water. *Electrophoresis,* vol. 25, pp. 1695-1704, 2004.

[10] Matsue, T., N. Matsumoto, and I. Uchida, Rapid micropatterning of living cells by repulsive dielectrophoretic force. *Electrochimica Acta,* vol. 42, pp. 3251-3256, 1997.

[11] Suzuki, M., T. Yasukawa, Y. Mase, D. Oyamatsu, H. Shiku, and T. Matsue, Dielectrophoretic micropatterning with microparticle monolayers covalently linked to glass surfaces. *Langmuir,* vol. 20, pp. 11005-11011, 2004.

[12] Ziemath, E.C. and M.A. Aegerter, Raman and Infrared Investigations of Glass and Glass-Ceramics with Composition $2Na_2O$-CENTER-DOT-1CaO-CENTER-DOT-$3SiO_2$. *Journal of Materials Research,* vol. 9, pp. 216-225, 1994.

[13] Kumatani, A. and P.A. Warburton, Characterization of the disaggregation

state of single-walled carbon nanotube bundles by dielectrophoresis and Raman spectroscopy. *Applied Physics Letters*, vol. 92, p. 243123, 2008.

[14] Takano, N., L.M. Doeswijk, M.A.F. van den Boogaart, J. Auerswald, H.F. Knapp, O. Dubochet, T. Hessler, and J. Brugger, Fabrication of metallic patterns by microstencil lithography on polymer surfaces suitable as microelectrodes in integrated microfluidic systems. *Journal of Micromechanics and Microengineering*, vol. 16, pp. 1606-1613, 2006.

[15] Krishnamurti, D., The raman spectrum of quartz and its interpretation. *Proceedings Mathematical Sciences,* vol. 47, pp. 276-291, 1958.

[16] Krupke, R., S. Linden, M. Rapp, and F. Hennrich, Thin films of metallic carbon nanotubes prepared by dielectrophoresis. *Advanced Materials,* vol. 18, pp. 1468-1470, 2006.

[17] Wu, M.-H. and G.M. Whitesides, Fabrication of arrays of two-dimensional micropatterns using microspheres as lenses for projection photolithography. *Applied Physics Letters*, vol. 78, pp. 2273-2275, 2001.

[18] Xia, Y. and G.M. Whitesides, Soft Lithography. *Annual Review of Materials Science*, vol. 28, pp. 153-184, 1998.

Chapter 4

Raman microscopy characterisation of dielectrophoretically manipulated nanoparticles

4.1 Introduction

In this chapter, the author will demonstrate the integration of Raman microscopy with the microfluidic-dielectrophoresis (microfluidic-DEP) device that was fabricated in the previous chapter. This novel integrated system will be efficiently used for the monitoring of suspended particles type and the direct mapping of their spatial concentrations. Nanoparticles of tungsten trioxide (WO_3) and polystyrene are used in the investigations, as they are Raman active and can be homogenously suspended in water. The microfluidic-DEP platform, consisting of curved microelectrodes, was fabricated as described in chapter 3. The outcome of this work was published as a full article in the journal of Lab-on-a-Chip [1].

The investigation of suspended micro and nanoparticles' properties is of utmost importance for the understanding and determination of their optical, electronic, mechanical and chemical behaviours. The investigation of particles in microfluidics has been carried out using a variety of methods such as resonant light scattering (RLS) [2], confocal microscopy combined with charged coupled device (CCD) cameras with or without fluorescent particles [3, 4] and PIN-based photo detectors [5]. However, the capability of these methods for simultaneous *in situ* measurements of both concentration and type of the suspended particles is limited. Even fluorescence microscopy, which is the most investigated method in dealing with such particles, has certain limitations as its capability is restricted to only fluorescent active materials, or fluorescent tagging. As an alternative, Raman spectroscopy allows such assessments and can be used for the pattern (“fingerprint”) acquisition of Raman active particle suspensions [6]. Its integration with microfluidics permits the mapping of both the concentration and type of micro and nanoparticles. Additionally, the intensity of Raman peaks is a function of particle concentration and the peak positions identify the material type.

There are reports on Raman-microfluidic devices which focus on the development of basic microfluidics, and lack effective methods for the manipulation of suspended nanoparticles [6-13]. However, some research is being conducted, such as that by *Tong et al.* [14] who demonstrated the use of optical tweezers to alter the concentration of colloids and study the effect on SERS signals. However, optical tweezing interferes with the collection of Raman measurements, which could potentially deteriorate the performance of their system. Moreover, optical tweezing requires significant optical intensity, which is unsuitable for constituents at the micron scale or larger. In addition, the application of laminar flow, as suggested by Keir *et al.* [15], does not provide an effective means for the real time manipulation of suspended nanoparticles. A potential solution is the application of DEP.

Dielectrophoretic manipulations have been widely applied to nano, meso and micro scale particles in microfluidics [16]. By changing the applied voltage and frequency, particles can be focused to, or repelled from pre-determined locations within the microchannel. Such a capability provides a perfect base for the demonstration of microfluidics and Raman spectroscopy as a tool for the mapping, recognizing and measuring of particles. The integration of microfluidics and DEP has been the key in the development of many new and exciting micro-platforms. These platforms have been used in applications such as particle counting [3, 17], particle sorting of both organic [18-23] and inorganic [16, 24] particles, opto-fluidics [25, 26] and for the creation of electronic devices [27, 28]. Systems involving DEP and optical measurements incorporate fluorescent particles into the solution, and measure the florescence intensity using a CCD module [3]. However, to date there are no reports on the integration of DEP and Raman systems for the *in situ* analysis of suspended particles.

In this chapter, the author will demonstrate that by integrating Raman spectroscopy with a microfluidic system, the resultant system can be used to map the concentration and type of suspended nanoparticles within the microchannel. To show the functionality of this system, DEP will be used for manipulating the nanoparticles, producing regions of high and low particle concentrations within the microchannel. It will be shown that the integration of DEP and Raman spectroscopy can be a powerful tool for *in situ* analysis of suspended inorganic (WO_3) and organic (polystyrene) particles.

4.2 Principals of performance and design

For accurate performance analysis of the microfluidic system, the author has conducted thorough DEP simulations in order to identify the most effective DEP settings for the investigation, and help to explain the particle behaviour inside the microchannel. The dielectrophoretic force experience by a spherical particle is [29, 30]:

$$\vec{F}_{DEP} = 2\pi r^3 \varepsilon_0 \varepsilon_{medium} \operatorname{Re}\left[f_{CM}(\omega)\right] \nabla E_{rms}^2 \tag{4.1}$$

where ε_o is the permittivity of free space, ε_{medium} is the relative permittivity of the suspending medium, r is the radius of particles, Re[f_{CM}] is the real part of the Clausius-Mossotti (CM) factor, ω is the angular frequency of the applied signal, and E_{rms} is the root-mean-square value of the induced electric field. The CM factor, which determines the relative polarisability of the particle with respect to the suspending medium, is defined for spherical particles as [30]:

$$f_{CM}(\omega) = \frac{\varepsilon^*_{particle} - \varepsilon^*_{medium}}{\varepsilon^*_{particle} + 2\varepsilon^*_{medium}} \tag{4.2}$$

where, $\varepsilon_{particle}{}^*$ and $\varepsilon_{medium}{}^*$ are the complex permittivities of the particle and the suspending medium, respectively, each defined as:

$$\varepsilon^* = \varepsilon - \frac{i\sigma}{\omega} \tag{4.3}$$

where, ε^* is the complex permittivity, ε is the relative permittivity, σ is the conductivity of the particle/medium and ω is the applied electric field frequency. Depending on the polarity of the f_{CM}, a particle experiences positive or negative dielectrophoretic forces, and consequently is pushed towards or away from the regions of high electric field strength [29]. Further simulations and details of the particle behaviour at different DEP frequencies are presented in the “Numerical analysis of the DEP system” section of this chapter.

The microfluidic channel was a simple rectangular structure, which was formed from poly-dimethylsiloxane (PDMS), and was 1200 µm long, 300 µm wide and 80 µm deep. Raman spectroscopy systems need to have unhindered access to the suspended materials. This is best achieved by operating the microfluidic device in an inverted fashion, where the Raman systems can take measurements of the materials through the quartz substrate without interference from the PDMS microchannel structure (Figure 4.1 and Figure 4.2(a)).

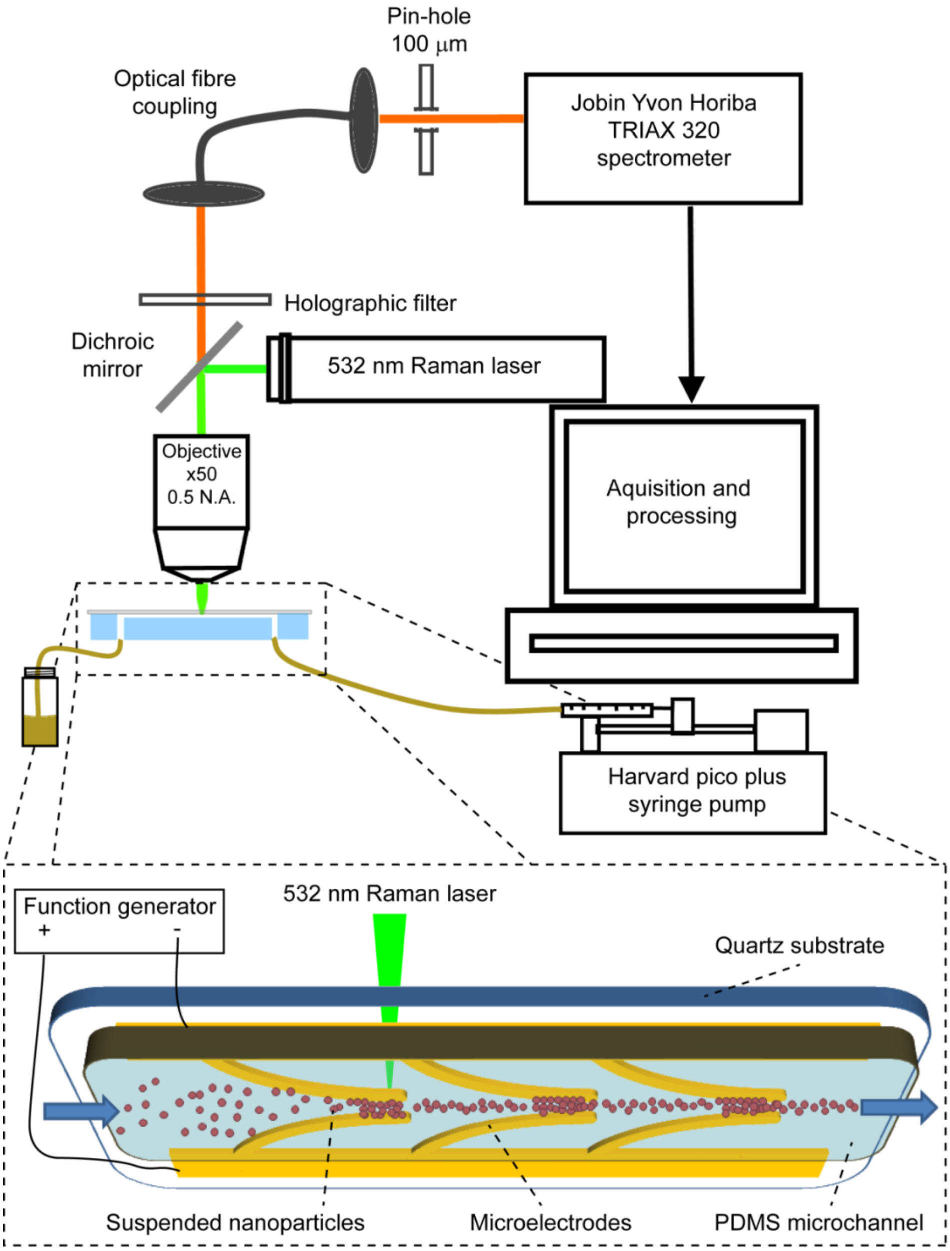

Figure 4.1: Schematic of Raman-microfluidic testing setup. Insert: demonstrating how the measurements are performed through the quartz substrate.

In these experiments curved DEP electrodes are used (Figure 4.1 and Figure 4.2). This particular design allows control of both hydrodynamic and dielectrophoretic forces to create a highly focused stream of particles in the microchannel [16, 20, 26, 31]. This is especially important as curved electrodes provide controlled and repeatable areas of high and low particle concentration, without producing turbulent flows near the electrode tips. This is necessary for the successful demonstration of *in situ* Raman spectroscopy. The platform contains 40 electrode pairs spanning the entire length of the microfluidic channel with individual dimensions detailed in Figure 4.2(b).

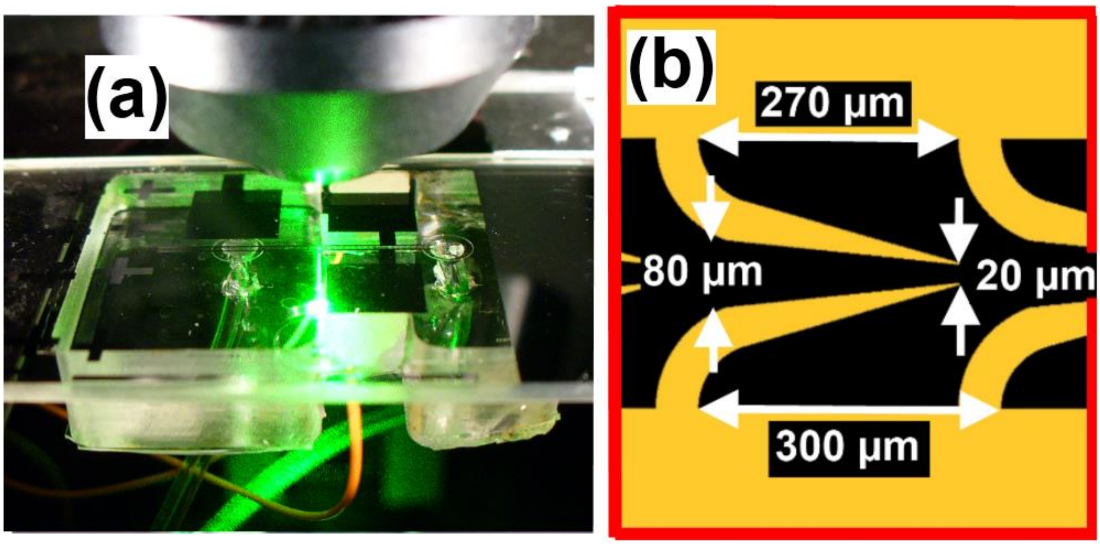

Figure 4.2: (a) Photo of complete DEP-Raman system under test (b) Curved DEP electrode design and layout.

4.3 Numerical analysis of the DEP system

Simulations were performed to determine the DEP forces on the particles, and at what frequency the DEP forces change from positive to negative. Simulations of this nature allow the determination of suitable electric field frequency settings for use during the experiments, which are designed around the crossover frequency. For these simulations the CM factor (equation (4.2)) was simulated over a range of applied electric field frequencies using MATLAB (MathWorks 2008b).

CM factor simulations require knowledge of the particle and medium permittivity parameters. As such, the suspending medium was measured to have a conductivity of 0.01 S.m^{-1} after the addition of X-305 surfactant to DI water, and a relative permittivity of 78. The conductivity of particles was governed by the total surface conductance composed of the contributions of the Stern layer and diffuse layer formed around the particles [32], and calculated as [30]:

$$\sigma_{particle} = \sigma_{particle-Bulk} + \frac{2K_{Surface}}{r} \tag{4.4}$$

where $K_{surface}$ is 10 and 27.5 pS·m^{-1} for WO_3 and polystyrene, respectively, assuming the surface conductance for WO_3 is similar to that of polystyrene [33, 34]. The bulk conductivities σ_p of WO_3 and polystyrene are 100 mS·m^{-1} and 19.8 mS·m^{-1} respectively [35, 36]. Using equation (4.4), the conductivity of particles were obtained as 100.5 and 20.3 mS·m^{-1} for WO_3 and polystyrene particles respectively. The permittivity of particles was also taken as 39 and 2.5 [37] respectively for WO_3 and polystyrene particles. Using the above values, the Re[f_{CM}] for polystyrene and WO_3 particles (equation (4.2)) were calculated over a range of frequencies and plotted (Figure 4.3). According to Figure 4.3, the polystyrene and WO_3 particles demonstrate crossover frequencies of 3.4 and 22.3 MHz, respectively, below which they show positive dielectrophoretic response.

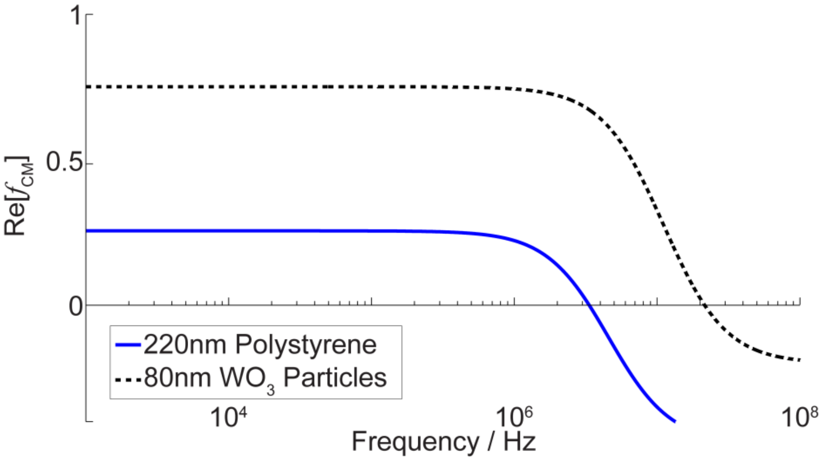

Figure 4.3: The variation of Re[f_{CM}] for polystyrene and tungsten trioxide particles at a medium conductivity of 0.01 S·m^{-1} within the frequency range of 1 kHz – 25 MHz.

In order to analyse the performance of the system, the dielectrophoretic force was simulated using the Fluent 6.3.26 software package (Fluent, Lebanon, NH, USA), as detailed in [31]. Dr. Khashayar Khoshmanesh from RMIT's School of Electrical and Computer Engineering assisted the author with performing the simulations.

Mesh generation for these simulations was conducted using Gambit 2.3.16 software (Fluent, Lebanon, NH, USA). A total number of 27,500 elements were generated on the quartz substrate for the 20 µm spaced microelectrodes. This included a combination of unstructured triangular elements covering the substrate, with smaller quadrilateral elements surrounding the boundaries of the microelectrodes, and additional unstructured triangular elements inside the microelectrode structures, as shown in Figure 4.4. The density of the mesh elements was chosen so as to provide highly accurate predictions of the behaviour at the microelectrode interface, and more specifically the behaviour at the microelectrode tip regions.

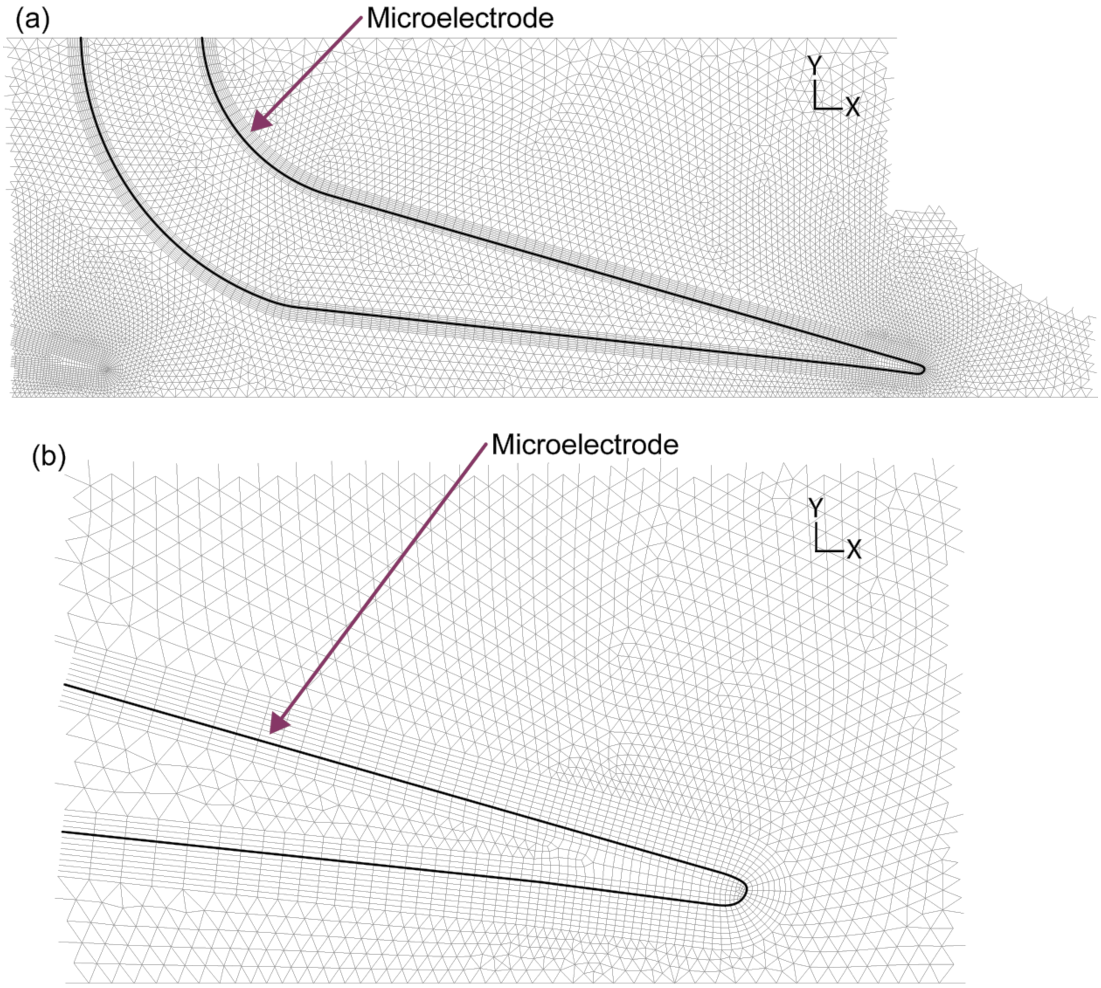

Figure 4.4: Images of the mesh used for the simulation of electric field and dielectrophoretic force (a) 2D overview of microelectrode mesh (b) close up of microelectrode tip, showing the distribution of the mesh at the microelectrode tip region.

Unstructured quadrilateral mesh elements were also projected along the height of the microchannel as shown in Figure 4.5. In doing so, the height of the channel was divided into 40 elements. The density of the quadrilateral elements was increased at areas around the microelectrode edges, where we expect the highest electric field gradients to be present. As presented in Figure 3.1 of chapter 3, the microelectrode array was constructed of multiple electrode pairs. As each microelectrode pair is identical, the simulations were shortened to study just a single electrode pair. This is also practical from a Raman microscopy perspective, as the Raman system can only be utilized to target the area around a single electrode pair at any one time. Additionally, only one electrode finger was simulated, as the other electrode finger is essentially a mirror image. These simplifications reduced the number of elements, and hence significantly reduced computational time.

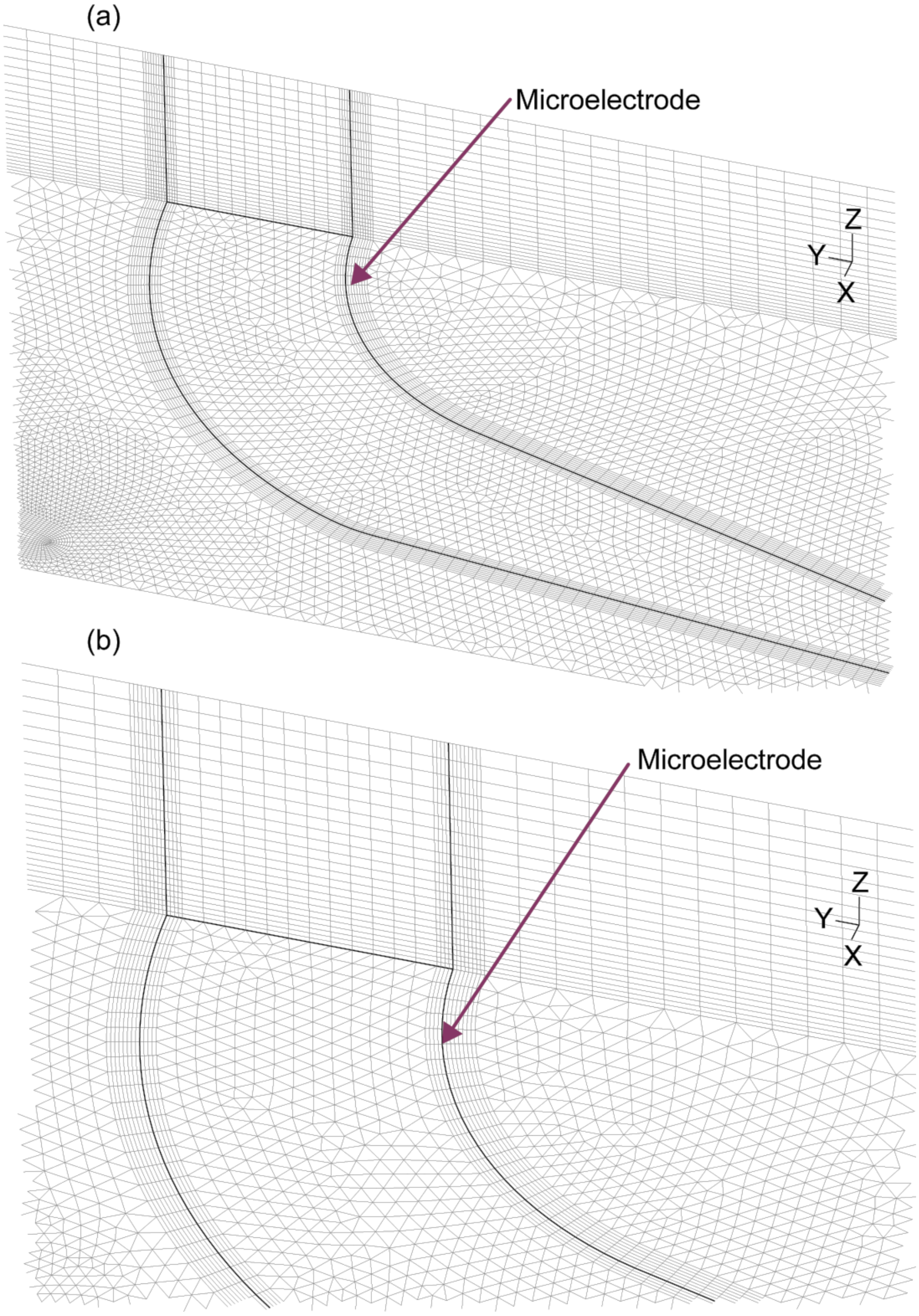

Figure 4.5: 3D images of the microelectrode simulation mesh (a) image depicting the microelectrode and side wall simulation mesh (b) close up of the corner of the microchannel showing how the mesh elements proceed along the z-axis of the microchannel.

In order to obtain the electric field strength, E_{rms}, it is assumed that the permittivity of the medium is homogenous, and hence solved the Laplace equation to acquire the scalar electric potential field, φ:

$$\nabla\varphi_{rms}^{2} = 0 \tag{4.5}$$

In doing so, electric potential boundary condition was applied at the microelectrodes, while zero electrical flux was applied to the other surfaces of the system, including the bottom, top and side walls as well as inlet and outlet of the channel. Next, the electric potential was differentiated to obtain the electric field, E:

$$E_{rms} = -\nabla\varphi_{rms} \tag{4.6}$$

The finite volume-based Fluent 6.3.26 software package (Fluent Inc, Lebanon, USA) was used as the solver. This software provides full control over the size and density of elements, enabling the 3D simulation of microfluidic systems. The results were calculated through several iterations until the difference in electric fields obtained from the previous iteration was less than 10^{-4} V·m^{-1}. Consequently, the values obtained for E_{rms} are used to calculate E_{rms}^{2} and ∇E_{rms}^{2}, and are substituted into the DEP force equation to obtain the DEP force magnitudes at locations around the microelectrodes. Taking advantage of the user defined scalar (UDS) modules of the Fluent software package, the author was able to readily substitute in the values of ∇E_{rms}^{2} into the DEP force equation at locations around the electrodes.

When a 15 V sinusoidal voltage at a frequency of 10 MHz is applied to the larger microelectrode pairs, the resultant electric field reaches a maximum value of 2.8×10^{6} V·m^{-1} at the tips, where the gap between the opposite microelectrodes is 20 μm and the width of microelectrodes is reduced to 5 μm (Figure 4.6(a)). At low frequencies, the particles exhibit a positive DEP response (Figure 4.3) as seen from the CM factor calculation, and are therefore driven towards the microelectrodes, provided that the dielectrophoretic force is strong enough to overcome the sedimentation force, F_{Grav}, as the microfluidic channel system is operated in an inverted mode. The density of particles between the microelectrodes is proportional to the magnitude of $F_{DEP} - F_{Grav}$ (Figure 4.6(b)). F_{DEP} is proportional to E^{2}, as previously calculated, and therefore the $F_{DEP} - F_{Grav}$ increases along the microelectrodes until reaching a peak at the tips. As such, the distribution of F_{DEP}–F_{Grav} applied on tungsten trioxide (WO_3) and polystyrene particles at 15 V and 10 MHz is shown at a plane 10 μm from the quartz substrate (Figure 4.6(b)). The WO_3 particles experienced a maximum force of 2×10^{-15} N at the tips of the electrodes, while the polystyrene particles experienced a maximum force of 2.4×10^{-14} N due to their larger dimensions.

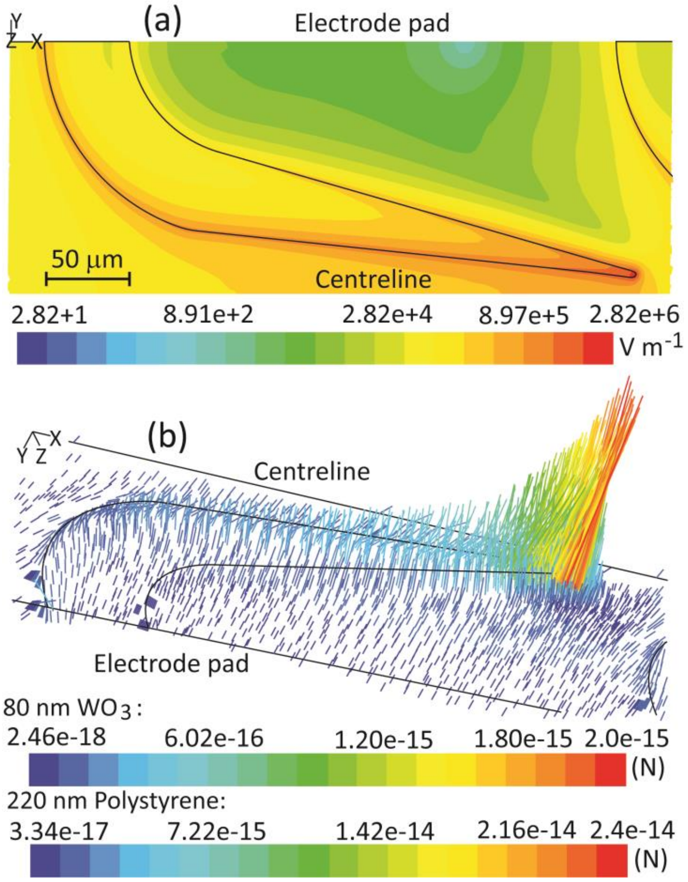

Figure 4.6: (a) The contours of electric field ($V\cdot m^{-1}$) at 15 V, and z=0 μm (surface of quartz substrate) (b) The vectors of $F_{DEP} - F_{Grav}$ (N) applied on WO_3 and polystyrene particles at 15 V and 10 MHz, and z=10 μm with respect to the surface of quartz substrate. Vectors are pseudo-coloured and lengthened according to the magnitude of $F_{DEP} - F_{Grav}$ force (N).

The sedimentation force, which pushes the particles downward, is calculated using equation (4.7), where ρ is the density (particle $\rho_{particle}$ and medium ρ_{medium}), r is the radius of the particle and g_z is the gravitational acceleration:

$$\vec{F}_{Grav} = \frac{4}{3}\pi r^3 (\rho_{particle} - \rho_{medium})\,\vec{g}_z \tag{4.7}$$

4.4 Materials and methods

Initially, silicon nanoparticle suspensions were used inside the microfluidic device. Silicon has an excellent Raman response, with a prominent peak at 520 cm^{-1} and is often used to calibrate Raman systems [38]. However, silicon nanoparticles were electro-statically attracted to the PDMS channel wall, and caused an undesirable memory-effect for the Raman signal [39]. Nanoparticles of zinc oxide (ZnO) and molybdenum trioxide (MoO_3) were also examined, however, these particles showed severe aggregation, despite trying a range of surfactants.

The DEP-microfluidic chip was trialled with well suspended and controlled WO_3 nanoparticles (diameter ~80 nm, 99%, Sigma Aldrich). WO_3 has been studied using Raman spectroscopy in the past [40] and is known to produce several strong peaks. Additionally, polystyrene nanoparticles (diameter ~220 nm, 90%, Bangs Laboratories Inc.) were also investigated, which were pre-suspended in DI water combined with SDS (sodium dodecyl sulfate) surfactant (0.1%) and are surface functionalised with –COOH groups. The particles were suspended in DI water, while Triton X-305 surfactant was also added to improve the homogeneous distribution of particles within the mixture. The mixtures were prepared at concentrations of 6.5 %*w/w* and 1.5 %*w/w* for WO_3 and polystyrene, respectively.

Samples of the particle mixtures were placed on glass slides and dehydrated. The samples were then viewed under a FEI Nova Nano SEM (scanning electron microscope). The SEM images help to provide confirmation of the particles configurations and dimensions (Figure 4.7).

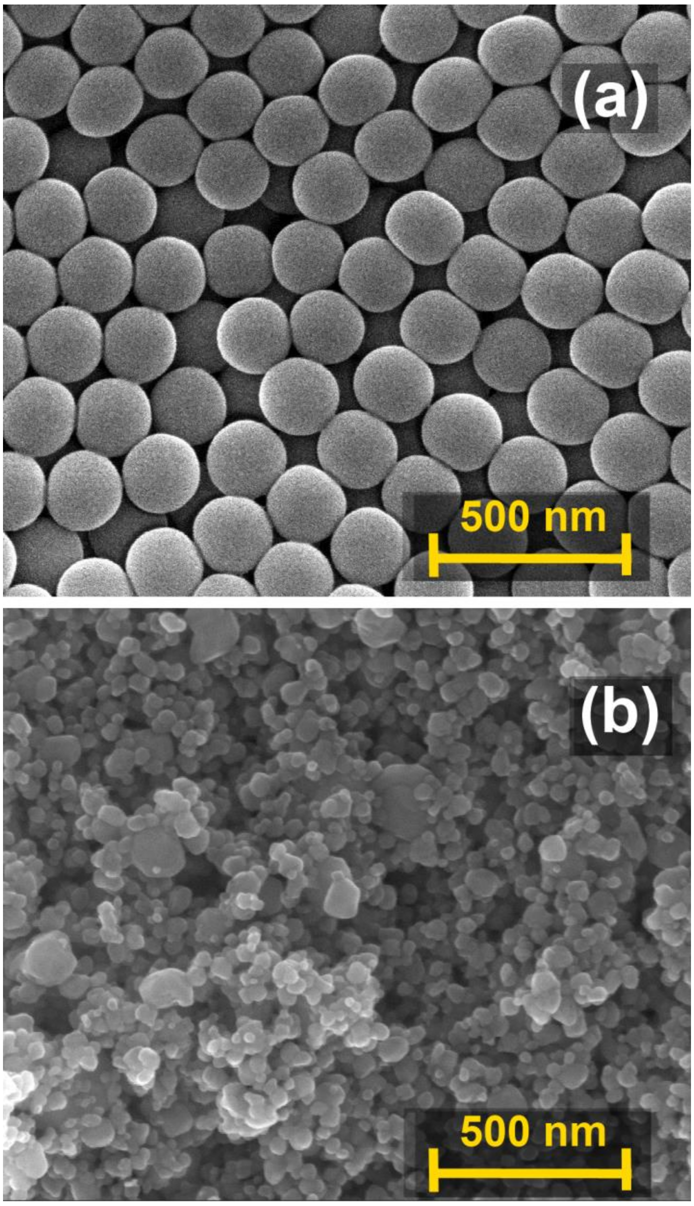

Figure 4.7: (a) SEM images of polystyrene nanoparticles. (b) SEM image of WO_3 nanoparticles.

Combined Raman spectroscopy and DEP were used for analysing the mixtures. The investigations were conducted at different electric field frequencies and at different positions within the microchannel. During these experiments, the flow rate was kept constant at 4 $\mu L \cdot min^{-1}$ using a syringe pump (Harvard Apparatus pico plus). The magnitude of the applied voltage was also held constant throughout each experiment at 15 V using a programmable function generator (Tabor Electronics 8200).

An Olympus BX41 confocal microscope, equipped with a Jobin Yvon Horiba TRIAX320 spectrometer and a thermoelectrically cooled CCD detector, was utilised to collect the Raman spectra. The system includes a white light source for the back lit upright microscope and a 532 nm laser source (rated power 1.1 mW) as the Raman excitation laser. The microscope objective was a ×50 with a numerical aperture of 0.5. This lens produced an excitation spot approximately 0.65 μm in diameter with a depth of field approximately 8 μm. All Raman spectra in this report were captured using a 20 second integration time with an average of 3 integrations, while the pinhole of the microscope was set to 100 μm (unless otherwise stated).

Raman spectra were captured under three different sets of conditions:

i. The frequency of the applied DEP field was varied, while focusing the Raman microscope focal point onto a constant position within the particle stream.
ii. The vertical location of the Raman microscope lens focal point was changed in depth (by moving the substrate vertically), while applying a fixed dielectrophoretic force.
iii. The Raman spectra were captured at several different locations around the electrodes, while applying a constant voltage and frequency.

4.5 Results and discussions

4.5.1 Inverted microscope analysis of DEP platform

Figure 4.8 depicts the suspended WO_3 nanoparticles at different applied DEP frequencies. Using DEP, it was possible to produce areas of high and low concentrations of particles within the microfluidics. This effect can be clearly seen in the optical images (Figure 4.8). The response of the particles relative to the frequency of the applied electric field was predicted using equation (4.1), assisting us in determining the DEP crossover frequencies for Raman studies. The frequency of the applied field was varied from 20 MHz to 100 kHz in order to observe changes in the Raman spectra of the particles.

At no applied signal, a uniform particle distribution was observed in the microchannel (Figure 4.8(a)). At 20 MHz, the WO_3 particles experienced weak DEP forces, and became trapped between the electrode tips. However, the DEP force was not strong enough to hold the particles against the drag force. As a result, most of the trapped particles were washed away, forming a wide stream of particles along the centre-line (Figure 4.8(b)). At 10 MHz, the DEP force became stronger and more particles were trapped. It not only extended the effective trapping region of the electrodes but also narrowed the dark particle stream along the centre-line (Figure 4.8(c)). At frequencies below 10 MHz (Figure 4.8(d)-(f)) the particle stream continued to form along the centre-line. However, as the DEP frequency was reduced further, the particle stream started to disperse as it approached the next electrode pair. This is because at low frequencies the DEP force is intensified, pushing more particles towards the electrodes. However, the particles did not have sufficient time to come to rest between the electrodes due to the high flow rate of the medium.

The behaviour of the WO_3 mixture closely follows the predicted behaviour, based on the calculated values of f_{CM}. The predicted crossover frequency of 22 MHz is very close to the observed DEP crossover at 20 MHz, which shows a weak stream of particles along the centre-line. Further, the relationship between the observed behaviour of WO_3 nanoparticles exposed to a DEP force at 10 MHz DEP is very consistent with the prediction from the simulations (Figure 4.6). Both the simulation and the Raman spectroscopy results are in good agreement with one another, confirming the validity of the approach and correct operation of the microfluidic device.

Figure 4.8 (g) depicts the polystyrene mixture in the no DEP voltage condition, in which particles were evenly distributed. Alternatively, Figure 4.8 (h) depicts the polystyrene nanoparticle mixture when exposed to a DEP voltage of 15 V at 500 kHz. A clear narrow band in the middle cannot be observed; however, the region between the electrodes exhibits diffraction due to the local ordering of the polystyrene particles. The refractive index of polystyrene is ~1.58, which is much closer to that of water ~1.33 in comparison to WO_3 (~2.3) [41, 42]. The smaller refractive index difference between the polystyrene nanoparticles and water makes it difficult to see any narrowband formed, hence only the two extreme cases (no DEP and strong trapping DEP force at 500 kHz) are shown.

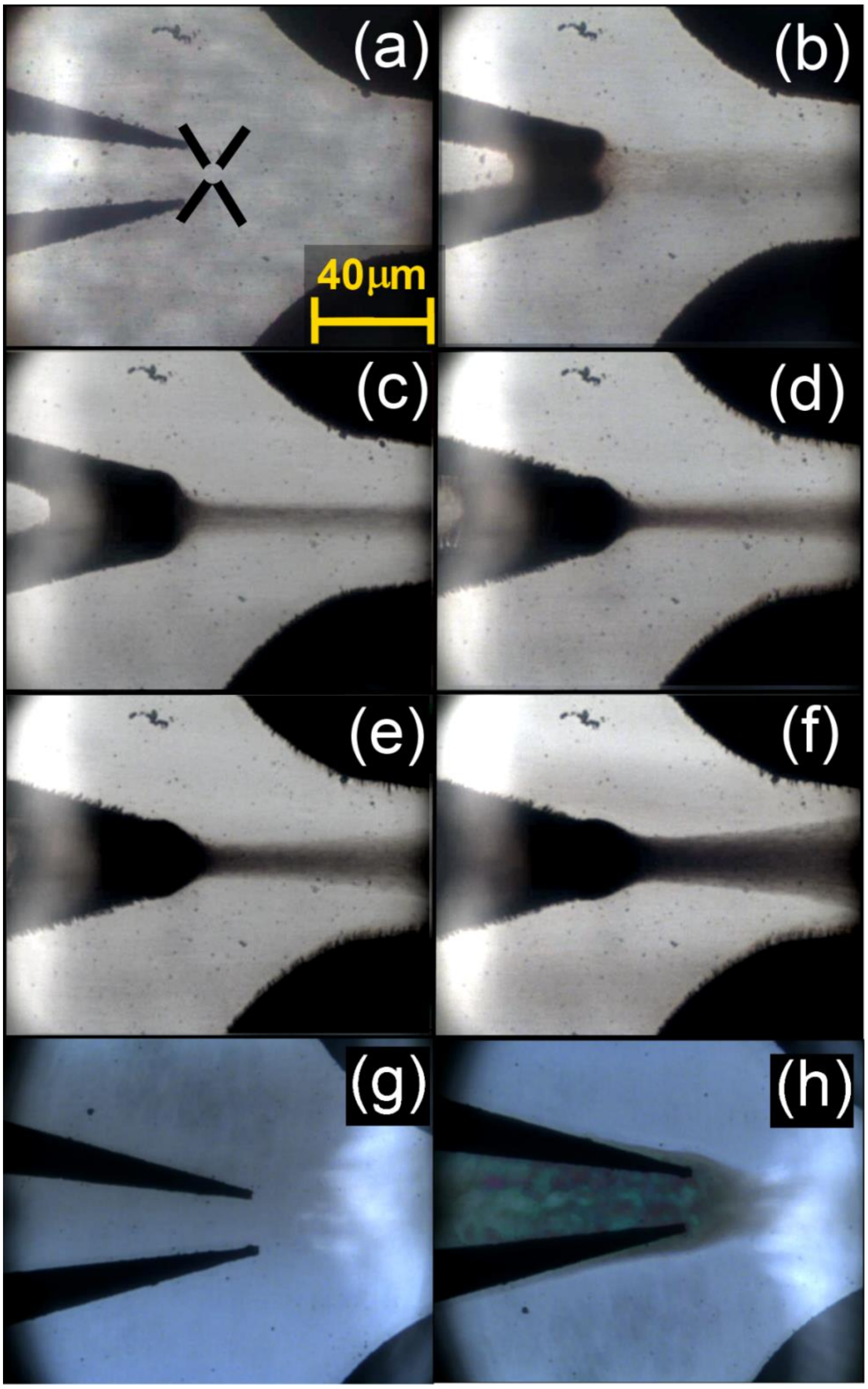

Figure 4.8: Inverted microscope images of DEP system with WO_3 nanoparticles at the following frequencies: (a) No-DEP voltage (b) 20 MHz (c) 10 MHz (d) 1 MHz (e) 750 kHz (f) 250 kHz; Inverted microscope images of DEP system with polystyrene nanoparticles at the following frequencies: (g) No-DEP voltage (a) 500 kHz.

4.5.2 Raman microscopic analysis at differing DEP settings

The focal point of the Raman microscope lens was placed immediately after the two electrode tips (as shown in Figure 4.8(a)) and Raman spectra of suspended WO_3 (Figure 4.9) and polystyrene (Figure 4.10) were collected. The measurements were conducted when the electrodes were in optical focus, the condition which will be refer to as the “top surface of the microchannel” in the rest of this chapter.

WO_3 exhibits two strong Raman peaks at 707 and 798 cm^{-1}, caused by the ν(O-W-O) stretching modes [43]. Peaks between 400 and 600 cm^{-1} are due to the δ(O-W-O) deformation modes, while any Raman peaks occurring below 400 cm^{-1} are WO_3 lattice modes. The most prominent peak of polystyrene exists at 993 cm^{-1}, which corresponds to the polystyrene $\nu 1$ ring-breathing mode [44].

The WO_3 nanoparticles behaved in a predicable fashion; at lower DEP frequencies the concentration of the particle stream increases while the applied voltage frequency is reduced (as observed in Figure 4.8). This trend is reflected in the Raman spectra taken in Figure 4.9, which show greater intensity counts for lower DEP frequencies. The Raman intensity observed for the no DEP and 20 MHz conditions were almost identical in magnitude, due to the low concentration of the particle streams in both cases.

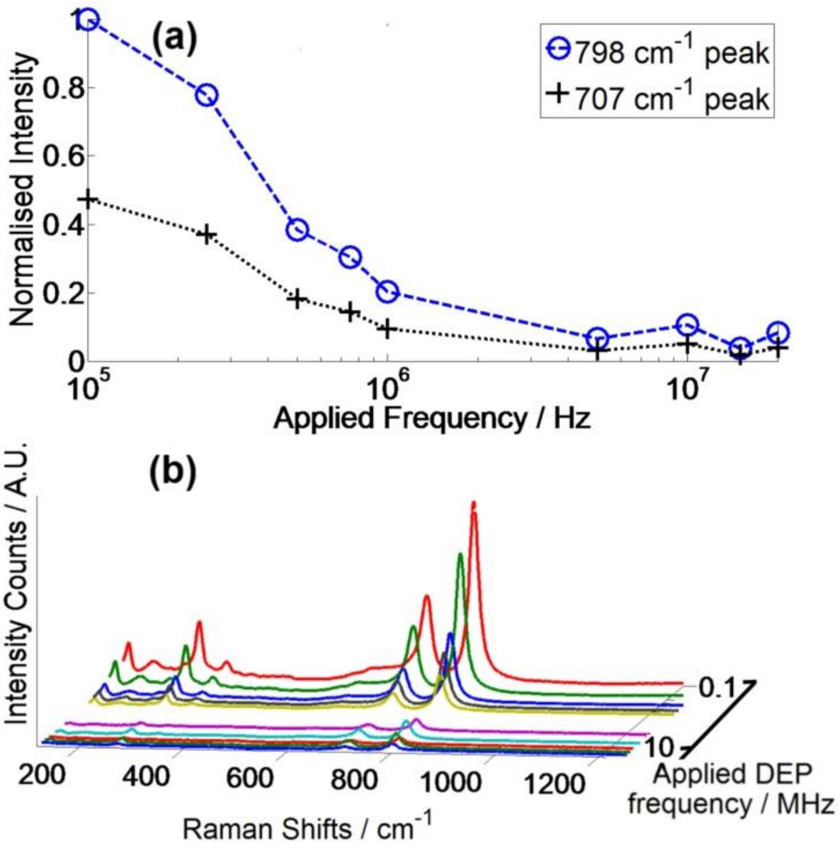

Figure 4.9: (a) Plot of normalised WO_3 nanoparticle Raman peak intensity *vs.* the applied DEP frequency (b) Plot of WO_3 nanoparticle Raman spectra at different DEP frequencies, decreasing in frequency along the z-axis.

Polystyrene particles have distinct Raman peaks in the dehydrated state, when particles concentrations are high [44]. However once the particles were diluted to 1.5 %*w/w*, and no DEP voltage was applied, the Raman peaks became indistinguishable from the background noise (Figure 4.10). Alternatively, when a DEP voltage of 15 V is applied, at frequencies as low as 500 kHz the Raman peaks of polystyrene were present. No significant difference was observed in the polystyrene nanoparticle Raman spectra when frequencies other than 500 kHz were applied. The observation of Raman signals, even small in magnitude, is an important outcome. Although the narrow band of polystyrene particles could be hardly visually resolved using the optical microscope, the presence of a Raman signal indicates their presence.

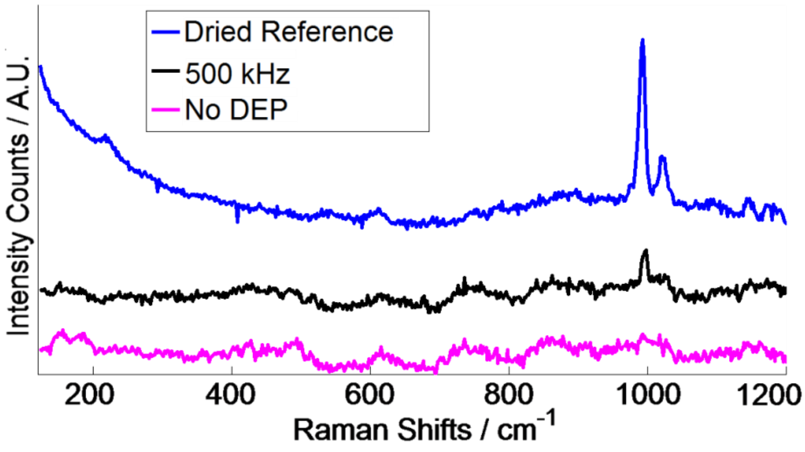

Figure 4.10: Plot of polystyrene Raman spectra under various conditions (see legend).

4.5.3 Raman response at varying depths

To investigate the behaviour of particles, and possibly their concentrations, along the depth of the microchannel, the DEP force was held constant by applying an AC signal of 15 V and 500 kHz. This frequency was chosen as it provides the greatest DEP force on the particles. The Raman microscope objective was then focused at different depths within the microchannel.

The possible drawback to this Raman depth profiling method can be excessive laser light scattering. As the Raman microscope focal point is placed deeper into the particle stream, the Raman signals are scattered off more particles. This possibly produces false reduction in the Raman signal intensity.

Figure 4.11(a) shows that the Raman spectra from the WO_3 particles decrease as the Raman laser is focused deeper into the microchannel. Figure 4.11(b) presents this relationship for both the 798 and 707 cm^{-1} peaks *vs.* depth. This demonstrates that the DEP force is large enough to overcome the sedimentation force and to push the particles towards the electrodes patterned on the top surface.

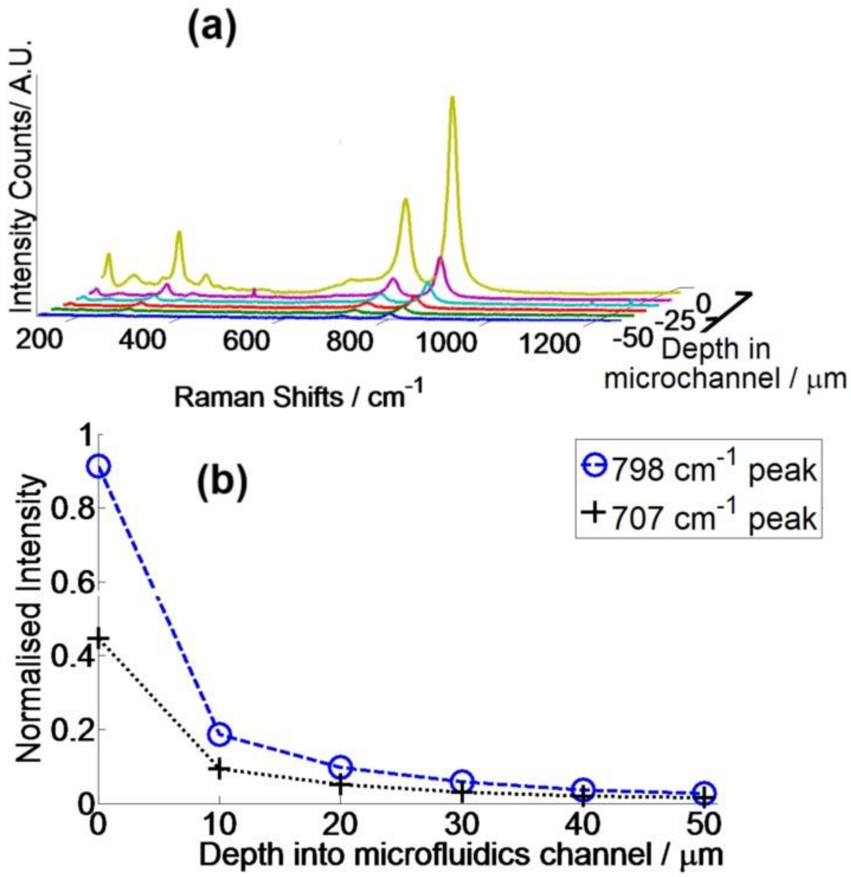

Figure 4.11: (a) Plot of WO_3-polystyrene normalised Raman peak intensity *vs* depth within the microfluidics channel (b) Plot of WO_3-polystyrene Raman spectra at varying depths within the microchannel, with a constant DEP force being applied. The closest plot represents the spectra 50 μm deep into the channel; the furthest plot represents the spectra at the top surface of the channel.

4.5.4 Lateral Raman response mapping

Raman spectra were captured from the top surface of the microchannel at varying lateral positions (Figure 4.12(a) – (b)). This allows for a deeper understanding of the particles distribution around the electrodes, while experiencing positive DEP forces, held constant by applying an AC signal of 15 V and 500 kHz. In order to quantify the concentration of particles using the Raman pattern peaks, all volume fractions were calculated in % and normalised against the zero DEP field Raman measurement, which corresponds to the 6.5 %*w/w*. The author used the intensity of the 6.5 %*w/w* WO_3 peak at 798 cm^{-1} as the reference to estimate the local concentration of particles at other lateral positions. Assuming that the WO_3 concentration increases linearly with the increase of the Raman peak intensity [6, 12, 45-47], and that at zero peak intensity there were no particles present, the author calculated the local volume fractions of WO_3 at the individual positions depicted in Figure 4.12. The calculated concentration values can be seen in Table 4.1.

Table 4.1: Particle concentration at the locations in Figure 4.12 (a).

Position of focal point	Concentration % *w/w* [a]	Concentration % *v/v* [b]
No DEP	6.5	0.91
A	5.7	0.80
B	85.2	11.9
C	6.5	0.91
D	5.9	0.82
E	23.5	3.28
F	5.9	0.82
G	6.0	0.84
H	7.8	1.09
I	10.3	1.44
J	5.9	0.82
K	5.6	0.78

[a] Calculated from data in Figure 4.12 (b).

[b] Calculated using a density of 7.16 $g \cdot ml^{-1}$ as per Sigma Aldrich WO_3 datasheet.

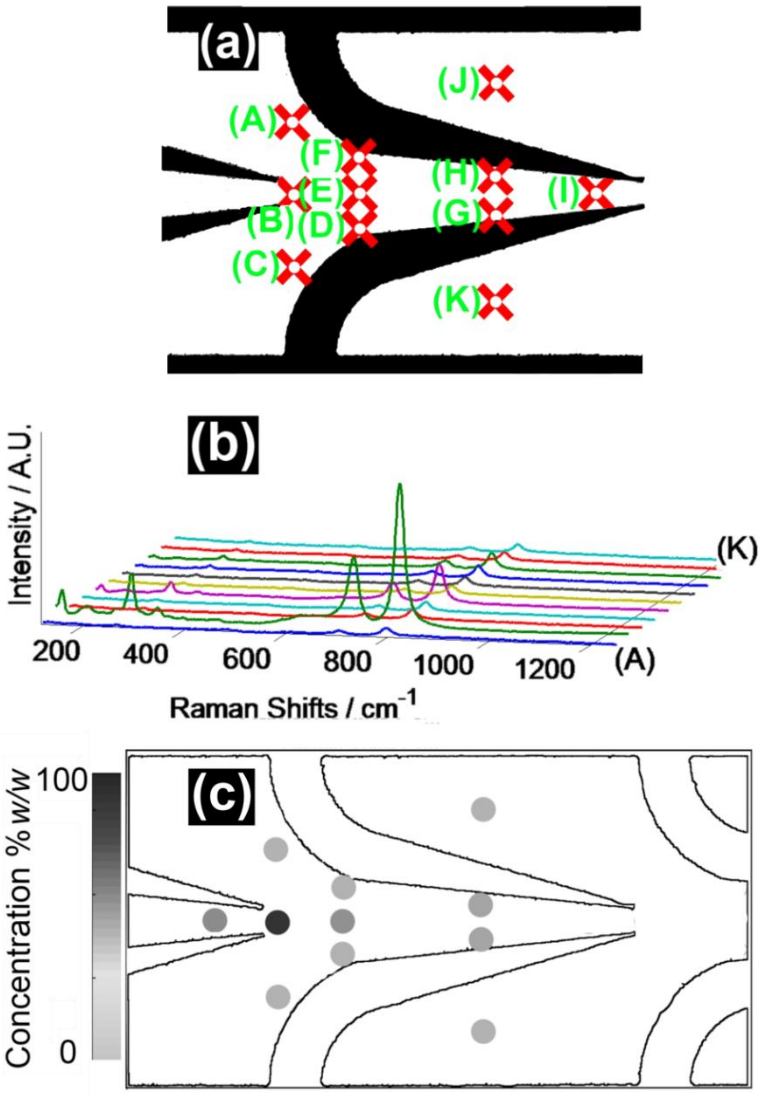

Figure 4.12: (a) Locations of Raman measurements (b) Results of Raman spectroscopy at the varying locations (A – K) (c) Overlay of local concentration values with grey-scale background, values based on Raman spectra intensity.

Figure 4.12(c) shows a grey-scale overlay depicting the measured levels of concentration. Interestingly, the figure indicates that the highest concentration of WO_3 nanoparticles can be found just after the tip of the electrode, at the beginning of the particle stream. These results illustrate the advantage of the Raman measurement, as this could not be discerned from the optical image (Figure 4.8(d)). This platform would be even more useful when dealing with completely transparent and non-transparent nanoparticle suspensions, where visual microscopy is impractical. From the figure, there is no optical contrast on the sides of the narrowband (Figure 4.8(d)), although the presence of particles is evidently confirmed by Raman patterns.

4.5.5 Raman peak intensity concentration relationship for suspended WO_3

In order to properly calibrate and understand the relationship between Raman peaks intensities and solution concentrations, several standard mixtures of different concentrations were prepared. To mimic the measurement flow conditions, these mixtures were then passed through the device at a flow rate of 4 µl·min^{-1}, while applying no electric field. Raman spectra for each mixture were taken from the “top surface of the microchannel”, and the Raman peaks of 798 cm^{-1} were plotted against the mixture concentration measured using DEP trapping.

Figure 4.13 shows the two plots correlate well for measurements up to 14 %*w/w*. However, at higher concentrations, the DEP focused nanoparticle intensity is almost doubled compared to the highest possible measured concentration in zero electric field condition. This suggests that Raman can reliably measure below 14 %w/w concentrations, although above this concentration the readings can be affected by sedimentation, permittivity and electric field issues.

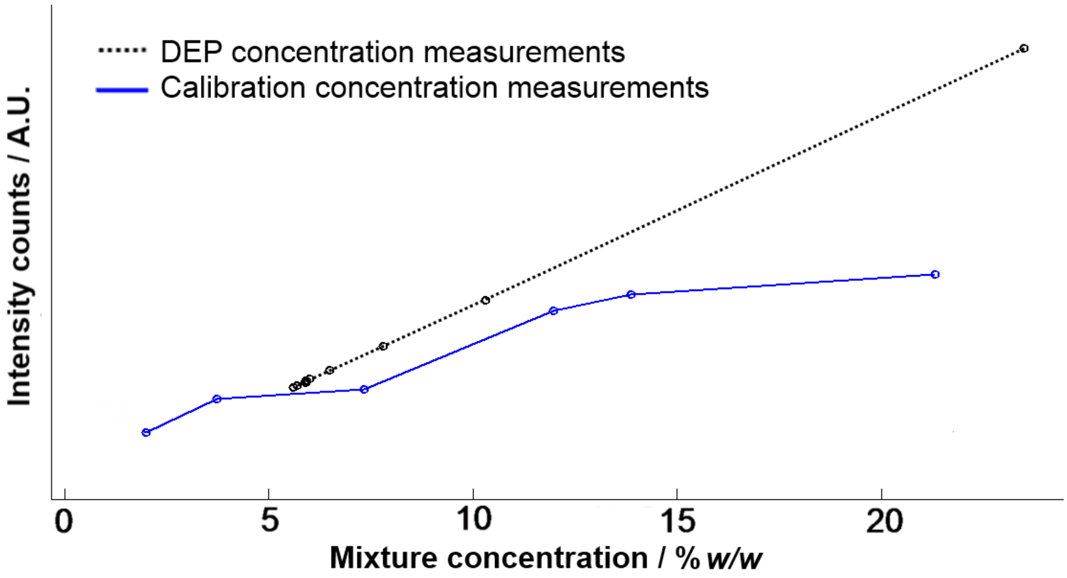

Figure 4.13: Relative intensity of the Raman band 798 cm^{-1} for WO_3 nanoparticles at various mixture concentration levels.

4.5.5.1 Permittivity of the media with suspended WO_3

It is possible that at high particle volume fractions, the effective dielectric constant of the medium is altered by the particles. At high volume fractions, the complex permittivity equation can be approximated using [48, 49]:

$$\frac{\varepsilon^* - \varepsilon^*_{medium}}{\varepsilon^* + 2\varepsilon^*_{medium}} \approx \left(\frac{\varepsilon^*_{particle} - \varepsilon^*_{medium}}{\varepsilon^*_{particle} + 2\varepsilon^*_{medium}} \right) \phi \tag{4.8}$$

where ϕ is the volume fraction of the disperse phase, and ε^* is the complex permittivity of the composite. This equation shows the permittivity of the dispersion system, ε^*, changes with volume fraction, and also changes relative to the applied DEP field frequency. To demonstrate this effect, simulations were performed using the applied DEP frequency range of 100 kHz to 20 MHz and volume fraction from 0 (no WO_3 particles present) to 1 (no suspending medium) show in Figure 4.14.

For normal Raman spectroscopy, the applied electric field is provided by the excitation laser source. This source is in the GHz frequency range, where permittivities can be considered to have only real values (as the ω term is very large). However, in this case, the applied electric field can be caused by both DEP electric fields and Raman excitation laser electric fields. For nanoparticles under investigation in this work, the electric field provided by the signal generator via electrodes is much greater in magnitude than that generated by the excitation laser.

Figure 4.14 shows how the DEP field alters the relative permittivity of the solution. It can be observed that when the frequency of the DEP field reduces below 10 MHz at volume fraction of 0.11, the relative permittivity increases from 73.6 to 91.6. This increase is approximately 25 % of the permittivity at 0.11 WO_3 volume fractions. If the Raman signal also increased by the same factor, the actual WO_3 concentration should be less or equal to 85.2 %*w/w* / 1.25 = 68.16 %*w/w* (9.5 %*v/v*).

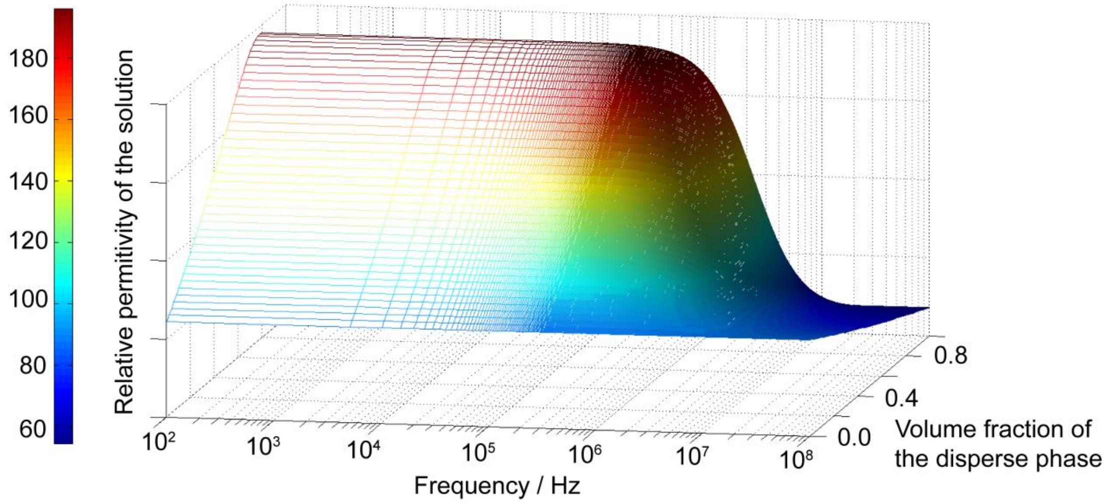

Figure 4.14: Relative permittivity of the solution as a function of the dispersed phase volume fraction at different frequencies.

4.6 Summary

The author has demonstrated the capability of a novel Raman-microfluidic platform to determine the concentration of suspended nanoparticles. Additionally, the ability of the system to perform optical Raman measurements on moving suspended nanoparticles that were manipulated using DEP was verified. With the DEP manipulation, it was possible to produce areas of high and low particle concentrations and then implemented a Raman system to assess the type and concentration of the particles. As an analytical tool, such a platform can create many exciting opportunities for research. The platform will allow for *in situ* analysis of particles, without the need to dehydrate the samples before performing Raman spectroscopy.

These simultaneous manipulations and Raman signal observations can be potentially used for understanding some of the fundamental phenomena occurring when particles are suspended in liquid media. Using DEP forces, suspended particles can be brought into close proximity to one another, allowing the exchange of electrons, photons and phonons between them. DEP permits the controlled manipulation of the particle spacing, allowing observations to be made at various particle conditions of interest.

The next chapter will focus on the control of particle spacing using DEP, with the aim of SERS enhancement. Silver nanoparticles are capable of producing strong SERS signals from their surface absorbed species when they are aggregated. It will be shown in the next chapter that a microfluidic-DEP platform can be used for controlling silver nanoparticle aggregation process in order to enhance the detection of dipicolinic acid.

References

[1] Chrimes, A.F., A.A. Kayani, K. Khoshmanesh, P.R. Stoddart, P. Mulvaney, A. Mitchell, and K. Kalantar-zadeh, Dielectrophoresis-Raman spectroscopy system for analysing suspended nanoparticles. *Lab on a Chip,* vol. 11, pp. 921-928, 2011.

[2] Mairhofer, J., K. Roppert, and P. Ertl, Microfluidic Systems for Pathogen Sensing: A Review. *Sensors,* vol. 9, pp. 4804-4823, 2009.

[3] Ghubade, A., S. Mandal, R. Chaudhury, R.K. Singh, and S. Bhattacharya, Dielectrophoresis Assisted Concentration of Micro-particles and their Rapid Quantitation Based on Optical Means. *Biomedical Microdevices,* vol. 11, pp. 987-995, 2009.

[4] Ocvirk, G., T. Tang, and D.J. Harrison, Optimization of confocal epifluorescence microscopy for microchip-based miniaturized total analysis systems. *Analyst,* vol. 123, pp. 1429-1434, 1998.

[5] Tung, Y.C., M. Zhang, C.T. Lin, K. Kurabayashi, and S.J. Skerlos, PDMS-based opto-fluidic micro flow cytometer with two-color, multi-angle fluorescence detection capability using PIN photodiodes. *Sensors and Actuators, B: Chemical,* vol. 98, pp. 356-367, 2004.

[6] Chen, L.X. and J.B. Choo, Recent advances in surface-enhanced Raman scattering detection technology for microfluidic chips. *Electrophoresis,* vol. 29, pp. 1815-1828, 2008.

[7] Abu-Hatab, N.A., J.F. John, J.M. Oran, and M.J. Sepaniak, Multiplexed microfluidic surface-enhanced Raman spectroscopy. *Applied Spectroscopy,* vol. 61, pp. 1116-1122, 2007.

[8] Grow, A.E., L.L. Wood, J.L. Claycomb, and P.A. Thompson, New biochip technology for label-free detection of pathogens and their toxins. *Journal of Microbiological Methods,* vol. 53, pp. 221-233, 2003.

[9] Hou, D., S. Maheshwari, and H.C. Chang, Rapid bioparticle concentration and detection by combining a discharge driven vortex with surface enhanced Raman scattering. *Biomicrofluidics,* vol. 1, p. 014106, 2007.

[10] Docherty, F.T., P.B. Monaghan, R. Keir, D. Graham, W.E. Smith, and J.M. Cooper, The first SERRS multiplexing from labelled oligonucleotides in a microfluidics lab-on-a-chip. *Chemical Communications,* vol. 1, pp. 118-119, 2004.

[11] Park, T., S. Lee, G.H. Seong, J. Choo, E.K. Lee, Y.S. Kim, W.H. Ji, S.Y. Hwang, and D.G. Gweon, Highly sensitive signal detection of duplex dye-labelled DNA oligonucleotides in a PDMS microfluidic chip: confocal surface-enhanced Raman spectroscopic study. *Lab on a Chip,* vol. 5, pp. 437-442, 2005.

[12] Wilson, R., S.A. Bowden, J. Parnell, and J.M. Cooper, Signal Enhancement of Surface Enhanced Raman Scattering and Surface Enhanced Resonance Raman Scattering Using in Situ Colloidal Synthesis in Microfluidics. *Analytical Chemistry,* vol. 82, pp. 2119-2123, 2010.

[13] Huh, Y.S., A.J. Lowe, A.D. Strickland, C.A. Batt, and D. Erickson, Surface-Enhanced Raman Scattering Based Ligase Detection Reaction. *Journal of the American Chemical Society,* vol. 131, pp. 2208-2213, 2009.

[14] Tong, L.M., M. Righini, M.U. Gonzalez, R. Quidant, and M. Kall, Optical aggregation of metal nanoparticles in a microfluidic channel for surface-enhanced Raman scattering analysis. *Lab on a Chip,* vol. 9, pp. 193-195, 2009.

[15] Keir, R., E. Igata, M. Arundell, W.E. Smith, D. Graham, C. McHugh, and J.M. Cooper, SERRS. In situ substrate formation and improved detection using microfluidics. *Analytical Chemistry,* vol. 74, pp. 1503-1508, 2002.

[16] Zhang, C., K. Khoshmanesh, F.J. Tovar-Lopez, A. Mitchell, W. Wlodarski, and K. Kalantar-zadeh, Dielectrophoretic separation of carbon nanotubes and polystyrene microparticles. *Microfluidics and Nanofluidics,* vol. 7, pp. 633-645, 2009.

[17] Constantino, C.J.L., T. Lemma, P.A. Antunes, and R. Aroca, Single-molecule detection using surface-enhanced resonance Raman scattering and Langmuir-Blodgett monolayers. *Analytical Chemistry,* vol. 73, pp. 3674-3678, 2001.

[18] Bhatt, K.H. and O.D. Velev, Control and Modeling of the Dielectrophoretic Assembly of On-chip Nanoparticle Wires. *Langmuir,* vol. 20, pp. 467-476, 2004.

[19] Fiedler, S., S.G. Shirley, T. Schnelle, and G. Fuhr, Dielectrophoretic Sorting of Particles and Cells in a Microsystem. *Analytical Chemistry,* vol. 70, pp. 1909-1915, 1998.

[20] Khoshmanesh, K., C. Zhang, F.J. Tovar-Lopez, S. Nahavandi, S. Baratchi, A. Mitchell, and K. Kalantar-zadeh, Dielectrophoretic-activated cell sorter based on curved microelectrodes. *Microfluidics and Nanofluidics,* vol. 9, pp. 411-426, 2010.

[21] Lapizco-Encinas, B.H., B.A. Simmons, E.B. Cummings, and Y. Fintschenko, Dielectrophoretic concentration and separation of live and dead bacteria in an array of insulators. *Analytical Chemistry,* vol. 76, pp. 1571-1579, 2004.

[22] Lapizco-Encinas, B.H., B.A. Simmons, E.B. Cummings, and Y. Fintschenko, Insulator-based dielectrophoresis for the selective concentration and separation of live bacteria in water. *Electrophoresis,* vol. 25, pp. 1695-1704, 2004.

[23] Pohl, H.A. and J.S. Crane, Dielectrophoresis of cells. *Biophysical Journal,* vol. 11, pp. 711-727, 1971.

[24] Green, N.G. and H. Morgan, Dielectrophoretic separation of nano-particles. *Journal of Physics D: Applied Physics,* vol. 30, pp. L41-L44, 1997.

[25] Kalantar-zadeh, K., K. Khoshmanesh, A.A. Kayani, S. Nahavandi, and A. Mitchell, Dielectrophoretically tuneable optical waveguides using nanoparticles in microfluidics. *Applied Physics Letters,* vol. 96, p. 101108, 2010.

[26] Kayani, A.A., C. Zhang, K. Khoshmanesh, J.L. Campbell, A. Mitchell, and K. Kalantar-zadeh, Novel tuneable optical elements based on nanoparticle suspensions in microfluidics. *Electrophoresis,* vol. 31, pp. 1071-1079, 2010.

[27] Lee, S.Y., T.H. Kim, D.I. Suh, N.K. Cho, H.K. Seong, S.W. Jung, H.J. Choi,

and S.K. Lee, A study of dielectrophoretically aligned gallium nitride nanowires in metal electrodes and their electrical properties. *Chemical Physics Letters,* vol. 427, pp. 107-112, 2006.

[28] Wang, D.Q., R. Zhu, Z.Y. Zhou, and X.Y. Ye, Controlled assembly of zinc oxide nanowires using dielectrophoresis. *Applied Physics Letters,* vol. 90, p. 103110, 2007.

[29] Pohl, H.A., *Dieletrophoresis*. 1978, Oklahoma: Cambridge University Press.

[30] Zhang, C., K. Khoshmanesh, A. Mitchell, and K. Kalantar-zadeh, Dielectrophoresis for manipulation of micro/nano particles in microfluidic systems. *Analytical and Bioanalytical Chemistry,* vol. 396, pp. 401-420, 2010.

[31] Khoshmanesh, K., C. Zhang, F.J. Tovar-Lopez, S. Nahavandi, S. Baratchi, K. Kalantar-zadeh, and A. Mitchell, Dielectrophoretic manipulation and separation of microparticles using curved microelectrodes. *Electrophoresis,* vol. 30, pp. 3707-3717, 2009.

[32] Morgan, H. and N. Green, G., *AC Eelectrokinetics: colloids and nanoparticles*. 2003, Baldock: Research studies press ltd.

[33] Cui, L., D. Holmes, and H. Morgan, The dielectrophoretic levitation and separation of latex beads in microchips. *Electrophoresis,* vol. 22, pp. 3893-3901, 2001.

[34] Durr, M., J. Kentsch, T. Muller, T. Schnelle, and M. Stelzle, Microdevices for Manipulation and Accumulation of Micro- and Nanoparticles by Dielectrophoresis. *Electrophoresis,* vol. 24, pp. 722-731, 2003.

[35] Gillet, M., K. Aguir, C. Lemire, E. Gillet, and K. Schierbaum, The structure and electrical conductivity of vacuum-annealed WO3 thin films. *Thin Solid Films,* vol. 467, pp. 239-246, 2004.

[36] White, C.M., L.A. Holland, and P. Famouri, Application of capillary electrophoresis to predict crossover frequency of polystyrene particles in dielectrophoresis. *Electrophoresis,* vol. 31, pp. 2664-2671, 2010.

[37] Biaggio, S.R., R.C. Rocha-Filho, J.R. Vilche, F.E. Varela, and L.M. Gassa, A Study of Thin Anodic WO_3 Films by Electrochemical Impedance Spectroscopy. *Electrochimica Acta,* vol. 42, pp. 1751-1758, 1997.

[38] Xie, C.G. and Y.Q. Li, Raman spectra and optical trapping of highly refractive and nontransparent particles. *Applied Physics Letters,* vol. 81, pp. 951-953, 2002.

[39] Strehle, K.R., D. Cialla, P. Rosch, T. Henkel, M. Kohler, and J. Popp, A Reproducible Surface-Enhanced Raman Spectroscopy Approach. Online SERS Measurements in a Segmented Microfluidic System. *Analytical Chemistry,* vol. 79, pp. 1542-1547, 2007.

[40] Souza, A.G., J. Mendes, V.N. Freire, A.P. Ayala, J.M. Sasaki, P.T.C. Freire, F.E.A. Melo, J.F. Juliao, and U.U. Gomes, Phase transition in WO_3 in microcrystals obtained by sintering process. *Journal of Raman Spectroscopy,* vol. 32, pp. 695-699, 2001.

[41] Ma, X.Y., J.Q. Lu, R.S. Brock, K.M. Jacobs, P. Yang, and X.H. Hu, Determination of complex refractive index of polystyrene microspheres from 370 to 1610 nm. *Physics in Medicine and Biology,* vol. 48, pp. 4165-4172, 2003.

[42] Washizu, E., A. Yamamoto, Y. Abe, M. Kawamura, and K. Sasaki, Optical and electrochromic properties of RF reactively sputtered WO_3 films. *Solid State Ionics,* vol. 165, pp. 175-180, 2003.

[43] Daniel, M.F., B. Desbat, J.C. Lassegues, B. Gerand, and M. Figlarz, Infrared and Raman-Study of WO_3 Tungsten Trioxides and WO_3, xH_2O Tungsten Trioxide Hydrates. *Journal of Solid State Chemistry,* vol. 67, pp. 235-247, 1987.

[44] Barthet, C., S.P. Armes, S.F. Lascelles, S.Y. Luk, and H.M.E. Stanley, Synthesis and Characterization of Micrometer-sized, Polyaniline-coated Polystyrene Latexes. *Langmuir,* vol. 14, pp. 2032-2041, 1998.

[45] Chon, H., C. Lim, S.M. Ha, Y. Ahn, E.K. Lee, S.I. Chang, G.H. Seong, and J. Choo, On-Chip Immunoassay Using Surface-Enhanced Raman Scattering of Hollow Gold Nanospheres. *Analytical Chemistry,* vol. 82, pp. 5290-5295, 2010.

[46] Piorek, B.D., S.J. Lee, J.G. Santiago, M. Moskovits, S. Banerjee, and C.D. Meinhart, Free-surface microfluidic control of surface-enhanced Raman spectroscopy for the optimized detection of airborne molecules. Presented at the Proceedings of the National Academy of Sciences of the United States of America, 2007.

[47] Quang, L.X., C. Lim, G.H. Seong, J. Choo, K.J. Do, and S.K. Yoo, A portable surface-enhanced Raman scattering sensor integrated with a lab-on-a-chip for field analysis. *Lab on a Chip,* vol. 8, pp. 2214-2219, 2008.

[48] Asami, K., T. Hanai, and N. Koizumi, Dielectric Approach to Suspensions of Ellipsoidal Particles Covered with a Shell in Particular Reference to Biological Cells. *Japanese Journal of Applied Physics,* vol. 19, pp. 359-365, 1980.

[49] Boned, C., J. Peyrelasse, M. Clausse, B. Lagourette, J. Alliez, and L. Babin, Numerical-Analysis of the Hanai Formula - Experimental Application to Dielectric Properties of Microemulsions. *Colloid and Polymer Science,* vol. 257, pp. 1073-1082, 1979.

Chapter 5

Dielectrophoretically controlled nanoparticles for surface-enhanced Raman scattering

5.1 Introduction

In this chapter, the author demonstrates an active microfluidic platform for the control of silver nanoparticles spacing as they flow through a microchannel. The author devised that the dielectrophoretic system demonstrated in the previous chapter can be implemented for careful control of the nanoparticles spacing, making it possible to effectively increase the Raman signals of analytes due to surface-enhanced Raman scattering (SERS). This can be achieved by augmenting the number of SERS-active hot-spots, while avoiding irreversible aggregation of the particles. In this chapter the author will present the implementation of this novel system, and demonstrate it for the detection of dipicolinate (2,6-pyridinedicarboxylic acid; DPA), which is an important bio-marker of *Bacillus anthracis*. The work presented in this chapter has been compiled and published in the Analytical Chemistry journal [1].

The detection of biomaterials and hazardous components in fluids is of high importance, not only for human health and safety [2, 3], but also for environmental and industrial applications [4]. Surface enhanced Raman scattering (SERS) spectroscopy has emerged as a powerful method for the *in situ* detection of such materials and components [5-8]. SERS spectroscopy offers unique features such as the enhancement of measured signal strength by several orders of magnitude in comparison with conventional Raman spectroscopy [9], the possibility of single molecule identification [10], the detection of bio-components with minimal requirement for labelling [11], and the possibility of multi-analyte detection using a single laser source [12].

The integration of SERS spectroscopy with microfluidics has also attracted significant interest from the scientific community [13-16] This integration offers additional benefits including the significant reduction in analyte and reagent volumes required for analysis, accurate control of flow rates and other environmental parameters, facile manipulation of analytes, and moreover, low costs of both instruments and measurement processes [17, 18].

Commonly in many SERS measurements, metal (such as gold or silver) nanostructures or nanoparticles are used to provide the enhancement for Raman scattering. The systems are either based on prefabricated nanostructured surfaces or agglomerated nanoparticles. Nanostructured surfaces or agglomerated nanoparticles show significant hot-spot enhancement when grains or particles form optimum spacing in the order of several to tens of nanometers [19, 20].

Despite all of the abovementioned advantages, SERS bio applications are still mainly limited to research laboratories. The main reason arises from the fact that the current systems are mostly passive, and there is minimal control over the formation of SERS enhancing nanostructures in either two or three dimensions in microfluidics [21]. Additionally, difficulties in the integration of nanoparticles and nanostructures into microfluidics, control of their spacing, limitation in the formation of nanostructures on the surfaces rather than in the bulk of the microfluidics, and costly procedures all add to the drawbacks [8]. Amongst these, the control of spacing between the flowing nanoparticles or the spacing between nanostructures anchored to the surface appears to be a crucial step, as this significantly influences the SERS signal intensity. The intensities of SERS signals are of particular importance for obtaining the low detection limits necessary for many bio-applications [15].

There have been many reports that focus on controlling the spacing of silver and gold nanostructures for SERS measurements. A recent study has revealed significant SERS enhancement from Rhodamine 6B on a layer of gold nano-spikes [22]. However the spacing between the tips of the spikes, where the majority of the SERS signals are generated, were randomly distributed. Kondo *et al.* conducted a comprehensive study to understand the effect of gold particle dimensions and spacings on the SERS response using specifically spaced gold nanoparticles, fixed in the pores of an alumina substrate [23]. Nonetheless in these cases, the dimensions and spacings of the nanostructures were permanent rendering them suitable for only a limited number of analytes.

As such, the author has implementing nanoparticles in microfluidics, instead of the nanostructured surfaces, as it provides the opportunity of controlling their spacings. There are several examples of SERS using suspended silver nanoparticles, including the recent works by Guerrini *et al.* [5] and Futama *et al.* [24] who successfully demonstrated the detection of selected analytes using suspended and dry silver nanoparticle aggregates. However, such examples are based on aggregating chemical agents, which suffer from many limitations. Obviously, these passive methods of the aggregation of nanoparticles are still limited in the control of the spacing to desired values and are mostly based on trial and error approaches. Additionally, the duration of the aggregation process is not readily controllable using chemicals, and the SERS signals are generally lost when the process continues.

Alternatively, an external force can be more efficiently used to control the real-time spacing between the particles. One advantage of such external forces, as opposed to passive chemical methods, is that the SERS analysis will become independent of the chemical aggregating agent. Another advantage is that any possible interference by aggregating agents on the SERS signals will be removed, creating a more reliable SERS platform for the target analyte. Finally, the system can be universally used for all SERS measurement scenarios with minimal requirements for changing the chemical recipes each time. Several examples exist for the non-chemical aggregation of suspended silver nanoparticles for SERS. One example is by Keir *et al.* [13], who demonstrated an increase in SERS signal using microchannels to focus the particles under laminar hydrodynamic force. However, laminar flow cannot be dynamically controlled with high precision due to the presence of fluid viscosity and particle density. Another example is laser tweezing as demonstrated by Tong *et al.* [25, 26]. Nevertheless, the optical powers required for single beam trapping of large particles can be very high, deteriorating the trapped particles.

The methods described demonstrate a need for an alternative approach for controlling the location of nanoparticles - one that does not need aggregating chemicals, does not interfere with Raman spectroscopy or require large amounts of power (optical or otherwise), and can provide real-time manipulation of the inter-particle spacing.

In this chapter, the author implements dielectrophoresis (DEP), the induced motion of neutral particles in non-uniform electric fields [27, 28], for controlling nanoparticles in the microfluidic channel, similar to the concept of the previous chapter. However, in this chapter, DEP forces are used for the manipulation of the positions, and hence, the inter-particle spacing of suspended silver nanoparticles dynamically. The advantages of an integrated Raman-DEP microfluidic system to actively control the spacing of nanoparticles to generate large SERS signals are discussed. The author will present a series of benchmarking measurements with different chemical analytes is presented to prove the validity of the approach.

5.2 Experimental details

5.2.1 Equipment

The experimental set-up for the work in this chapter is identical to that depicted in Chapter 4, Figure 4.1. The DEP-microfluidic device used for this experiment is designed with an electrode spacing of 5 μm at the tips (Figure 3.1(b)) and microchannel dimension of 50 μm high, 120 μm wide and 1000 μm long (Figure 3.2(c)). The detail for the fabrication of electrodes and microfluidics is presented in Chapter 3.

The DEP voltage was applied to the electrodes from a Tabor 8200 signal generator, and the microscopy work was performed on a backlit, upright Olympus BX41 microscope. A μEye 154 digital camera was used to take digital still images of the device during its operation. An Nd:YAG 532 nm laser was used as SERS excitation, and had a measured power of 0.9 mW at the output of the objective. A ×50 objective, with a numerical aperture value of 0.5 was used. This produced a spot size of 0.65 μm diameter with a depth of field ~8 μm. The spectrometer was fibre coupled to the microscope, and fitted with a pin hole of 100 μm. The spectrometer used was a thermally cooled Jobin Yvon Horiba TRIAX320 fitted with a diffraction grating of 1200 cm^{-1}. Acquisition times were 120 seconds, with only one spectrum taken (no averages).

The author also conducted several complimentary experiments, including Fourier transform infrared (FTIR), ultraviolet–visible (UV-Vis), and X-ray photoemission spectroscopy (XPS). The equipment used for XPS data collection was a Thermo Scientific K-Alpha apparatus with a monochromatic Cu Kα radiation source and a 400 μm spot size. Survey and peaks were scanned at 200 and 50 eV pass energies, respectively. FTIR spectra were taken using a Perkin Elmer Spectrum Spotlight 400 imaging FTIR microscope using reflection geometry on dried samples. Transmission electron microscopy (TEM) imaging was conducted using a JEOL 2010 microscope with an acceleration voltage of 200 kV. An FEI Nova-nano Scanning electron microscopy (SEM) was used for all SEM images in this manuscript, with a spot size of 3.0, working distance of 5 mm and an excitation voltage of 3 kV.

5.2.2 Chemicals

Citrate-capped silver nanoparticles (Sigma-Aldrich) were used as the SERS substrates, with an average diameter of ~60 nm obtained by TEM. TEM images were taken from dried silver nanoparticle samples on a lacy carbon TEM grid. The TEM used for imaging was a Jeol 2010, with a high tension voltage of 200 kV. Figure 5.1 shows two TEM images of the nanoparticles, showing an average size of 60 nm, and a roughly spherical shape. Silver was chosen as the desired SERS colloid as it is most suitable for 532 nm laser excitation Raman systems due to its 435 nm absorption peak (Figure 5.13).

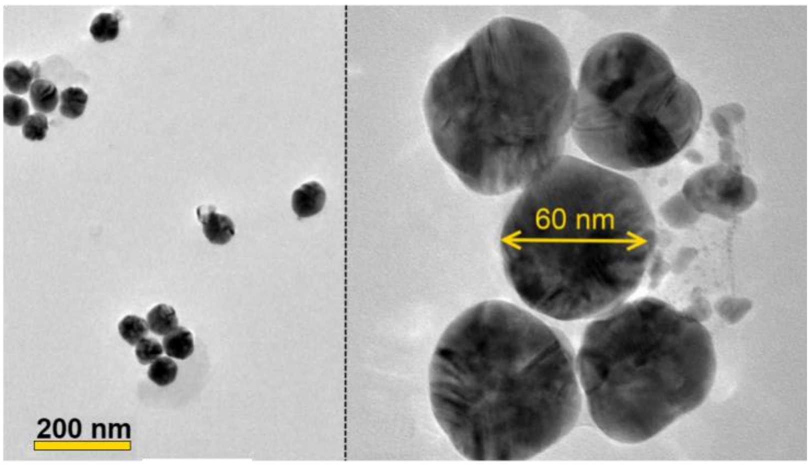

Figure 5.1: TEM image of dried silver nanoparticles.

The as-purchased mixture had a silver concentration of 0.02 mg·mL^{-1} in aqueous buffer stabilised using trisodium citrate. A stock solution of 5 mM DPA was prepared in deionised (DI) water. A silver solution for detecting DPA was made by mixing silver nanoparticles with 5 mM DPA solution at a volume ratio of 100:1. This created a final concentration of DPA at 50 μM, or approximately 10 ppm in the solution, and a final silver concentration of 0.0198 g·mL^{-1}. The silver-DPA mixture was left to incubate for 12 hours at room temperature in order to allow sufficient binding of DPA onto the surface of silver.

A second solution of 1 ppm DPA mixed with silver nanoparticles was also created. However, the low concentration of DPA on the silver nanoparticle surface caused irreversible aggregation of the nanoparticles under the application of DEP forces. Therefore, in order to overcome this, a thin layer of polyacrylic acid (PAA) was coated on the silver nanoparticles after the initial DPA coating. This additional second coating provided an electrical insulating layer, reducing the instances of irreversible aggregates forming.

The intrinsic properties of the suspension play an important role in the process, as the target analyte properties have a significant effect on the system. For this system to function correctly, the silver nanoparticle suspension should remain stable. Target analyte alteration of the surface chemistry and charge of the silver mixture can cause unwanted coagulation of the particles, due to Van der Waals and other forces, which is undesired and should be carefully avoided via the measured control of the adsorbed analytes.

5.2.3 DEP and flow parameters

DEP has been used for the creation of silver nanowires, and indeed wires of any metal types [29-32]. However, these methods use DEP in its most basic form, and the process of wire creation is automatically stopped once the two DEP electrodes have been electrically shorted together. As such, for the experiments presented in this chapter, an electrical short-circuit was very much undesired. Other limiting factors which were considered in the integration of DEP and SERS with silver nanoparticles include: attention to the size of silver nanoparticles as the reduction in particle size decreases the effective DEP force acting on them; and the addition of analytes to DI water reduces the electro-hydrolysis voltage of the solution, producing gas bubbles at the surface of the electrodes. The author desired to reduce the formation of irreversible silver nanoparticle deposits at the tips of the DEP electrodes, and focused his attention on repeatable engineering of particle spacing. Comprehensive numerical simulations were conducted by the author in order to provide a better understanding of the DEP system, as detailed in the following “Simulations” section of this chapter.

In these experiments, an AC signal of 10 V and 20 MHz was applied to the electrodes. The flow rate was kept at the optimum value of 0.15 $\mu l \cdot min^{-1}$, as at larger flow rates no particles could be trapped, while at lower flow rates the particles quickly chained between the electrodes and caused a short circuit. At 20 MHz, the silver nanoparticles were more polarized than the surrounding medium and were attracted towards the electrodes (positive DEP motion) [33] (see the following “Simulations” section of this chapter). Moreover, application of such a high frequency minimized the joule heating effect and the associated electro-thermal disturbances at the tip of microelectrodes [34].

5.2.4 Simulations

5.2.4.1 Clausius-Mossotti factor

For a homogenous spherical particle, the Clausius-Mossotti (CM) factor (f_{CM}), which describes the polarization of suspended particles with respect to their surrounding medium, is calculated as follows:

$$f_{CM} = \frac{\varepsilon^*_{particle} - \varepsilon^*_{medium}}{\varepsilon^*_{particle} + 2\varepsilon^*_{medium}} \tag{5.1}$$

where ε^* is the complex permittivities of the particle and the medium defined as below:

$$\varepsilon^* = \varepsilon - \frac{i\sigma}{\omega} \tag{5.2}$$

in which $i = \sqrt{-1}$, σ is the electric conductivity, ε is the relative permittivity and ω is the angular frequency of the electric field.

The Re[f_{CM}] given by equation (5.1) corresponds to a single-shell structure. However, the low concentration DPA silver nanoparticles used by the author in this work have a more complicated structure, composed of a core of silver coated with a thin layer of PAA (Figure 5.2). The common approach for analysing the dielectric response of such structures is to use the double-shell spherical model [35].

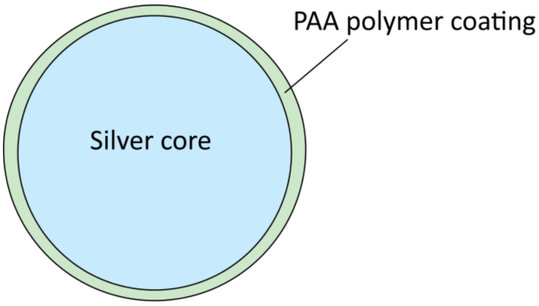

Figure 5.2: The structure of PAA-coated silver nanoparticles.

For double-shell spherical models the equivalent complex permittivities of the silver core and the PAA thin layer are calculated using equation (5.3) [35].

$$\varepsilon^*_{silver+PAA} = \varepsilon^*_{pm} \frac{\left[\dfrac{r_{PAA}}{r_{silver}}\right]^3 + 2\left[\dfrac{\varepsilon^*_{silver} - \varepsilon^*_{PAA}}{\varepsilon^*_{silver} + 2\varepsilon^*_{PAA}}\right]}{\left[\dfrac{r_{PAA}}{r_{silver}}\right]^3 - \left[\dfrac{\varepsilon^*_{silver} - \varepsilon^*_{PAA}}{\varepsilon^*_{silver} + 2\varepsilon^*_{PAA}}\right]} \tag{5.3}$$

The obtained $\varepsilon^*_{silver+PAA}$ was then substituted in equation (5.1) as $\varepsilon^*_{particle}$ to calculate the Re[f_{CM}] of PAA coated silver nanoparticles. The dielectric properties of the different layers of silver nanoparticle structure as well as the surrounding medium are given in Table 5.1:

Table 5.1: The dielectric properties used to analyse the DEP response of particles [36, 37].

Compartments	**Property**	**Value**
Silver core	Diameter	60 nm
	Conductivity	6.3×10^{7} $S\cdot m^{-1}$
	Dielectric constant	27
PAA polymer	Thickness	0.7 nm
	Conductivity	2.5×10^{-3} $S\cdot m^{-1}$
	Dielectric constant	110
DI water	Conductivity	Variable
	Dielectric constant	78

The real part of the CM factor (Re[f_{CM}]) from equation (5.1) is calculated over a frequency range of 1 kHz to 100 MHz, with medium conductivities ranging between 10^{-4} to 10^{-1} $S\cdot m^{-1}$ as shown in Figure 5.3. The nanoparticles exhibit positive DEP behaviour at all the above mentioned frequencies and medium conductivities due to the high conductivity of their silver core as given in Table 5.. At medium conductivities of 10^{-4} to 10^{-3} $S\cdot m^{-1}$ the Re[f_{CM}] remains relatively constant at 0.97 ± 0.01. At the medium conductivity of 10^{-2} $S\cdot m^{-1}$, Re[f_{CM}] reduces to 0.76 ± 0.01 at frequencies lower than 100 kHz, while at medium conductivities of 10^{-1} $S\cdot m^{-1}$, Re[f_{CM}] reduces to 0.025 ± 0.003 at frequencies lower than 200 kHz. At 20 MHz the DEP response of the nanoparticles becomes independent of the medium conductivity as the Re[f_{CM}] converges to 0.95 for all medium conductivities (as shown in Figure 5.3). Moreover, application of such a high frequency minimizes joule heating effects, and the associated electro-thermal motions at the tips of the microelectrodes.

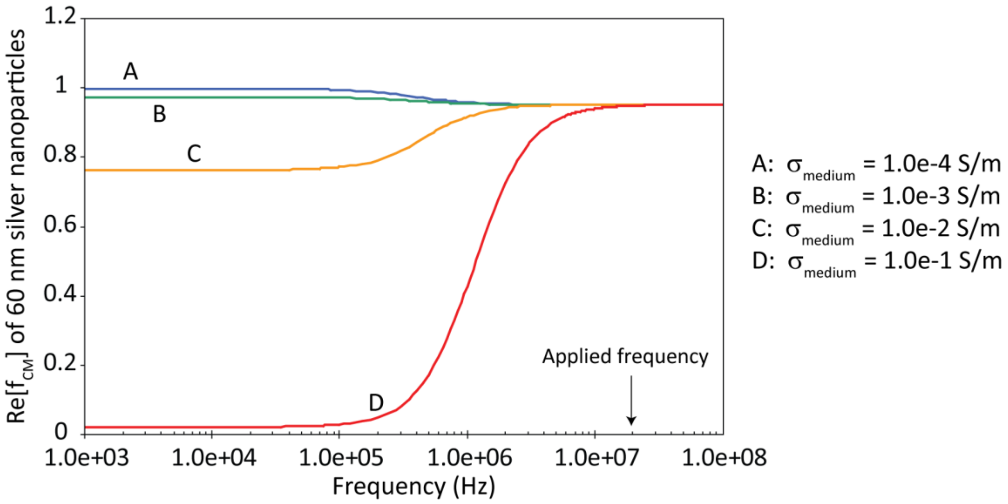

Figure 5.3: Variations of Re[f_{CM}] for PAA coated silver nanoparticles used in the experiments.

5.2.4.2 Dielectrophoretic force

DEP relies on several key properties of particles and their suspending mediums. The DEP force experienced by spherical particles is calculated as [38, 39]:

$$\vec{F}_{DEP} = 2\pi r^3 \varepsilon_0 \varepsilon_{medium} \operatorname{Re}\left[f_{CM}(\omega)\right] \nabla E_{rms}^2 \tag{5.4}$$

where ε_o is the permittivity of free space, ε_{medium} is the relative permittivity of the suspending medium, r is the radius of particles, Re[f_{CM}] is the real part of the CM factor, ω is the angular frequency of the applied signal, and E_{rms} is the root-mean-square value of the induced electric field [33, 40, 41].

The simulations are designed to show the two extreme cases of system performance: one in the absence of conductive nanoparticles, and the other in the presence of nanoparticles chaining to form a nanowire between the opposite electrodes. If particles have semiconducting or insulating coatings the distribution of the electric field and the DEP force will be something between these two extremes.

The simulations were based on the procedure developed by Khoshmanesh, *et al.* [42] as discussed in Chapter 4. The geometry of the electrodes used in this chapter uses an electrode tip spacing of 5 µm. The generated mesh for this electrode design uses a total number of 19,500 elements. This includes a combination of unstructured quadrilateral elements covering the substrate and the microelectrode surface.

Additionally, high density quadrilateral elements are generated at the edges of the microelectrodes, where high electric field gradients are expected. The density of the elements was chosen to accurately predict the behaviour at the microelectrode tip region, as shown in Figure 5.4.

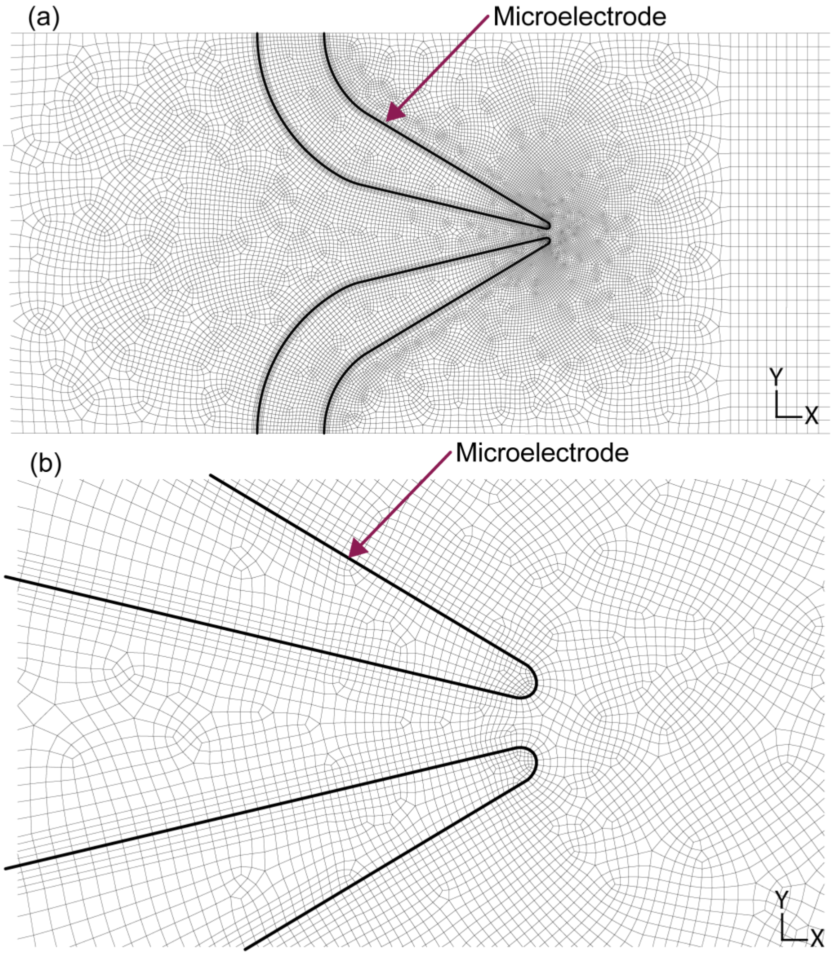

Figure 5.4: Images of the mesh used for the simulation of electric field and dielectrophoretic force (a) 2D overview of microelectrode mesh (b) close up of microelectrode tip, showing the distribution of the mesh at the microelectrode tip region.

Unstructured quadrilateral elements were also generated on the height of the microchannel as shown in Figure 5.5. The channel height was divided into 40 elements, and again the density of the quadrilateral elements was increased at the areas near the microelectrode edges. The simulation is conducted for just one microelectrode pair to reduce the number of elements and the overall simulation time. However, unlike the previous chapter, this simulation uses both microelectrodes.

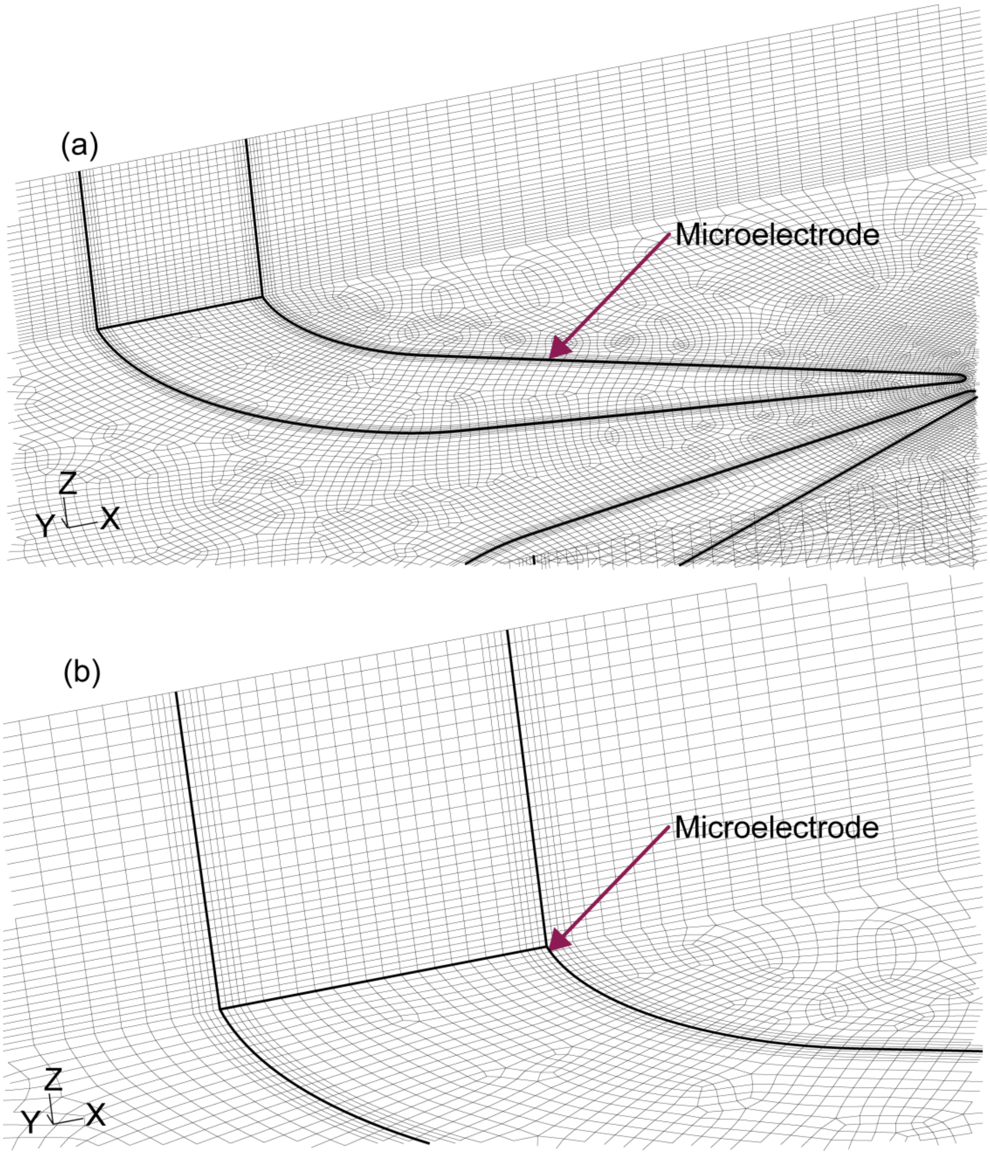

Figure 5.5: 3D images of the microelectrode simulation mesh (a) image depicting the microelectrode and side wall simulation mesh (b) close up of the corner of the microchannel showing how the mesh elements proceed along the z-axis of the microchannel.

These simulations show that a strong electric field is induced across the electrode gap, which produces sufficient DEP force to attract silver nanoparticles (Figure 5.6(a) – (b)). Once there, the immobilized silver particles, without any coatings, act as an extension to the electrodes. This not only reduces the gap between the opposite electrodes but produces large electric field gradients due to the antenna effect [43], and hence large DEP forces at the free end of the immobilized particle aggregations (Figure 5.6(c) – (d)) (see “SEM analysis of aggregated nanoparticles” Figure 5.12 in the “Results and discussions” section of this chapter). This selfexciting mechanism is dampened once the silver particles bridge between the electrodes.

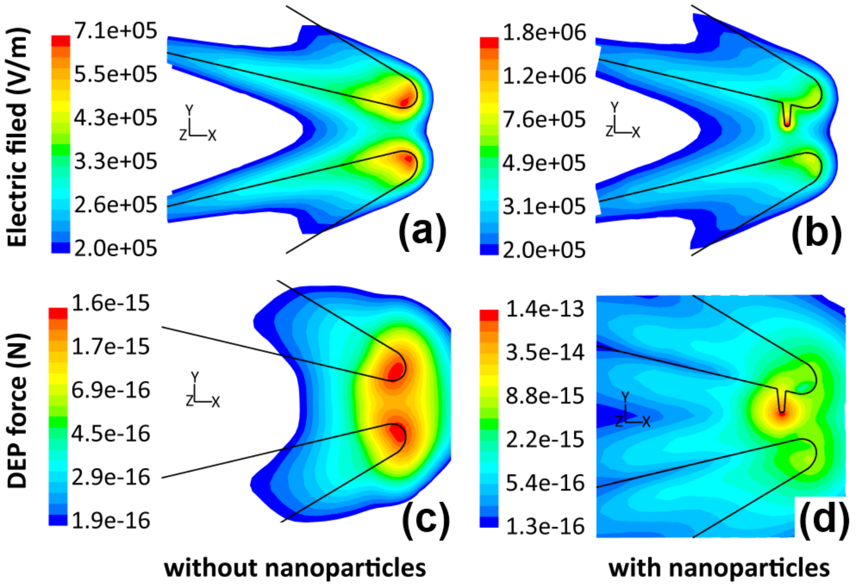

Figure 5.6: Numerical simulations reveal how the immobilisation of silver particles change the performance of the DEP system: (a) Electric field contours without silver particles, (b) Electric field contours with immobilised silver particles, (c) DEP force contours without silver particles, (d) DEP force contours with immobilised silver particles.

5.3 Results and discussions

5.3.1 Characterization of the DEP response

A batch of silver nanoparticles coated with approximately 10 ppm DPA, which is a bio-marker used for the detection of *Bacillus anthracis*, was prepared according to the procedure explained in the “Experimental details” section of this chapter. The behaviour of suspended ~10 ppm DPA silver nanoparticle mixture in the microfluidic system can be summarized into three main regimes, as shown in Figure 5.7.

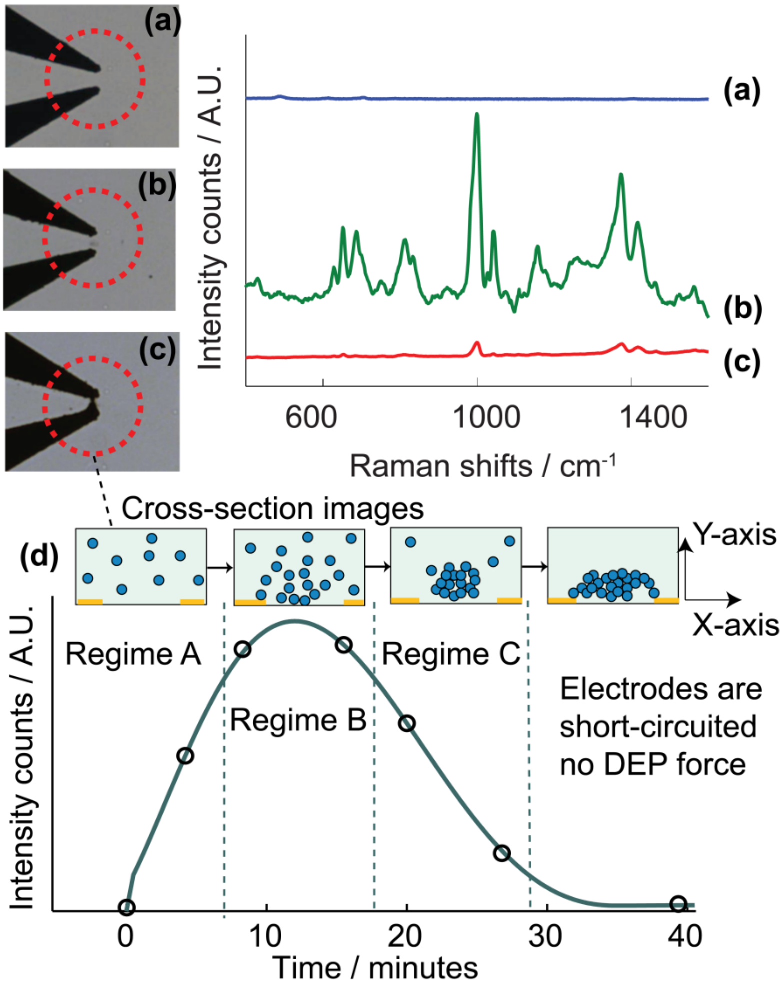

Figure 5.7: Three main silver nanoparticles configuration regimes, showing the resulting aggregation of particles and their corresponding SERS spectra for: (a) no DEP force, (b) combination of DEP and flow forces – controlled particle focusing - and (c) DEP force applied for a long time - large particle aggregation. (d) Intensity of the 1005 cm^{-1} peak over a period of 40 minutes, inserts show cross-sectional images of the electrode tip regions for each of the three regimes.

Regime (a), in the absence of DEP force the particles freely move under the hydrodynamic drag force and form no aggregations; Regime (b), under the appropriate combination of DEP and hydrodynamic forces, the particles are focused at the electrode tips to form highly packed areas of nanoparticles (the area between the two electrodes becomes grey under the upright microscope as shown in Figure 5.7 (b), indicating the presence of higher concentration of nanoparticles that have not been aggregated); and Regime (c), decreasing the flow rate leads to chaining of particles across the electrode tips, initially causing strong aggregation and eventually electrical short circuiting of the electrodes (the area between the two electrodes becomes completely dark as shown in Figure 5.7 (c), indicating a strong aggregation of nanoparticles, see “SEM analysis of aggregated nanoparticles” Figure 5.12 in the “Results and discussions” section of this chapter. Measurements showed resistance of approximately 30 Ω between the electrode tips at the end of the experiments, supporting the hypothesis of electrodes electrical short-circuiting after the application of the DEP force for a long time. This behaviour is in excellent agreement with the DEP simulation results presented in Figure 5.6, where the silver nanoparticles experience a strong positive DEP force at any applied electric field frequency. Further, due to high conductivity of the particles there is a clear formation of nano-aggregates at the microelectrode tips, as shown in the optical microscope images (Figure 5.7). These appear to significantly increase the electric field gradients at the tip regions and encourage even more nanoparticle to aggregate. This self-perpetuating mechanism continues until the electrodes finally short-circuit, reducing the electric field intensity.

It takes minutes to reach Regime (b) after applying the DEP force and over twenty minutes to reach Regime (c). Before reaching Regime (c), Regimes (a) and (b) were switchable, as once the DEP force was removed the particles could re-suspend, and be washed away by the flow system. In order to prove this repeatable switching effect, the SERS response of DPA was monitored over time under the application of a DEP force (20 MHz, 10 V). After 8 minutes the DEP force was turned off, at which point the SERS signatures for DPA are no longer present. Figure 5.8 shows the results of these repeatability measurements.

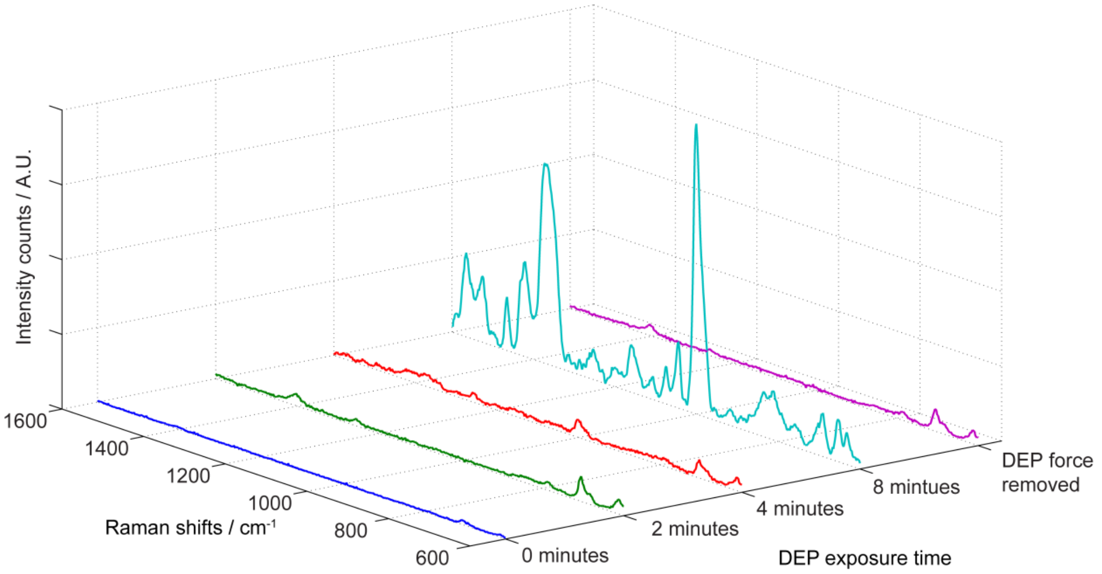

Figure 5.8: SERS response of DPA as a function of time. Zero minute represents the time at which the DEP field was applied. After 8 minutes a spectrum was saved, the DEP field was removed and another spectrum was saved (DEP force removed). This spectra shows the reduction of DPA SERS, and hence the repeatable usage of the device.

Raman spectra were taken in all three Regimes using the ~10 ppm DPA mixtures as plotted in Figure 5.7, with the laser spot positioned in between the electrode tips. Experimental conditions include electrode spacing of 5 µm, flow rate of 0.15 µl·min^{-1} and a particle concentration of 0.0198 g·mL^{-1}. The Figure shows that the highest SERS intensity occurs in Regime (b), where the particles are brought in close proximity without forming larger aggregates.

There have been previous studies detailing the detected SERS peaks from DPA, which reveal common DPA peaks of 655, 815, 1005, 1185, 1376, 1427 and 1561 cm^{-1} [44-49]. The Raman measurements performed on the visible cloud of silver nanoparticles formed in Regime (B) show a strong Raman response of DPA, which is in agreement with the Raman peaks described previously [44-49]. After reaching Regime C hardly any further particle aggregation occurs, which could have resulted in expected coupled localized surface Plasmon (LSP) peaks shift to longer wavelengths [50, 51]. This can be due to the fact that the electrodes become short circuited at this regime and the DEP force disappears.

5.3.2 Estimation of the "mean" statistical inter-particle spacing between silver nanoparticles

In order to numerically justify the creation of SERS hot-spots, investigations of the DEP-microfluidic platform were conducted by the author for determining the spacings between silver nanoparticles. Silver nanoparticles used in these experiments remain in stable suspension for months at room temperature, due to the Brownian motions of the nanoparticles. Einstein theory on Brownian motions suggests that, at specific times, the spacings' between suspended particles in a liquid have a Gaussian distribution, which can be described as [52]:

$$p(x) = \frac{1}{\sqrt{4\pi D}} e^{-\left(\frac{(x-x_m)^2}{4D}\right)} \tag{5.5}$$

where x_m is the mean value for the spacings, x is the displacement from x_m, and $D = kT/f$ is the diffusion constant, with T the absolute temperature, k the Boltzmann constant and f the friction factor, which has a comparatively large value for freely moving nanoparticles. Before applying the DEP force (Figure 5.10 (a)): particles have a Gaussian distribution defined by a statistical "mean" inter particle spacing value and a standard deviation that shows the divergence from this mean (Figure 5.9). The mean value is thus the average of inter-particle spacing and the real spacing between the particles can be either lower or higher than this mean according to the Gaussian distribution. For the calculation of the mean value, the author assumes negligible standard deviation in particle spacing, dictating that particles are a uniformly distributed within the medium, where a realistic standard deviation can be later incorporated.

The mass fraction of silver nanoparticles is equal to 0.0198 g·ml^{-1} and its density is equal to 10.5 g·cm^{-3} this results in the particle volume fraction of:

$$\frac{concentration\ of\ particles}{particle\ density} = \frac{0.0198}{10.5} = 0.00188 = 0.188\%\ v/v \tag{5.6}$$

Calculating the volume of each particle as:

$$\frac{4}{3}\ \pi\,(\frac{60}{2}nm)^3 = 1.13\times10^{-22}\ m^3 \tag{5.7}$$

The number of particles per unit volume is equal to:

$$\frac{0.00188\times1}{1.13\times10^{-22}} = 1.66\times10^{19} \tag{5.8}$$

As a result, the spacing "mean" value between the particles is calculated as:

$$\frac{1}{(60\times10^{-9} + mean\ \ spacing\ )^3} = 1.66\times10^{19} \tag{5.9}$$
$$\Rightarrow\ mean\ spacing\ _{before\ DEP} = 549\ nm$$

According to the Gaussian distribution definition, 68.2 % of the particles have the spacing in the range of $550 \pm \sqrt{2D}$ nm.

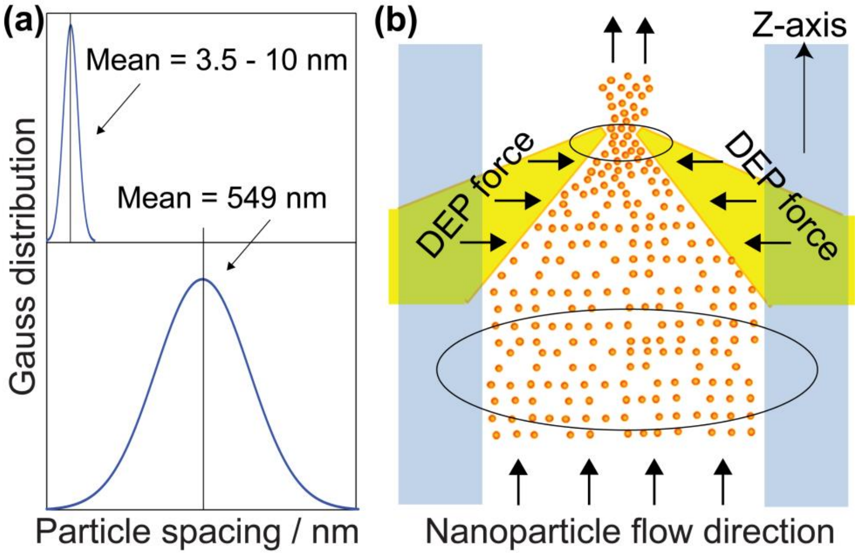

Figure 5.9: Estimation of particle spacing distributions. (a) The distribution is assumed to be Gaussian both far from and near the electrode tips (b) Schematic (not to scale) of the nanoparticle' distributions far from and near to the tips.

After applying the DEP force (Figure 5.10(b)): particles are focused between the microelectrode tips without being attached to each other as described for the regime B case. According to the simulations, the focusing mainly occurs along the cross sectional plane (*xy* plane) of the microchannel and not along the longitudinal axis (*z*-axis) as the particles continuously passed through the microchannel with the same flow rate and that the hydrodynamic flow force is significantly larger than the DEP force in the *z* direction. Therefore, the author assumes that the mean of the particle inter-spacing in the *z* direction remains 550 nm (Figure 5.9(b)). The microscopic observations showed that particles form into approximate rectangular regions in the *xy* plane at the cross section, while focused at the microelectrode tips. As shown in Figure 5.10(b), those semi-rectangular regions estimated to have a width of ~2.5 µm (half of the microelectrode gap) and a height of ~20 µm (one fourth of the microchannel height). As a result, the "statistical mean" of the focused particles' interspacing in the *xy* plane can be calculated as:

$$\begin{gathered} 550\ nm \times \text{focusing ratio}_{x-axis} \times \text{focusing ratio}_{y-axis} \times \frac{1}{\text{focusing efficiency}} = \\ 550\ nm \times \frac{2.5}{150} \times \frac{20}{80} \times \frac{1}{\lambda_{\text{focusing}}} \approx \frac{2.29}{\lambda_{\text{focusing}}}\ (nm) \end{gathered} \tag{5.10}$$

in which $\lambda_{focusing}$ corresponds to efficiency of particle focusing at the tip region. The variation of average inter-particle spacing at different focusing efficiencies is shown in Figure 5.10(c). At the focusing efficiencies of 22.5 – 65 %, the statistical mean for inter-particle spacing are calculated to be in a range of 3.5 to 10 nm (Figure 5.9(a)). This focusing efficiency can be adjusted by setting the applied voltage, frequency and flow rate. In our system, those conditions are obtained at 10 V, 20 MHz and 0.15 µL·min^{-1} (regime (b)). This crude approximation is in good agreement with previous SERS hot-spot studies, which demonstrate hot-spot enhancement at spacing between 1 –10 nm [53].

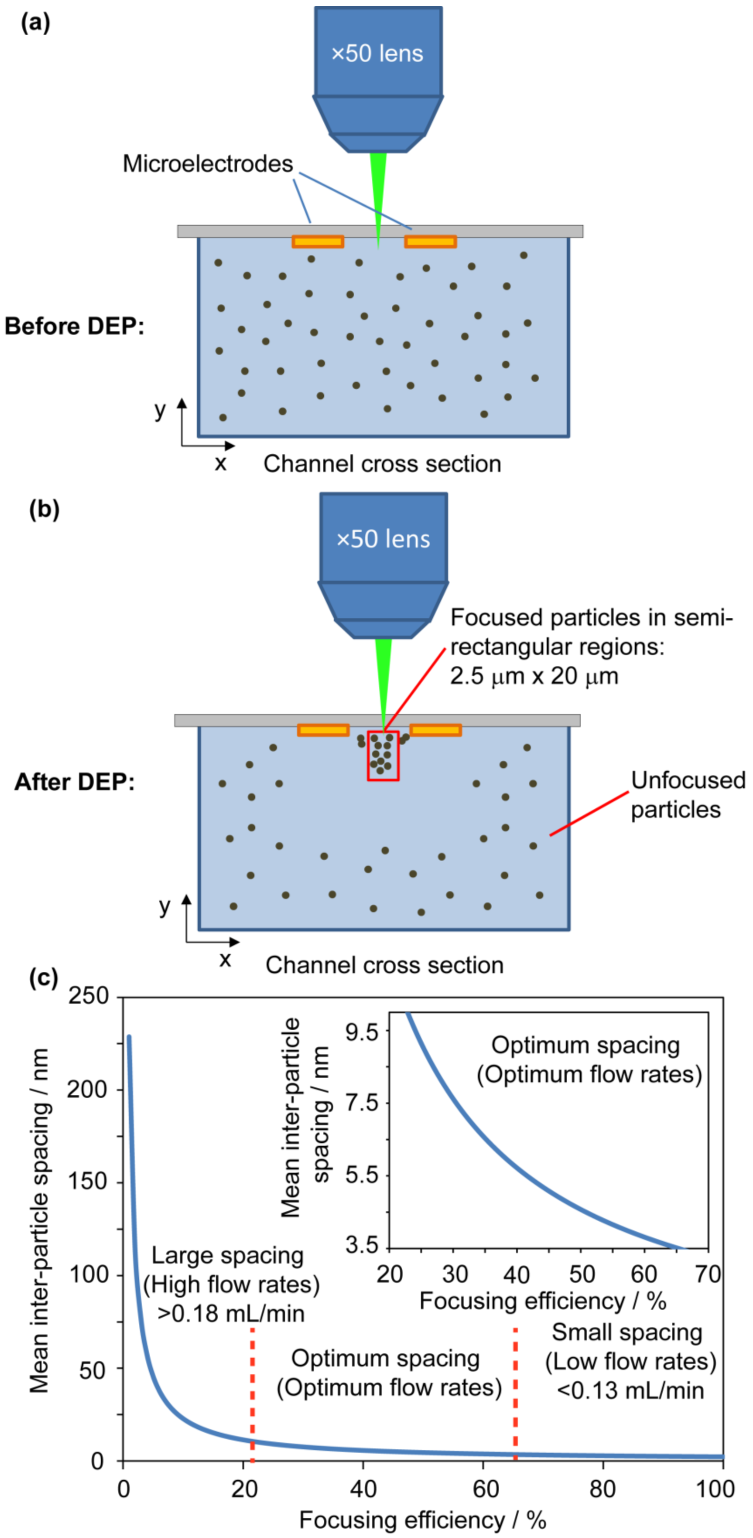

Figure 5.10: Schematic of the particles' distribution in the *xy* plane: (a) before applying the DEP force, and (b) after applying the DEP force. (c) The value of "statistical mean" for inter-particle spacing as a function of focusing efficiency.

5.3.3 Detection at low concentrations

The author assessed the capability of the system for bio-analyte detection at lower concentrations, the Raman response of silver nanoparticles was also acquired at a lower concentration of DPA (~1 ppm). However in this case, it was found that after applying the DEP force, the electrodes were short-circuited very quickly by the silver nanoparticles chaining in-between them. It appears that the silver nanoparticles were not fully covered with DPA at these lower concentrations, leaving their surface void of insulating materials. Even in the case of full DPA coverage assumption, it is likely that the thickness of the DPA layer was sufficiently small that the electrons could easily tunnel between the closely spaced silver nanoparticles. In order to overcome this problem, for the detection of lower concentrations of DPA, after incubating the silver particles in ~1 ppm DPA, they were further incubated by adding 1 part of 5 mM aqueous poly-acrylic acid (PAA) to 100 parts of solution for a further 24 hours to ensure the surface of the particles were covered with a thick layer of insulating material.

This treatment significantly reduced the agglomerating forces experienced by the silver nanoparticles, and also helped to prevent the electrodes from short-circuiting. The ~1 ppm mixture could now be tested in the same fashion as the ~10 ppm, and the Raman spectra are shown in Figure 5.11(a) – (b). For both ~1 and ~10 ppm DPA cases, the Raman spectra show distinguishable detection of DPA, with many characteristic peaks present. There are a few small differences between the two spectra, most obviously the peak at 890 cm^{-1} which is only present in the spectrum for ~1 ppm DPA. This peak can be attributed to the C-COOH stretching mode of the PAA [54], thus reaffirming that PAA strongly binds to the silver-DPA system and provides an insulating polymer layer for enhancing the sensitivity of DPA detection using DEP. Additionally, using the magnitude and peak area of the 1005 cm^{-1} peak of both the ~10 and ~1 ppm solutions and considering a linear calibration curve, the minimum detection limit for this system was determined to be ~100 ppb, making this method more sensitive than previously researched methods [46, 49].

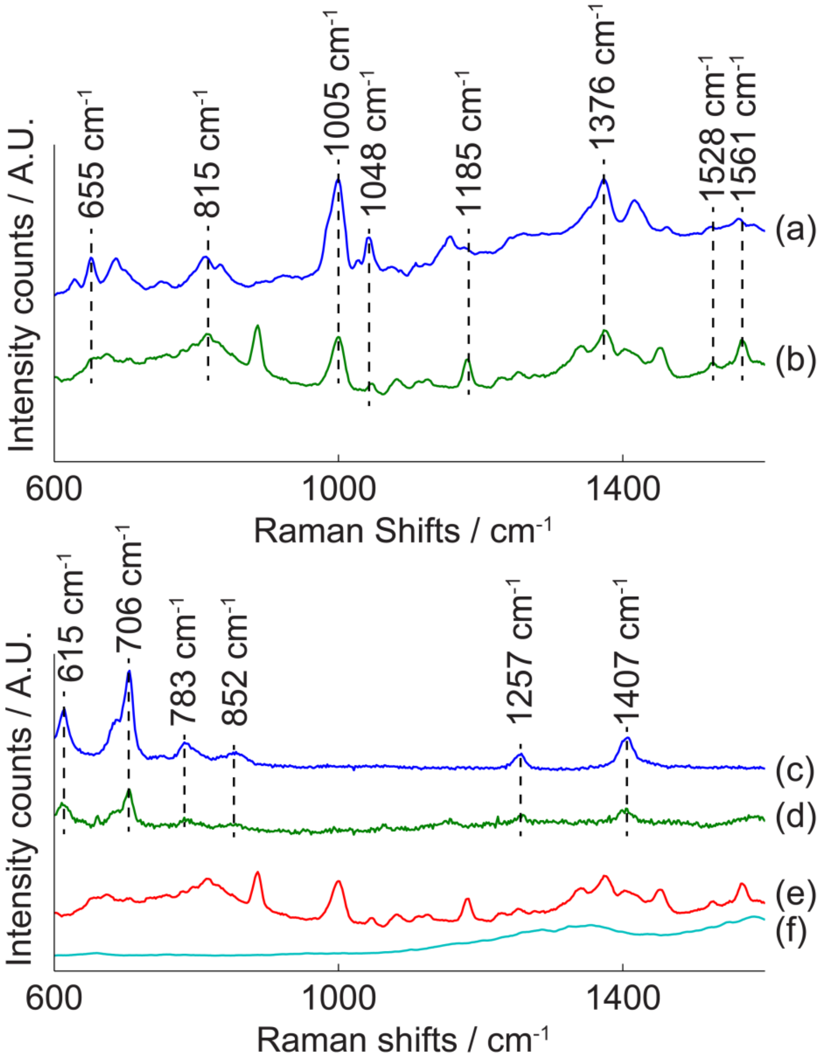

Figure 5.11: Raman spectra of DPA at (a) ~10 ppm concentration and (b) ~1 ppm concentration (after PAA incubation) Raman spectra showing (c) PDMS spectra (d) as-purchased pristine silver nanoparticles (e) ~1 ppm DPA Spectra (f) PAA spectra.

5.3.4 SEM analysis of aggregated nanoparticles

The author characterised the silver nanoparticles aggregates and took high resolution SEM of the microelectrode regions (FEI Nova-nano200 - with a spot size of 3, a working distance of 5 mm and an excitation voltage of 3 kV). He took SEM of the area between electrodes after each regime. The SEM images were taken after removing the PDMS microchannel structure and drying the surface of the microelectrodes. When the DEP force (voltage of 20 MHz and 10 V) was not applied (regime A – produces no Raman signal) or applied for less than a few minutes, (regime B – produces strong Raman signal) there is no silver nanoparticles agglomerate between the electrodes (Figure 5.12(a)) and also no large agglomeration of nanoparticles was seen to leave the microfluidics channel. This backs the authors claim that there is “dynamic” control over the “mean” of particles spacing. They are only brought closer to each other, but they do not form static agglomerates. However, after 20 minutes of applying the DEP force (regime C – produces weak Raman signals), the author observed the formation of agglomerates between the electrodes (Figure 5.12(b)). They strongly attached to each other, and could not be removed by the hydrodynamic force of the flow anymore.

This is in agreement with the in situ optical observations shown in Figure 5.7(a) - (c). Figure 5.7(a), regime (a), shows no observable formation between the electrodes, Figure 5.7(b), regime (b) (dynamic case), shows a grey spot in between electrodes, and Figure 5.7(c), regime (c) (static case), the spot became larger and almost black.

The simulations also back these observations. Regime (c) occurs when silver nanoparticles are attached to each other. This occurs when silver particles start forming chains (Figure 5.6(b)) and produce a very large electric field, which cause strong agglomeration silver nanoparticles even further.

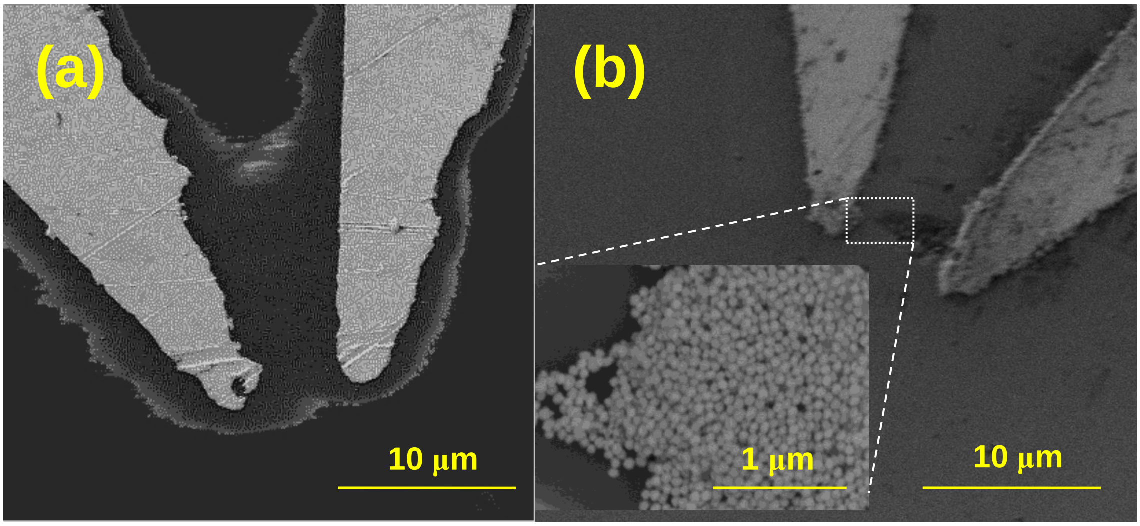

Figure 5.12: (a) SEM image of the microelectrodes after regime B (b) SEM images of the microelectrodes after regime C, insert image shows close up view of the microelectrode edge.

5.3.5 Characterization of the adsorbed chemical onto silver nanoparticles

To confirm that the Raman spectra observed in Figure 5.7 and Figure 5.11(a) – (b) have originated from DPA, and not from other contaminants and components in the system, Raman spectra were also taken from the poly dimethylsiloxane (PDMS) surrounding the microchannel, the as-purchased pristine silver nanoparticles solution and finally a solution containing a mixture of silver nanoparticles and PAA. Figure 5.11(c) – (f) shows the spectra of these three tests compared with the ~1 ppm DPA/PAA sample spectrum. The Raman spectra for the PDMS channel shows several characteristic peaks, the peaks at 1257 and 1407 cm^{-1}, which correspond to the C-H asymmetrical bending modes of the PDMS. The peak at 852 cm^{-1} is the CH_3 asymmetrical rocking mode, 783 cm^{-1} is the C-Si-C asymmetrical stretching mode, 706 cm^{-1} is the C-Si-C symmetrical stretching mode, and 615 cm^{-1} is the quadrifunctional unit mode of the PDMS structure [55]. Raman spectra for the as-purchased silver show minor PDMS peaks, due to the presence of the PDMS microchannel structure, with an additional peak at 1157 cm^{-1}, which can be attributed to the carboxylic functional group of trisodium citrate buffer [56]. As can be seen, the silver with PAA coating only shows two broad Raman peaks at 1585 and 1353 cm^{-1}, which are known to be amorphous carbon peaks [57]. The ~1 ppm DPA Raman spectrum does not show any artefacts from the PDMS microchannel, or any significant peaks from the PAA, further suggesting that DPA is tightly bound to the surface of silver nanoparticles, and demonstrating that system was indeed detecting the SERS spectra of anthrax biomarker DPA molecules.

Further spectroscopy studies, including ultraviolet–visible (UV-Vis), Fourier transform infrared (FTIR), and X-ray photoemission spectroscopy (XPS) were also undertaken on all silver mixtures and samples to complement and support the results obtained by Raman spectroscopy.

5.3.6 UV-Vis analysis of silver nanoparticle solutions

Figure 5.13 shows the UV-Vis absorbance spectra of silver in combination with various analytes using a Cary 50 Bio-spectrophotometer with a spectral resolution of 2 nm. The pristine Ag nanoparticles showed a characteristic SPR signature peak at 435 nm, without any shift in Ag SPR feature after binding of DPA or PAA molecules. The absorbance peak at 270 nm is the organic peak produced by both DPA and PAA. Figure 5.13 shows this peak to be small for the pristine silver sample, and larger in magnitude for mixtures of silver with DPA and PAA, indicating a presence of DPA and PAA in the mixed samples.

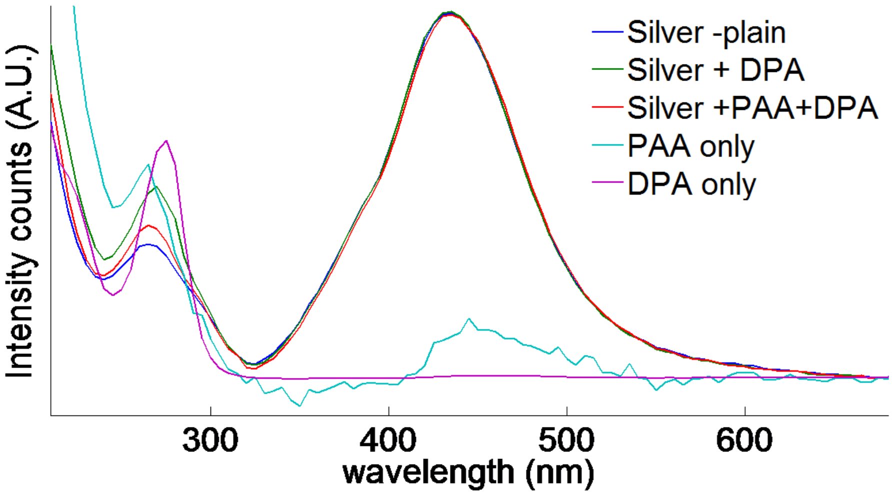

Figure 5.13: UV-Vis absorbance spectra of pristine silver nanoparticles in combination with the various analytes used in this study.

5.3.7 FTIR spectroscopy

FTIR data for the silver nanoparticles, with and without the various analytes are shown in Figure 5.14. Comparison of characteristic FTIR peak of DPA at *ca*. 1700 cm^{-1} (see Figure 5.14 (f)) in different samples containing DPA clearly shows that although in a sample containing ~10 ppm DPA, DPA binds directly to silver nanoparticles in the absence of PAA (Figure 5.14(c), a minor hump at *ca*. 1700 cm^{-1}), the binding of DPA to silver nanoparticles is much stronger when PAA is added to a ~1 ppm DPA sample (Figure 5.14(a), a strong shoulder at *ca*. 1700 cm^{-1}). For comparison, the FTIR spectrum of PAA is also shown (Figure 5.14(e)), which does not have an FTIR signature at *ca*. 1700 cm^{-1}, however possesses a distinct feature at *ca*. 1300 cm^{-1}. These two features of PAA make its FTIR spectrum clearly discernible from that of DPA (compare Figure 5.14(e) and (f)), and thus highlights the binding behaviour of these two molecules on silver surface. The binding of PAA to the silver- DPA sample is evident from a shoulder feature present at *ca*. 1300 cm^{-1} (Figure 5.14(a)).

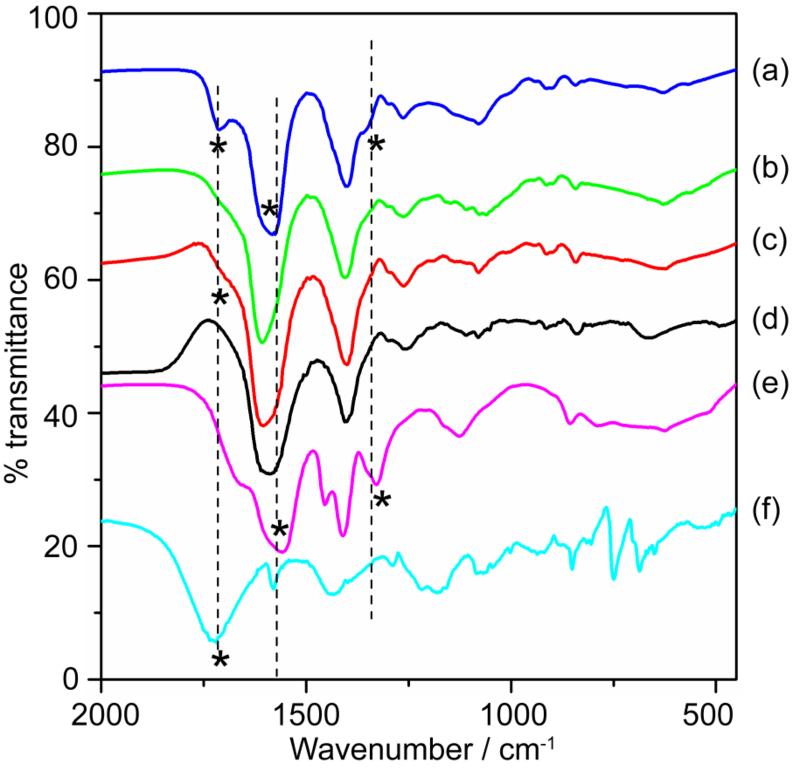

Figure 5.14: FTIR spectra of (a) silver nanoparticles with PAA and ~1 ppm DPA (b) silver nanoparticles with PAA (c) silver nanoparticles with ~10 ppm DPA (d) pristine as-purchased silver nanoparticles (e) PAA only (f) DPA only.

The surprising increase in DPA FTIR signals on silver nanoparticles in the solution containing ~1 ppm DPA with PAA mixture, as opposed to ~10 ppm DPA in the absence of PAA, is most likely due to long chains of PAA polymer molecules facilitating DPA-PAA complexation on silver surface by promoting hydrogen bonding, when mixed together. This observation is highly encouraging and suggests the unique possibility of utilizing polymeric molecules such as PAA for concentration of lower concentration of disease biomarkers typically observed in natural samples onto SERS active silver substrates. This may result in increasing the detection limit of such biomarkers.

5.3.8 XPS analysis

XPS was further utilized to understand the binding behaviour of DPA to silver (Ag) nanoparticles in the presence of PAA molecules (Figure 5.15). For XPS analysis, C 1s, N 1s and Ag 3d core level spectra for pristine Ag nanoparticles, Ag-DPA and Ag-DPA-PAA samples were acquired. Binding energies (BEs) of all the core levels were aligned to adventitious C 1s BE of 285 eV, and spectra were corrected for any background signals using the Shirley algorithm [58] prior to curve fitting using a Gaussian-Lorentzian function [59]. Figure 5.15 shows the Ag 3d core level spectra obtained from pristine Ag nanoparticles (a), Ag-DPA (b), and Ag-DPA-PAA (c). All the three Ag 3d core levels could be satisfactorily fitted into spin-orbit pairs with distinct Ag $3d_{5/2}$ and Ag $3d_{3/2}$ BE components. As expected, pristine Ag nanoparticles (a) showed Ag $3d_{5/2}$ BE component at 366.7 eV, which is in good agreement with published values for Ag(0) in silver nanoparticles [60]. However, in Ag-DPA sample (b), Ag $3d_{5/2}$ BE component of Ag nanoparticles shifted towards higher BE of 367.7 eV, which strongly indicates that DPA molecules are associated with Ag nanoparticles *via* the nitrogen atom in its pyridine ring. Interestingly, when PAA was introduced in Ag-DPA system, Ag 3d XPS spectra could only be satisfactorily fitted into two spin-orbit pairs with Ag $3d_{5/2}$ BEs of 367.6 and 368.5 eV, respectively (c). The highly electronegative –COO groups present in PAA polymer chains can be accounted responsible for a positive BE shift in Ag $3d_{5/2}$ BE, leading at 368.5 eV component. This suggests close association between PAA polymer chains to Ag-DPA system, which most likely results from H-bonding between these molecules.

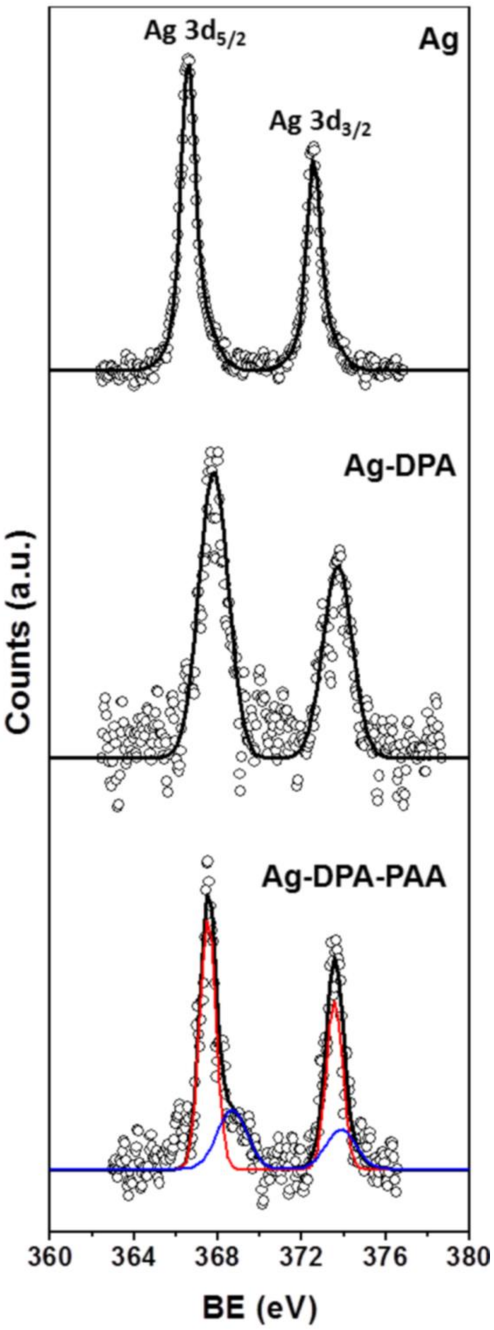

Figure 5.15: XPS spectra showing Ag 3d core levels of (a) pristine Ag nanoparticles, (b) Ag-DPA, and (c) Ag-DPA-PAA.

The presence of DPA in Ag-DPA and Ag-DPA-PAA samples was further confirmed by N 1s core level (Figure 5.16). N 1s core level could be fitted in a single BE component at 399.6 eV in Ag-DPA sample, which corresponds to pyridine N of DPA molecules associated with Ag nanoparticles [60]. In Ag-DPA-PAA sample, a +0.6 eV shift in N 1s BE leading to BE maximum at 400.2 eV is observed. This positive shift in N 1s BE also supports the interaction of –COO rich, highly electronegative, PAA polymer chains with DPA molecules bound to Ag nanoparticles.

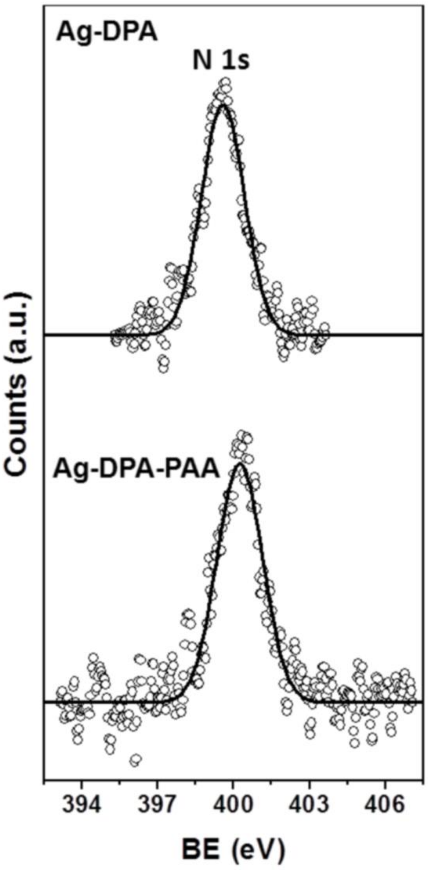

Figure 5.16: XPS spectra showing N 1s core levels of (a) Ag-DPA, and (b) Ag-DPA-PAA.

Furthermore, both Ag-DPA and Ag-DPA-PAA samples showed C 1s core levels, which could be stripped into three components with BEs at 285, 286.5 and 288 eV and are assigned to the electron emission from the adventitious carbon and the carbons coordinated to pyridine ring and carboxylic groups. Since nitrogen is present only in DPA molecules, nitrogen to silver signal ratios were compared in Ag-DPA and Ag-DPA-PAA samples, which corresponded to 0.86 and 1.35, respectively, in these two samples. This confirms that presence of PAA molecules promotes association of DPA marker molecules to Ag nanoparticles, leading to 57 % increase in the binding of DPA to Ag nanoparticles in the presence of PAA polymer chains. It is this aspect that may also allow for the increased SERS detection of DPA at ~1 ppm concentration levels in the Ag-DPA-PAA samples.

XPS analysis not only revealed a close association between PAA polymer chains and silver-DPA but also confirmed that presence of PAA molecules indeed promote strong association of DPA marker molecules to silver nanoparticles. It is this aspect that may also allow for the increased SERS detection of DPA at ~1 ppm concentration levels in silver-DPA-PAA samples.

5.4 Summary

In this chapter, the author presented a combination of DEP and hydrodynamic forces for demonstrating for the active control of suspended silver nanoparticle and their inter-particle spacing in a microfluidic system. The system was able to manipulate the suspended silver particles and produce well-controlled hot-spots to augment the SERS signals. The detection of DPA at both ~1 and ~10 ppm concentration levels was shown using the analysis of the Raman spectra, and under ideal conditions, the procedure was reversible (i.e., once the DEP force is removed the particles could re-suspend, and be washed away by the flow system). Characterisation techniques of UV-Vis and FTIR spectroscopy as well as XPS analysis were implemented to confirm the presence of DPA on silver particles and the validity of the system's performance.

This system could be used for the analysis of bio-components other than DPA, as the DEP-SERS microfluidic unit can be readily adapted to analyse any chemical that has a Raman signature. The system can be used as a universal template for bio-sensing, and it can also be tailored for use in the field, where access to specific chemical aggregating agents may be limited. Additionally, the particle focusing process under DEP is reversible, allowing the unit to be reused for different applications.

In the following chapter, the author will present SERS detection of live cells, as an extension to SERS on analytes presented here. The system will continue to utilise the 5 μm tip spacing microelectrodes for trapping cells in the microfluidics. In the next chapter the author will use multivariable data analysis techniques, used for breaking down the complex cell SERS spectra into coherent components.

References

[1] Chrimes, A.F., K. Khoshmanesh, P.R. Stoddart, A.A. Kayani, A. Mitchell, H.

Daima, V. Bansal, and K. Kalantar-zadeh, Active Control of Silver Nanoparticles Spacing Using Dielectrophoresis for Surface-Enhanced Raman Scattering. *Analytical Chemistry,* vol. 84, pp. 4029-4035, 2012.

[2] Rodil, R., A.M. Carro, R.A. Lorenzo, and R. Cela Torrijos, Selective Extraction of Trace Levels of Polychlorinated and Polybrominated Contaminants by Supercritical Fluid-Solid-Phase Microextraction and Determination by Gas Chromatography/Mass Spectrometry. Application to Aquaculture Fish Feed and Cultured Marine Species. *Analytical Chemistry,* vol. 77, pp. 2259-2265, 2005.

[3] Younglai, E.V., W.G. Foster, E.G. Hughes, K. Trim, and J.F. Jarrell, Levels of Environmental Contaminants in Human Follicular Fluid, Serum, and Seminal Plasma of Couples Undergoing In Vitro Fertilization. *Archives of Environmental Contamination and Toxicology,* vol. 43, pp. 121-126, 2002.

[4] Kim, K., D. Shin, K.L. Kim, and K.S. Shin, Electromagnetic field enhancement in the gap between two Au nanoparticles: the size of hot site probed by surface-enhanced Raman scattering. *Physical Chemistry Chemical Physics,* vol. 12, pp. 3747-3752, 2010.

[5] Guerrini, L., S. Sanchez-Cortes, V.L. Cruz, S. Martinez, S. Ristori, and A. Feis, Surface-enhanced Raman spectra of dimethoate and omethoate. *Journal of Raman Spectroscopy,* vol. 42, pp. 980-985, 2011.

[6] Wilson, R., S.A. Bowden, J. Parnell, and J.M. Cooper, Signal Enhancement of Surface Enhanced Raman Scattering and Surface Enhanced Resonance Raman Scattering Using in Situ Colloidal Synthesis in Microfluidics. *Analytical Chemistry,* vol. 82, pp. 2119-2123, 2010.

[7] Strelau, K.K., R. Kretschmer, R. Moller, W. Fritzsche, and J. Popp, SERS as tool for the analysis of DNA-chips in a microfluidic platform. *Analytical and Bioanalytical Chemistry,* vol. 396, pp. 1381-1384, 2010.

[8] Lee, S., S. Joo, S. Park, S. Kim, H.C. Kim, and T.D. Chung, SERS decoding of micro gold shells moving in microfluidic systems. *Electrophoresis,* vol. 31, pp. 1623-1629, 2010.

[9] Bantz, K.C., A.F. Meyer, N.J. Wittenberg, H. Im, O. Kurtulus, S.H. Lee, N.C. Lindquist, S.H. Oh, and C.L. Haynes, Recent progress in SERS biosensing. *Physical Chemistry Chemical Physics,* vol. 13, pp. 11551-11567, 2011.

[10] Constantino, C.J.L., T. Lemma, P.A. Antunes, and R. Aroca, Single-molecule detection using surface-enhanced resonance Raman scattering and Langmuir-Blodgett monolayers. *Analytical Chemistry,* vol. 73, pp. 3674-3678, 2001.

[11] Strehle, K.R., D. Cialla, P. Rosch, T. Henkel, M. Kohler, and J. Popp, A Reproducible Surface-Enhanced Raman Spectroscopy Approach. Online SERS Measurements in a Segmented Microfluidic System. *Analytical Chemistry,* vol. 79, pp. 1542-1547, 2007.

[12] Kim, K., H.S. Lee, and N.H. Kim, Silver-particle-based surface-enhanced resonance Raman scattering spectroscopy for biomolecular sensing and recognition. *Analytical and Bioanalytical Chemistry,* vol. 388, pp. 81-88, 2007.

[13] Keir, R., E. Igata, M. Arundell, W.E. Smith, D. Graham, C. McHugh, and J.M. Cooper, SERRS. In situ substrate formation and improved detection using microfluidics. *Analytical Chemistry,* vol. 74, pp. 1503-1508, 2002.

[14] Connatser, R.M., L.A. Riddle, and M.J. Sepaniak, Metal-polymer nanocomposites for integrated microfluidic separations and surface enhanced Raman spectroscopic detection. *Journal of Separation Science,* vol. 27, pp.

1545-1550, 2004.

[15] Park, T., S. Lee, G.H. Seong, J. Choo, E.K. Lee, Y.S. Kim, W.H. Ji, S.Y. Hwang, and D.G. Gweon, Highly sensitive signal detection of duplex dye-labelled DNA oligonucleotides in a PDMS microfluidic chip: confocal surface-enhanced Raman spectroscopic study. *Lab on a Chip,* vol. 5, pp. 437-442, 2005.

[16] Hou, D., S. Maheshwari, and H.C. Chang, Rapid bioparticle concentration and detection by combining a discharge driven vortex with surface enhanced Raman scattering. *Biomicrofluidics,* vol. 1, p. 014106, 2007.

[17] Figeys, D. and D. Pinto, Lab-on-a-chip: A revolution in biological and medical sciences. *Analytical Chemistry,* vol. 72, pp. 330A-335A, 2000.

[18] Skoog, D.A., *Fundamentals of analytical chemistry*. 8 ed. 2004: Thomson-Brooks/Cole.

[19] Kneipp, K., M. Moskovits, and H. Kneipp, *Surface-enhanced raman scattering: physics and applications*. 2006: Springer.

[20] Sabur, A., M. Havel, and Y. Gogotsi, SERS intensity optimization by controlling the size and shape of faceted gold nanoparticles. *Journal of Raman Spectroscopy,* vol. 39, pp. 61-67, 2008.

[21] Canamares, M.V., J.V. Garcia-Ramos, S. Sanchez-Cortes, M. Castillejo, and M. Oujja, Comparative SERS effectiveness of silver nanoparticles prepared by different methods: A study of the enhancement factor and the interfacial properties. *Journal of Colloid and Interface Science,* vol. 326, pp. 103-109, 2008.

[22] Plowman, B., S.J. Ippolito, V. Bansal, Y.M. Sabri, A.P. O'Mullane, and S.K. Bhargava, Gold nanospikes formed through a simple electrochemical route with high electrocatalytic and surface enhanced Raman scattering activity. *Chemical Communications,* pp. 5039-5041, 2009.

[23] Kondo, T., K. Nishio, and H. Masuda, Surface-Enhanced Raman Scattering in Multilayered Au Nanoparticles in Anodic Porous Alumina Matrix. *Applied Physics Express,* vol. 2, p. 3, 2009.

[24] Futamata, M., Y.Y. Yu, and T. Yajima, Elucidation of Electrostatic Interaction between Cationic Dyes and Ag Nanoparticles Generating Enormous SERS Enhancement in Aqueous Solution. *Journal of Physical Chemistry C,* vol. 115, pp. 5271-5279, 2011.

[25] Tong, L.M., V.D. Miljkovic, and M. Kall, Optical Manipulation of Plasmonic Nanoparticles Using Laser Tweezers. in *Optical Trapping and Optical Micromanipulation Vii*. vol. 7762, Dholakia, K. and G. C. Spalding, Eds., ed Bellingham: Spie-Int Soc Optical Engineering, 2010.

[26] Tong, L.M., M. Righini, M.U. Gonzalez, R. Quidant, and M. Kall, Optical aggregation of metal nanoparticles in a microfluidic channel for surface-enhanced Raman scattering analysis. *Lab on a Chip,* vol. 9, pp. 193-195, 2009.

[27] Krupke, R., S. Linden, M. Rapp, and F. Hennrich, Thin films of metallic carbon nanotubes prepared by dielectrophoresis. *Advanced Materials,* vol. 18, pp. 1468-1470, 2006.

[28] Pohl, H.A., *Dieletrophoresis*. 1978, Oklahoma: Cambridge University Press.

[29] Ranjan, N., M. Mertig, G. Cuniberti, and W. Pompe, Dielectrophoretic Growth of Metallic Nanowires and Microwires: Theory and Experiments. *Langmuir,* vol. 26, pp. 552-559, 2009.

[30] Suehiro, J., N. Nakagawa, S.-i. Hidaka, M. Ueda, K. Imasaka, M.

Higashihata, T. Okada, and M. Hara, Dielectrophoretic fabrication and characterization of a ZnO nanowire-based UV photosensor. *Nanotechnology,* vol. 17, pp. 2567-2573, 2006.

[31] Wang, D.Q., R. Zhu, Z.Y. Zhou, and X.Y. Ye, Controlled assembly of zinc oxide nanowires using dielectrophoresis. *Applied Physics Letters,* vol. 90, p. 103110, 2007.

[32] Wang, T., X.G. Hu, J.L. Wang, and S.J. Dong, Surface-enhanced Raman scattering from surfactant-free 3D gold nanowire networks substrates. *Talanta,* vol. 75, pp. 455-460, 2008.

[33] Khoshmanesh, K., S. Nahavandi, S. Baratchi, A. Mitchell, and K. Kalantar-zadeh, Dielectrophoretic platforms for bio-microfluidic systems. *Biosensors & Bioelectronics,* vol. 26, pp. 1800-1814, 2011.

[34] Khoshmanesh, K., J. Akagi, S. Nahavandi, J. Skommer, S. Baratchi, J.M. Cooper, K. Kalantar-Zadeh, D.E. Williams, and D. Wlodkowic, Dynamic Analysis of Drug-Induced Cytotoxicity Using Chip-Based Dielectrophoretic Cell Immobilization Technology. *Analytical Chemistry,* vol. 83, pp. 2133-2144, 2011.

[35] Morgan, H. and N.G. Green, *AC Electrokinetics: Colloids and Nanoparticles*. 2003, Baldock: Research Studies Press.

[36] Griffiths, D.J., *Introduction to electrodynamics*. 1999: Prentice Hall.

[37] Ho, C.H., C.D. Liu, C.H. Hsieh, K.H. Hsieh, and S.N. Lee, High dielectric constant polyaniline/poly(acrylic acid) composites prepared by in situ polymerization. *Synthetic Metals,* vol. 158, pp. 630-637, 2008.

[38] Ermolina, I. and H. Morgan, The electrokinetic properties of latex particles: comparison of electrophoresis and dielectrophoresis. *Journal of Colloid and Interface Science,* vol. 285, pp. 419-428, 2005.

[39] Stamenković, J.V., P.I. Premović, and S.V. Mentus, Electrical conductivity of poly(acrylic acid) gels. *Journal of the Serbian Chemical Society,* vol. 62, pp. 945-950, 1997.

[40] Zhang, C., K. Khoshmanesh, A. Mitchell, and K. Kalantar-zadeh, Dielectrophoresis for manipulation of micro/nano particles in microfluidic systems. *Analytical and Bioanalytical Chemistry,* vol. 396, pp. 401-420, 2010.

[41] Kayani, A.A., A.F. Chrimes, K. Khoshmanesh, V. Sivan, E. Zeller, K. Kalantar-zadeh, and A. Mitchell, Interaction of guided light in rib polymer waveguides with dielectrophoretically controlled nanoparticles. *Microfluidics and Nanofluidics,* vol. 11, pp. 93-104, 2011.

[42] Khoshmanesh, K., C. Zhang, S. Nahavandi, F.J. Tovar-Lopez, S. Baratchi, Z. Hu, A. Mitchell, and K. Kalantar-zadeh, Particle trapping using dielectrophoretically patterned carbon nanotubes. *Electrophoresis,* vol. 31, pp. 1366-1375, 2010.

[43] Yu, J., S.J. Ippolito, W. Wlodarski, M. Strano, and K. Kalantar-zadeh, Nanorod based Schottky contact gas sensors in reversed bias condition. *Nanotechnology,* vol. 21, 2010.

[44] Zhang, X., J. Zhao, A.V. Whitney, J.W. Elam, and R.P. Van Duyne, Ultrastable Substrates for Surface-Enhanced Raman Spectroscopy: Al_2O_3 Overlayers Fabricated by Atomic Layer Deposition Yield Improved Anthrax Biomarker Detection. *Journal of the American Chemical Society,* vol. 128, pp. 10304-10309, 2006.

[45] Zhang, X.Y., M.A. Young, O. Lyandres, and R.P. Van Duyne, Rapid

detection of an anthrax biomarker by surface-enhanced Raman spectroscopy. *Journal of the American Chemical Society,* vol. 127, pp. 4484-4489, 2005.

[46] Bell, S.E.J., J.N. Mackle, and N.M.S. Sirimuthu, Quantitative surface-enhanced Raman spectroscopy of dipicolinic acid-towards rapid anthrax endospore detection. *Analyst,* vol. 130, pp. 545-549, 2005.

[47] Farquharson, S., A.D. Gift, P. Maksymiuk, and F.E. Inscore, Rapid dipicolinic acid extraction from bacillus spores detected by surface-enhanced Raman spectroscopy. *Applied Spectroscopy,* vol. 58, pp. 351-354, 2004.

[48] Nelson, W.H., R. Dasari, M. Feld, and J.F. Sperry, Intensities of calcium dipicolinate and Bacillus subtilis spore Raman spectra excited with 244 nm light. *Applied Spectroscopy,* vol. 58, pp. 1408-1412, 2004.

[49] Quang, L.X., C. Lim, G.H. Seong, J. Choo, K.J. Do, and S.K. Yoo, A portable surface-enhanced Raman scattering sensor integrated with a lab-on-a-chip for field analysis. *Lab on a Chip,* vol. 8, pp. 2214-2219, 2008.

[50] Willets, K.A. and R.P. Van Duyne, Localized surface plasmon resonance spectroscopy and sensing. in *Annual Review of Physical Chemistry*. vol. 58, ed Palo Alto: Annual Reviews, 2007, pp. 267-297.

[51] Sriram, S., M. Bhaskaran, S. Chen, S. Jayawardhana, P.R. Stoddart, J.Z. Liu, N.V. Medhekar, K. Kalantar-zadeh, and A. Mitchell, Influence of Electric Field on SERS: Frequency Effects, Intensity Changes, and Susceptible Bonds. *Journal of the American Chemical Society,* vol. 134, pp. 4646-4653, 2012.

[52] Morgan, H. and N.G. Green, *AC electrokinetics: colloids and nanoparticles*. 2003: Baldock Research Studies Press.

[53] Hao, E. and G.C. Schatz, Electromagnetic fields around silver nanoparticles and dimers. *Journal of Chemical Physics,* vol. 120, pp. 357-366, 2004.

[54] Dong, J., Y. Ozaki, and K. Nakashima, Infrared, Raman, and near-infrared spectroscopic evidence for the coexistence of various hydrogen-bond forms in poly(acrylic acid). *Macromolecules,* vol. 30, pp. 1111-1117, 1997.

[55] Jayes, L., A.P. Hard, C. Sene, S.F. Parker, and U.A. Jayasooriya, Vibrational spectroscopic analysis of silicones: A Fourier transform-Raman and inelastic neutron scattering investigation. *Analytical Chemistry,* vol. 75, pp. 742-746, 2003.

[56] Suh, J.S. and J. Kim, Three distinct geometries of surface-adsorbed carboxylate groups. *Journal of Raman Spectroscopy,* vol. 29, pp. 143-148, 1998.

[57] Tamor, M.A. and W.C. Vassell, Raman Fingerprinting of Amorphous-Carbon Films. *Journal of Applied Physics,* vol. 76, pp. 3823-3830, 1994.

[58] Shirley, D.A., High-Resolution X-Ray Photoemission Spectrum of the Valence Bands of Gold. *Physical Review B,* vol. 5, p. 4709, 1972.

[59] Bansal, V., A. Syed, S.K. Bhargava, A. Ahmad, and M. Sastry, Zirconia Enrichment in Zircon Sand by Selective Fungus-Mediated Bioleaching of Silica. *Langmuir,* vol. 23, pp. 4993-4998, 2007.

[60] Kemp, M.M., A. Kumar, S. Mousa, T.-J. Park, P. Ajayan, N. Kubotera, S.A. Mousa, and R.J. Linhardt, Synthesis of Gold and Silver Nanoparticles Stabilized with Glycosaminoglycans Having Distinctive Biological Activities. *Biomacromolecules,* vol. 10, pp. 589-595, 2009.

Chapter 6

Surface-enhanced Raman scattering from nano-silver coated yeast cells

6.1 Introduction

In this chapter, the author reports on a microfluidic system, integrating dielectrophoresis and surface enhanced Raman scattering (SERS), for the trapping and real time monitoring of cells and their functions. The device presented by the author in the previous chapters will be implemented again here for the trapping of yeast cells. The yeast cells are coated with silver nanoparticles to enable highly sensitive SERS analysis, and are examined under various physical conditions: live *vs*. dead and isolated *vs*. grouped. The novel work presented by the author in this chapter demonstrates a highly sensitive cell analysis platform capable of assessing non-specific chemicals on the surface and in the vicinity of cells. Additionally, the author will illustrate the feasibility of this system for *in situ* cell monitoring and analysis of secreted chemicals during their growth, metabolism, proliferation and apoptosis. The work in this chapter has been compiled and submitted to the Biosensors & Bioelectronics journal [1].

There are still many unknowns about the functions of living cells and their communications. Many aspects of cell wall chemical constituents and cell metabolisms have been studied using a variety of techniques, including Raman spectroscopy [2-6]. Raman spectroscopy enables the acquisition of large amounts of information from cells. In particular, it can be efficiently used for identifying molecules inside the cells and on their surface [7-11]. The intensity of obtained

Raman signals is low for studies that focus on only a limited number of cells because of the small concentration of the target molecules. Surface-enhanced Raman scattering (SERS) is frequently used for enhancing the detection of molecules in low concentrations [12-16]. Additionally, SERS allows the Raman signals to be obtained at much smaller time intervals and at lower power levels, reducing the chance of harming the cells under investigation. For SERS, the surface of cells must be covered with SERS inducing nanoparticles such as gold [17] or silver [13]. SERS has been successfully utilized for processes such as differentiating between various cell types [14] and for cell recognition and diagnostics [18]. There are also reports showing the inter-cellular transport pathways using gold nanoparticles [19]. However, despite the obvious capabilities of SERS there are no reports using SERS for investigating the secretion of chemicals from different types of cells, at different group sizes and under various environmental conditions.

In order to study cells in different environmental conditions, microfluidic systems are ideal platforms which allow the facile manipulation of the cells' surroundings. However, SERS imaging requires that the cells be kept still during the entire data acquisition period; therefore the cells must be immobilized. Many methods of cell immobilization are possible in microfluidics [20]; however, not all of them are appropriate for SERS. For example, mechanical trapping techniques require microstructures to hold a cell in place; and these microstructures are generally made of materials that have strong Raman signal intensities, interfering with SERS [21]. Acoustic, hydrodynamic and magnetic immobilization methods are effective, although they are not capable of trapping individual cells [20]. Optical tweezing and thermal trapping are widely applied to cells but have the potential to cause damage and stress to the cells [22]. Dielectrophoresis (DEP), the induced motion of dielectric particles in a non-uniform electric field, has proven to be an effective method of trapping cells in microfluidics and can efficiently allow the control of cell group sizing [23-25]. DEP is especially compatible with SERS, as the smooth surface of metallic microelectrodes does not produce any interfering Raman signals and the microelectrodes can generate strong localized electric fields to trap both individual cells and cells in groups of specific sizes.

In light of these important considerations, the author will present a microfluidic system where DEP is utilized to immobilize a desired number of cells in either direct contact or greater than 10 μm from each other. The author will show that nano-silver coated yeast cell SERS can clearly differentiate between live and dead cells. Subsequently, the author will demonstrate the microfluidic system for studying live cells that are immobilized into “isolated” and “grouped” cell clusters in order to investigate the differences in molecule secretion.

6.2 Experimental details

6.2.1 Equipment

6.2.1.1 Raman System

The Raman microscopy system uses a Horiba TRIAX 320 spectrometer, with a CCD resolution of 0.06 nm. The spectrometer is fibre coupled to an Olympus BX41 confocal microscope, fitted with a 50×, 0.5 numerical aperture (NA) objective lens. The laser system operates at 532 nm with 1 mW optical power output, creating a final spot size of 0.65 μm in diameter. The SERS spectra from the cells were acquired for 20 seconds with no additional accumulations.

6.2.1.2 Microfluidic systems

The microfluidic-DEP device used in this chapter is identical to that used in Chapter 5 (Figure 6.1(a)). The microfluidic system is driven by a syringe pump (Harvard Pico Plus) in withdraw mode. Once the yeast cells are inside the microchannel DEP is applied to immobilize the cells onto the quartz substrate (Figure 6.1(b)), after which the SERS targeted cells are chosen by visual inspection using optical microscopy (Figure 6.1(c)).

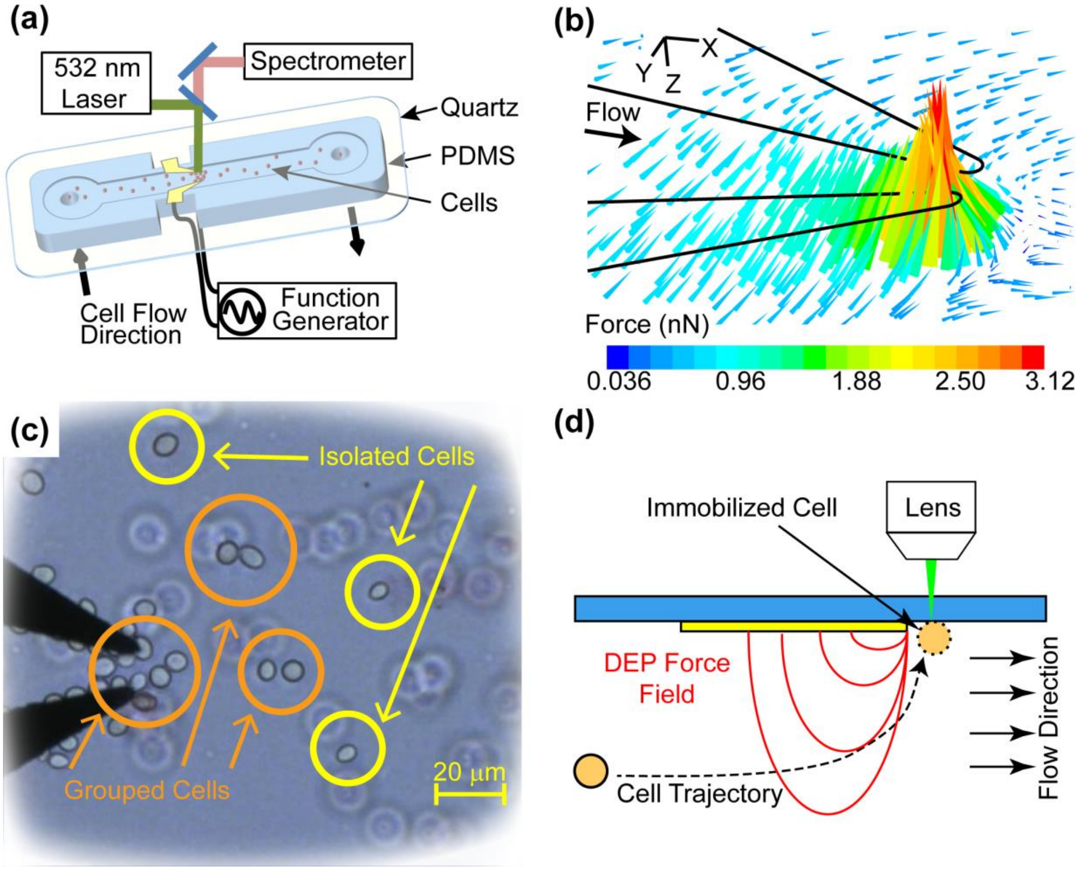

Figure 6.1: The microfluidic system, simulation and cell trapping are shown. (a) Schematic of the microfluidic device with microchannel dimensions of 150 × 70 µm and length of 12 mm, integrated microelectrodes with 15 µm spacing at the tips, and a 532 nm, 1 mW Raman system. (b) The distribution of net trapping force composed of dielectrophoretic, hydrodynamic drag and sedimentation forces at a plane 10 µm from the quartz substrate. (c) Formation of “isolated” and “grouped” yeast cells at the tip of a microelectrode pair (d) Schematic side view of microchannel showing the expected cell trajectory when exposed to DEP and hydrodynamic forces and the eventual cell immobilization.

One drawback to using DEP for yeast manipulation is that exposure to high electric fields can possibly deteriorate the viability of the cells [26]. This deterioration is mostly caused by the Joule heating effect due to the presence of strong electric fields in the high electrical conductivity medium surrounding the cells; moreover, effects such as trans-membrane potential and cell elongation must also be considered when choosing appropriate DEP conditions for biological elements such as yeast cells [23, 26-32]. The author was able to minimize these adverse effects by applying the DEP electrical signals at a relatively high frequency of 20 MHz [23, 27] and using a relatively low voltage of 5 V (see “Dielectrophoresis simulations” in this chapter). Additionally, the author only applied the electric field to the microelectrodes for 30–60 seconds, which is sufficient for efficient cell trapping and permanent immobilization. Once an adequate number of cells were trapped the electric field was turned off to minimize any issues that could arise from electric field exposure [33].

The yeast cells have spherical to ellipsoidal geometries, with diameters in the range of 6 to 10 μm, such that their dielectrophoretic response is approximated by multi-shell spherical model with a cell diameter of 8 μm [23, 26, 34]. In order to characterize the dielectrophoretic response of the system and select the suitable frequency for the applied electric field, simulations of the electric field strength and Clausius–Mossotti (CM) factor are conducted (see “Dielectrophoresis simulations” in this chapter). Figure 6.1(b) depicts the distribution of net trapping force composed of dielectrophoretic, hydrodynamic drag and sedimentation forces at a plane 10 μm from the quartz substrate. The density of trapped cells is proportional to the magnitude of the net trapping force, as shown in Figure 6.1(b). The author has presented details of numerical simulations in the “Dielectrophoresis simulations” section of this chapter. Figure 6.1(c) also depicts the formation of “isolated” and “grouped” cell clusters at microelectrode tips. “Isolated cell” refers to cells that have been immobilized but are not in the vicinity of other cells (i.e. > 1 cell distance). “Grouped cells” refer to cells that are in the intimate contact with one another.

6.2.2 Chemical details

6.2.2.1 Silver nanoparticles

The silver nanoparticles were fabricated using a modified method based on the one described by Panacek *et al*. [35]. Briefly, colloidal silver particles were synthesized by the reduction of $[Ag(NH_3)_2]^+$ complex with glucose. Then 50 mM ammonium hydroxide (5 mL) was added to 2 mM silver nitrate (25 mL). The reaction system was left aside for two hours to allow for the $[Ag(NH_3)_2]^+$ complex to form. Next 25 mM D-glucose (20 mL) was added to the reaction system. Immediately, 100 mM of NaOH solution (1 mL) was added to the reaction system to initiate the reduction and control the growth rate. The reaction system was stirred gently every few minutes. The reaction was performed at room temperature. Transmission electron microscope (TEM) images were taken of the particles at various magnifications to demonstrate the size and shape of the particles. Figure 6.2 below shows the nanoparticles from two different groups. A lacy carbon TEM grid was used to support the nanoparticles for imaging. Imaging was conducted using a Jeol 2010

TEM with a 200 kV acceleration voltage and a spot size of 2. Images were captured using a Gatan digital camera attached to the TEM.

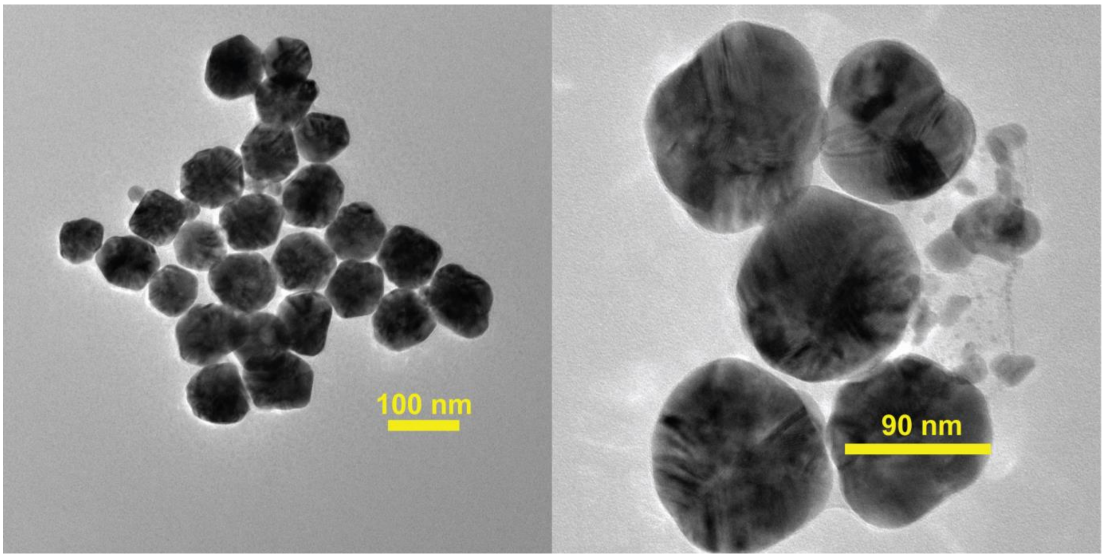

Figure 6.2: TEM images of the fabricated silver nanoparticles.

6.2.2.2 Yeast-silver mixtures

The author used *Saccharomyces cerevisiae* (yeast) cells for the work in this chapter, as they are frequently employed as an ideal model of eukaryotic cells [5, 10, 11, 36, 37]. For obtaining strong SERS signals the cells are coated with 90 nm diameter silver nanoparticles (Figure 6.2). The silver mixture was added directly to the suspended yeast sample and left for 15 minutes to allow the absorption of silver nanoparticles onto the surface of the yeast (Figure 6.3(b)). It should be noted that the size of the silver nanoparticles directly affects the antibacterial activity of the silver nanoparticles [38]. It has been determined that the antibacterial behaviour decreases when the particle size is increases. Anti-bacterial effects of silver nanoparticles of ~90 nm diameters are far less than those of nanoparticles of 40 nm or less diameters. Additionally the uptake of the 90 nm nanoparticles inside the cells is not high and the majority of the particles are only immobilized onto the surface of the cell membrane.

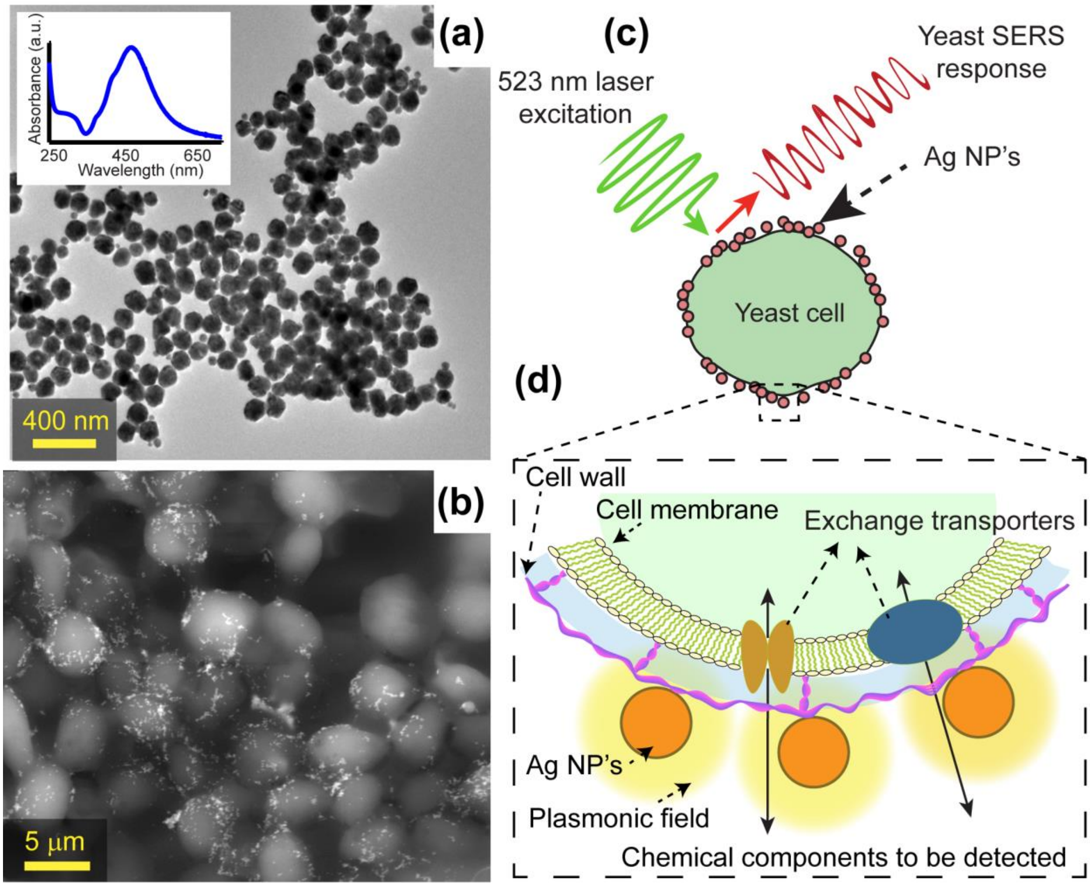

Figure 6.3: Details of silver nanoparticle properties and images showing the silver's attachment to the surface of yeast cells. (a) Transmission electron microscope image of silver nanoparticles synthesized using the described method in [35]. Insert: ultraviolet visible absorbance spectra of the silver nanoparticle suspension. (b) Environmental scanning electron microscope image of yeast cells coated with silver nanoparticles. (c) Schematic of silver bonding to yeast cell wall, the exposure to the light source and the consequent generation of SERS signals. (d) Insert schematic of the silvers attachment to the cell wall showing the chemical component exchanges in and out of cell. The chemicals pass near the silver nanoparticles plasmonic SERS enhancement area.

Mixtures involving dead yeast cells were created by adding 50 %*v/v* methanol to the mixture. The addition of methanol causes instantaneous death of cells, without causing cell apoptosis or destroying the bond between silver particles and the yeast cell walls [26].

6.2.3 Dielectrophoresis (DEP) simulations

The three main forces applied on cells are the dielectrophoretic, hydrodynamic drag, and sedimentation forces, which are described as below [39]:

$$\overline{F}_{DEP} = 2\pi\ r_{cell}^{3}\ \varepsilon_{medium}\ \mathrm{Re}[\ f_{CM}\ ]\ \nabla E_{rms}^{2} \tag{6.1}$$

$$F_{Drag} = 6\pi\, r_{cell}\, \mu_{medium}\, (\vec{U}_{medium} - \vec{v}_{cell}) \tag{6.2}$$

$$F_{Sedimentaton} = \frac{4}{3}\pi\, r_{cell}^{3}\, (\rho_{cell} - \rho_{medium})\, \vec{g}_z \tag{6.3}$$

In equation (6.1), r_{cell} is the radius of the cell, ε_{medium} is the permittivity of the medium, E_{rms} is the root-mean-square (rms) value of the applied electric field, and Re[f_{CM}] is the real part of the Clausius-Mossotti (CM) factor, representing the polarisation of cells with respect to their surrounding medium. In equation (6.2), μ_{medium} and $\vec{U}_{medium}$ are the dynamic viscosity and velocity of the medium, and $\vec{v}_{cell}$ is the velocity of cells. Finally in equation (6.3), ρ_{cell} *and* ρ_{medium} are the density of the cell and the medium, and $\vec{g}_z$ is the gravitational acceleration.

The f_{CM} of homogenous spherical particles is described as below, where ε^* is the complex permittivity, σ is the electrical conductivity, $\varepsilon_o = 8.85\times10^{-12}$ F·m^{-1} is the permittivity of the vacuum, ε is the dielectric constant, and ω is the angular frequency of the applied AC signal [27, 40].

$$f_{CM} = \frac{\varepsilon_{cell}^{*} - \varepsilon_{medium}^{*}}{\varepsilon_{cell}^{*} + 2\varepsilon_{medium}^{*}} \tag{6.4}$$

$$\varepsilon^{*} = \varepsilon_{\circ}\,\varepsilon - \frac{i\sigma}{\omega},\; i = \sqrt{-1} \tag{6.5}$$

However, most bio-particles including cells have a more complicated structure, comprised of several layers of materials with different dielectric properties. For example, the yeast cells are considered as spherical structures comprised of cytoplasm, plasma membrane and an outer wall, as shown in Figure 6.4 [27]:

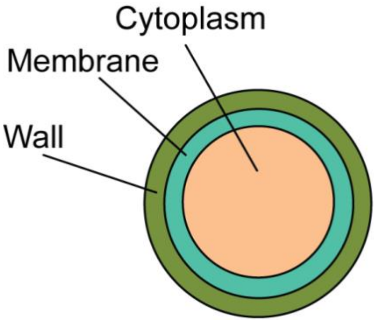

Figure 6.4: Yeast cells are considered as spherical structures comprised of cytoplasm, plasma membrane and an outer wall.

The common approach to predict the f_{CM} of such complicated biological structures is to apply the multi-shell model, as given below for double-shell yeast cells [27]:

$$\varepsilon^*_{cyt-mem} = \varepsilon^*_{mem} \frac{\left[\dfrac{r-t_{wall}}{r-t_{wall}-t_{mem}}\right]^3 + 2\left[\dfrac{\varepsilon^*_{cyt} - \varepsilon^*_{mem}}{\varepsilon^*_{cyt} + 2\varepsilon^*_{mem}}\right]}{\left[\dfrac{r-t_{wall}}{r-t_{wall}-t_{mem}}\right]^3 - \left[\dfrac{\varepsilon^*_{cyt} - \varepsilon^*_{mem}}{\varepsilon^*_{cyt} + 2\varepsilon^*_{mem}}\right]} \tag{6.6}$$

$$\varepsilon^*_{cell} = \varepsilon^*_{wall} \frac{\left[\dfrac{r}{r-t_{wall}}\right]^3 + 2\left[\dfrac{\varepsilon^*_{cyt-mem} - \varepsilon^*_{wall}}{\varepsilon^*_{cyt-mem} + 2\varepsilon^*_{wall}}\right]}{\left[\dfrac{r}{r-t_{wall}}\right]^3 - \left[\dfrac{\varepsilon^*_{cyt-mem} - \varepsilon^*_{wall}}{\varepsilon^*_{cyt-mem} + 2\varepsilon^*_{wall}}\right]} \tag{6.7}$$

The dielectric properties of live and dead (methanol treated) yeast cells as well as the medium were taken as below [26, 34]:

Table 6.1: Variables used for the calculation of dielectrophoretic force for a yeast cell.

Live yeast	**Dead yeast**	**DI water**
$D = 8\ \mu m$	$D = 7\ \mu m$	$\sigma_{medium} = 0.002\ S \cdot m^{-1}$
$\sigma_{cytoplasm} = 0.2\ \ S \cdot m^{-1}$	$\sigma_{cytoplasm} = 0.007\ S \cdot m^{-1}$	$\varepsilon_{medium} = 78$
$\varepsilon_{cytoplasm} = 50$	$\varepsilon_{cytoplasm} = 50$	
$\sigma_{membrane} = 25 \times 10^{-8}\ \ S \cdot m^{-1}$	$\sigma_{membrane} = 16 \times 10^{-5}\ S \cdot m^{-1}$	
$\varepsilon_{membrane} = 6$	$\varepsilon_{membrane} = 6$	
$t_{membrane} = 8\ nm$	$t_{membrane} = 8\ nm$	
$\sigma_{wall} = 0.014\ S \cdot m^{-1}$	$\sigma_{wall} = 15 \times 10^{-4}\ S \cdot m^{-1}$	
$\varepsilon_{wall} = 60$	$\varepsilon_{wall} = 60$	
$t_{wall} = 220\ nm$	$t_{wall} = 220\ nm$	

However, addition of silver nanoparticles to the medium not only changes the dielectric properties of the cells (as the silver nanoparticles coat the surface of cells) but also changes the dielectric properties of the medium (as a large portion of silver nanoparticles remain suspended in the medium). To take into account the silver nanoparticles coating the surface of cells, it is assumed that there is a homogenous layer of particles covering the outer wall of yeast cells, which is compatible with multi-shell spherical model, as shown in Figure 6.5:

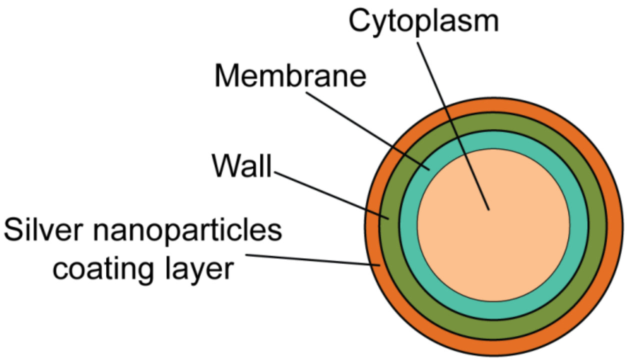

Figure 6.5: It is assumed that a homogenous layer of particles is covering the outer wall of yeast cells, to take into account the silver nanoparticles coating the surface of the cells.

To consider the incomplete and inhomogeneous coating of the yeast cells, the author defined a coating efficiency as $\lambda_{Coating}$ and considered the dielectric properties of this additional layer proportional to silver nanoparticles conductivity and permittivity:

$$\sigma_{Coating\,layer} = \varphi_{Silver\ nanopartiles} \times \lambda_{Coating} \times \sigma_{Silver\ nanopartiles} \tag{6.8}$$

$$\varepsilon_{Coating\,layer} = \varphi_{Silver\,nanopartiles} \times \lambda_{Coating} \times \varepsilon_{Silver\,nanopartiles} \tag{6.9}$$

In which, $\varphi_{Silver\ \ nanoparticles} = 0.0198\ \mathrm{g.ml^{-1}}$ is the volume fraction of silver nanoparticles within the medium.

To take into account the presence of silver nanoparticles still suspended in the medium, the author calculated the equivalent complex permittivity of the medium as below [27]:

$$\varepsilon^{*}_{Silver+medium} = \varepsilon^{*}_{medium} \cdot \frac{1+2\ \varphi_{Silver\ nanopartiles} \times (1-\lambda_{Coating}) \times \varepsilon^{*}_{Silver}}{1-\ \varphi_{Silver\ nanopartiles} \times (1-\lambda_{Coating}) \times \varepsilon^{*}_{Silver}} \tag{6.10}$$

The DEP response of live and dead yeast cells were calculated in a variety of coating efficiencies ranging from 10 % to 100 %, as shown in Figure 6.6. Curves 1 and 2 represent the DEP response of original yeast cells (without any silver nanoparticles either coated on their surface or within the medium) while curves 3 – 6 represent the DEP response of live yeast cells covered with different coating efficiencies of 10 – 100%, instead curves 7 – 10 represent the DEP response of dead yeast cells with different coating efficiencies of 10 – 100%. Interestingly, the addition of SERS silver nanoparticles significantly changed the DEP response of original yeast cells. The Re[f_{CM}] of live yeast cells remained constant throughout the frequency spectrum of 10 kHz – 20 MHz at different coating efficiencies. Alternatively, the Re[f_{CM}] of dead yeast cells was very sensitive both to frequency and coating efficiency, reducing at high frequencies and low coating efficiencies. This is consistent with the author’s experimental observations: while most live yeast cells were trapped close to the tips of microelectrodes the dead yeast cells were scattered at a larger area.

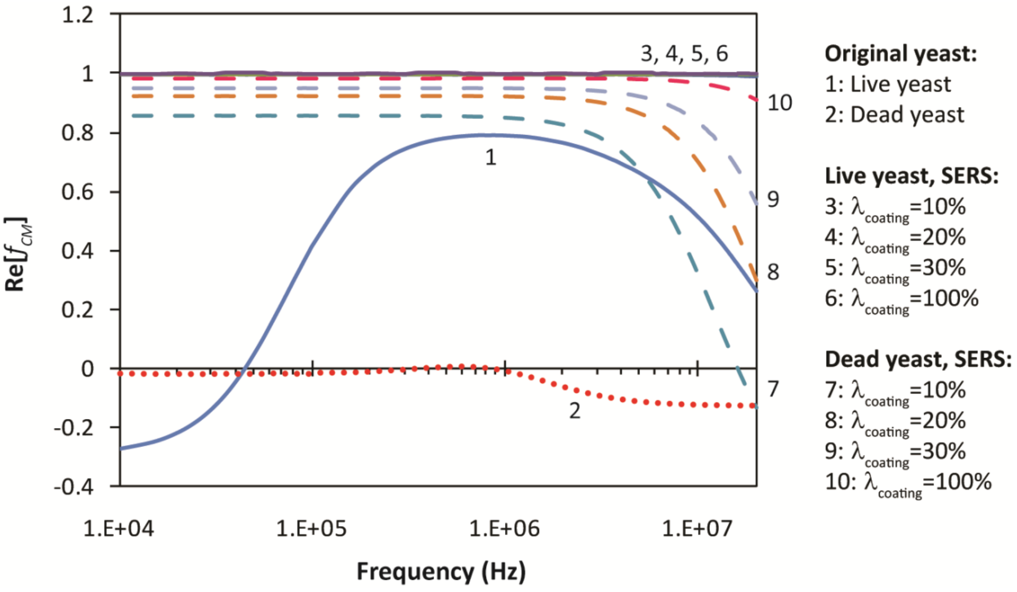

Figure 6.6: Analysing the DEP response of live and dead yeast cells at different coating efficiencies.

Additionally, electric field simulations of the DEP microelectrodes were conducted using equations 4.4 and 4.5 and associated simulation procedures from Chapter 4. The simulation reveals the sharp increase of electric field over the microelectrode tips [21].

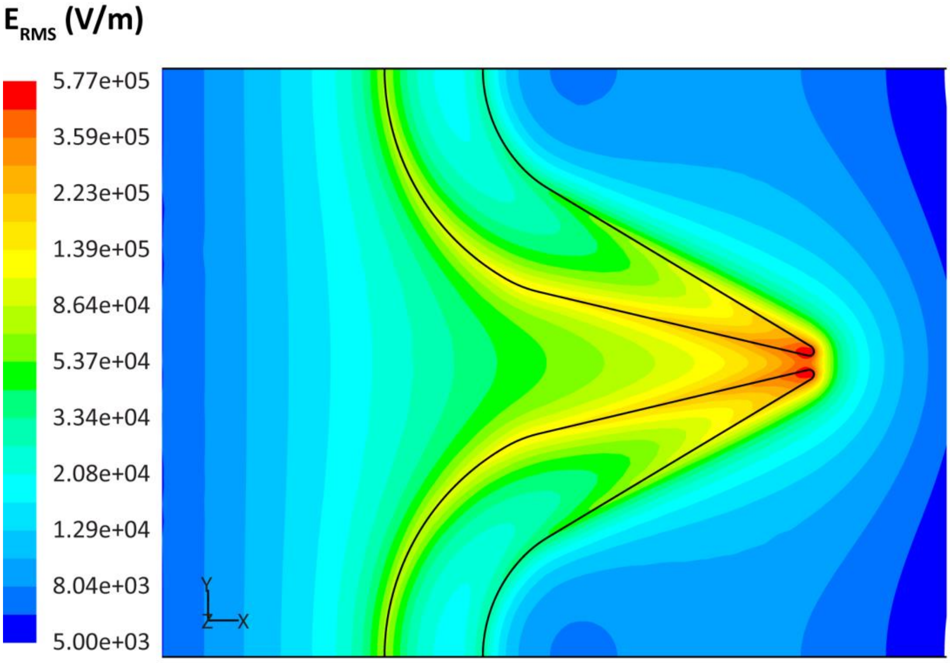

Figure 6.7: The distribution of induced electric field ($V\cdot m^{-1}$) at the surface of the quartz substrate with 5 V applied, obtained by numerical simulation.

6.2.4 Principal component analysis spectral preparation method

Principal component analysis (PCA) is used to visualize and examine the trends in the SERS datasets, as PCA is an efficient means for resolving hidden patterns in spectral data [41, 42]. The loading plots for several principal components (PC's) are used to determine which spectral region most contributed to the variances in the dataset, and ultimately for the determination of potential chemical differences and communications between cells.

The author prepared the SERS spectra for PCA analysis using a two-step approach. First, the spectra were background corrected using a built in MATLAB function called 'msbackadj'. This function estimates the baseline by using a multiple shifted window with a width of 200 cm^{-1}. It then estimates the baseline using a spline approximation, and consequently adjusts the baseline of spectral data. After the background correction function is performed, the data is smoothed using another built in MATLAB function called 'mssgolay', which uses a least-squared digital polynomial filter [43]. The filter is set to have a span width of 15 cm^{-1}, and the centre of the span is incremented by 1 to include both edges of the spectrum.

6.3 Results and discussions

6.3.1 SERS variation

The image in (Figure 6.3) clearly shows silver nanoparticles on the surface of the yeast cells. The distribution of silver over the yeast cells is highly inhomogeneous, which can influence the intensity and Raman shift peaks from the cells. To demonstrate clearly how SERS signals from yeast vary between cells, Figure 6.8 depicts two immobilized cells. The SERS spectra corresponding to the cells is also displayed, which shows that some important Raman shift peaks remain constant (such as the peaks at 624, 724 and 1554 cm^{-1}) while the other change in magnitude, likely due to the various chemical interactions between the silver and the yeast cells [44]. Furthermore, cell morphology differences could also have an impact on the collected SERS signals. These facts could be improved by incorporating cross linking chemicals to allow the nanoparticles to attach to the yeast cells in a more uniform manner. However this approach is not adopted for this work, instead the author employed a statistical analysis approach in order to obtain meaningful results from a large number of samples (>50 in each case) regardless of the silvers inhomogeneous coverage. Additionally, it has been suggested that that >10 SERS spectra from a single cell (distributed evenly on the sample) is generally sufficient for its identification due the angle variation effect on Raman signals [37]. Therefore, the cell spectra presented in this chapter are studied using statistical analysis in order to minimise the effects of natural variation on the outcomes.

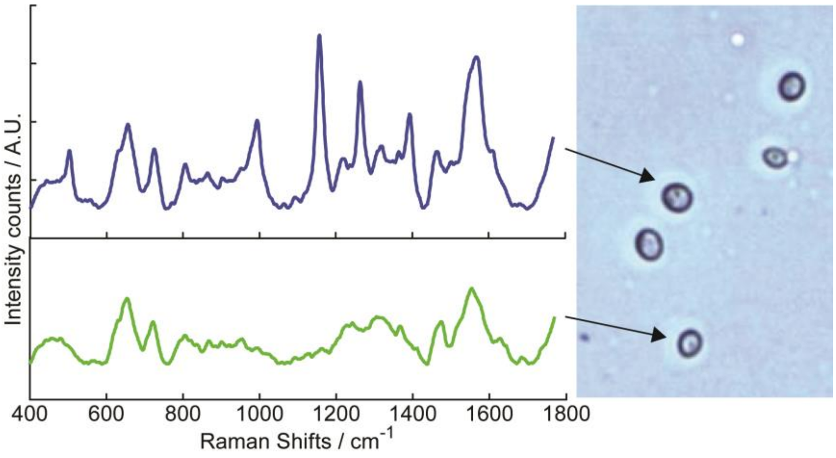

Figure 6.8: Due to the non-homogeneous distribution of silver over the surface of cells, SERS signals from two cells demonstrate significant difference. The two cells imaged here have been prepared in the same batch with identical preparation methods.

6.3.2 Control experiments

Examples of SERS of nanoparticle-yeast (silver and yeast mixed together) Raman spectra for both live and dead cells are presented in Figure 6.9(a) and Figure 6.9(b). As a benchmark, Raman spectrum of silver nanoparticles and pristine yeast cells (no added silver) are also demonstrated (Figure 6.9(c) and Figure 6.9(d), respectively). All data acquisitions are background corrected and obtained inside the microfluidic channel.

The Raman spectrum of a typical pristine yeast cell (Figure 6.9(d)) shows only three low intensity peaks near the 600 cm^{-1} range; and it is determined that those peaks belong to the PDMS from microchannel structure.[21, 45] These PDMS peaks always appear in spectra taken with long acquisition times (120 seconds). For comparison the Raman spectrum of PDMS is shown in Figure 6.9(e). A short acquisition time (20 seconds) is possible for the yeast silver nanoparticles covered cells, causing minimal degradation of the cells by the Raman laser source and eliminating the PDMS signals. The SERS pattern from pristine silver nanoparticles (Figure 6.9(c)) shows strong peaks of D-glucose, as it is present in the liquid surrounding the silver nanoparticles as a by-product in the synthesis process.[35] Both dead (Figure 6.9(a)) and live (Figure 6.9(b)) nanoparticle coated yeast cells show strong SERS signals, even at small acquisition durations of 20 seconds. These signals do not appear to come from pure D-glucose, confirming the validity of the

SERS measurements for identifying cells' Raman peak shifts.

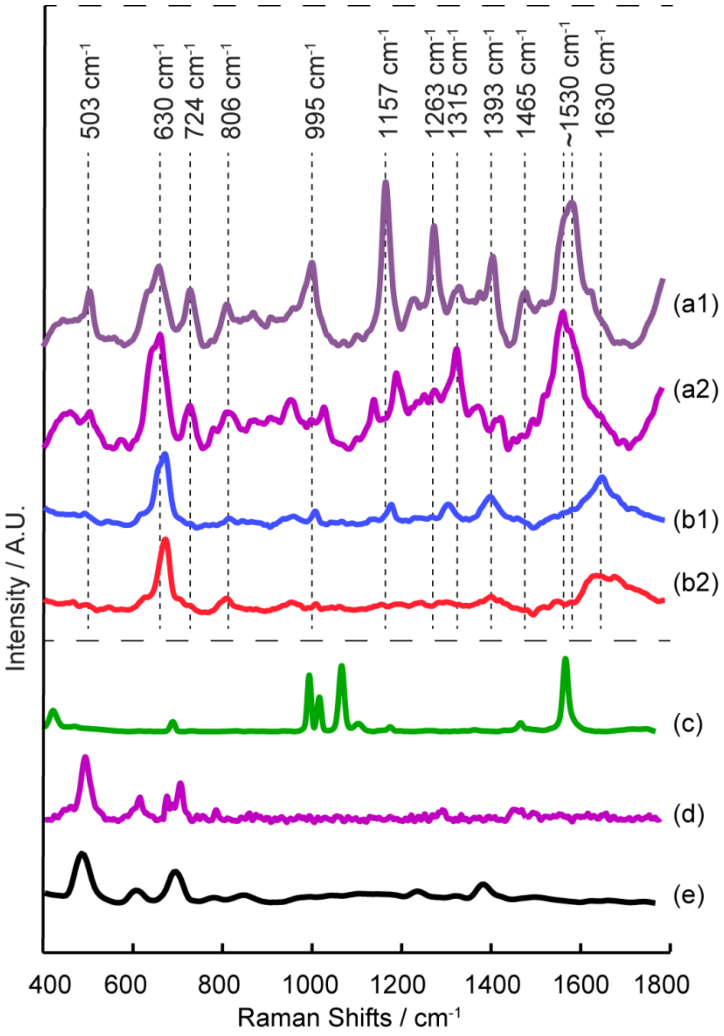

Figure 6.9: Raman spectra for control experiments showing: (a) two examples of live yeast cell SERS (acquisition time of 20 seconds), (b) two examples of dead yeast cell SERS (acquisition time of 20 seconds), (c) pristine suspended silver nanoparticles Raman spectrum (acquisition time of 10 seconds) (d) an example of live pristine yeast Raman spectrum (without nanoparticles coating - acquisition time of 120 seconds) and (e) PDMS Raman spectrum (acquisition time of 10 seconds).

6.3.3 Dead and live yeast cell characterization

The author conducted a series of experiments to assess the capability of the system, and show the outcomes from comparison of dead *vs.* live and grouped *vs.* isolated SERS datasets. For this experimental procedure, live cells were introduced into the channel and trapped using DEP, as shown in Figure 6.1(c). It appeared that the cells do indeed form formations at the electrode tips as predicted by the simulations (Figure 6.7). Additionally, the cells also adhere to the quartz substrate at areas much further away from the electrodes than predicted (Figure 6.1(d)). Isolated cells were targeted with the Raman system, and the resulting spectra were saved. The channel was then cleaned and dead cells were introduced. Again, DEP was used to trap the cells and the SERS spectra from isolated dead cells were saved. The DEP behaviour of dead yeast cells also matches with simulations (Figure 6.6), where silver-coated yeast cells experience positive DEP forces at the applied electric field frequency. Finally, in order to confirm that the cells in the dead SERS test were actually dead, the cells are removed from the microchannel and stained with Trypan blue. The image in Figure 6.10(a) shows a mixture of dead and live cells spread out onto a glass slide, proving that the dead cell mixture does indeed contain dead yeast cells [26]. Only isolated cells are used for comparison of live and dead cell SERS signatures.

Figure 6.10(b) depicts the average SERS patterns of live and dead cells. It is clear that there is a significant difference between the two spectra. The live cell SERS average demonstrates many characteristic peaks for yeast cells walls such as shift peaks from COO– wagging (620 cm^{-1} and 1520 cm^{-1}), amide I (1680 cm^{-1}), δCH_2 (1446 cm^{-1}) and amide II (1518 cm^{-1}) [10, 13, 46, 47]. Alternatively, the average of the spectra from dead yeast cells shows very different Raman shift peaks at 530, 783 and 883 and 1503 cm^{-1}.

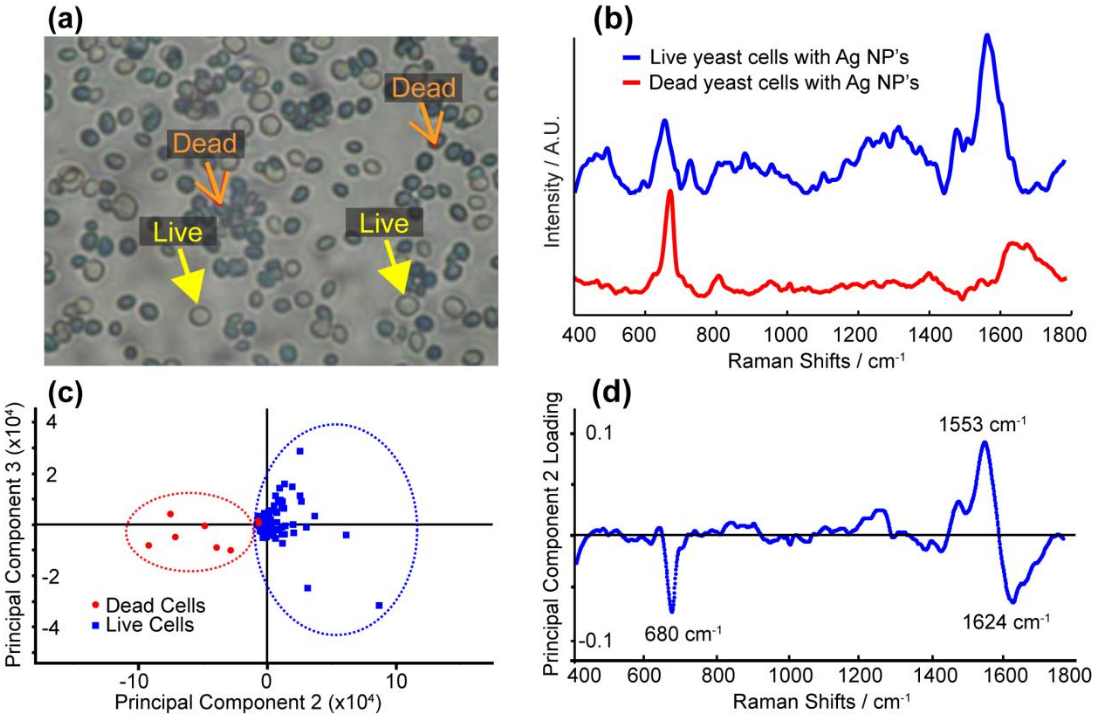

Figure 6.10: Results from SERS of dead and live yeast cells. (a) Image of live and dead cells; dead cells have been stained to highlight them in the image. (b) SERS patterns of live and dead yeast cells covered with silver nanoparticles. (c) PCA score plot for live (blue squares) and dead (red dots) yeast cells, showing live cells with positive PC2 scores, and dead cells with negative PC2 scores (d) loadings plot for PC2 which shows that live cells with positive PC2 scores contain peaks from the positive loading plot, and dead cells SERS with negative PC2 scores contain peaks from the negative side of the PC2 loading plot.

Further assessment of the live and dead yeast cell spectra was carried out using PCA. The output from the analysis is shown in Figure 6.10(c) – (d). The PCA scores plot for PC2 *vs.* PC3 shows a clear distinction between dead (red score dots) and live (blue score squares), which depicts the majority of the variation between the two datasets is along the PC2. The corresponding PC2 loadings plot shows a shift in the SERS peak around 1590 cm^{-1}. More specifically, for live cells, which have positive PC2 scores, the prominent Raman peak shift is at ~1553 cm^{-1} (mainly from amide II) [15]. This peak shifts towards ~1624 cm^{-1} (towards amide I) [46] for the dead cells, which have negative PC2 scores. This peak shift can be attributed to a decrease in amide II levels on the cell wall when a cell undergoes apoptosis, possibly caused by denaturation of the surface glycoproteins induced by the addition of methanol [26]. Additionally, dead cells demonstrate a new SERS peak at 680 cm^{-1}, which can be attributed to C-C stretching peaks from methanol residue.

6.3.4 Behaviour of yeast when isolated or grouped

To investigate targeted cell functions, and possible communications between cells, the author conducted further testing on live yeast cells. Live yeast cells are sorted into isolated and grouped cell clusters using the DEP-microfluidic device, as indicated in Figure 6.1(c), and SERS is conducted from the two types of cell configurations. A particularly interesting observation is that isolated cells exhibit budding (after one hour) whereas for cells in groups budding was very uncommon (as seen in Figure 6.11(a)). The SERS patterns of the isolated cells are tested against the SERS patterns from yeast cells in groups of two or more. The plot in Figure 6.11(b) depicts four randomly chosen SERS patterns, two from each dataset. There is a clear difference between the two cell groupings, with isolated cells demonstrating more "active" SERS patterns than the grouped cells.

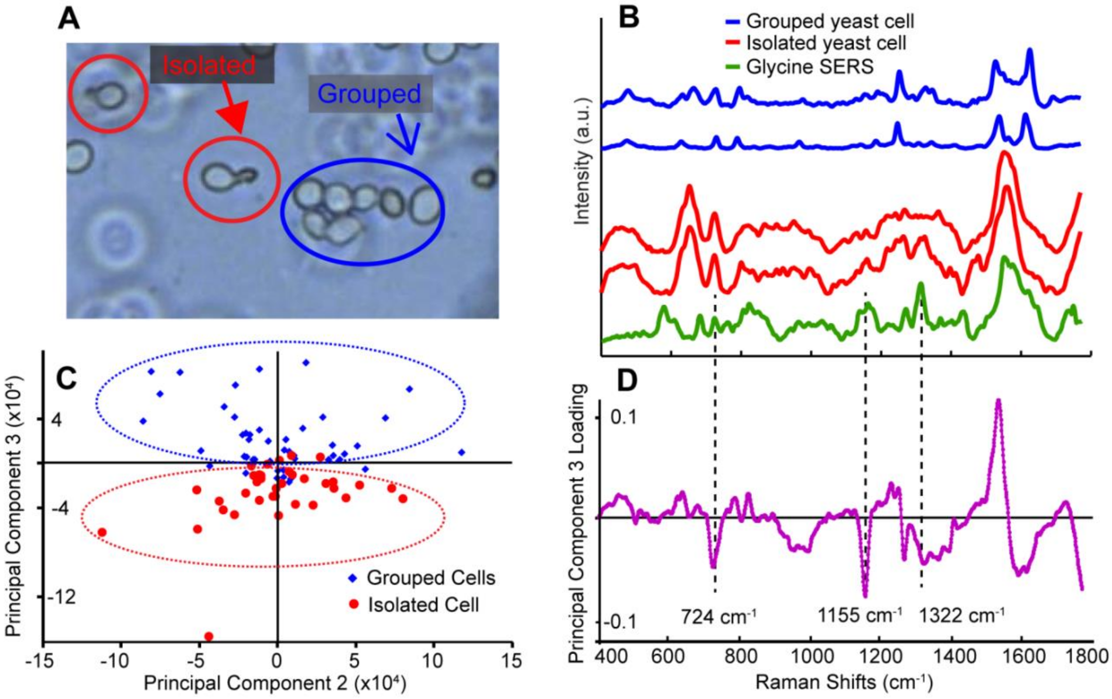

Figure 6.11: Results from SERS of yeast cells either isolated from one another, or in intimate contact. (a) Image of isolated yeast cells budding, and grouped yeast cells being rather stagnant. (b) SERS patterns of isolated yeast cells, grouped yeast cells and pristine glycine. (c) PCA scores plot for isolated and grouped cells showing that isolated cells have negative PC3 scores, while cells in groups have positive PC3 scores. (d) Loadings plot for PC3, one cell SERS contain peaks from the negative side of the PC3 loading, while SERS from grouped cells contain peaks from the positive side of the PC3 loading.

The PCA output is displayed in Figure 6.11(c) – (d); it depicts the scores plot for PC3 *vs.* PC2; indicating that the distinguishing variation between the two cell groupings (isolated and grouped) is mostly due to the PC3 component. The loadings for PC3 are also shown in Figure 6.11(d), which demonstrate the spectra from cells in groups of two or more contain a Raman shift peak at 1532 cm^{-1} (COO–) [15, 46]. Alternatively, when cells are isolated they demonstrate many peaks such as those at 724 (COO– deformation) [46], 1155 (NH_3^+ deformation) [13, 46] and 1322 cm^{-1} (CH_2 wagging) [13, 46].

The peaks present for isolated cells have generally been attributed to either *N*-acetyl-D-glucosamine (NAG) [4, 47-50], cyclic adenosine-5′-monophosphate (cAMP) [51], Ser/Thr Protein [52] or Glycine [46]. However, careful study of the SERS peaks generated by NAG, cAMP and Ser/Thr rule them out as possible candidates, as they all contain phosphate groups whose SERS peaks are not present in the PC3 loading. Instead, glycine is a possible perfect fit for the variance of the SERS patterns between the isolated and grouped cell clusters (Figure 6.11(b)). Additionally, in most of the isolated cell signals the dissolved CO_2 ν_u band also appears at ~1385 cm^{-1}.[53] The presence of dissolved CO_2 makes sense as yeast produce CO_2 during the budding process.[54-56] Furthermore, the sharp peak shift of amide II around ~1550 cm^{-1} is much larger in grouped cells than the isolated cells.[15] This can be due to the budding process disrupting the cell membrane in isolated cells, hence reducing this peak intensity. Interestingly, a slightly shifted and broadened peaks shift around ~1580 cm^{-1} is always seen for the isolated cells. This peak, and the broad peak in the region of 900 to 100 cm^{-1} only seen in the isolated cell signals, can be a combination of several Raman peak shifts that yet to be investigated and identified.

Specifically, the sharp peaks at 724, 1155 and 1323 cm^{-1} (Figure 6.11(b)) are all present in isolated cell spectra, and are likely caused by the different components of the glycine structure (NH_2CH_2COOH) [46]. It is known that glycine, as an amino acid used in cells for one-carbon metabolism, can play an important role in the synthesis of metabolites needed for cell growth and cell division [3, 57, 58]. One carbon metabolism is also important for cell wall synthesis, since a metabolite from the pathway, L-serine, makes up a significant proportion of many cell wall proteins [59]. Additionally, yeast cells have very active chemical transporters that take up or release glycine [3]. Recently, similar observations have also been reported regarding the presence of glycine during cancer cell slow proliferation [60] and that the concentration of glycine outside such cancer cells is high. It seems that, similar to cancer cells with a low rate of proliferation, yeast cell glycine production may exceed endogenous cell requirement and the excess is released to the environment. The other possible candidate that would explain the presence of glycine peaks is the secretion of proteins that contain this amino acid unit as a functional group, which should be investigated further.

6.3.5 Complimentary cell proliferation tests

In order to assess the effects of glycine on cell proliferation, and help support the hypothesis that glycine does indeed play a role in the process, the author conducted a set of experiments. A single batch of yeast cells was prepared in a similar fashion to the previous SERS tests. The yeasts were divided into two equal volumes where each volume was mixed with test sugars as follows: (i) 10 % glucose and 10 % glycine and (ii) 10 % glucose and 0.5 % glycine. The number of cells was assessed every 10 minutes for the duration of three hours.

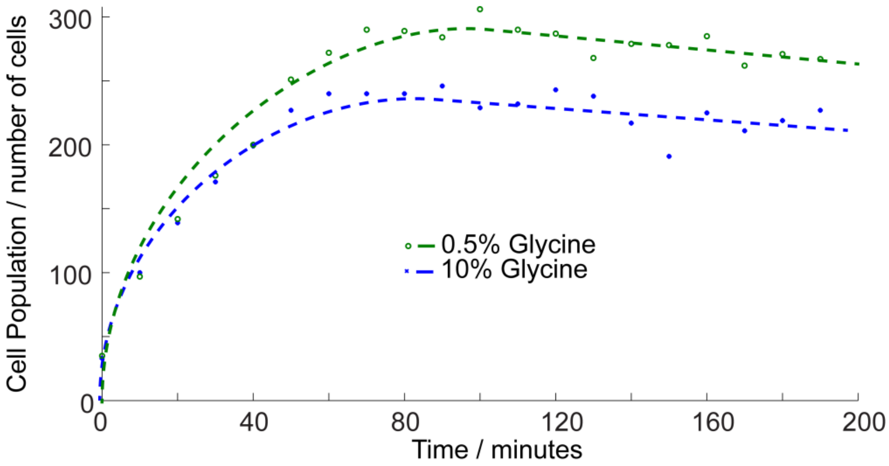

Figure 6.12: The cell population density over time during two tests with different levels of added glycine, where the test which contained more added glycine had a reduced cell count.

The author observed that while yeast proliferation was high for test (ii), the conditions of test (i) were the least favourable for the proliferation of yeast cells (Figure 6.12). It confirms that the presence of excess amounts of glycine retard the proliferation process, and do play a potential roll in the process.

6.4 Summary

In this chapter, the author demonstrated that *in situ* SERS measurements can be utilized to investigate the targeted functions of cells covered with silver nanoparticles. The integration of silver nanoparticles increases the intensity of SERS signals, making it possible to keep the DEP immobilized cells under chemical surveillance in the microfluidic environment. PCA was able to define and classify a large number of SERS patterns into distinct groups based on selected physiological properties (i.e., live/dead, isolated/grouped). The thorough analysis of results can draw conclusions about the cells' biological behaviour, in this case, signifying the presence of chemicals and proteins around isolated cells before the budding process, a condition that is not observed for grouped cells. This chapter has highlighted the novel work conducted by the author for the investigation of cells in microfluidic environments, coupled with multivariable analysis, for determining potential chemical transmitters. In the following chapter, the author presents a summary of his PhD thesis, and discusses future work related to his PhD research project.

References

[1] Chrimes, A.F., K. Khoshmanesh, T. Shi-Yang, B.R. Wood, P.R. Stoddart, S.S.E. Collins, A. Mitchell, and K. Kalantar-zadeh, In situ SERS probing of nano-silver coated individual yeast cells. *Biosensors & Bioelectronics*, 2013 - Under review.

[2] Seaston, A., G. Carr, and A.A. Eddy, Concentration of Glycine by Preparations of Yeast *Saccharomyces-Carlsbergensis* Depleted of Adenosine-Triphosphate - Effects of Proton Gradients and Uncoupling Agents. *Biochemical Journal*, vol. 154, pp. 669-676, 1976.

[3] Piper, M.D., S.P. Hong, G.E. Ball, and I.W. Dawes, Regulation of the balance of one-carbon metabolism in Saccharomyces cerevisiae. *Journal of Biological Chemistry*, vol. 275, pp. 30987-30995, 2000.

[4] Zelada, A., R. Castilla, S. Passeron, and M.L. Cantore, Reassessment of the effect of glucagon and nucleotides on Candida albicans germ tube formation. *Cellular and Molecular Biology*, vol. 42, pp. 567-576, 1996.

[5] Taylor, A.F., M.R. Tinsley, F. Wang, Z.Y. Huang, and K. Showalter, Dynamical Quorum Sensing and Synchronization in Large Populations of Chemical Oscillators. *Science*, vol. 323, pp. 614-617, 2009.

[6] von Stockar, U., P. Duboc, L. Menoud, and I.W. Marison, On-line calorimetry as a technique for process monitoring and control in biotechnology. *Thermochimica Acta*, vol. 300, pp. 225-236, 1997.

[7] Singh, G.P., C.M. Creely, G. Volpe, H. Grotsch, and D. Petrov, Real-time detection of hyperosmotic stress response in optically trapped single yeast cells using Raman microspectroscopy. *Analytical Chemistry*, vol. 77, pp. 2564-2568, 2005.

[8] Thevelein, J.M., Signal Transduction in Yeast. *Yeast,* vol. 10, pp. 1753-1790, 1994.

[9] Lipke, P.N. and R. Ovalle, Cell wall architecture in yeast: New structure and new challenges. *Journal of Bacteriology,* vol. 180, pp. 3735-3740, 1998.

[10] Honigberg, S.M., Cell Signals, Cell Contacts, and the Organization of Yeast Communities. *Eukaryotic Cell,* vol. 10, pp. 466-473, 2011.

[11] Chen, M.T. and R. Weiss, Artificial cell-cell communication in yeast Saccharomyces cerevisiae using signaling elements from Arabidopsis thaliana. *Nature Biotechnology,* vol. 23, pp. 1551-1555, 2005.

[12] Li, J.F., Y.F. Huang, Y. Ding, Z.L. Yang, S.B. Li, X.S. Zhou, F.R. Fan, W. Zhang, Z.Y. Zhou, D.Y. Wu, B. Ren, Z.L. Wang, and Z.Q. Tian, Shell-isolated nanoparticle-enhanced Raman spectroscopy. *Nature,* vol. 464, pp. 392-395, 2010.

[13] Sujith, A., T. Itoh, H. Abe, K.I. Yoshida, M.S. Kiran, V. Biju, and M. Ishikawa, Imaging the cell wall of living single yeast cells using surface-enhanced Raman spectroscopy. *Analytical and Bioanalytical Chemistry,* vol. 394, pp. 1803-1809, 2009.

[14] Sayin, I., M. Kahraman, F. Sahin, D. Yurdakul, and M. Culha, Characterization of Yeast Species Using Surface-Enhanced Raman Scattering. *Applied Spectroscopy,* vol. 63, pp. 1276-1282, 2009.

[15] Sujith, A., T. Itoh, H. Abe, A.A. Anas, K. Yoshida, V. Biju, and M. Ishikawa, Surface enhanced Raman scattering analyses of individual silver nanoaggregates on living single yeast cell wall. *Applied Physics Letters,* vol. 92, pp. 103901:1-3, 2008.

[16] Xie, W., L. Su, A.G. Shen, A. Materny, and J.M. Hu, Application of surface-enhanced Raman scattering in cell analysis. *Journal of Raman Spectroscopy,* vol. 42, pp. 1248-1254, 2011.

[17] Guo, X., Z.Y. Guo, Y. Jin, Z.M. Liu, W. Zhang, and D.Q. Huang, Silver-gold core-shell nanoparticles containing methylene blue as SERS labels for probing and imaging of live cells. *Microchimica Acta,* vol. 178, pp. 229-236, 2012.

[18] Feng, S.Y., J.Q. Lin, M. Cheng, Y.Z. Li, G.N. Chen, Z.F. Huang, Y. Yu, R. Chen, and H.S. Zeng, Gold Nanoparticle Based Surface-Enhanced Raman Scattering Spectroscopy of Cancerous and Normal Nasopharyngeal Tissues Under Near-Infrared Laser Excitation. *Applied Spectroscopy,* vol. 63, pp. 1089-1094, 2009.

[19] Ando, J., K. Fujita, N.I. Smith, and S. Kawata, Dynamic SERS Imaging of Cellular Transport Pathways with Endocytosed Gold Nanoparticles. *Nano Letters,* vol. 11, pp. 5344-5348, 2011.

[20] Kayani, A.A., K. Khoshmanesh, T.G. Nguyen, G. Kostovski, A.F. Chrimes, M. Nasabi, D.A. Heller, A. Mitchell, and K. Kalantar-zadeh, Dynamic manipulation of modes in an optical waveguide using dielectrophoresis. *Electrophoresis,* vol. 33, pp. 2075-2085, 2012.

[21] Chrimes, A.F., A.A. Kayani, K. Khoshmanesh, P.R. Stoddart, P. Mulvaney, A. Mitchell, and K. Kalantar-zadeh, Dielectrophoresis-Raman spectroscopy system for analysing suspended nanoparticles. *Lab on a Chip,* vol. 11, pp. 921-928, 2011.

[22] Liang, H., K.T. Vu, P. Krishnan, T.C. Trang, D. Shin, S. Kimel, and M.W. Berns, Wavelength dependence of cell cloning efficiency after optical trapping. *Biophysical Journal*, vol. 70, pp. 1529-1533, 1996.

[23] Khoshmanesh, K., S. Nahavandi, S. Baratchi, A. Mitchell, and K. Kalantar-zadeh, Dielectrophoretic platforms for bio-microfluidic systems. *Biosensors & Bioelectronics,* vol. 26, pp. 1800-1814, 2011.

[24] Lapizco-Encinas, B.H., B.A. Simmons, E.B. Cummings, and Y. Fintschenko, Dielectrophoretic concentration and separation of live and dead bacteria in an array of insulators. *Analytical Chemistry,* vol. 76, pp. 1571-1579, 2004.

[25] Pohl, H.A. and J.S. Crane, Dielectrophoresis of cells. *Biophysical Journal,* vol. 11, pp. 711-727, 1971.

[26] Khoshmanesh, K., C. Zhang, F.J. Tovar-Lopez, S. Nahavandi, S. Baratchi, A. Mitchell, and K. Kalantar-zadeh, Dielectrophoretic-activated cell sorter based on curved microelectrodes. *Microfluidics and Nanofluidics,* vol. 9, pp. 411-426, 2010.

[27] Morgan, H. and N.G. Green, *AC Electrokinetics: Colloids and Nanoparticles*. 2003, Baldock: Research Studies Press.

[28] Muller, T., A. Pfennig, P. Klein, G. Gradl, M. Jager, and T. Schnelle, The potential of dielectrophoresis for single-cell experiments. *IEEE Engineering in Medicine and Biology Magazine,* vol. 22, pp. 51-61, 2003.

[29] Valic, B., M. Golzio, M. Pavlin, A. Schatz, C. Faurie, B. Gabriel, J. Teissie, M.P. Rols, and D. Miklavcic, Effect of electric field induced transmembrane potential on spheroidal cells: theory and experiment. *European Biophysics Journal with Biophysics Letters,* vol. 32, pp. 519-528, 2003.

[30] Krassowska, W. and J.C. Neu, Response of a Single-Cell to an External Electric-Field. *Biophysical Journal,* vol. 66, pp. 1768-1776, 1994.

[31] Kononenko, V.L. and J.K. Shimkus, Stationary deformations of erythrocytes by high-frequency electric field. *Bioelectrochemistry and Bioenergetics,* vol. 52, pp. 187-196, 2000.

[32] Neek-Amal, M., A. Lajevardipour, and H.R. Sepangi, Electric field effects on Nano-Scale bio-membrane of spherical cells. *Physica A: Statistical Mechanics and its Applications,* vol. 388, pp. 120-128, 2009.

[33] Sriram, S., M. Bhaskaran, S. Chen, S. Jayawardhana, P.R. Stoddart, J.Z. Liu, N.V. Medhekar, K. Kalantar-zadeh, and A. Mitchell, Influence of Electric Field on SERS: Frequency Effects, Intensity Changes, and Susceptible Bonds. *Journal of the American Chemical Society,* vol. 134, pp. 4646-4653, 2012.

[34] Urdaneta, M. and E. Smela, Multiple frequency dielectrophoresis. *Electrophoresis,* vol. 28, pp. 3145-3155, 2007.

[35] Panacek, A., L. Kvitek, R. Prucek, M. Kolar, R. Vecerova, N. Pizurova, V.K. Sharma, T.j. Nevecna, and R. Zboril, Silver colloid nanoparticles: Synthesis, characterization, and their antibacterial activity. *Journal of Physical Chemistry B,* vol. 110, pp. 16248-16253, 2006.

[36] Delfino, I., A.R. Bizzarri, and S. Cannistraro, Single-molecule detection of yeast cytochrome c by Surface-Enhanced Raman Spectroscopy. *Biophysical Chemistry,* vol. 113, pp. 41-51, 2005.

[37] Rosch, P., M. Harz, M. Schmitt, and J. Popp, Raman spectroscopic identification of single yeast cells. *Journal of Raman Spectroscopy,* vol. 36, pp. 377-379, 2005.

[38] Martínez-Castañón, G.A., N. Niño-Martínez, F. Martínez-Gutierrez, J.R. Martínez-Mendoza, and F. Ruiz, Synthesis and antibacterial activity of silver nanoparticles with different sizes. *Journal of Nanoparticle Research,* vol. 10, pp. 1343-1348, 2008.

[39] Khoshmanesh, K., S. Baratchi, F. Tovar-Lopez, S. Nahavandi, D. Wlodkowic, A. Mitchell, and K. Kalantar-zadeh, On-chip separation of *Lactobacillus* bacteria from yeasts using dielectrophoresis. *Microfluidics and Nanofluidics,* vol. 12, pp. 597-606, 2012.

[40] Pethig, R., Dielectrophoresis: Status of the theory, technology, and applications. *Biomicrofluidics,* vol. 4, pp. 022811-35, 2010.

[41] Wold, S., Pattern recognition by means of disjoint principal components models. *Pattern Recognition,* vol. 8, pp. 127-139, 1976.

[42] Wood, B.R., E. Bailo, M.A. Khiavi, L. Tilley, S. Deed, T. Deckert-Gaudig, D. McNaughton, and V. Deckert, Tip-Enhanced Raman Scattering (TERS) from Hemozoin Crystals within a Sectioned Erythrocyte. *Nano Letters,* vol. 11, pp. 1868-1873, 2011.

[43] Di Anibal, C.V., L.F. Marsal, M.P. Callao, and I. Ruisánchez, Surface Enhanced Raman Spectroscopy (SERS) and multivariate analysis as a screening tool for detecting Sudan I dye in culinary spices. *Spectrochimica Acta Part A: Molecular and Biomolecular Spectroscopy,* vol. 87, pp. 135-141, 2012.

[44] Manikantan Syamala, K., H. Abe, Y. Fujita, K. Tomimoto, V. Biju, M. Ishikawa, Y. Ozaki, and T. Itoh, Inhibition Assay of Yeast Cell Walls by Plasmon Resonance Rayleigh Scattering and Surface-Enhanced Raman Scattering Imaging. *Langmuir,* vol. 28, pp. 8952-8958, 2012.

[45] Chrimes, A.F., K. Khoshmanesh, P.R. Stoddart, A.A. Kayani, A. Mitchell, H. Daima, V. Bansal, and K. Kalantar-zadeh, Active Control of Silver Nanoparticles Spacing Using Dielectrophoresis for Surface-Enhanced Raman Scattering. *Analytical Chemistry,* vol. 84, pp. 4029-4035, 2012.

[46] Stewart, S. and P.M. Fredericks, Surface-enhanced Raman Spectroscopy of Peptides and Proteins Adsorbed on an Electrochemically Prepared Silver Surface. *Spectrochimica Acta Part a-Molecular and Biomolecular Spectroscopy,* vol. 55, pp. 1615-1640, 1999.

[47] Downes, A. and A. Elfick, Raman Spectroscopy and Related Techniques in Biomedicine. *Sensors,* vol. 10, pp. 1871-1889, 2010.

[48] Jarvis, R.M. and R. Goodacre, Discrimination of bacteria using surface-enhanced Raman spectroscopy. *Analytical Chemistry,* vol. 76, pp. 40-47, 2004.

[49] Chaffin, W.L., J.L. Lopez-Ribot, M. Casanova, D. Gozalbo, and J.P. Martinez, Cell wall and secreted proteins of Candida albicans: Identification, function, and expression. *Microbiology and Molecular Biology Reviews,* vol. 62, pp. 130-180, 1998.

[50] Castilla, R.o., S. Passeron, and M.a.L. Cantore, N-Acetyl-d-Glucosamine Induces Germination in Candida albicans through a Mechanism Sensitive to Inhibitors of cAMP-Dependent Protein Kinase. *Cellular Signalling,* vol. 10, pp. 713-719, 1998.

[51] Ervin, K.M., E. Koglin, J.M. Sequaris, P. Valenta, and H.W. Nürnberg, Surface enhanced Raman spectra of nucleic acid components adsorbed at a silver electrode. *Journal of Electroanalytical Chemistry and Interfacial Electrochemistry,* vol. 114, pp. 179-194, 1980.

[52] Zhang, D., C. Ortiz, Y. Xie, V.J. Davisson, and D. Ben-Amotz, Detection of the site of phosphorylation in a peptide using Raman spectroscopy and partial least squares discriminant analysis. *Spectrochimica Acta Part A: Molecular and Biomolecular Spectroscopy,* vol. 61, pp. 471-475, 2005.

[53] Liu, N., C. Aymonier, C. Lecoutre, Y. Garrabos, and S. Marre, Microfluidic approach for studying CO2 solubility in water and brine using confocal Raman spectroscopy. *Chemical Physics Letters,* vol. 551, pp. 139-143, 2012.

[54] Kaspar von Meyenburg, H., Energetics of the budding cycle of Saccharomyces cerevisiae during glucose limited aerobic growth. *Archiv für Mikrobiologie*, vol. 66, pp. 289-303, 1969.

[55] Novak, B. and J.M. Mitchison, Change in the rate of CO_2 production in synchronous cultures of the fission yeast Schizosaccharomyces pombe: a periodic cell cycle event that persists after the DNA-division cycle has been blocked. *Journal of Cell Science,* vol. 86, pp. 191-206, 1986.

[56] Lumsden, W.B., J.H. Duffus, and J.C. Slaughter, Effects of CO_2 on Budding and Fission Yeasts. *Journal of General Microbiology,* vol. 133, pp. 877-881, 1987.

[57] Wu, G., Amino acids: metabolism, functions, and nutrition. *Amino Acids,* vol. 37, pp. 1-17, 2009.

[58] Flynn, N.E., M.E. Patyrak, J.B. Seely, and G. Wu, Glycine oxidation and conversion into amino acids in Saccharomyces cerevisiae and Candida albicans. *Amino Acids,* vol. 39, pp. 605-608, 2010.

[59] Tsoi, B.M., A.G. Beckhouse, C.L. Gelling, M.J. Raftery, J. Chiu, A.M. Tsoi, L. Lauterbach, P.J. Rogers, V.J. Higgins, and I.W. Dawes, Essential Role of One-carbon Metabolism and Gcn4p and Bas1p Transcriptional Regulators during Adaptation to Anaerobic Growth of Saccharomyces cerevisiae. *Journal of Biological Chemistry,* vol. 284, pp. 11205-11215, 2009.

[60] Jain, M., R. Nilsson, S. Sharma, N. Madhusudhan, T. Kitami, A.L. Souza, R. Kafri, M.W. Kirschner, C.B. Clish, and V.K. Mootha, Metabolite Profiling Identifies a Key Role for Glycine in Rapid Cancer Cell Proliferation. *Science,* vol. 336, pp. 1040-1044, 2012.

Chapter 7

Conclusions and future work

7.1 Concluding remarks

The author's vision for this PhD involved creating microfluidic devices, integrated with optical sensing systems, for the detection and monitoring of suspended materials including inorganic, organic and live cells. This vision was realised using Raman microscopy, which provides spectral information from target materials, and could be readily integrated with microfluidic devices. Additionally, the integration of dielectrophoresis (DEP) into the microfluidic devices provided the controlling feature for manipulating the positions of suspended materials, helping to immobilise particles in preparation for Raman microscopy studies. The author sought to develop this system for high sensitivity detection of biological materials, and worked towards surface-enhanced Raman scattering of analytes and cells.

In the course of preparing this research the author observed many reports on Raman microscopy-microfluidics integrations. However, a comprehensive review on Raman microscopy in microfluidic environments was lacking. As a result, the author has submitted for publication a review article which provides readers with a detailed understanding of the capabilities of such systems and the potential applications that they offer. The article highlighted the need for effective control mechanisms over suspended material in microfluidics, a research area where information is lacking. As such, the author's research was organised and conducted in three distinct stages so as to target the previously identified research deficiencies. In the first stage, he demonstrated the Raman microscopy detection of suspended metal oxide and polystyrene particles. These particles were readily manipulated using DEP, and

Raman microscopy was utilized for studies of the particles in process, including spatial mapping, depth profiling and applied electric frequency profiling for DEP. Subsequently, the second stage implemented the DEP control of suspended metallic silver nanoparticles for the SERS detection of organic materials such as dipicolinic acid and glucose. The third and final stage of this PhD research project implemented SERS monitoring of live cells in a microfluidic channel, where DEP was utilized to immobilise the cells into specific clusters prior to analysis.

The major findings in each stage of this PhD research project are summarised as follows:

7.1.1 Stage 1

- In the first stage of the research, the author demonstrated the capability of a novel microfluidic-Raman system to determine the concentration of suspended nanoparticles, specifically tungsten trioxide and polystyrene nanoparticles. The author verified the ability of the system to perform optical Raman measurements on moving suspended nanoparticles that were manipulated using DEP. The integration of DEP produced areas of high and low particle concentrations, where a Raman system was implemented to assess the type and concentration of the particles.
- Detailed simulations for the operation of the microfluidic-DEP device were presented by the author. The simulation material provided the author with insight into the operation and behaviour of the DEP platform, specifically in which cases the applied DEP force is positive of negative in nature, and the magnitude and direction of the applied DEP force on a particle. This information is invaluable when coupled with Raman microscopic studies for applications such as determining the relationship between applied electric field frequency and Raman signal intensities from the suspended materials that originates from their concentrations and spacing.
- The novel integration of Raman microscopy, microfluidics and DEP was employed to study nanoparticle aggregate formations at the tip areas of the DEP microelectrodes. Raman signatures from the suspended materials were utilized to map the positions and densities of suspended particle aggregates in the area around the microelectrodes. Furthermore, the Raman microscopy system was

capable of providing concentration information as a function of depth into the microchannel. These unique findings can be used for further understanding the behaviour of particles in the microfluidic-DEP device.

- To the best of the author's knowledge, this was the first demonstration of Raman microscopy integrations with a microfluidic-DEP system for the spatial studies of suspended materials. This is of utmost importance, as an analytical tool, such a platform can create many exciting opportunities for research. The platform will allow for *in situ* analysis of particles, without the need to dehydrate the samples before performing Raman spectroscopy.

7.1.2 Stage 2

- In this stage, the author presented a novel combination of DEP and hydrodynamic forces for actively manipulating and controlling suspended SERS generating metallic colloids. The unique integration provided facile control over the colloid particles spacings in order to maximise SERS intensities. Dipicolinic acid (DPA) was used as the target analyte, and was measured to concentration levels as low as ~1 ppm.
- The system was able to manipulate the suspended silver particles and produce well-controlled hot-spots to augment the SERS signals. This was confirmed through several simulations and theoretical calculations which determined the mean inter-particle spacing for DEP focussed particles as 3.5 – 10 nm, within the known range for SERS hot-spot creation. The procedure was reversible, as once the DEP force was removed the particles could re-suspend and be washed away by the flow system.
- Characterization techniques of UV-Vis and FTIR spectroscopy as well as XPS analysis were implemented to confirm the presence of DPA on silver particles and the used to verify the results of the Raman detection of DPA.
- This was the first implementation of a tuneable microfluidic-DEP device for the SERS detection of suspended analytes using suspended nanoparticles of silver.

7.1.3 Stage 3

- In the final stage, the author conducted research into live cells utilising *in situ* SERS measurements studied in the previous stage. Silver nanoparticles were used for generating SERS signals from the surface of cells in order to investigate the targeted functions of cells. The integration of DEP is utilized for immobilizing cells so as to implement Raman microscopy for chemical surveillance in the microfluidic environment.

- The author conducted simulations of dielectrophoretic force experience by yeast cells, including those detailing the behaviour of cells that are alive or dead. This information assisted in determining optimal DEP force parameters for trapping cells, providing the information needed to tune the DEP force of isolating single cells from larger cell clusters.
- The author implemented multivariable principal component analysis (PCA) in order to define and classify the large number of SERS patterns into distinct groups based on selected physiological properties (i.e., live/dead, isolated/grouped). The analysis of results allowed the author to draw conclusions about the cells' biological behaviour. This result demonstrated a potential role for glycine in the proliferation of yeast cells, either as an independent amino acid unit, or integrated into a larger protein structure.
- The research conducted by the author in this stage was the first demonstration of *in situ* SERS monitoring of dielectrophoretically trapped cells in a fluid environment. Additionally, this unique work combines PCA into the data analysis process in order to classify and determine the chemical differences between cells from different life stages and cluster formations.

In conclusion, this research project has successfully bought new knowledge and ideas to the fields of microfluidics and biosensing. The outcomes of this PhD research have been published in prestigious peer reviewed scientific journals and conference proceedings. A complete list of publications by the author since the beginning of his PhD research project, are as follows:

7.2 Journal publications:

- **Chrimes, A.F.**, K. Khoshmanesh, P.R. Stoddart, A. Mitchell, and K. Kalantar-zadeh, Microfluidics and Raman microscopy: current applications and future challenges. *Chemical Society Reviews*, 2013 doi: 10.1039/c3cs35515b.
- **Chrimes, A.F.**, K. Khoshmanesh, P.R. Stoddart, A.A. Kayani, A. Mitchell, H. Daima, V. Bansal, and K. Kalantar-zadeh, Active Control of Silver Nanoparticles Spacing Using Dielectrophoresis for Surface-Enhanced Raman Scattering.

Analytical Chemistry, vol. 84, pp. 4029-4035, 2012.

- **Chrimes, A.F.**, A.A. Kayani, K. Khoshmanesh, P.R. Stoddart, P. Mulvaney, A. Mitchell, and K. Kalantar-zadeh, Dielectrophoresis-Raman spectroscopy system for analysing suspended nanoparticles. *Lab on a Chip*, vol. 11, pp. 921-928, 2011.
- **Chrimes, A.F.**, K. Khoshmanesh, T. Shi-Yang, B.R. Wood, P.R. Stoddart, S.S.E. Collins, A. Mitchell, and K. Kalantar-zadeh, In situ SERS probing of nano-silver coated individual yeast cells. *Biosensors & Bioelectronics*, 2013 - Under review.
- Yi, P., A.A. Kayani, **A.F. Chrimes**, K. Ghorbani, S. Nahavandi, K. Kalantar-zadeh, and K. Khoshmanesh, Thermal analysis of nanofluids in microfluidics using an infrared camera. *Lab on a Chip*, vol. 12, pp. 2520-2525, 2012.
- Kayani, A.A., K. Khoshmanesh, T.G. Nguyen, G. Kostovski, **A.F. Chrimes**, M. Nasabi, D.A. Heller, A. Mitchell, and K. Kalantar-zadeh, Dynamic manipulation of modes in an optical waveguide using dielectrophoresis. *Electrophoresis*, vol. 33, pp. 2075-2085, 2012.
- Kayani, A.A., **A.F. Chrimes**, K. Khoshmanesh, V. Sivan, E. Zeller, K. Kalantar-zadeh, and A. Mitchell, Interaction of guided light in rib polymer waveguides with dielectrophoretically controlled nanoparticles. *Microfluidics and Nanofluidics*, vol. 11, pp. 93-104, 2011.

7.3 Conference publications:

- **Chrimes, A.F.**, A. Kayani, K. Khoshmanesh, and K. Kalantar-zadeh, Dielectrophoresis-Raman Spectroscopy System for Analysing Suspended WO_3 Nanoparticles. Proc. SPIE 8031, *Micro- and Nanotechnology Sensors, Systems, and Applications III*, 2011, pp. 803135; doi:10.1117/12.887300.
- Khoshmanesh, K., F.J. Tovar-Lopez, S. Baratchi, C. Zhang, A.A. Kayani, **A.F. Chrimes**, S. Nahavandi, D. Wlodkowic, A. Mitchell, and K. Kalantar-zadeh, Dielectrophoresis of micro/nano particles using curved microelectrodes. Proc. SPIE 8204, *Smart Nano-Micro Materials and Devices*, 2011, pp. 82040G; doi:10.1117/12.903183.
- Kayani, A.A., **A.F. Chrimes**, K. Khoshmanesh, K. Kalantar-zadeh, and A. Mitchell, Tuneable Optical Waveguide Based on Dielectrophoresis and Microfluidics. Proc. SPIE 8031, *Micro- and Nanotechnology Sensors, Systems,*

and Applications III, 2011, pp. 803134; doi:10.1117/12.887184.

- Kayani, A., **A.F. Chrimes**, K. Khoshmanesh, K. Kalantar-zadeh, and A. Mitchell, *Dielectrophoresis of Nanoparticles for Polymer Waveguide Manipulation.* in Optical Society of America, 2011, pp. JWA109.

7.4 Recommendations for future work

Significant strides have been made in Raman-microfluidic integrations as part of this PhD research project, however the author feels that there are still numerous opportunities for continuing research in the alignment with those presented in this thesis, and recommends the following as future work:

- The evolution of microfluidic fabrication will allow for the fabrication of advanced microfluidic platforms for manipulating suspended materials. Specifically, the fabrication of three dimensional microelectrode structures would allow for immobilising of particles in the centre of the microfluidic channels. This can reduce Raman noise from substrate materials, and reduce the interaction of materials with the microchannel walls, which could possibly cause interfering Raman signals.
- The application of other forces such as magnetic [1] and acoustic [2], can be used for trapping and manipulating suspended materials in combination with DEP forces to provide even more accurate particle control. Such combinations can provide further sorting and filtering abilities as particles can be separated and trapped based not only on their dielectric properties, but also magnetic susceptibility and particle elasticity.
- Research into fully integrated Lab-on-a-chip systems which can be integrated with Raman microspectroscopy is needed. It is envisioned that compact Raman-microfluidic systems will be widespread for both commercial and private use. Raman analysis may be used for quality control in production factories dealing with fluids such as milk, beverages, water, oils and other fluid products [3, 4]. Low-cost Raman microfluidics may even be introduced in systems operated by smart phones. Such systems could assist individual users with the determination of unknown liquid samples or could be used as accurate personal health monitors.
- There is a potential for Raman microscopy in microfluidics to be performed using other optical platforms that those integrating bulky microscopes. Optical

waveguides and be fabricated in line with the DEP microelectrodes to allow for Raman analysis of the material in contact with the waveguide at lower costs [5].

- Improvements are still needed in the areas of multivariable data analysis of Raman microscopy spectra.[6, 7] Systems are need to be able to break down the Raman data from complex mixtures of biological samples commonly found at crime scenes, body fluids, food and water. The fine tuning of Raman analysis techniques will ultimately allow for the true multiplexing of material detection, in particular the real time analysis of complex biological materials. Suitable analytical techniques can open up the applications of Raman-microfluidic systems for use in medical monitoring of patients, real-time monitoring of blood and saliva, studies on the effect of drugs and other compounds on organisms and even environmental monitoring. To achieve this more effectively, "libraries" of the standardised Raman spectra from many common samples, similar to those that exist already for X-Ray diffraction and FTIR analyses, must be established.
- Simultaneous manipulations and Raman signal observations can be potentially used for understanding some of the fundamental phenomena occurring when particles are suspended in liquid media. Using DEP forces, suspended particles can be brought into close proximity to one another, allowing the exchange of electrons, photons and phonons between them. DEP permits the controlled manipulation of the particle spacing, allowing observations to be made at various particle conditions of interest. As such, further research should be made into the behaviour of suspended materials for studying the behaviour of the material.

References

[1] Jeong, J.S., J.W. Lee, C.Y. Lee, S.Y. Teh, A. Lee, and K.K. Shung, Particle manipulation in a microfluidic channel using acoustic trap. *Biomedical Microdevices,* vol. 13, pp. 779-788, 2011.

[2] Basore, J.R. and L.A. Baker, Applications of microelectromagnetic traps. *Analytical and Bioanalytical Chemistry,* vol. 403, pp. 2077-2088, 2012.

[3] Adar, F., M. Delhaye, and E. DaSilva, Evolution of Instrumentation for Detection of the Raman Effect as Driven by Available Technologies and by Developing Applications. *Journal of Chemical Education,* vol. 84, p. 50, 2007.

[4] Ashok, P. and K. Dholakia, Microfluidic Raman Spectroscopy for Bio-chemical Sensing and Analysis. in *Optical Nano- and Microsystems for Bioanalytics*. vol. 10, Fritzsche, W. and J. Popp, Eds., ed Berlin Heidelberg: Springer, 2012, pp. 247-268.

[5] Ashok, P.C., G.P. Singh, H.A. Rendall, T.F. Krauss, and K. Dholakia,

Waveguide confined Raman spectroscopy for microfluidic interrogation. *Lab on a Chip*, vol. 11, pp. 1262-1270, 2011.

[6] Berman, M., A. Phatak, R. Lagerstrom, and B.R. Wood, ICE: a new method for the multivariate curve resolution of hyperspectral images. *Journal of Chemometrics*, vol. 23, pp. 101-116, 2009.

[7] Wood, B.R., P.R. Stoddart, and D. McNaughton, Molecular Imaging of Red Blood Cells by Raman Spectroscopy. *Australian Journal of Chemistry*, vol. 64, pp. 593-599, 2011.